DAMAGE TOLERANCE OF BONDED COMPOSITE AIRCRAFT REPAIRS FOR METALLIC STRUCTURES

by

RANDAL JOHN CLARK

B. Eng., Carleton University, 1995

M. A. Sc., University of British Columbia, 2000

A THESIS SUBMITTED IN PARTIAL FULFILLMENT OF

THE REQUIREMENTS FOR THE DEGREE OF

DOCTOR OF PHILOSOPHY

In

THE FACULTY OF GRADUATE STUDIES

(Mechanical Engineering)

The University of British Columbia

April 2007

Abstract

This thesis describes the development and validation of methods for damage tolerance substantiation of bonded composite repairs applied to cracked plates. This technology is used to repair metal aircraft structures, offering improvements in fatigue life, cost, manufacturability, and inspectability when compared to riveted repairs. The work focuses on the effects of plate thickness and bending on repair life, and covers fundamental aspects of fracture and fatigue of cracked plates and bonded joints. This project falls under the UBC Bonded Composite Repair Program, which has the goal of certification and widespread use of bonded repairs in civilian air transportation.

This thesis analyses the plate thickness and transverse stress effects on fracture of repaired plates and the related problem of induced geometrically nonlinear bending in unbalanced (single-sided) repairs. The author begins by developing a classification scheme for assigning repair damage tolerance substantiation requirements based upon stress-based adhesive fracture/fatigue criteria and the residual strength of the original structure. The governing equations for bending of cracked plates are then reformulated and line-spring models are developed for linear and nonlinear coupled bending and extension of reinforced cracks. The line-spring models were used to correct the Wang and Rose energy method for the determination of the long-crack limit stress intensity, and to develop a new interpolation model for repaired cracks of arbitrary length. The analysis was validated using finite element models and data from mechanical tests performed on hybrid bonded joints and repair specimens that are representative of an in-service repair. This work will allow designers to evaluate the damage tolerance of the repaired plate, the adhesive, and the composite patch, which is an airworthiness requirement under FAR (Federal Aviation Regulations) 25.571.

The thesis concludes by assessing the remaining barriers to certification of bonded repairs, discussing the results of the analysis, and making suggestions for future work. The developed techniques should also prove to be useful for the analysis of fibre-reinforced metal laminates and other layered structures. Some concepts are general and should be useful in the analysis of any plate with large in-plane stress gradients that lead to significant transverse stresses.

Table of contents

List of tables

List of figures

List of symbols

a	half crack length
p	pressure
r	radius
t	thickness or distance from centre of crack
u	crack face deflection
y	coordinate taken from centre of crack
z	coordinate taken from plate centre line
k	spring stiffness
c	spring compliance
D	plate bending constant, $Et^3/12$
G	strain energy release rate or shear modulus
K	stress intensity factor
E	Young's modulus
S	stiffness ratio, $E_r t_r / E_p t_p$
M	line moment, or moment per unit length acting on a cut in a plate
N	line force, or force per unit length acting on a cut in a plate
Y	geometry correction factor
α	normalized crack length or coefficient of thermal expansion
θ	rotation
μ	shear modulus
ν	Poisson's ratio
η	effective Poisson's ratio for transversally isotropic plate, $\eta = \nu^z \sqrt{E/E^z}$
σ	normal stress
τ	shear stress
κ	parameter arising from differential equations

Subscripts

p	plate
r	reinforcement
a	adhesive

m	membrane
b	bending
w	denotes relation to transverse deflection
ϕ	denotes relation to pressurization effects
ψ	denotes relation to transverse shear effects

Superscripts

r	reinforced result from interpolation model
n	numerical result from line-spring model
0	nominal result without including crack bringing springs
∞	long crack limit result including crack bringing springs
z	transverse property
pres.	correction for transverse pressurization
shear	correction for transverse shear

Acknowledgments

I would like to thank my advisor, Dr. Douglas Romilly, for his guidance and patience with this large body of work. This is a long thesis covering a broad topic and the last year of proofreading, editing, and journal submission has required constant attention. I must also extend my gratitude to my committee, and particularly Dr. Gary Schajer, for their support and advice. I would also like to take the opportunity to mention Mr. Don Raizenne and the staff of the Canadian National Research Council Institute for Aerospace Research, who deserve much credit for their advice and for their help in the manufacture and instrumentation of the bonded composite repair and hybrid bonded joint specimens employed in this research.

Second, I would like to thank my colleagues in the lab and office for the years of support and companionship during the (at times) destitution of student living and the inevitable low points of post-graduate work. Never again shall we eat 'fridge stew'!

And finally, I dedicate this thesis to friends and family, the people who make life a joy.

It has been a long road.

Co-authorship statement

The six main chapters of this thesis (Chapters 2 through 7) have been published or will be published as co-authored papers with authorship as indicated in the heading of each chapter. The authors have maintained a traditional supervisor/graduate student relationship through all stages of the work, with the student becoming more independent as the program progressed, as would be expected. Details are provided below for each stage of the work as they are defined by the University of British Columbia Faculty of Graduate Studies requirements for the co-authorship statement.

The identification and design of the overall research project was accomplished by Dr. Romilly, with the stated goals of the University of British Columbia Bonded Repair Program being defined in research grant applications allowing provision of laboratory equipment and supplies, travel, and training. The identification and design of the specific steps in the research work for this thesis were carried out by R.J. Clark under the supervision of Dr. D.P. Romilly and following from the goals of the greater research program.

Both the research work and the data analysis were performed by R.J. Clark, with Dr. D.P. Romilly providing supervision, guidance, and oversight. The AMRL specimen used to obtain the test results reported in Chapter 2 was manufactured by A. Albat, and the strain gauge instrumentation was installed by the technical staff of the Canadian National Research Council – Institute for Aerospace Research. Hybrid bonded joint specimen manufacture and instrumentation was carried out by R.J. Clark.

Initial manuscript preparation (i.e. completed first drafts) was performed by R.J. Clark, with Dr. D.P. Romilly reviewing the manuscripts, providing constructive comments and suggesting both technical and presentation-oriented additions to the text. R.J. Clark served as corresponding author on all submissions.

When the examining committee signs the Dissertation/Thesis Approval Form, this shall be a confirmation of the accuracy of this co-authorship statement.

Chapter 1: Damage tolerance of bonded composite aircraft repairs

R.J. Clark

University of British Columbia Department of Mechanical Engineering

1.1 Introduction

A typical bonded repair is a multi-layer composite patch bonded to a weak or damaged aircraft structure. The repair acts to reduce stresses in the damaged region and to prevent crack growth by restricting the opening of any cracks. In this opening chapter, the bonded composite repair technology applied for life extension of aluminum airframes is introduced. The chapter begins with a description of the technology, including an overview of its history, benefits and limitations, the materials used for patch construction, and application methods. Some terminology specific to bonded composite repairs is introduced, along with some basic concepts for assessing damage tolerance, durability, and assurance of structural integrity. The second section is a detailed literature review of subjects related to the damage tolerance analysis of repairs, and includes a critical review identifying predominant issues that need to be addressed in order to certify a repair. Finally, in light of the difficulties facing the technology, the objectives of this thesis are defined and the content of upcoming chapters is described.

1.2 Bonded composite repair technology

A bonded composite repair is a filamentary composite and epoxy patch bonded to a cracked or damaged aircraft structure. The original use of this repair technology was for life extension of military aircraft and rapid repair of battle damage in the field. The most common methods of application involve either pre-cured composite repairs that are bonded to the damaged structure using an epoxy adhesive, or repairs built up from layers of composite 'pre-preg', which are co-cured with the epoxy onto the underlying structure. The result is a hybrid structure consisting of the original damaged structure, a layer of epoxy adhesive, and an outer layer of composite material. If accessible, repairs are applied to both sides of the structure to prevent induced bending and hence reduce the stresses in the adhesive.

The bonded patch technology originates in bonded metal reinforcements used to strengthen fatigue-prone components in military and commercial aircraft. Metal patches have also been considered for the repair of cracked structures, but have primarily been

used for reinforcement, lowering stresses in fatigue-prone parts with simple surfaces. There are several reasons for metal patches being limited to a reinforcing role – first, it is difficult to inspect through a metallic repair to see if a crack is growing, meaning metallic repairs shouldn't be used over riveted plates or to repair cracks. Second, it is difficult to apply enough reinforcement to prevent crack growth using a matching material as it requires at least a doubling of the thickness of the structure to return the strength, and perhaps an even thicker patch to prevent induced bending. And finally, it provides a second metallic surface that must be chemically treated for bonding. It will be demonstrated that the durability (i.e. the long term strength in service) of adhesive/metal bonds is a formidable obstacle to bonded repairs. In practice, boned composite repairs are more commonly made from composite materials such as boron-epoxy, which is three times stiffer and much stronger than aluminum, and hence can be made very thin compared to the original structure. Boron-epoxy also provides the advantage of inspectability, as eddy-current probes can be used to detect crack growth through a patch. There is also significant interest in GLARE (a fibreglass and aluminum laminate) as a low cost material that is easier to apply. GLARE has lower modulus and strength than boron-epoxy but is more impact-resistant and is reasonably compatible with eddy-current inspection. A final advantage of a composite repair is the ability to tailor the stiffness of the patch to the stresses in the structure, allowing one to provide reinforcement only in the direction required. This minimizes changes in the load flow within the broader aircraft structure caused by the application of the repair, as an overly stiff patch may detrimentally attract load to the region in which it is applied. Carbon fibre reinforced polymers have also been considered as a repair material but are limited by concerns regarding larger thermally induced strains, corrosion, and inspectability.

A repair attracts loads from the surrounding structure due to its high stiffness, which is the means by which it provides reinforcement. Generally, the larger and stiffer the repair, the more it attracts loading from the underlying structure. The load transfer from the structure to the repair occurs through adhesive shear stresses that build up near the edges of the repair, and about the crack. Accordingly, the repair acts both to reduce stresses in the vicinity of the crack, and prevent the crack from opening. These beneficial effects may be partially offset by thermal stresses arising both during patch application and during service due to mismatched thermal expansion coefficients in the patch and structure materials, and by attraction of loads from the surrounding structures due to the increase in stiffness caused by the patch. In this thesis the term repair will refer to a bonded patch used to repair a cracked or damaged structure, and reinforcement will apply to a patch used to strengthen an undamaged or sound structure.

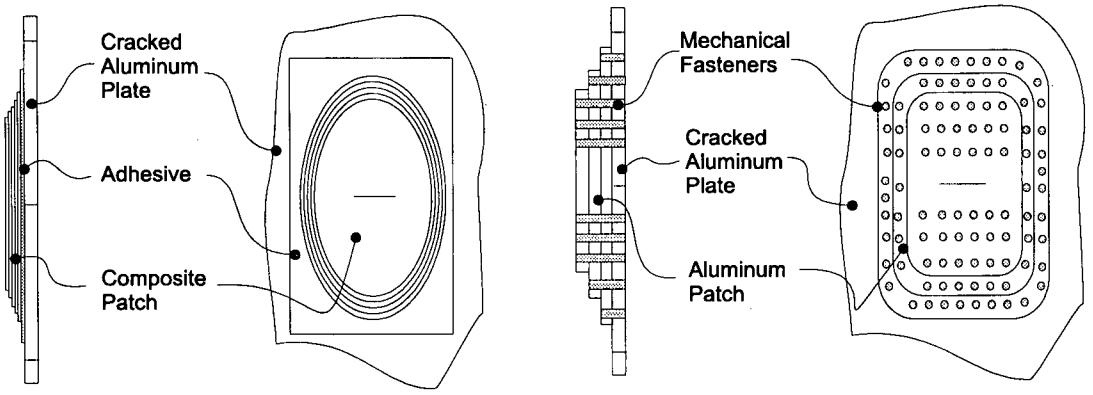

Figure 1-1: Bonded (left) and mechanically fastened (right) repairs

Figure 1-1 illustrates a bonded and a conventional repair. Bonding offers many advantages over mechanical fastening. The principal advantages are the smooth load transfer provided by bonding, the high stiffness and hence high load transfer capability of the composite materials, and the restraint that a bonded patch provides against crack opening. These advantages make possible a many-fold increase in fatigue life. Other advantages include improvements in manufacturability, cost, and inspectability. Despite this potential, the bonded composite repair technology has not seen widespread use outside of military applications. Examples of commercial application include a Boeing demonstration program where small reinforcing doublers were applied to sound structures to test the technology for the fast repair of engine cowling bird-strikes and for localized fuselage fatigue enhancement or repair of localized damage. Another example is the application of very large bonded composite reinforcements during the overhaul of Lockheed L-1011 passenger aircraft to repair cracking doorframes, enabling the return to service of a fleet of aircraft. Primarily, the issues of damage tolerance and bond durability prevent airworthiness certification and widespread use [1,2]. Damage tolerance refers to the ability of a structure to hold up under design loads in a damaged state without failure or excessive deformation before the damage can be detected and repaired. Damage can arise from a number of sources including fatigue, corrosion, manufacturing flaws, or accidental loads such as impacts. Durability refers to the ability of a structure to withstand environmental exposure and mechanical loading without undue or unpredictable degradation. This is a significant issue for bonded repairs, as poorly applied adhesives are prone to failure under service loads and environmental exposure. It is presently very difficult and costly to certify a major bonded composite repair, as it requires all of the damage tolerance, materials and process controls that are necessary for the certification of any primary composite structure.

1.2.1 Assurance of structural integrity

Regulatory authorities are rightly concerned about the structural integrity of bonded repairs over the life of the structure. Repairs are generally applied to highly loaded structures that have already experienced significant damage. By FAR 25.571, damage tolerance analysis is required for bonded composite repairs and is one of the three means of assuring the structural integrity, as summarized below [3].

(1) Safe-life: cracking will not occur during the life of the repair,

(2) Fail-safe: multiple load paths prevent catastrophic failure before detection, or

(3) Damage tolerance: inspections during service ensure adequate residual strength.

It is a widely held view that a damage tolerance analysis is the only way to ensure the structural integrity of a bonded repair [3] for Principal Structural Elements (PSE) and Structurally Significant Items (SSI) on an aircraft. A PSE is an element of an aircraft whose failure could result in catastrophic failure of the aircraft. An SSI is a structure that contributes significantly to the carrying of flight, ground, or pressurization loads. In this thesis, we will simply refer to these safety-critical components as primary structure. Safe life methods alone are not feasible for repairs applied to cracked structures, as both crack growth and disbonding are likely to occur. Stopping crack growth requires significant restraint against crack opening, and hence, large adhesive stresses near the crack, which will promote disbonding. The best that can be achieved is a compromise to optimize the life of the repair. Baker has proposed that a safe life approach to certification could be used about the edges of a patch [3] to ensure that adhesive disbonding will not occur under environmental and fatigue loading. Safe life methods may also be useful for bonded reinforcements that act to strengthen weak or weakened structures without cracks. This would preclude an analysis of disbonding from the edges of the repair or reinforcement, but would require stresses to be kept very low, which can be accomplished by tapering the edges of the patch. The remaining method, damage tolerance, is then the method of choice and will require a means for predicting the rate of damage accumulation and load-carrying capacity of the patch, such that failures are preventable through a program of inspections during service.

1.2.2 Durability

Durability issues complicate the damage tolerance assessment of bonded joints [4-10]. Durable bonds predictably withstand wear and tear; they last, are stable, and will degrade in a consistent manner. Poorly formed bonds exhibit unpredictable and varying damage rates and are sensitive to environmental conditions, particularly intermittently hot and wet environments. This sensitivity is due to the nature of the adhesive/metal oxide interface, and oxide instability in the service environment [11-21]. As chemical bonds at the

adhesive/oxide interface tend to hydrate, surface treatments are designed to increase their strength in the presence of water and ensure a reversible reaction, allowing them to re-form when the solvent (water) is removed [22]. Process variability, contamination, and surface treatment errors result in reduced durability. Variations in primer thickness, silane surface treatment concentration, surface abrasion, and etching treatments can impact durability [13]. Metal oxide layers may be initially weak or corrode in service [15]. Adhesive porosity weakens the joint and speed the transport of water [23-26], and results from gases or liquids entrapped during assembly, evaporation of water absorbed by the adhesive prior to curing, and by entrapment of gases formed by chemical reactions. Accordingly, bond degradation under the effects of stress, moisture and temperature depends greatly on the control exerted over shop cleanliness, material storage, surface preparation, and other aspects of design and fabrication.

Bond durability is difficult to assess, as there is no non-destructive test for it. Instead, it is evaluated by destructive testing of 'travellers' – test coupons made with adhesives from the same lot and from aluminum or composite adherends that have received a surface treatment concurrently with the aircraft structure [16]. Physical tests in a hot and wet environment, performed on wedge specimens made from the traveller, ensure the durability of the adhesive/oxide interface. The assumption is that loss of durability due to bonding process errors or contaminated materials will be detected by early failure of the traveller. A poor traveller result must be seen as a reflection of the facilities' process control and quality assurance regime and not just the lack of fitness of an individual component. The goal is to reliably produce sound bonds with controlled processes, and to have a track record of good results – possibly a challenge for smaller repair facilities or in the field.

Adhesive bonds are a common joining method for aerospace structures, and methods exist to ensure bond durability. As such, this issue alone should not impede certification. The required quality assurance controls, training, and extra steps in the manufacturing process are onerous but not undue given the risks. The main issue for bonded repairs when compared to other bonded structures is the existence of cracks in the underlying structure, and the presence of a highly stressed bond line that might severely test a poor bond. In this thesis, the issue of bond durability will only be examined indirectly, by providing a means for the assessment and hence reduction of the adhesive stresses (particularly peel stresses) in the region of the repaired crack.

1.3 Literature review

In this section, the author isolates the elements that are required for the damage tolerance analysis of a repair, and reviews the literature for significant experimental and analytical work that has relevance to the subject. The section begins with a review of

mechanical testing that has been carried out to evaluate the repair technology, a review of the failure mechanisms that have been observed, and an assessment of the regulatory controls and requirements for damage tolerance analysis. The section continues with a review of techniques available for assessing the mechanical behaviour and hence the life and strength of a repair, and concludes with a critical assessment of the capabilities and shortcomings of the available methods for damage tolerance assessment of a repair.

1.3.1 Repair experiments and failure modes

Many experiments have been performed to investigate failure mechanisms, to demonstrate the predictive performance of models, and to evaluate repair materials and mechanical phenomena in a repair. A widely used repair specimen is the Australian Aeronautical and Maritime Research Laboratories (AMRL) specimen, described in detail in Appendix B. This test article consists of two repaired plates that are bonded to an aluminum honeycomb employed to restrict the bending induced by the neutral axis offset of the repair and to model the support of underlying structures that often exist in highly stressed sections of aircraft. Baker has published experimental results for the AMRL specimen that illustrate the effects of cure cycle parameters [26,27], disbonding [26,28], patch shear deformation [27,29], adhesive plasticity [29], and test temperature [26] on performance. In Canada, the AMRL specimen has been used by the National Research Council - Institute for Aerospace Research (NRC-IAR) to examine the effects of load spectrum, compressive loading, and adverse environments on patch performance [30,31], and by Albat and Romilly [32] to evaluate thermal strains. Without bending, the failure mode of the repair has consistently been continued cracking of the existing crack in the aluminum plate with accompanying adhesive disbonding. Testing of double lap-shear specimens has been used to investigate the effects of patch shear deformation and adhesive plasticity on the apparent stiffness of the patch in the region of the crack [29]. Patch shear deformation and adhesive plasticity have been shown to reduce patch life by reducing the restraint against crack opening imposed by the repair. It has also been shown that increasing the cure cycle temperature and time can impose two penalties on patch performance; 1) tensile thermal residual stresses from a mismatch in thermal expansion coefficients can accelerate fatigue crack growth, and 2) crack growth retardation is reduced due to annealing of crack tip plasticity-induced residual stresses. Sharp, Clayton, and Clark [37] have examined the effects of adhesive infiltration into the crack, which was found to increase the stress required to open the crack, and hence improve the fatigue life.

Researchers have also examined bonded repair issues using other types of bonded repair specimens. Poole, Lock, and Young [33] have investigated fatigue damage propagation in thick aluminum plates repaired with graphite/epoxy patches. Similar to the AMRL

specimen, repaired plates were bonded to a honeycomb core and tested in pairs to restrict bending. They examined the effect of the FALSTAFF loading spectrum on repair performance, and compared the results to boundary element analyses that included the effects of adhesive plasticity. The results showed lifetime improvement by a factor of 3.2 for the FALSTAFF loaded specimen, and up to 17 for a constant-amplitude cycled specimen when compared to an unrepaired sheet. Denney and Mall [34-36] have investigated boron/epoxy repairs applied to a single side of a thin centre-cracked aluminum panel, where patch bending is a significant factor due to an offset of the neutral axis. They investigated the effect of variously sized disbonds at different locations within the repair, and concluded that disbonds over the crack reduce patch life whereas disbonds away from the crack are not detrimental. They suggested that disbonds away from the crack may increase patch life by reducing the apparent size and stiffness of the patch and hence the amount of load it attracts from the surrounding structure. Failure occurred due to crack growth in the aluminum and little disbonding was noted. Klug et al. [38] performed a similar test using thick and thin unbalanced repairs, and noted significant disbonding near the crack and near the edges of the patch for a thick repair and only near the crack for a thin repair. For these specimens, the patch was not tapered, leading to increased stresses about the edge of the repair.

Jones, Chiu, and Smith [39] have presented a thorough review of the failure modes and locations of damage experienced in laboratory testing and military use of bonded repairs. While most of the work reported in the literature examines the primary failure modes of the repair, i.e. substrate cracking and accompanying cohesive disbonding of the adhesive, they conclude that the assessment should also include composite failure modes such as fibre failure, adhesive failure, cohesion failure at the patch-adhesive interface, adhesive failure at the adhesive-substrate interface, and inter-laminar failure and delamination. In practice, unexpected failure due to crack growth and disbonding about the crack has not been a problem, as mitigation of this form of crack growth is the primary design goal of the repair and it is well accounted for in the analysis, testing and inspection regimes. Another factor is that the technology has mainly been limited to double-sided repair of flat plates, to structures with bending restraint, and to structures with residual strength. Unexpected composite failures have usually only occurred during laboratory testing for evaluation of a repair, rather than during service. FAA Advisory Circular 25.571-1A identifies the failure modes and locations of damage that must be considered, and requires the assessment of the effects of impact damage, inter-ply delamination, and disbonding on the composite, adhesive, and substrate.

Composite and adhesive damage mechanisms are most likely to arise in areas of high stress, or due to impact damage or manufacturing flaws. Generally, the fatigue strength of a composite laminate is high unless it is damaged by environmental degradation or

impact, or it is loaded in a weak direction. One would not expect growth of inter-ply or impact damage unless it is accompanied by fibre damage or occurs in a region experiencing significant bending and through-thickness stresses, compressive loads, or very large transfers of load through shear, such as might exist near a repaired crack or about the edges of the patch. In practice, this has proven to be true, with experimental results suggesting that delamination growth from impact damage or manufacturing flaws away from load transfer regions is minimal [34].

A final concern is the possibility of undetected widespread or multi-site fatigue damage in the region of the repair, which must be considered when designing repairs for older structures. The Australian Air Force has had some experience in crack patching with widespread fatigue damage [1], and Molent and Jones [43] have successfully applied bonded repairs to heavily damaged transport aircraft lap joint sections, demonstrating that the technology can be applied in areas of widespread or multi-site damage.

1.3.2 Certification and damage tolerance analysis

Regulations require the damage tolerance analysis of all components of the repair system. According to FAA Advisory Circular 25.571-1A, the damage tolerance evaluation must "define the loading and the environmental conditions, extent of damage or degradation of the structure, adhesive and repair, conduct of the associated structural tests or analyses, or both, used to substantiate that the repair design objective has been achieved, and establish data for inspection programs necessary to ensure detection of damage". Damage tolerance assessment is required for impacts, manufacturing flaws corresponding to limits of inspection methods, and progressive failure near the crack in the underlying structure. The result is that the certification of a repair must meet most of the requirements for the design of a new composite structure. Baker [3] has postulated that the outer edge of the repair could be treated in a safe life manner, with the inner region over the repaired crack being subject to damage tolerance assessment.

The somewhat unpredictable nature of the failure mechanism and strength of composite structures has lead to the general requirement for physical testing of representative specimens to catch unexpected failure modes. Requirements for certification include the documentation and control of the manufacturing process such that the test articles closely match the actual composite parts in service. The only possible exceptions to the rule are for structures that are very similar in loading, composition, and manufacture to ones that have already been tested and certified. Jones et al. [39] have suggested a policy for damage tolerance assessment based on FAA requirements, by incorporating a two-stage approval process whereby a repair may be certified for a short term based on static strength analysis and testing. Physical testing of representative structures in a representative environment would be required for cases where sufficient test data or

operational experience from similar structures was not available. Continuing operation of the aircraft would require the registration of a detailed damage tolerance analysis including an inspection plan.

Jones et al [39] stress the need to perform residual strength analysis based on the limits of the inspection criteria, rate of damage growth, and strength of the damaged structure, including the possibility of wide-spread fatigue damage (the possibility of many cracks smaller than the detection limit). FAA circular 25.571-1A effectively makes this a requirement. It is stated that, unless stresses are so low that serious damage growth is extremely improbable, the structure must be shown to always be capable of supporting the design limit loads, and that the rate of damage growth and the inspectability of the structure provide a practical basis for an inspection program. Experimental testing of similar articles in representative environments must support the analysis. Damage may be simulated by saw-cuts, manufactured disbonds or delaminations, and by low-energy impacts, with the caveat that the damage must be placed in regions of maximum stress, where the residual strength of the structure will be most affected, or in areas where the additional compliance caused by damage will cause increased loads in surrounding structural elements and elevated stresses in the region of the patch. It is also required to examine the consequences of failure – e.g. structural failure and redundancy or criticality of the component, engine intake of loose parts, excessive drag, etc.

Jones et al [39] also outline the analysis and testing requirements for static strength analysis and damage tolerance of the composite patch itself. Design allowables for the laminate must be generated through testing in appropriate environments, unless such data already exists or service experience shows that the performance of the material is unaffected. In addition, the static strength and damage tolerance of the composite must be tested as an entire system for the given application. The testing must include load dwells, and the specimens must be produced according to the production specifications. They also emphasized the need to include several composite-specific failure modes in the damage tolerance analysis of the patch system. These include failure by fibre failure, adhesive failure, cohesion failure at the patch-adhesive interface, adhesive failure at the adhesive-substrate interface, and inter-laminar failure.

1.3.3 Mechanics of a repair

Several methods are available for the stress analysis of a bonded repair, including both numerical and closed-form approaches. Many researchers have used finite element analysis to investigate the mechanical response of a repair. Early studies by Ratwani [44] used three-dimensional linear finite element analysis to develop correction factors to account for bending, and Jones [45] developed 'three layer' finite element models that required fewer computational resources by modeling the underlying structure and the

repair as plates, and by modelling the adhesive as shear and extensional springs. More recent work includes nonlinear analysis performed by Klug et al. [38] and by Naboulsi and Mall [46,47], where three-layer solutions have been used to assess the effects of nonlinear deformation and stress-stiffening in a single-sided repair. These techniques have the advantage of allowing evaluation of complex geometries and loading, but tend to be computationally demanding due to the large number of elements required to accurately model the crack in the substrate and the stresses in the load transfer regions of the patch. They also demand a large amount of operator time to accurately model a repair scenario. An alternative choice is the boundary element method, whereby the patch and plate are modelled as cracked plates, with the deflection, plate loads, and stress intensity being characterized by Green's functions, and the adhesive being modelled as independent shear and extensional springs. Erdogan and Arin [48] first used the boundary element techniques to analyze the problem of a disbonding patch bonded to a cracked aluminum plate without bending. Ratwani [44] has shown that this model provides accurate results for determining the stress intensity when compared with finite element analysis and experiments. Dowrick, Cartwright, and Rooke [49] and Young, Cartwright, and Rooke [50-52] have developed a boundary element model applicable to highly orthotropic patches. Here, the patch is divided into cells, each of which is 'riveted' at regular intervals to the underlying plate. The 'rivets' each have a shear spring stiffness determined from the adhesive thickness and shear modulus, and the area of the patch represented by the cell. This model also has the capability to include nonlinear adhesive response. Poole, Lock, and Young [53] have verified this model against experimental results for a graphite/epoxy patch applied to a thick cracked plate. More recent efforts have applied the dual method, a means of simplifying the analysis of the region near the crack, to solve the problem of combined bending and extension of a repaired plate [54,55].

An analytic method for analysis of a repair is to consider the load transfer region about the crack separately from the one about the edges of the repair, and is known as the two-step method [56]. The presence of the crack and its accompanying adhesive load transfer region is the distinguishing characteristic for a repair versus a reinforcement, differentiating between the safe life (outer) and damage tolerance (inner) regions, and allowing significant conveniences to the analyst. The implicit assumption is that the change in compliance introduced by the crack and disbond do not significantly affect load transfer about the edges of the repair. This is justified only for large and stiff repairs, where limited disbonding or crack growth do not greatly affect the interaction of the patch and the greater structure of the aircraft. Figure 1-2 shows these load transfer areas.

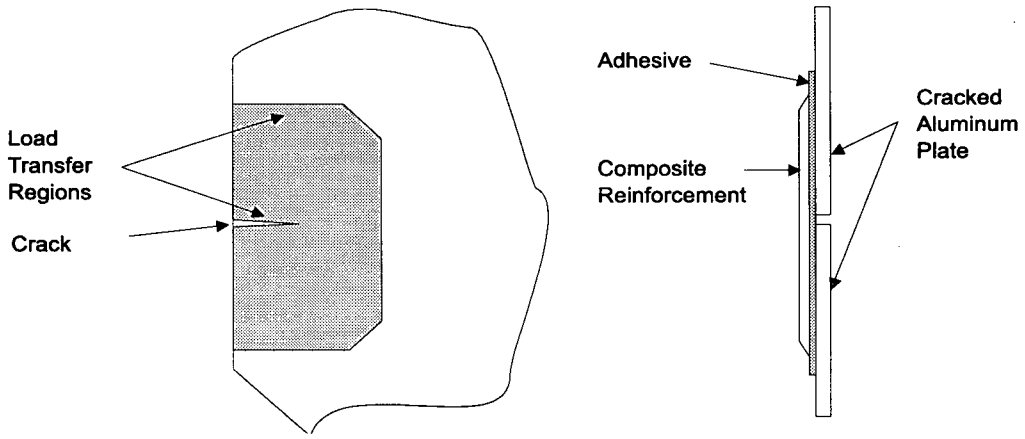

Figure 1-2: Load transfer regions

For a stiff repair the load transfer regions are small compared to the planar dimensions of the patch, effectively become independent, and may be analysed separately [56-60]. The problem then resolves into two steps: (1) finding the stresses in a reinforcement, and (2) determining the state of the repair by introducing a crack and solving the resulting crack bridging problem. This two-step process simplifies the analysis, making closed-form solutions feasible. The state of the repair may then be determined by superposition of the reinforcement and fracture mechanics solutions. This process is shown in Figure 1-3, where (a) shows the stresses in a reinforced plate, (b) shows the stresses resulting from a crack-bridging analysis by applying the crack-plane stresses from (a) as crack-opening stresses, and (c) shows their superposition.

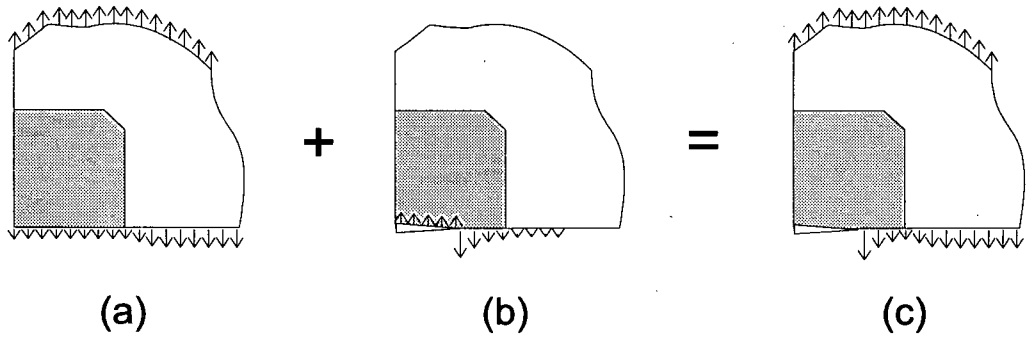

Figure 1-3: Two step method

In the first step, the patch acts as a 'reinforcement' and may be considered as a stiffened inclusion. The inclusion attracts load - the larger and stiffer it is, the more load it attracts from the surrounding structure. Analytical solutions allow the calculation of the distribution of stresses within and about the stiffened inclusion, providing the stresses in the underlying plate. Due to the reinforcing effect of the patch, these stresses are reduced from the remote applied stresses. In addition to the stresses resulting from the inclusion

analogy, the reinforcement may experience detrimental bending stresses due to a neutral axis offset, and due to thermal residual stresses from curing of the adhesive. For the second step, a crack is introduced and the reinforcement, now referred to as a 'repair' is modelled as springs bridging the crack. Here, the stresses found in the first step are applied as crack opening tractions and the springs restrict the opening of the crack reduce the stress intensity. This crack-bridging problem occurs often in materials science, and its solution determines the stress intensity at the crack tip and the adhesive stresses near the crack, characterizing the effects of adhesive load transfer about the crack.

Rose refined this inclusion analogy and applied it to the crack-patching problem [56], applying the analytical result for a stiffened elliptical inclusion developed by Eshelby [61]. In addition to the stresses resulting from the inclusion analogy, patch bending and process-induced thermal residual stresses may also occur. Patch bending results from the offset in neutral axis caused by the patch, and may be estimated using simple beam theory [44]. Residual stresses occur when the patch application process requires an elevated temperature cure cycle and the patch and plate have differing thermal expansion coefficients. Residual stresses are particularly large for laboratory specimens which are often cured without restraint against thermal expansion. The residual stress in the region of the crack may be calculated by analytical means, where solutions have been provided by Rose [60] for an isotropic repair, by Wang et al [62] for a circular orthotropic repair, and by Albat and Romilly [63] for a tapered repair. These stresses depend upon the cure temperature of the adhesive and the degree of physical restraint available during curing, i.e. whether the cure was accomplished with local heating or immersion in an autoclave and on the support conditions of the cracked plate. Local heating and mechanical restraint can significantly reduce residual stresses. Without support, thermal strains can result in significant bending, or warpage. To calculate the thermal residual strains, it is necessary to know the effective stress free temperature, i.e. the temperature at which thermal residual strains vanish. Albat and Romilly [32] tested an instrumented AMRL specimen, and found an effective stress free temperature of 81 °C, significantly lower than the often-used cure temperature.

For the second part of the analysis, a crack is introduced and the reinforcement, now referred to as a repair, may be modelled as springs bridging the crack. Here, the stress found in the first step is applied as a crack opening traction and the springs bridging the crack partially prevent the crack from opening, reducing the stress intensity. This crack-bridging problem occurs often in materials science. Its solution determines the stress intensity at the crack tip and the adhesive stresses near the crack, and characterises the adhesive load transfer about the crack, allowing the determination of the rate of crack growth and near-crack disbonding. Crack-bridging calculations may be accomplished

using finite elements, boundary elements, or analytical solutions based on interpolation between limit states.

Exact analytical solutions exist for the limiting cases of a patch over a very short crack or a very long crack. No exact closed-form solution exists for an arbitrary length crack. For small cracks, the stress intensity closely approaches the basic fracture mechanics solution for a crack with an opening pressure equal to the edge traction found in the first step of the analysis. This solution becomes less valid as the crack length, and hence, the crack opening displacement, increase. In the limit state of a very long crack, the crack opening displacement well away from the crack tip can be considered to be constrained only by the stiffness of the patch bridging the crack, and the state of the crack tip becomes independent of crack length. Rose [60] has examined this problem and developed an interpolation model which asymptotically approaches these two limit cases, and provides accurate results for an arbitrary crack length. Cox and Rose [64] have extended this approximate solution to the cases of near-tip reinforcement and elastic-perfectly plastic springs. One considerable limitation of this method is that the reinforcement is assumed to act at the faces of the cracks.

Baker [3] has investigated the effects of disbonding and temperature on fatigue crack re-initiation and growth. In this study, he developed a few simple relations for estimating the effect of a measured disbond on the crack-tip stress intensity and patching efficiency. Here, the limit case of a long crack is modified to account for the additional compliance of a disbonded portion of patch. The disbonding geometry is limited to a disbond of a constant size extending across the entire patch. Building on this work, Albat and Romilly [65] developed solutions that are applicable for any degree of patch disbonding and include the effect of thermal residual stresses, patch lay-up, and cracked plate geometry. Thermal residual stresses were shown to contribute significantly toward reducing patch efficiency, particularly for laboratory specimens, where little restraint exists during the curing cycle to reduce thermal residual stresses. Clark and Romilly [66] tested this model against a boundary element model and found that the results were valid for a wide range of patch stiffness parameters, and extended the models to include adhesive plasticity and allow the calculation of adhesive stresses and the load carried by the patch.

1.3.4 Damage mechanics

Here, we seek to define the best practice for predicting damage growth and failure of the various components of a repair: the plate, the adhesive joint connecting the plate and patch, and the composite patch itself. The damage mechanics of a metal plate, being a topic of undergraduate or graduate courses, are generally well understood. For a cracked plate, fracture and fatigue may be characterized by the stress intensity, but difficulties can arise due to load interaction and crack closure, load spectrum, adverse environments, and

plasticity or thickness effects. These topics often require the use of experiments for evaluation of structural integrity under realistic conditions; examples are the load spectrum testing of airframes and the use of empirical models for crack-closure. For bonded repairs, Duong and Wang [67] have noted that inadequate methods for characterizing fatigue of cracked plates experiencing bending loads are a significant impediment to life assessment. They have proposed the use of a modified stress intensity, developed by linear interpolation between two limit states where the crack growth rate can be accurately assessed: for a crack experiencing only a membrane stress intensity, and a crack with equal membrane and bending stress intensities. The method provided good results when applied to the analysis of unbalanced repairs.

Mechanical analysis of bonded joints is a complex subject, as the adhesive stresses are related to the loading, the bending and extensional stiffness of the adherends, and the elastic/plastic properties and thickness of the adhesive. In general, both shear and peel (transverse normal) adhesive stresses arise. For a repair, it is necessary to assess both the adhesive stresses and the stiffness of the patch as it acts to restrict the opening of the crack. Closed-form elastic and elastic/perfectly plastic solutions for the shear and peel stresses are available for simple geometries, usually developed by modeling the adhesive as a row of shear and extensional springs connecting the adherends. The standard techniques are the shear-lag solution for lap joints developed by Volkerson [67] and the bending analysis of Goland and Reissner [68]. Hart-Smith [69] has used these to develop elastic-plastic failure criteria and analytical closed-form solutions for several practical geometries. Delale et al. [70] and Bigwood and Crocombe [71] have improved on these solutions by including mechanical coupling of the bending and extensional responses of the joint. Coupling occurs due to moments resulting from the adhesive shear stress acting at the adhesive/adherend interface, and from adhesive shear stresses induced by rotation of the adherends under bending. In practice, finite elements are often used to analyse the complex geometries that arise in the design of airframes, with the closed-form equations used to inform the design process. The methods of Hart-Smith have been prevalent in the analysis of bonded repairs. For life assessment, bonded joints are often treated in a safe-life manner, where peak stresses are controlled by tapering the adherends, using a long overlap length, and choosing an appropriate adhesive thickness. This approach does not work for a repair, as it is usually not possible to reduce the adhesive stresses near the crack to the point where safe-life methods may be applied.

Damage mechanics analysis of bonded joints poses similar challenges. Here, two modes of cracking may occur, cohesive and adhesive. Cohesive failures occur when the adhesive fails by yielding and cracking, while adhesive failures occur at the bond line. There is debate over whether pure interfacial failure can occur or if it instead occurs by low-energy fracture of the weaker material due to constraint from the stiffer and (usually)

stronger material. Adhesive failures should not occur unless a poorly prepared surface results in low durability, as discussed in section 1.2.2. Several different parameters have been used to characterize adhesive fatigue and fracture, including the plastic or elastic strain range [e.g. 59], strain energy release rate [e.g. 38], or stress intensity. The strength and stiffness of an adhesive results from molecular and inter-molecular forces, exhibiting strain-rate, moisture, and temperature sensitivity, while the stresses near the fracture zone are dependent on the joint geometry, including the location of the crack within the adhesive and type of loading. Illustrating the effects of the crack location on fracture, for a boron-epoxy repair, interfacial crack growth may require 230 J/m^2 compared to over 3000 J/m^2 for cohesive failure [3].

Fundamentally, the use of energy-based fracture parameters is complicated by the dependence of the stresses on the geometry and composition of the joint. This violates the similarity criterion, whereby in fracture mechanics it is assumed that cracks have similarly-shaped stress distributions regardless of crack length, position, or geometry. This explains why different geometries and loading conditions lead to different critical strain energy release rate and disbond growth rate parameters [66, 72], even though the same adhesive has been employed. Strain energy release rates are used to predict fracture and fatigue of materials for which the rate of plastic work with disbond or crack growth is either negligible, or the rate of plastic work is constant, for an increment in crack growth [73]. For bonded joints, this means that there should not be a discernible critical strain energy release rate as a material property – instead, the adhesive must be evaluated on a case-by-case basis where test data must be developed for a particular joint composition. Hart-Smith [69] has noted that strength under static loading depends mainly on the adhesive strain energy, and advocates an energy-density criterion for crack growth, which may necessitate a detailed assessment of the elastic/plastic strains in the adhesive at the tip of the crack. This method explicitly considers the strains near the crack tip, and has been used [2] to develop damage tolerance criteria for bonded joints. An alternative approach is to use alternating plastic strains, or an approach based on the rate of plastic work with disbond growth. Either alternative directly accounts for the effects of geometry. An additional advantage is that the adhesive shear strength provides a very simple and direct approach with which to include the effects of temperature, loading rate, and environment on disbond growth rates. It is noted that test data is readily available for FM73M, the adhesive most commonly used in bonded repairs.

Strength and fatigue analysis for axial loading of unidirectional composites is relatively straight-forward. Accurate estimates of the ultimate strength of the laminate may be found by considering the strain in the fibres and matrix to be equal, a reasonable assumption for high stiffness laminates with long fibres [74]. For a polymer-reinforced composite such as boron-epoxy, composite failure occurs when the stress in the boron

fibres reaches its maximum, corresponding to a nominal tensile stress in the orthotropic solid. This is the principal strength of the composite. Fatigue of composites under such loading may be characterized by a stress-life (S-N) diagram, with small reductions in stiffness and strength occurring as the matrix cracks and delaminates near fibre breaks and stress concentrations. When bending is a significant component of the load on the plate, transverse stresses and interlaminar failure have a detrimental effect on fatigue life and strength. Tensile interlaminar stresses develop due to the buckling of fibres on the compression side of the plate, and transverse stresses may cause interlaminar failure.

The mechanisms of failure under transverse loading are matrix failure by fracture and interfacial failure, and by fibre splitting if they are weak in the transverse direction [74]. Stiff fibres lead to stress concentrations in the matrix, causing it to fail before the nominal transverse stress exceeds the strength of the matrix. Models for predicting such failures are often developed by using a periodic fibre distribution to characterize the peak stresses, whereby a stress concentration or strength reduction factor is applied to the matrix and used as a failure criteria for the composite. From mechanical testing and fractography, it has been shown that the exact geometrical distribution of the fibres has a significant role, and more recent attempts to predict failure strength have used finite element analysis to predict the matrix stresses given a randomly determined fibre spacing or by arranging the fibres in a configuration consistent with the manufacturing technique [75]. In all cases, the thrust of the analysis is the same, to predict the stresses in the matrix and fibre given a nominal loading, and then develop failure criteria.

1.3.5 Critical analysis

Airworthiness certification of a bonded repair requires the assessment of the resulting structure's damage tolerance considering all plausible damage sources and failure modes, including an inspection plan to detect damage growth before catastrophic failure. Bond durability is a persistent problem, but one that can be ameliorated by adopting best practices in the manufacturing processes and reducing the adhesive stresses to whatever degree possible. Baker [3] has argued that the design of the outer, tapered portion of the patch could be governed by safe life principles, but the fitness of the design can also be assured through damage tolerance analysis, which would ensure adequate life in the instance of an impact or manufacturing flaw. In this region the repair does not vary significantly from other types of bonded joints, and an analysis suitable to certification should be possible by standard methods. It is possible, however, that the inner and outer regions of the repair could be assessed independently, as Denney and Mall [34] have shown that damage in this outer region can actually improve the efficiency of the repair by reducing stresses in the region of the crack. For the inner part of the repair, applied over the original damaged aircraft structure, three types of damage must be assessed: 1)

cracking in the structure beneath the repair, 2) disbonding of the adhesive joining the patch to the structure, and 3) interply delamination or composite failure in the region of the crack. The issues that prevent widespread use of the technology are related to these final three forms of damage, with near-crack disbonding and composite failure being issues that have lead to unexpected rapid failure during proof testing and fatigue life assessment. To address these issues, the damage tolerance assessment must consider all of the following elements, which need to be in place to assure structural integrity of a repair.

(1) Loading conditions: assessment of the fatigue loading, service environment, and thermal stresses. The repair must be able to carry the design limit load.

(2) Failure modes: the type of damage, location, and mechanisms for growth must be identified. Crack growth and accompanying disbonds are expected, but damage may also arise from process errors (e.g. adhesive voids) or accidents (e.g. impact damage).

(3) Damage parameters: means of calculating parameters such as stress intensity that are used to predict damage growth rates with a given service loading and environment.

(4) Test data: empirical relations correlating damage growth rates observed in testing with the damage parameter, and structural test data for representative repair specimens.

(5) Inspection methods: inspection methods must be qualified to ensure that they can detect the damage and that the inspections will occur often enough to prevent failures.

All of these elements must be combined to ensure that the structure will meet a set of safety goals, which may be statistical and/or deterministic in nature. An example of a very broad statistical goal would be a 10^{-7} chance of catastrophic failure over the operational life of the part, which is a rough industry guideline for primary structures. An example of a deterministic goal would be the specification that the part must be capable of withstanding the design limit load throughout its working life. Widespread use of bonded composite repairs will not occur until all of these elements and a set of acceptable safety goals can be presented in a form that is easy to understand and apply.

An assessment of the service loads in the structure is an element of the analysis. For aircraft manufacturers, load data is available in design and flight test documents. For overhaul and repair facilities, this data is often not available, and loads must be estimated by analysis of the existing structure. Here, the goal is to return the static and fatigue strength without disrupting the flow of load in surrounding structures. When compared to riveted repairs, the only unique issue is the assessment of thermal stresses arising from mismatched thermal expansion coefficients.

There are three types of damage growth unique to a bonded repair: 1) substrate cracking and accompanying disbonding, 2) interply delamination, or 3) composite failure. The

damage tolerance analysis requires accepted methods by which damage parameters may be calculated and compared with test data in order to predict the life and strength of the repair. The two-step process and the reduction of the mechanics of a repair to a crack-bridging problem are fundamental concepts for assessment of these types of damage growth, but several difficulties arise. These include: a) thickness effects in fracture mechanics energy analysis, b) the coupled and geometrically nonlinear membrane and bending responses of the repair, c) difficulties inherent in the stress analysis of hybrid bonded joints, and d) complications in predicting the fracture and fatigue of bending plates, adhesive joints, and interlaminar failure of composites. These problems are inherent to the mechanical analysis of a repair and will be discussed in more detail below.

The final element is identification of all damage to the structure, including initial damage, repair application flaws, and damage accrued during subsequent service. The existing damage may be assessed by the conventional means of visual, dye penetrant, and eddy current inspection, with macroscopic defects such as fatigue cracks and corrosion characterized by measured defect sizes and locations. Widespread fatigue damage and/or undetectable discrete cracks must be assumed to exist, and included in the worst possible locations. Guidelines for the design of new aluminum aircraft structures exist whereby small cracks of a specified size are assumed to exist at rivet holes and other stress-raisers, and certification requires life assessment under the assumption that these flaws are present. For widespread damage, undetectable flaws should be assumed to exist at locations adjacent to stress-raisers, and the possibility of crack interaction should be investigated.

Several deficiencies may be noted in the application of the two-step analysis process and interpolation model. The first problem is in the analysis of geometrically nonlinear bending of a repair. The two-step method relies on superposition, and, strictly speaking, is only applicable to linear problems. Rose [60] has calculated the long-crack limit for the strain energy release in the presence of nonlinear bending by applying composite beam theory. This calculation provides the total available strain energy but does not separate it into bending and membrane components. A general method is required for the treatment of geometrically nonlinear bending. Perhaps worse, energy methods have been effectively abandoned as Wang and Rose [76,77] have shown that for linear coupled bending and extension, they incorrectly predict the membrane and bending stress intensity. An additional problem arises due to the somewhat arbitrary application of plane stress or plane strain conditions at the crack tip. For extension of generalized plane strain cracked plates, Wang and Rose [78] have shown that, when transverse stresses are considered, the crack tip is effectively in a state of plane strain. For bending of cracked plates, the actual state of the crack tip is less clear. Joseph and Erdogan [79] have noted that classical plate bending models employing the Kirchoff boundary condition lead to

conflicting definitions of the stress intensity depending on whether a stress- or strain-based definition is employed. Errors greater than 60% have been demonstrated when the classical model is compared to more sophisticated plate bending models that include shear deflections and allow the satisfaction of all three plate bending boundary conditions. Wang and Rose [80] have developed a numerical line-spring model for linear coupled bending and extension of repairs, but it employs a plane stress plate extension model and the Reissner plate bending model, both of which neglect the important role of transverse normal stresses. Hence, methods must be made available to properly account for plate thickness effects if energy methods are to be accurately applied and design equations for combined bending and extension to be developed. As a final point, interpolation solutions such as those originally developed by Rose [60] hold great promise for regulatory purposes and stochastic risk analysis or optimization analyses, but have not been properly developed for the case of coupled extension and bending due to difficulties in developing appropriate long-crack limits.

Putting aside issues specific to the analysis of bonded composite repairs, there are difficulties inherent in the stress analysis of hybrid bonded joints which must be accounted for. In particular, it is necessary to include all of the relevant deformation modes particular to orthotropic composite adherends when calculating the stiffness of the repair, the stresses in the adhesive, and the load carried by the composite repair as it acts to restrict the opening of an underlying crack. Complications also exist in the prediction of the fracture and fatigue of bending plates, adhesive joints, and interlaminar failure of composites. It appears that in the absence of a universally acceptable model, the best approach is to characterize the potential for composite failure by calculating the plate loads and hence stresses in the composite, and attempt to reduce them however possible by design. Guidelines for what is an acceptable level of peel stress will develop over time as experience with the technology develops.

Finally, there is a deficiency in the available experimental data. The AMRL specimen, which has proven invaluable in the assessment and development of the bonded composite repair technology, has not been tested under varying degrees of bending restraint. Such testing would provide data that may help in the avoidance of unexpected failures due to patch bending. It would also prove to be useful to carry out testing in the manner of Baker [29] whereby lap joint specimens would be tested under varying degrees of bending restraint to examine the response of the repair as it acts to bridge the crack. The best practice when safety is a critical issue is to perform mechanical testing to determine whether transverse failure/delamination is a problem. Analytical modeling and strength prediction remain useful in order to understand the problem and to minimize it. In design, it is always good practice to minimize transverse stresses wherever possible.

1.4 Thesis objectives

The objective of this thesis is the development and validation of a basic damage tolerance analysis methodology to assure the structural integrity of a repair, with particular attention to the effects of bending and plate thickness on the crack tip stress intensity, adhesive stresses, and interlaminar composite failure. The desired product is a set of validated engineering equations that capture the relevant physical phenomena in a conservative manner, and are based upon a theoretical analysis of the mechanics of a repair. This necessitates experimental work for the investigation of bonded composite repair failure mechanisms and the validation of developed predictive models, and theoretical work on the fracture of bending plates with reinforced cracks and fracture mechanics of repairs under non-linear bending conditions. This will enable the damage tolerance assessment and certification of a repair.

This project falls under a larger research and development program at UBC directed toward certification and widespread use of bonded repairs in civilian aviation. Advancements to this program have been made through the development of design and damage tolerance analysis tools and test methods for repairs. With the assistance of the NRC-IAR, much effort has been applied toward the design, analysis, manufacture, and testing of repair specimens. Assistance and co-operation has also been obtained from the AMRL, who pioneered the use of this technology for military applications. With the completion of a Ph.D. dissertation by Andreas Albat and a M.A.Sc. thesis by Randal Clark, this thesis marks the third graduate degree devoted to this work. Seven AMRL repair specimens have been constructed, including an instrumented specimen used to study thermal stresses. Procedures for the manufacture and application of repairs have been documented, and the two-step model for double-sided repairs has been extended to include the effects of patch-edge tapering, thermal strains, adhesive plasticity, cracked-plate geometry correction factors, and disbonding. The result is a set of validated closed-form models suitable for engineering analysis, optimization, or use in codes and standards. The goal of this thesis is to provide a similar analysis capability for single-sided, or unbalanced repairs.

The bonded composite repair technology has great potential in the management and life extension of ageing transport airframes. It is now common practice to rebuild and re-fit aircraft to extend their life, often repeatedly. Ultimately, aircraft are retired when the cost of this refurbishment and the requirements for inspection become too onerous or the design of the airframe has become obsolete and is too inefficient to compete with newer models. Other financial factors are also important: e.g. an aircraft maintains its value if new aircraft of the same type are still being built but may lose a large amount of value if the line is discontinued. For aircraft in an advanced stage of usage, the consequential defects are well known and documented, and many of them could profitably be returned

to useful service with a few well-placed bonded repairs. There is also a significant opportunity for the use of repairs on newer aircraft, as when such a defect is initially discovered it is likely that it can be permanently repaired with a bonded patch, instead of being 'managed' using conventional riveted repairs. Obsolete or discontinued aircraft often see service in utility markets, such as cargo transport or forest firefighting and it can be profitable to refit an airframe that has virtually no value as a passenger transport aircraft into a new role. Given the advantages of the bonded repair technology in terms of cost, applications time, and effectiveness, there is a very large market for the application of the technology. At any given time, there are literally thousands of aircraft that are approaching a refit or retirement, and even most aircraft that are receiving their first overhaul would benefit from bonded repairs for defects that may ultimately manifest themselves into a life-threatening problem if a riveted patch is employed. This illustrates the importance of realizing an easy-to-use damage tolerance methodology that will allow them to compete against conventional riveted repairs and be more widely used.

Several barriers prevent the realization of a comprehensive damage tolerance analysis of a repair as required for certification. Significant limitations exist in our ability to include the effects of finite plate thickness and nonlinear coupled bending and extension on the performance of repairs. Significant issues also affect our ability to predict the strength and rate of fatigue of bending plates, hybrid bonded joints, and composites under transverse loading. Engineering methods for analysis of repairs generally ignore composite failures, and there is a lack of experimental data available for validation of mechanical models of geometrically non-linear bending of bonded composite repairs and fatigue of hybrid bonded joints. To address these issues, a program of experimental and theoretical analysis has been carried out, involving the testing of a heavily instrumented repair with and without bending constraints, the construction and testing of representative lap joint specimens, the development of line-spring models for cracked plates that include the relevant through-thickness effects, and the reformulation of the energy methods for repair analysis to allow the calculation of the parameters governing the life of a repair.

Chapter two describes the structural testing of an instrumented repair specimen, with and without bending restraint, which is used to validate a three-dimensional finite element model of a repair. The results are used as a basis for the development of a methodology and criteria for damage tolerance substantiation of a repair.

The issue of plate thickness effects is addressed in Chapter three by adoption of a generalized plane strain plate model, allowing the analysis of transversally isotropic plates of arbitrary thickness. Engineering equations are developed that relate the stress intensity factor to the strain energy release rate, and the Rose model, a classical model for analysis of repaired plates is shown to hold for a generalized plane strain plate.

In Chapter four, a series of engineering plate models are developed to illustrate the effects of through-thickness stresses, shear forces, and shear deflection on the bending of cracked transversally isotropic plates. The result is a set of equations relating the bending stress intensity to the strain energy release rate, which are used to extend the Rose model to the analysis of bending in reinforced cracked plates.

In Chapter five, the problems of coupled linear bending and extension of a cracked plate repaired with an isotropic patch are addressed. A line-spring model, developed from the results of Chapters three and four, is used to develop a new interpolation model applicable to repaired plates with arbitrary crack lengths.

In Chapter six, this model is extended to the analysis of an orthotropic repair by the adoption of more sophisticated bonded joint models that take in to consideration several composite-specific deformation modes and more accurate analysis of the coupling of the extensional and bending responses of an unbalanced joint.

In Chapter seven, nonlinear effects caused by stress-stiffening of the repair are accounted for by the use of the generalized Rose model, and by the extension of the new interpolation model to the nonlinear analysis of a repair, allowing the calculation of the extensional and bending stress intensity factors under a single-sided repair.

In Chapter 8, the results of the work are reviewed in the light of the thesis objectives, topics for future work are discussed, and the contributions of this work are outlined.

1.5 Summary

This chapter has introduced the bonded composite repair technology, demonstrated the need for damage tolerance assessment of a repair, identified shortcomings in the understanding of repair mechanics that make it difficult to certify a bonded composite repair, and described the objectives and content of this thesis. This goal of this work is to develop the elements required for the damage tolerance analysis of a repair. Subsequent chapters will describe experimental and analytical work directed toward this result.

1.6 References

[1] R. Jones. Assessing and maintaining continued airworthiness in the presence of widespread fatigue damage: an Australian perspective. Engineering Fracture Mechanics 60, 1998, 109-130.

[2] R. Jones, WK Chiu, J. Paul. Designing for damage tolerant bonded joints. Composite Structures 25, 1993, 201-207.

[3] AA Baker. On the certification of bonded composite repairs to primary aircraft structure. Proceedings of ICCM-11, Gold Coast, Australia, 1997, I-1 to I-23.

[4] AA Baker. Evaluation of adhesives for fibre composite reinforcement of fatigue-cracked aluminum panels. SAMPE Journal, March/April, 1979, 10-17.

[5] J Cognard. Influence of water on the cleavage of adhesive joints. International Journal of Adhesion and Adhesives 8/2, 1988, 93-99.

[6] AD Crocombe. Durability modelling concepts and tools for cohesive environmental degradation of bonded structures. International Journal of Adhesion and Adhesives 17, 1997, 229-238.

[7] WP deWilde, G VanVinckenroy, L Tirry, AH Cardon. Effects of the environment and curing on the strength of adhesive joints. Journal of Adhesion Science and Technology 9/2, 1995, 149-158.

[8] M Fernando, WW Harjoprayitno, AJ Kinloch. A fracture mechanics study of the influence of moisture on the fatigue behaviour of adhesively bonded joints. International Journal of Adhesion and Adhesives 16, 1996, 113-119.

[9] WS Johnston, LM Butkus. Considering environmental conditions in the design of bonded structures: a fracture mechanics approach. Fatigue and Fracture of Engineering Materials 21, 1998, 465-478.

[10] AN Rider, DR Arnott, AR Wilson, O Vargas. Influence of simple surface treatments on the durability of bonded aluminium alloy plates. Materials Science Forum 189-190, 1995, 235-240.

[11] KB Armstrong. Long-Term Durability in Water of Aluminium Alloy Adhesive Joints Bonded with Epoxy Adhesives', International Journal of Adhesion and Adhesives 17, 1997, 89-105.

[12] MR Bowditch, SJ Shaw. Adhesive bonding for high-performance materials. Advanced Performance Materials 3, 1996, 325-342.

[13] NC Cave, AJ Kinloch. The effects of silane deposition conditions on the durability of aluminum joints pretreated using 3-aminopropyltrimethoxysilane. Journal of Adhesion 34, 1991, 175-18.

[14] GD Davis, TS Sun, JS Ahearn, JD Venables. Application of surfgace behaviour diagrams to the study of hydration of phosphoric acid-anodized aluminum. Journal of Materials Science 17, 1982, 1807-1818.

[15] RP Digby, DE Packham. Pretreatment of aluminium: topography, surface chemistry and bond durability. International Journal of Adhesion and Adhesives 15, 1995, 61-71.

[16] LJ Hart-Smith. A peel-type durability test coupon to assess interfaces in bonded, co-bonded, and co-cured composite structures. International Journal of Adhesion and Adhesives 19, 1999, 181-191.

[17] JD Minford. Durability evaluation of adhesive bonded structures. Adhesive Bonding. Plenum Press, New York, USA, 1991, 239-290.

[18] PJ Pearce, FC Tolan. Epoxy silane - a preferred surface treatment for bonded aluminium repairs. International Conference on Aircraft Damage Assessment and Repair, 1991, 188-193.

[19] AN Rider, DR Arnott. Boiling water and silane pre-treatment of aluminum alloys for durable adhesive bonding. International Journal of Adhesion and Adhesives 20, 2000, 209-220.

[20] W Thiedman, FC Tolan, PJ Pearce, CEM Morris. Silane coupling agents as adhesion promoters for aerospace structural adhesives', Journal of Adhesion 22, 1987, 197-210.

[21] JRJ Wingfield. Treatment of composite surfaces for adhesive bonding. International Journal of Adhesion and Adhesives 13/3, 1993, 151-156.

[22] DR Arnott, PR Pearce, AR Wilson, RJ Chester. The effect on mechanical properties of void formation during vacuum bag processing of epoxy film adhesives. Second Pacific International Conference on Aerospace Science and Technology, 1995, 811-816.

[23] WD Bascom, RL Cottington. Air entrapment in the use of structural adhesive films. Journal of Adhesion 4, 1972, 193-209.

[24] RJ Chester, JD Roberts. Void minimization in adhesive joints. International Journal of Adhesion and Adhesives 9/3, 1989, 129-138.

[25] PR Pearce, DR Arnott, A Camilleri, MR Kindermann. Cause and effect of void formation during vacuum bag curing of epoxy film adhesives. Journal of Adhesion Science and Technology 12/6, 1998, 567-584.

[26] AA Baker. Repair efficiency in fatigue-cracked aluminum components reinforced with boron/epoxy patches. Fatigue and Fracture of Engineering Structures 16/7, 1993, 753-765.

[27] AA Baker. Fiber composite repair of cracked metallic aircraft components - practical and basic aspects. Composites 18/4, 1987, 293-308.

[28] AA Baker. Bonded composite repair of metallic aircraft components - overview of Australian activities. AGARD - 79th Meeting of the Structures and Materials Panel. Specialists Meeting: Composite Repairs of Military Aircraft Structures, 1994, 1-14.

[29] AA Baker, JD Roberts, LRF Rose. Experimental study of overlap joint parameters relevant to k eduction due to crack patching. 28th National SAMPE Symposium, 1983, 627-639.

[30] MD Raizenne, TJ Benak, JBR Heath, DL Simpson, AA Baker. Bonded composite repair of thin metallic materials: variable load amplitude and temperature cycling effects. AGARD - 79th Meeting of the Structures and Materials Panel. Specialists Meeting: Composite Repairs of Military Aircraft Structures, 1994, 5-1.

[31] P Hucalek, MD Raizenne, RF Scott. Influences of environment and stress history on the composite patch repair of cracked metallic structures. Canadian Aeronautics and Space Institute Journal. 34/2, 1988, 85-91.

[32] AM Albat, DP Romilly, MD Raizenne. Thermal residual strain measurement in a composite repair on a cracked aluminum structure. ICCM-11, Gold Coast, Australia, 14th to 18th July 1997, p. VI-279-VI-288.

[33] P Poole, D Lock, A Young. Composite patch repair of thick aluminum sections. International Conference on Aircraft Damage Assessment and Repair, 1991, 85-91.

[34] J Denney, S Mall. Characterization of disbond effects on fatigue crack growth behavior in an aluminum plate with a bonded composite patch. Engineering Fracture Mechanics 57, 1997, 507-525.

[35] J Denney, S Mall. Fatigue behaviour in thick aluminum panels with a composite repair. Collection of Technical Papers, 39th Annual AIAA-ASME-ASCE-AHS Structures, Structural Dynamics, and Materials Conference 3, 1998, 2434-2443.

[36] J Denney, S Mall. Effect of disbond on fatigue behavior of cracked aluminum panel with bonded composite patch. American Institute of Aeronautics and Astronautics AIAA-96-1322-CP, AIAA, 1996, 14-21.

[37] PK Sharp, JQ Clayton, G Clark. Retardation and repair of fatigue cracks by adhesive infiltration. Fatigue and Fracture of Engineering Materials and Structures 20/4, 1997, 605-614.

[38] J Klug, S Malley, CT Sun. Characterization of fatigue behavior of bonded composite repairs. Journal of Aircraft 36/6, 1999, 1017-1022.

[39] R Jones, WK Chiu, R Smith. Airworthiness of composite repairs: failure mechanisms. Engineering Failure Analsysis 2, 1995, 117-128

[40] F.A.A. Advisory Circular 25.1529-1. Instructions for continued airworthiness of structural repairs on transport airplanes. U.S. Department of Transportation, Federal Aviation Administration, 1991.

[41] F.A.A. Advisory Circular 20.107A,. Composite aircraft structure. U.S. Department of Transportation, Federal Aviation Administration, 1984.

[42] F.A.A. Advisory Circular 25.571-1C. Damage tolerance and fatigue evaluation of structures. U.S. Department of Transportation, Federal Aviation Administration, 1998.

[43] L Molent, R Jones. Crack growth and repair of muli-site damage of fuselage lap joints. Engineering Fracture Mechanics 44/4, 1993, 627-637.

[44] Ratwani M.M., 1979. Cracked, adhesively bonded laminated structures. AIAA Journal 17(9), 988-994.

[45] Jones R, Calinan RJ, Aggarwal KC, 1983. Analysis of bonded repairs to damaged fibre composite structures. Engineering Fracture Mechanics 17(1), 37-46.

[46] S Naboulsi, S Mall. Modeling of cracked metallic structure with bonded composite patch using three layer technique. Composite Structures 35, 1996, 295-308.

[47] S Naboulsi, S Mall. Nonlinear analysis of bonded composite patch repair of cracked aluminum panels. Composite Structures 41, 1998, 303-313.

[48] F Erdogan, K Arin. A sandwich plate with a part-through and disbonding crack. Engineering Fracture Mechanics 4, 1972, 449-458.

[49] G Dowrick, DJ Cartwright, DP Rooke. Boundary effects for a reinforced cracked sheet using the boundary element method. Theoretical and Applied Fracture Mechanics 12, 1990, 251-260.

[50] A Young, DJ Cartwright, DP Rooke. Influence of tapering on the stresses in repair patches. Proceedings of the Third International Conference on Numerical Methods in Fracture Mechanics, 1984, 721-737.

[51] A Young, DP Rooke, DJ Cartwright. A numerical study of balanced patch repairs to cracked sheets. Aeronautical Journal, 1989, 327-334.

[52] A Young, DP Rooke, DJ Cartwright. Boundary element method for analyzing repair patches on cracked finite sheets. Aeronautical Journal 92, 1988, 416-421.

[53] P Poole, D Lock, A Young. Composite repair of thick aluminum alloy sections. International Conference on Aircraft Damage Assessment and Repair, 1991, 85-91.

[54] NK Salgado, MH Aliabadi. The boundary element analysis of cracked stiffened sheets, reinforced by adhesively bonded patches. International Journal for Numerical methods in Engineering 42, 1998, 195-217.

[55] PH Wen, MH Aliabadi, A Young. Boundary element analysis of flat cracked panels with adhesively bonded patches. Engineering Fracture Mechanics 69, 2002, 2129-2146.

[56] LRF Rose. An application of the inclusion analogy for bonded reinforcements. International Journal of Solids and Structures 17, 1981, 827-838.

[57] LRF Rose. A cracked plate repaired by bonded reinforcements. International Journal of Fracture 18/2, 1982, 135-144.

[58] LRF Rose. Crack reinforcement by distributed springs. Journal of the Mechanics and Physics of Solids 35/4, 1987, 383-405.

[59] LRF Rose. Basic concepts in assessing the efficiency of bonded repairs. International Conference on Aircraft Damage Assessment and Repair, Melbourne, Australia, 1991, 202-208.

[60] LRF Rose. Theoretical aspects of crack-patching. In: AA Baker, R. Jones. Bonded repair of aircraft structures. Martinus Nijhoff, Dordrecht, The Netherlands, 1988.

[61] JD Eshelby. The determination of the elastic field of an elliptical inclusion, and related problems. Proceedings of the Royal Society of London A241, 1957, 376-391.

[62] CH Wang, LRF Rose, R Callinan, AA Baker. Thermal stresses in a plate with a circular reinforcement. International Journal of Solids and Structures 37, 2000, 4577-4599.

[63] AM Albat, DP Romilly. Direct linear-elastic analysis of double symmetric bonded joints and reinforcements. Composites Science and Technology 59/7, 1999, 1127-1137.

[64] BN Cox, LRF Rose. A self-consistent approximation for crack bridging by elastic/perfectly plastic ligaments. Mechanics of Materials 22, 1996, 249-263.

[65] AM Albat. Thermal residual stresses in bonded composite repairs on cracked metal structures. Ph.D. thesis, The University of British Columbia, 1998.

[66] RJ Clark, DP Romilly. Fatigue damage prediction for bonded composite repairs applied to metal aircraft structures. 2001 SAE Transactions - Journal of Aerospace, 10 p.

[67] Volkersen O. Rivet strength distribution in tensile-stresses rivet joints with constant cross-section. Luftfahrforschung 1938;15(1):41-47.

[68] Goland M and Reissner E. The stresses in cemented lap joints. Journal of Applied Mechanics, Transactions of the ASME 1944;66:A17-A27.

[69] Hart-Smith LJ. Stress analysis: a continuum mechanics approach. In: Developments in Adhesives, volume 2, applied science publishers, London, 1973.

[70] Delale F, Erdogan F, Aydinoglu MN. Stresses in adhesively bonded joints: a closed-form solution. Journal of Composite Materials, 1981;15:249-271.

[71] Bigwood DA and Crocombe AD. Elastic analysis and engineering design formulae for bonded joints. International Journal of Adhesion and Adhesives 1989;9(4):229-242.

[72] C Lin, K M Lietchi. Similarity concepts in the fatigue fracture of adhesively bonded joints. Journal of Adhesion 21, 1987, 1-24.

[73] D Broek, Elementary engineering fracture mechanics, revised 4th edition, Kluwer academic publishers, Dordrecht, The Netherlands, 1997.

[74] BD Agarwal, LJ Broutman. Analysis and performance of fibre Composites. 2nd Edition, John Wiley and Sons, Inc., New York, 1990.

[75] VN Bulsaraa, R Talrejab, J Qua. Damage initiation under transverse loading of unidirectional composites with arbitrarily distributed fibres. Composites Science and Technology, 59, 1999, 673-682.

[76] CH Wang, LRF Rose. On the design of bonded patches for one-sided repair. Proceedings of the 11th International Conference on Composite materials, Gold Coast, Australia, 5, 1997, 347-356.

[77] CH Wang, RJ Callinan, LRF Rose. Analysis of out-of-plane bending of a one-sided repair. International Journal of Solids and Structures 35/14, 1998, 1653-1675.

[78] CH Wang, LRF Rose. Bonded repair of cracks under mixed-mode loading. International Journal of Solids and Structures 35/21, 1998, 2749-2773.

[79] PF Joseph and F Erdogan. Surface crack problems in plates. International Journal of Fracture 41, 1989, 105-131.

[80] CH Wang, LRF Rose. A crack bridging model for bonded plates subjected to tension and bending. International Journal of Solids and Structures 36, 1991, 1985-2014.

Chapter 2: Bending of bonded composite repairs: an experimental and finite element design study*

R. J. Clark and D. P. Romilly

University of British Columbia Department of Mechanical Engineering

2.1 Introduction

This chapter describes an experimental and finite element study of a bonded composite repair applied to a metallic aircraft structure. The experimental study involves the fatigue testing and fractographic examination of 2024-T3 aluminum plates repaired with boron/epoxy composite patches. The two plates are tested simultaneously in a sandwich panel configuration with and without an aluminum honeycomb spacer to provide bending restraint. The specimen was heavily instrumented, with strains being measured on the surface of the patch at many locations, thus allowing the validation of a three-dimensional finite element model and an assessment of the effects of geometrically nonlinear bending, buckling, and crack closure on the mechanical response and strength of the repair. The experimental and finite element results illustrate the large influence of bending and composite failure modes on the life and strength of the repair. The authors use the experimental results and the validated finite element analysis to evaluate the effectiveness of the methods and data currently available in the open literature for damage tolerance substantiation, and then, by applying probabilistic methods and the principle of compounded conservatism to the findings, propose a new process for classifying bonded repairs and for assigning testing and inspection requirements.

A bonded composite patch is a fibre-reinforced epoxy doubler used to reinforce weak structure or repair cracked aircraft structure. The patch acts both to reduce stresses in the underlying structure, and to restrict the opening of cracks that may lie beneath it. These effects and the smooth load transfer inherent to bonding offer the potential for a significant increase in the fatigue life when compared to mechanically fastened repairs. The technology also offers improvements in cost, weight, and inspectability. One of the main barriers to the widespread use of this technology is the lack of a comprehensive process for damage tolerance analysis, particularly regarding the mechanical assessment of the structure in the presence of significant bending loads, which can lead to early failure. The other significant impediment is the assurance of bond line durability for repairs applied in a maintenance and repair facility.

---

* A version of this chapter will be submitted for publication. R.J. Clark, D.P. Romilly, "Bending of bonded composite aircraft repairs: an experimental and finite element design study", AIAA Journal.

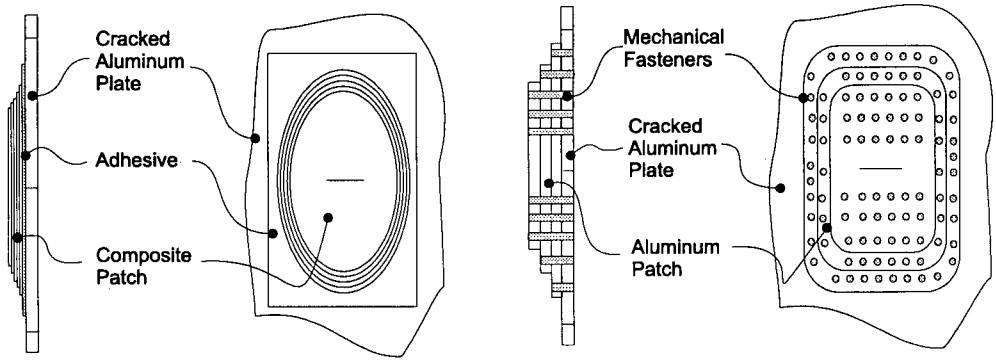

Figure 2-1: A bonded repair and a mechanically fastened repair

Many experiments have been performed to investigate failure mechanisms, to demonstrate the predictive performance of models, and to evaluate repair materials and mechanical phenomena in a repair. A widely used repair specimen is the Australian Aeronautical and Maritime Research Laboratories (AMRL) specimen, which is the type of specimen used for this study. The AMRL test article consists of two repaired plates that are bonded to an aluminum honeycomb support to restrict the bending induced by the neutral axis offset of the repair and to model the support of underlying structures that often exist in the highly stressed regions of an aircraft. Engineering drawings of the AMRL specimen are provided in Appendix B. Baker has published experimental results for the AMRL specimen that illustrate the effects of cure cycle parameters [1,2], disbonding [1,3], patch shear deformation [2,4], adhesive plasticity [4], and test temperature [1] on performance. In Canada, the AMRL specimen has been used by the National Research Council - Institute for Aerospace Research (NRC-IAR) to examine the effects of load spectrum, compressive loading, and adverse environments on patch performance [5,6], and by Albat and Romilly [7] to evaluate thermal strains. With the honeycomb bending restraint, the failure mode of the repair has consistently been continued cracking of the aluminum with accompanying adhesive disbonding. Double lap-shear hybrid bonded joint specimens matching the composition and geometry of the AMRL specimen geometry have been used to investigate the effects of patch shear deformation and adhesive plasticity on the apparent stiffness of the patch in the region of the crack [4], to determine the rate of disbonding in the region of the crack [8], to examine disbonding at the edges of the repair. Patch shear deformation and adhesive plasticity have been shown to reduce patch life by reducing the restraint against crack opening imposed by the repair [4]. It has also been shown that increasing the cure cycle temperature and time can impose two penalties on patch performance; 1) tensile thermal residual stresses from a mismatch in thermal expansion coefficients can accelerate fatigue crack growth, and 2) crack growth retardation is reduced due to annealing of crack tip

plasticity-induced residual stresses. Sharp, Clayton, and Clark [9] have also examined the effects of adhesive infiltration into the crack, which was found to increase the stress required to open the crack and hence improve fatigue life.

Other researchers have examined both similar and distinctly different types of specimens to assess the effects of bending on the life of a repair. Poole, Lock, and Young [10] have investigated fatigue damage propagation in thick aluminum plates repaired with graphite/epoxy patches to investigate structural failure behaviour and assess fatigue life. Similar to the AMRL specimen, repaired plates were bonded to a honeycomb core and tested in pairs to restrict bending. They examined the effect of the FALSTAFF loading spectrum on repair performance, and compared the results to boundary element analyses that included the effects of adhesive plasticity. The results showed improvements on life of a factor of 3.2 for the FALSTAFF spectrum-loaded specimen, and up to a factor of 17 for a constant-amplitude cyclically loaded specimen when compared to an unrepaired sheet. Denney and Mall [11-13] have investigated boron/epoxy repairs applied to a single side of a thin center-cracked aluminum panel (i.e. an unbalanced repair), where patch bending is a significant factor due to an offset of the neutral axis. They investigated the effect of variously sized disbonds at different locations within the repair, and concluded that disbonds over the crack reduce life whereas disbonds away from the crack are not detrimental. They suggested that disbonds away from the crack may actually increase patch life by reducing the apparent size and stiffness of the patch and hence the amount of load attracted from the surrounding structure. During this testing, failure occurred due to crack growth in the aluminum and little disbonding was noted. Klug et al. [14] performed a similar test using both thick and thin unbalanced repairs, and noted significant disbonding near the crack and near the edges of the patch for a thick repair and only near the crack for a thin repair. For these specimens, the patch was not tapered, leading to increased stresses about the edge of the repair. In more recent work, Sabelkin et al. [15] performed tests to investigate the effects of a supporting stringer on the life of a single-sided repair applied to a thin cracked aluminum plate. Their results show that the stiffeners have an important role in reducing the stress intensity, and that the thermal residual stresses must be accurately evaluated. As previously observed for repair of thin plates, they found that disbonding extended only a few millimeters from the edge of the crack.

Jones, et al. [16] have presented a thorough review of the failure modes and locations of damage experienced in laboratory and military use of bonded repairs. While most of the work reported in the literature examines the primary failure modes of the repair, i.e. substrate cracking and accompanying cohesive disbonding of the adhesive, Jones et al. state that any damage tolerance assessment must also include composite failure modes such as fiber failure, adhesive failure, cohesion failure at the patch-adhesive interface,

adhesive failure at the adhesive-substrate interface, and inter-laminar failure and delamination. In practice, unexpected failure due to crack growth and disbonding about the crack has not been a problem, as mitigation of this form of crack growth is the primary design goal of the repair and it is well accounted for in the analysis, testing and inspection regimes. Another important factor is that the technology has mainly been limited to double-sided repairs of flat plates, to structures with bending restraint, and to structures with residual strength. Accordingly, unexpected composite failures have usually only occurred during laboratory testing for evaluation of a repair, rather than during service. FAA Advisory Circular 25.571-1A identifies the failure modes and locations of damage that must be considered, and requires the assessment of the effects of impact damage, inter-ply delamination, and disbonding on the composite, adhesive, and substrate.

This paper describes a unique experimental study investigating the bending mechanics of a bonded composite structural repair tested with and without bending restraint. The specimen is relatively thick and is repaired with a patch of sub-optimal planar dimensions, an extreme case that allows the authors to assess the potential effects of induced bending on early failure of the structure. The specimen was comprised of two edge-cracked aluminum panels, each repaired with a boron-epoxy patch and joined together as an aluminum honeycomb sandwich. Strain results are reported for the fatigue-damaged specimen under both tensile and compressive applied loading, and before and after removal of the honeycomb separating the aluminum panels. Strain data from gauges fitted to the surface of the repair in the region of the crack are used to validate a three-dimensional finite element model, allowing the calculation of the stress intensity and the stresses in the adhesive and the patch as it acts to reinforce the cracked plate. Fractographic examination of the failure surfaces of the cracked plate and the composite patch illustrate the failure mechanisms active in a bending repair. It is shown that geometrically nonlinear bending and stress stiffening have a significant role in the type of failure and rate of damage, thus decreasing the time to failure of the structure. In addition, a technique is described for three-dimensional finite element linear elastic fracture analysis of a structure experiencing large deflections. The method employs the stress-based definition of the stress intensity factor, meaning that the analyst does not need to assume a state of plane stress or plane strain. Finally, the authors attempt to use the finite element stress intensity factor, adhesive stresses, and composite stresses near the repaired crack to calculate the residual strength of the repair and rate of damage progression in light of the failure modes observed during the fatigue test. It is shown that significant problems remain for the damage tolerance assessment of repairs, particularly in the characterization of the observed composite and adhesive failure modes.

2.2 Experimental study

The experimental study involves the fatigue testing of a symmetrical honeycomb sandwich structure, comprised of two edge-cracked aluminum panels, each repaired with a boron-epoxy patch, as shown in Figures 2-2 through 2-4. This specimen was originally developed by the AMRL, and has also been used extensively by both the NRC-IAR. As described in the introduction, the AMRL specimen has seen extensive use in the evaluation of the bonded composite repair technology for balanced or symmetric double-sided repairs. Without bending, the failure mode of the repair has consistently been found to be continued cracking of the aluminum with accompanying adhesive disbonding. In this study, the authors test the specimen with and without the bending restraint provided by the aluminum honeycomb spacer in order to: 1) investigate the failure mechanics of a repair under bending and 2) to collect strain data to validate models of bending repairs. It should be noted that the AMRL specimen was designed to model a repair applied to cracked plates that are supported by underlying structures (e.g. ribs, stringers, etc.). If designed as a one-sided, or unbalanced repair, a much larger patch would typically be used to reduce the bending loads in the cracked region. As such, the AMRL specimen without bending restraint provides an extreme test of the technology.

Figure 2-2 shows a picture of the instrumented patch and the testing apparatus. A photoelastic coating was applied to the upper half of one of the patches to reveal the distribution of strains and estimate the extent of disbonding. An AC potential drop probe was used to measure the crack length. Unfortunately, the utility of the potential drop probe was greatly affected by electrical contact between the honeycomb core and aluminum face-sheets, which had been electrically insulated in specimens built by the AMRL. A traveling microscope was used to estimate the degree of disbonding at the edge of the patch. To investigate the stress distribution within the repair, strain gauges were applied to the specimen by technicians at the NRC-IAR.

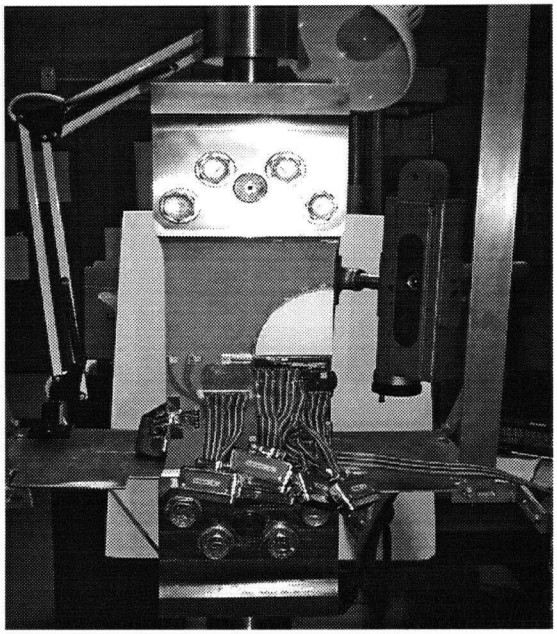

Figure 2-2: Experimental apparatus

The specimen contains 100 strain gauges, most in 10-gauge strips, located as shown in Figure 2-3. Engineering drawings illustrating the type, orientation, and location of the gauges are included in Appendix B. This chapter will mainly report the strain in gauges located above the repaired crack (location A on the figure), as this region has the greatest influence on cracking and disbonding. The gauges at location B allow the examination of the stresses about the edges of the repair and the gauges at locations C and D measure the strains in the patch as a disbond forms during fatigue testing. The gauges at location E allow the measurement of the strains in the tapered region of the repair and the stresses at the apex of the patch, where a stress concentration in the aluminum plate is known to exist. The remaining gauges allow the assessment of the distribution of the strains in the structure, and allow the analyst to evaluate the grip boundary conditions. Note that the gauges will, in general, over-report any strains caused by bending as due to the thickness of the gauge and the adhesive used to bond it to the structure, particularly when the gauge is applied to the surface of a disbonded portion of the repair, which is fairly thin (~1 mm). This effect was taken into consideration during subsequent analysis of the measured strain data.

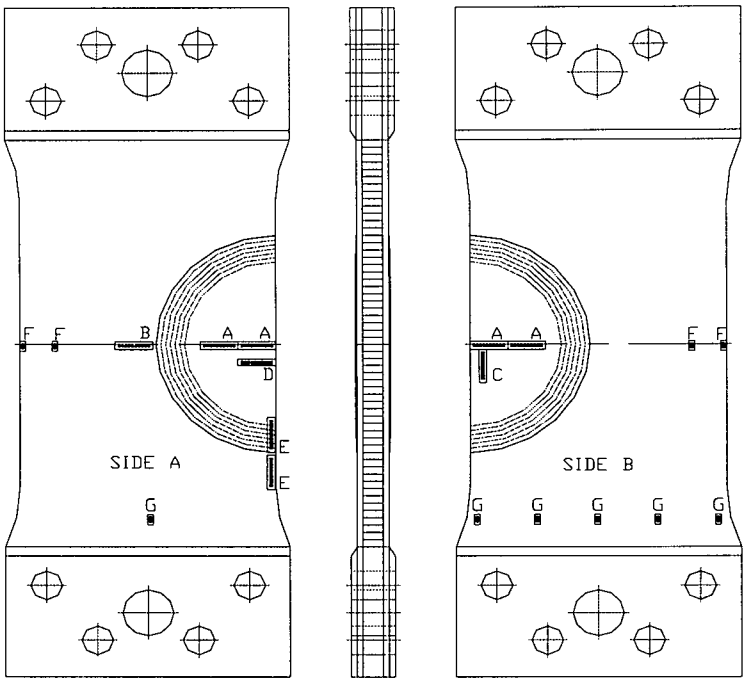

Figure 2-3: Strain gauge locations

The fatigue testing was carried out with a load (expressed as a remote applied stress) of 138 MPa at an applied stress ratio R = 0.1 and test frequency of 3 Hz. Strain measurements were taken at several stages, including at the start of the test and after 175,000 cycles, at which point the honeycomb support joining the specimens was removed to evaluate the bending of a restrained and an unrestrained patch. The initial fatigue pre-crack length was 19.9 mm, and the crack length when the honeycomb was removed was 45 mm, as measured by fractographic examination. Also at 175,000 cycles, isopropyl alcohol and ink were injected into the adhesive disbond, revealing a disbond of up to 6.4 mm extending from each side of the crack. Strains were measured during static testing using a Schlumberger Solartron Orion datalogger, 10 gauges at a time, using a 3-wire strain guage connection. During each measurement, the strain readings at each location were taken for remote applied stresses ranging from 138 MPa to –55 MPa with the honeycomb support, and from 138 to -28 MPa without the honeycomb support, allowing the evaluation of both non-linear bending and buckling. A complete record of the measured strain gauge data is tabulated in Appendix C.

Figure 2-4 shows the deflections of the structure under maximum tensile and compressive loads with the honeycomb removed. Under tension the neutral axis of the patch moves to the load line, causing large moments and accompanying adhesive peel stresses. Under compressive loads the structure bows outward, approaching collapse. This clearly demonstrates the large influence of bending on the mechanics of the structure.

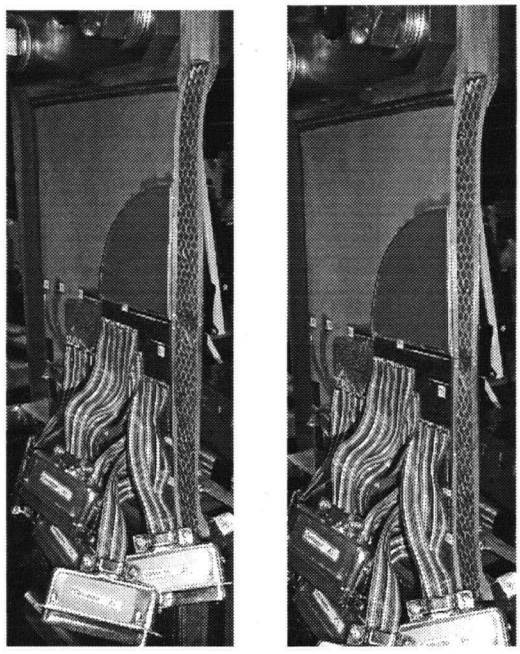

Figure 2-4: Bending under tension (left) and compression (right)

Figure 2-5 shows the extent of the disbonding at 175,000 cycles and at failure after 185,000 cycles, revealing that the specimen failed rapidly after removal of the honeycomb spacer that provided resistance to bending. This demonstrates the need to account for induced bending during damage tolerance assessment of a single-sided repair.

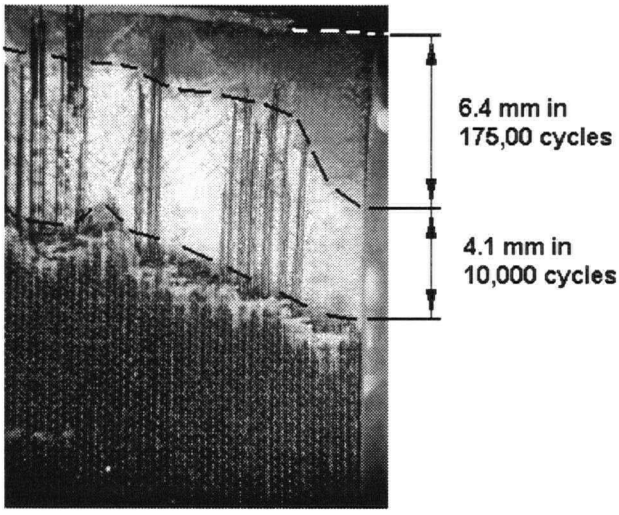

Figure 2-5: Adhesive failure surface

The disbond was initiated by the failure of the adhesive that infiltrated the crack during curing, followed by cohesive disbond growth towards the adhesive/composite interface. The disbond then grew along the interface with the scrim carrier and boron fibres. Final failure occurred by simultaneous failure of the composite patch and fracture of the

cracked plate. Figure 2-6 shows the interfacial failure surface. Fibres that failed after removal of the bending restraint remained bonded to the underlying plate and pieces of adhesive remain attached to the boron fibres, indicating high-energy failure and good interfacial bond strength.

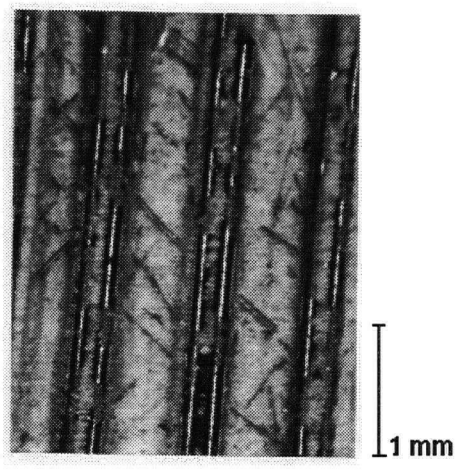

Figure 2-6: Interfacial failure surface

Figure 2-7 shows the failure surface of the aluminum plate. The left picture shows the fatigue pre-crack and the right figure shows the transition from high to low cycle fatigue after removal of the honeycomb at 175,000 cycles. Up to this point the crack front grew at an angle, indicating that bending affected crack growth even before removal of the honeycomb. After removal of the honeycomb, the surface attains rougher appearance and begins to show signs of shear failure.

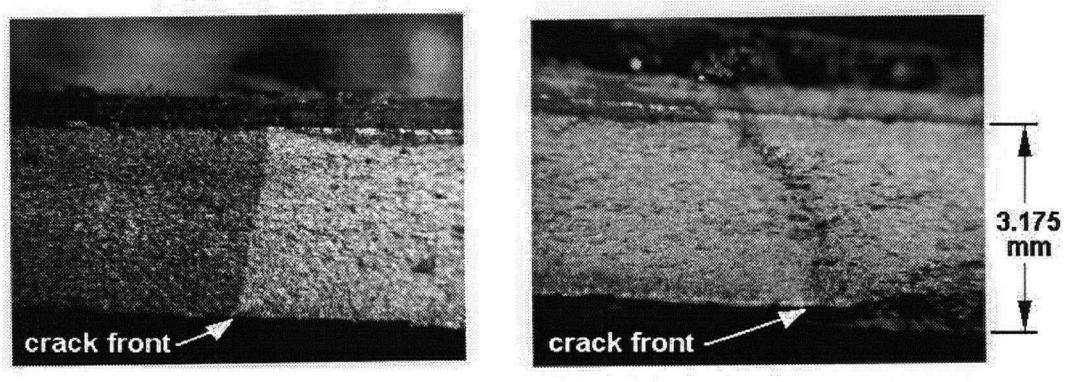

Figure 2-7: The crack face after pre-cracking (left) and after 175,000 cycles (right)

Selected strain measurements from this study are used in subsequent sections to validate a finite element model of the tested repair. A complete record of the strain measurements is provided in Appendix C. Strain results will be compared to finite element data in subsequent sections.

2.3 Finite element modeling

The authors have constructed a finite element model to simulate the experiments described above. The model was developed using ANSYS [17], and consists of 'SOLID 95' 20-node brick elements with 15 node wedges at the crack tip. Table 2-1 shows the material properties used in the model. The Textron 5521 boron-epoxy prepreg composite patch is modeled as an orthotropic solid. The Cytec FM73M adhesive and 2024-T3 aluminum plate are modelled as isotropic solids, and the aluminum honeycomb spacer is modelled as an orthotropic solid with a young's modulus of 1.86 GPa in the through-thickness direction and very low modulii in all other directions.

Material	E, GPa	G, GPa	ν	α, $\mu\varepsilon/^0$C	t, mm
Patch, longitudinal	210.0	7.24	0.21	4.61	--
Patch, transverse	2.5	1.0	0.019	25.87	0.924
Adhesive	2.14	0.805	0.33	50	0.25
Plate	72.4	27.2	0.33	23.45	3.125
Honeycomb	1.86 0.001	0.001	0	23.45	6.35

Table 2-1: Material properties and dimensions

Thermal residual strains imparted by the cure process and operating temperature are a very important consideration for bonded composite repairs, and can be characterized by an effective stress free temperature that accounts for creep of the adhesive and polymer matrix as the specimen is cooled during the cure cycle. For the materials systems and specimen geometry used for this experiment, using a cure temperature of 121^0C, it has been shown that the effective stress-free temperature for this specimen is 81^0C [7]. The experiments were conducted at room temperature (approximately 20^0C), and accordingly a temperature difference of 61^0C was applied in the finite element model.

Figures 2-8 is a planar view of the model. Inset (a) shows the crack tip elements and (b) shows the aluminum substrate symmetry and pressure boundary conditions for a crack of length a and patch of radius r (~75 mm). To model the constraint of the grips, the nodes at the loaded edge are forced to move together in the direction of the load. As in the static testing, the applied stress was varied from 138 to –55 MPa for the double-sided configuration and 138 to –28 MPa for the single-sided configuration.

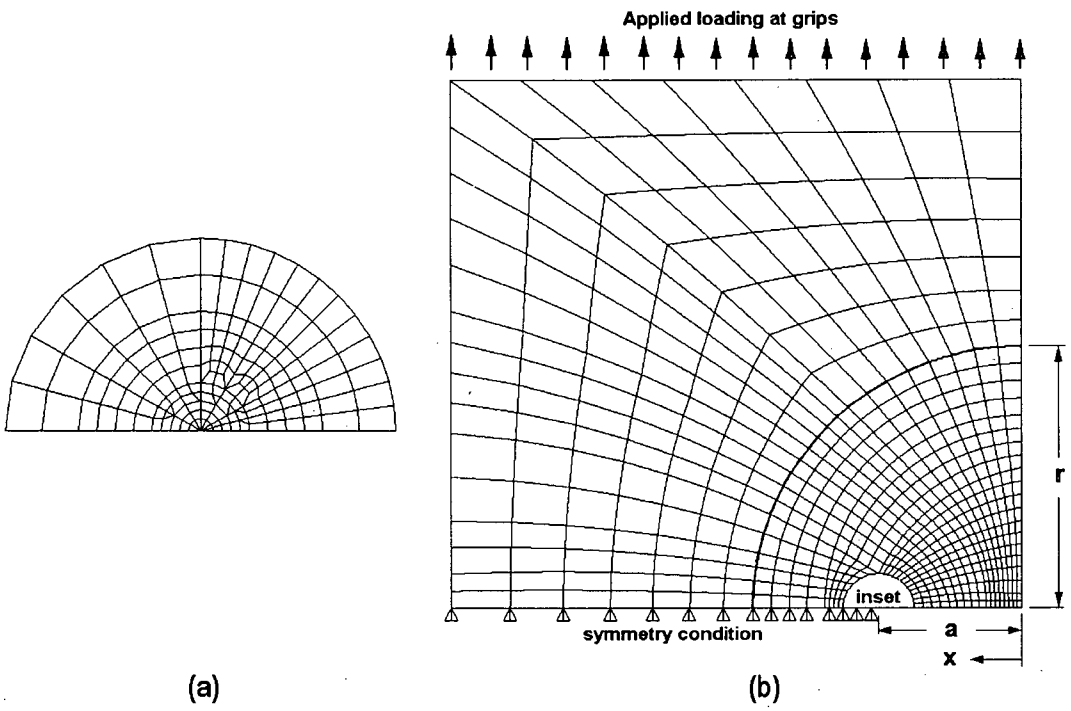

Figure 2-8: Finite element mesh, (a) the crack tip and (b) the entire model

The model was solved using a Newton-Raphson method with an iterative solver, large deflections, and stress stiffening. Pivot checking was disabled to allow the use of singularity elements. A user-defined macro generated singular elements that were properly oriented with respect to the crack tip and with mid-side nodes placed at the quarter-point position. A stress-based method was employed to calculate the stress intensity through the thickness of the plate, as described in reference 18. The membrane and bending stress intensities K_m and K_b were calculated as the average stress intensity and first moment of the stress intensity through the thickness of the plate, and were obtained by a linear least-squares fit to the stress intensities calculated at the integration point planes near the crack tip. Figure 2-9 shows a three-dimensional view of the finite element model in the region of the repaired crack, illustrating the singular crack tip elements and the layering of the plate, adhesive, and composite patch elements.

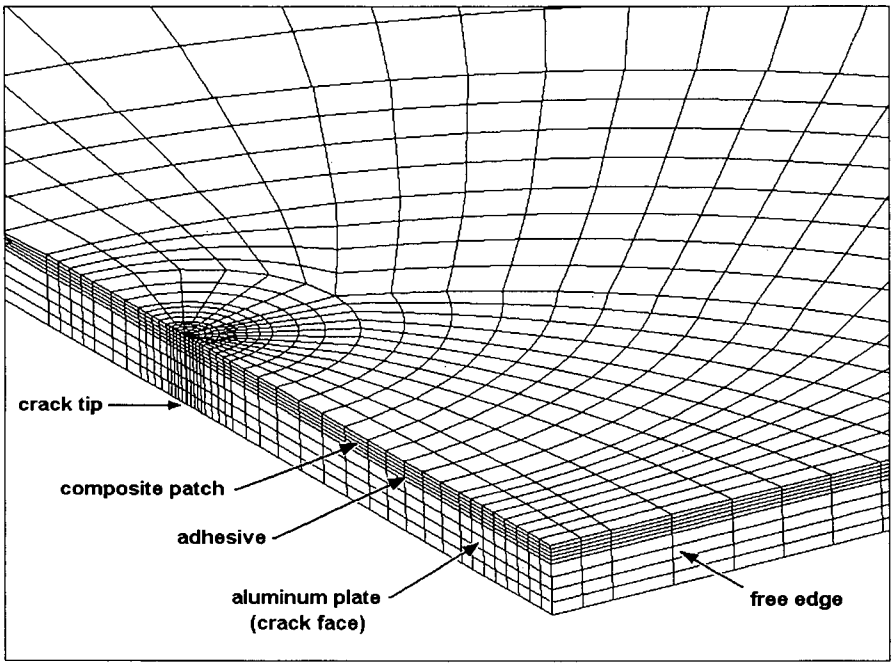

Figure 2-9: Three-dimensional view of the cracked region

The experimental and finite element strain data are compared in the next section to demonstrate the mechanics of a repair and validate the finite element model.

2.4 Validation

For validation, the finite element model was solved in an edge-cracked tension configuration, as shown in Figure 2-8(b). Figure 2-10 compares the finite element model strain results to the strains measured on the outside of the patch, as recorded before the specimen was subjected to fatigue loading. In this section, the distance x from the free edge of the repair will be referred to repeatedly, and is shown on Figure 2-8(b). The finite element model strains have been adjusted to include the effect of gauge thickness, as the strain gauge sensing element is offset from the surface of the repair by a small but not insignificant distance that tends to amplify bending effects. The experimental strains are reported as the average strain for gauges mounted on the patches on either side of the specimen and results are shown for an applied tensile stress of 138 MPa and a compressive stress of -55 MPa. In this case, the crack was 19.9 mm long.

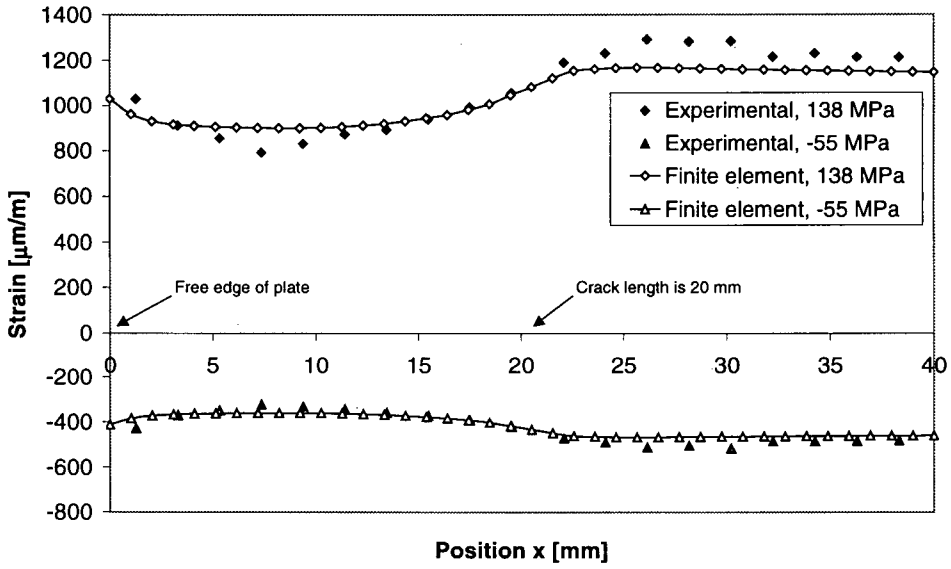

Figure 2-10: Strain distribution in undamaged repair

The strains determined for the outer surface of the patch are lowest in the region of the crack in both the model and experiments. This is contrary to what might be expected, as load should be diverted to the patch as it bridges the crack, increasing the strain. The cause is induced bending due to the neutral axis offset caused by the crack and the overlying patch, which reduces the surface strain in the patch. Even with the honeycomb support, under tensile loads the structure experienced bending sufficient to noticeably reduce the strains on the outer surface of the patch.

After 175,000 cycles, the crack was nearly 45 mm long, and the interface between the patch and underlying cracked plate had a disbond of approximately 5 mm in length. Figure 2-11 shows the adhesive layer mesh, where the grey elements have been removed to impose the disbond condition observed in the fatigue experiment after 175,000 cycles.

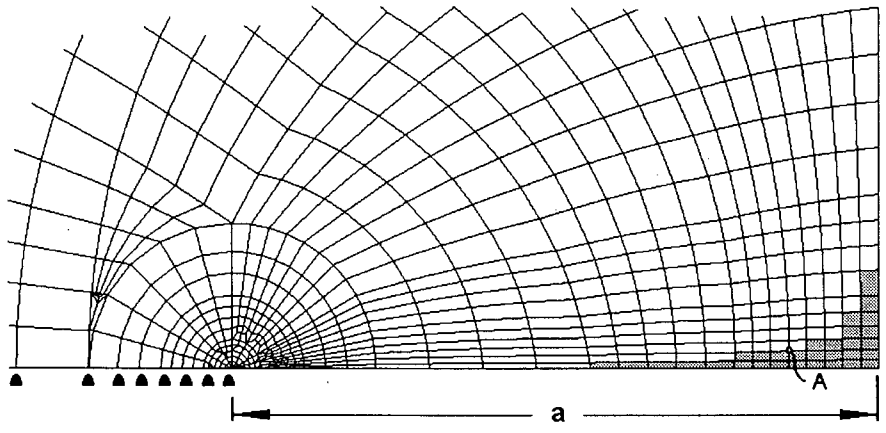

Figure 2-11: Adhesive elements in the region of the crack, showing the disbond

Similar to Figure 2-10, Figure 2-12 shows the surface strains in the patch as it reinforces the cracked plate. It is unfortunate that the strain gauges did not extend far enough to measure the strains at the crack tip, but much can still be made of the results. For both the finite element model and the actual specimen, the strains reach a peak at the free edge of the patch. A traditional centre-cracked repair model would predict a maximum strain at this location, but it should be reached gradually. There are two reasons for this abrupt peak: 1) the edge-cracked geometry of the plate has as significantly lower stiffness than a centre-cracked plate at this location and hence it will shed more load to the patch, and 2) that the disbonded part of the patch has a low bending stiffness and will carry mainly axial loads, an effect that increases when the honeycomb core is removed. The increase in load at the edge of the patch and adhesive edge effects also lead to larger adhesive stresses and a faster rate of disbonding near the free edge.

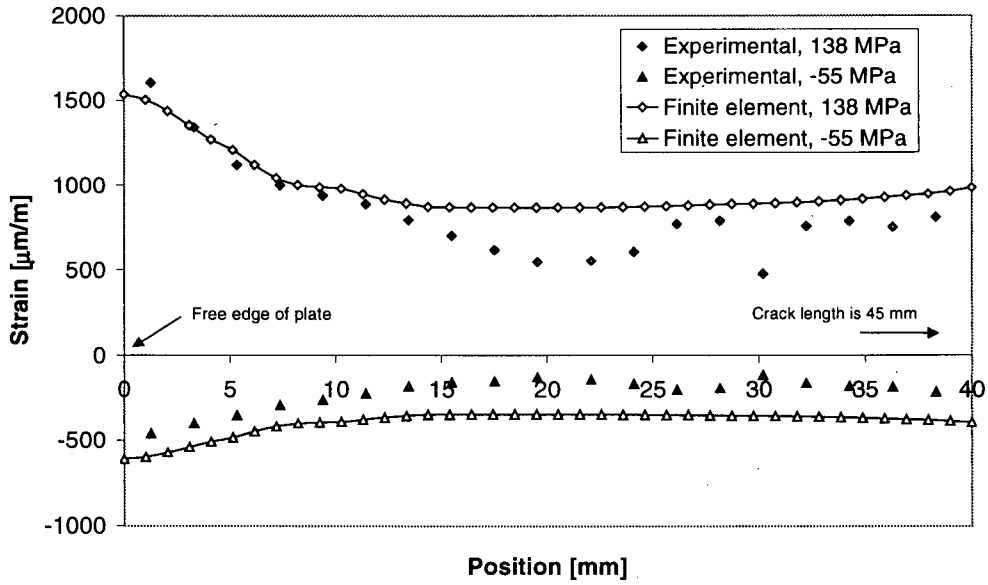

Figure 2-12: Strain distribution, with honeycomb

Figure 2-13 shows the surface strains measured by selected gauges plotted against the remote applied stress. The gauges are shown at selected distance from the free edge of the repair. The strains are linear until the applied stress is well into the compressive region, when tensile residual stresses in the substrate are overcome and crack closure reduces the proportion of the load carried by the repair. The distances in the legend are the position of the strain gauges, (i.e. x on Figure 2-8(b)). The finite element results are from a linear model, and do not include crack closure, which is seen to reduce the compressive strains observed in the experimental results when compared to the strains measured under tensile loading.

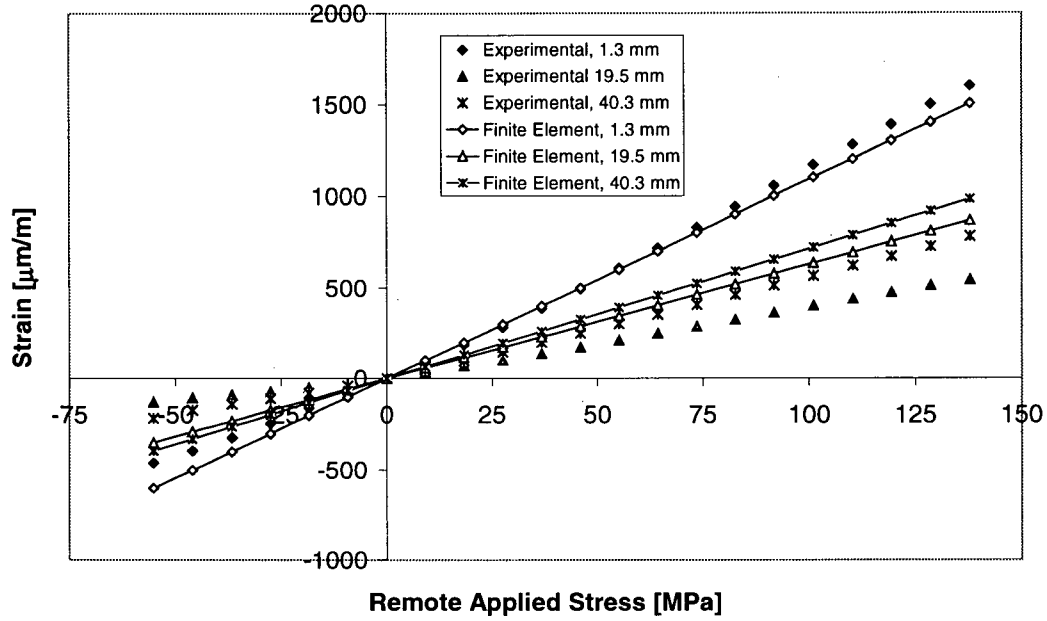

Figure 2-13: Variation of strains with applied stress, with honeycomb

The next stage of testing occurred after the removal of the honeycomb core separating the aluminum plates. The specimen experienced no further fatigue cycling at this point, so the crack and disbond sizes are the same as for the previous case. Figure 2-14 again plots the strain distribution on the surface of the repair. Note that applied tension results in compressive strains on the surface of the patch. The honeycomb provided a large degree of constraint against bending, and now that it has been removed, bending stresses dominate the response of the repair. This bending and the resulting adhesive peel stresses must be accounted for in order to predict the rate at which a repair will fail. After removal of the honeycomb, the maximum applied compressive stress was only -28 MPa, and the patch appeared to be approaching collapse. Here, the effect of the edge-cracked plate geometry combined with the reduced bending stiffness of the disbonded section of the patch is again evident in the dramatically increasing strains near the edge of the patch. It can be seen that crack closure plays a significant role for compressive loading for both the finite element model results and the measured strains, and hence crack-face contact should be included to obtain accurate results under compressive loading.

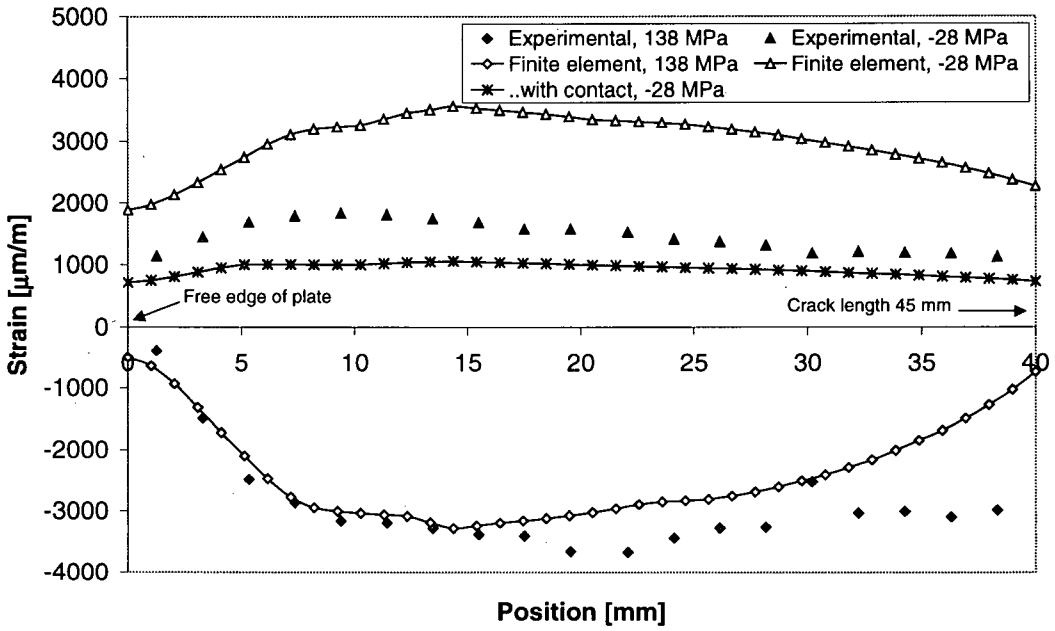

Figure 2-14: Strains, without honeycomb

In Figure 2-15, selected strain results are plotted against applied load. The strains are clearly non-linear without the honeycomb support, and show good agreement except at 40.3 mm, the strain gauge nearest to the crack tip. This discrepancy is likely due to a small amount disbonding near the crack tip or adhesive plasticity, neither of which was included in the finite element model. Both of these effects would act to relieve the severity of bending of the composite patch as it bridges the crack. The compression results again show the importance of crack closure, which acts to unload the patch near the crack.

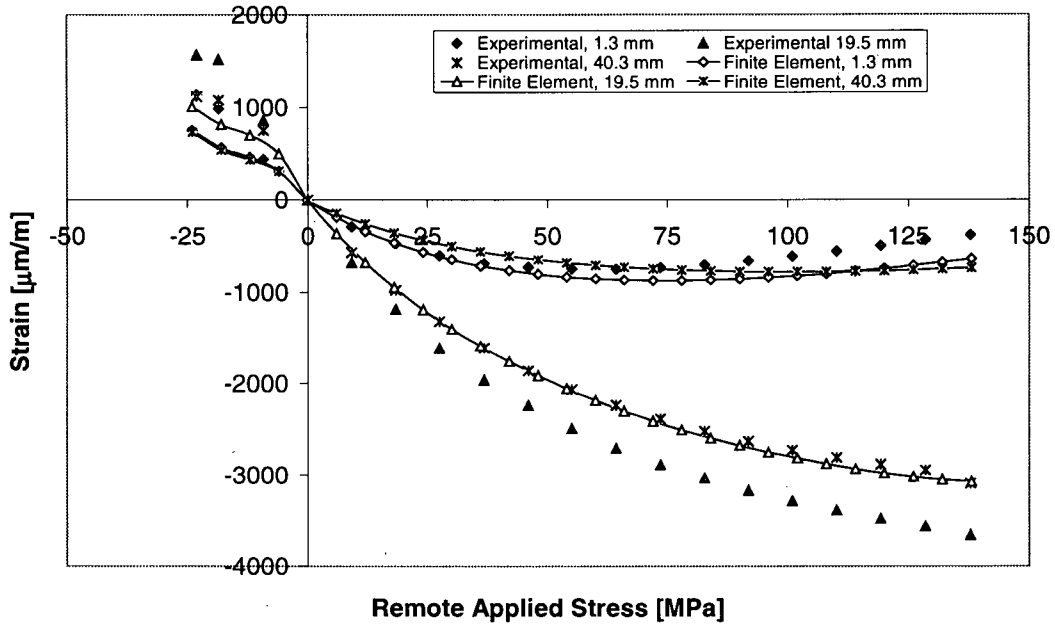

Figure 2-15: Variation of strain with applied stress, without honeycomb

The finite element model and experimental results capture the geometrically nonlinear mechanical response of the bending repair and demonstrate the importance of bending on the stresses within the patch itself. The importance of modeling the finite geometry of the edge-cracked plate has also been demonstrated, as a significant peak in the patch strains was observed at the edge of the repair. Crack closure was also shown to have a large role under compressive loading, acting to greatly relieve the load carried by the patch. This beneficial effect, however, is offset by the potential for elastic buckling, which appeared to be imminent for the unsupported repair under an applied compressive stress of only –28 MPa. In the next section, this validated finite element model will be used to calculate the residual strength of the repair and to examine factors affecting its fracture strength and fatigue life.

2.5 Residual strength and damage tolerance assessment

The fractographic examination illustrates the failure mechanisms at work in the repair. One important observation is that crack growth and disbond growth appear to occur together, which should be expected, as crack growth in the aluminum plate will generally shed load to the patch and promote disbonding. Similarly, disbond or delamination growth will reduce the effective stiffness of the patch as it bridges the crack and promote further cracking in the aluminum. The final failure of the structure occurred by simultaneous fracture of the composite patch and the repaired plate. Another important observation is that composite delamination and composite fracture are significant failure modes when a repair is free to bend, neither of which are often observed in double-sided

repairs or repairs with bending restraint. It is clear that in order to assess the strength of a one-sided repair, full account must be made of the potential for failure in three areas: a) cracking in the aluminum substrate, b) failure of the adhesive and c) failure of the composite. The following sections address these three areas of concern and place into perspective the relative merits of both existing and proposed methods of evaluation (resulting from the current investigations) for the purposes of damage tolerant design of bonded composite repairs on metallic structures.

2.5.1 Aluminum substrate fracture

Figure 2-16 shows K_m and K_b as predicted by the finite element model for two cases: i.e. with and without the honeycomb bending restraint. The predicted results reflect the previously experimentally observed nonlinear deformations, with stress-stiffening acting to reduce the rate of increase in stress intensity under larger applied loads. This happens when the structure moves toward the load line and sheds load to regions remote from the crack.

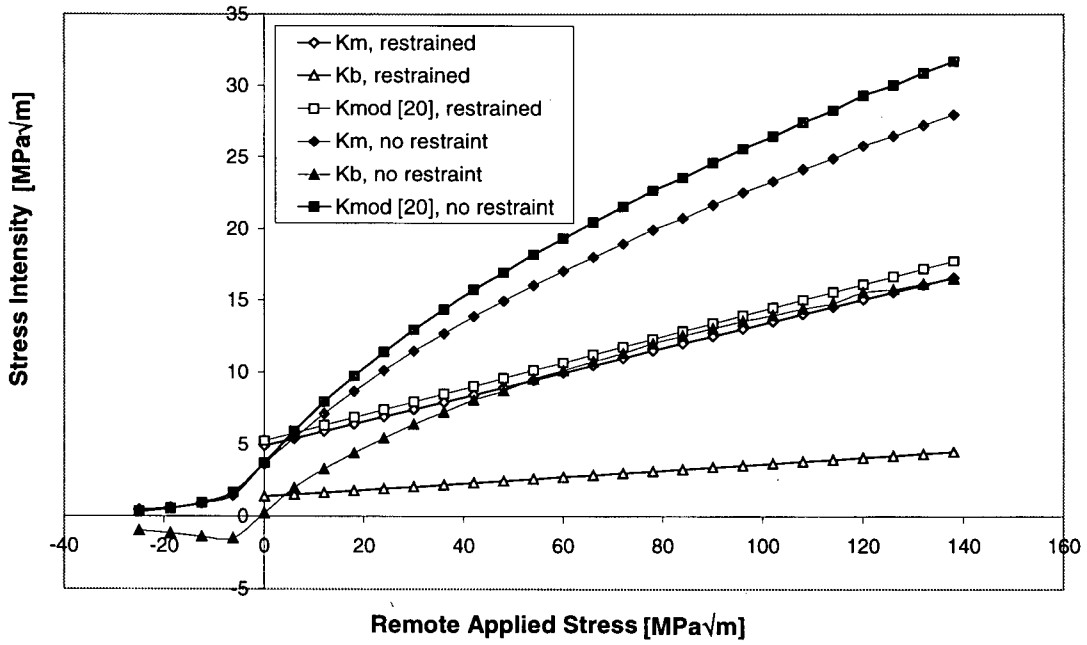

Figure 2-16: Membrane and bending stress intensity factors

By LEFM (Linear Elastic Fracture Mechanics) criteria, fracture is considered imminent when the sum of K_m and K_b exceeds the plane strain fracture toughness, K_{1c}. For thin aircraft skins, the actual fracture toughness (denoted as K_c) is often used. K_c is usually obtained from testing and as it is often significantly greater than K_{1c}, it will result in a longer critical crack length thus can greatly easing inspection requirements. The increasing acceptance of the NASGRO [19] damage tolerance software package allows

the use of a calculated K_c in most circumstances, but caution is required for short cracks where the non-singular stresses near the crack-tip are significant. For the 2024-T3 plate used in this investigation $K_{1c}=34\,MPa\sqrt{m}$ [20], whereas for a 3.175 mm thickness 2024-T3 plate NASGRO provides a K_c value that is over twice as large. For the AMRL specimen with a crack size of 45 mm, K_{1c} is exceeded by $K_m + K_b$ with an applied remote stress of nearly 90 MPa for unrestrained bending, but requires well over 140 MPa to exceed K_{1c} with the honeycomb bending restraint present.

Fatigue is also well characterized by the stress intensity, with crack growth properties being catalogued in well-accepted software tools such as NASGRO or AFCRACK. Difficulties can arise due to load interaction and crack closure, load spectrum, adverse environments, and plasticity or thickness effects, often requiring the use of experiments to evaluate crack growth under realistic conditions. Doung and Wang [21, Eq. 5] have characterized crack growth under combined bending and extension using a modified stress intensity, K_{mod}, which, when compared to test data for AL7075 specimens, demonstrates good results. K_{mod} is developed by interpolation between two states for which crack growth can be accurately assessed: 1) a crack experiencing only a membrane stress intensity, and 2) a crack with equal membrane and bending stress intensities. From Figure 2-16 it can be seem that there is a significant increase in K_{mod} after removal of the honeycomb. Given that as little as a 15% increase in ΔK can halve fatigue life, it is apparent that bending has a large role.

2.5.2 Adhesive failure

Adhesive failure is dependent on the adhesive stress or strain state that develops as the repair acts to bridge the crack. Figure 2-17 shows the peak shear and peel stresses at the edge of the crack for location A on Figure 2-11. The results exhibit nonlinear behaviour, with the adhesive stresses for the unconstrained case nearly vanishing under a compressive remote applied stress, where the crack will close as the thermal residual strains are overcome. These results include thermal residual strains in the adhesive using an effective stress-free temperature of 81°C [7]. It must be noted that in the finite element model, the peel and pressurization stresses vary significantly through the thickness of the adhesive, an observation that other researchers have also observed in bonded joint models. It was not possible to examine this effect in detail with the developed finite element model because of size restrictions on the university version of ANSYS. Similarly, finite element results for the adhesive compression in the unrestrained case are likely to be over-reported as no attempt was made to model crack closure between the

surfaces of the adhesive disbond. Closure of the adhesive crack faces would be expected to act to relieve a portion of the compressive adhesive stresses in the restrained specimen.

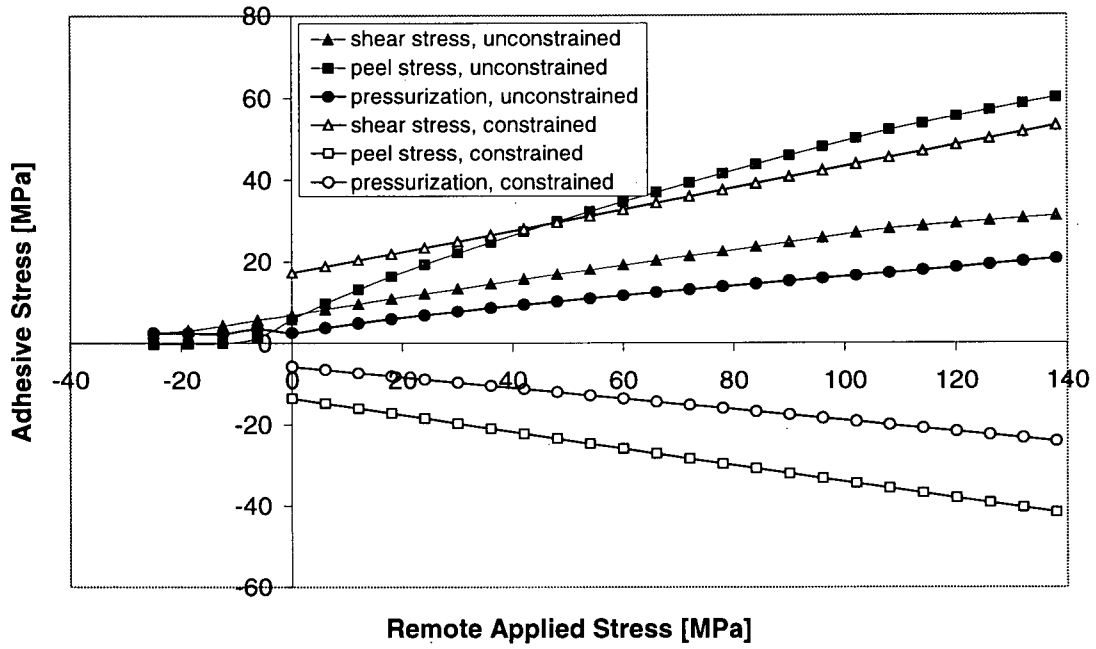

Figure 2-17: Adhesive stresses

Adhesive strength depends on whether yielding or fracture is prevalent. In hot and wet conditions, high temperatures and the plasticizing effect of absorbed water act to make yielding dominant. At low temperatures associated with high altitude flight, fracture becomes prevalent. The main design criterion is the adhesive stress, which should be kept low to ensure that fatigue failures will not initiate and gross yielding will not occur under limit loads. Shear and peel stresses are controlled by using an appropriate adhesive thickness, providing long joint overlap lengths to minimize bending loads and peel stresses, and by tapering the edges of the joint. The strength of the Cytec FM73M adhesive under various degrees of constraint and for laboratory or hot and wet environmental conditions is well characterized by the work of Chalkley and van den Berg [22] and by Ignjatovic, Chalkley and Wang [23,24]. The failure surface for this adhesive is pressure-dependant, and is best characterized by the Drucker-Prager cap plasticity model [23], particularly in the presence of compressive pressurization. It can be seen in Figure 2-17 that compression of the adhesive is not a concern for unbalanced repairs (see the curves for the no constraint case under compressive remote loading), as the crack faces will close and the aluminum will carry the stresses, unloading the adhesive. The authors use a simpler model, based on [22] and [23], whereby the adhesive will obey the Tresca or von Mises criterion under compression, and the modified Tresca or modified von Mises criterion under tensile pressures, thus providing the limit shear yield strength as defined below.

$$\tau_y = \begin{cases} 38.6MPa & p < 0MPa \\ 38.6MPa - 1.13p & p \geq 0MPa \end{cases} \quad (1)$$

This best fit criterion is plotted in Figure 2-18 along with a second criterion that has been developed to account for environmental effects, and employs a penalty factor of two against both the shear and pressurization stresses, as suggested by Chalkley and Baker [26] for the shear stress allowable. It is noted that RAAF design guidelines allow adhesive loading to 80% of the allowable shear strain [25]. For comparison, allowable shear stress results from ASTM D5656 testing (pure shear) by Chalkley and van den Berg [22] are shown in Figure 2-18 for various environmental conditions.

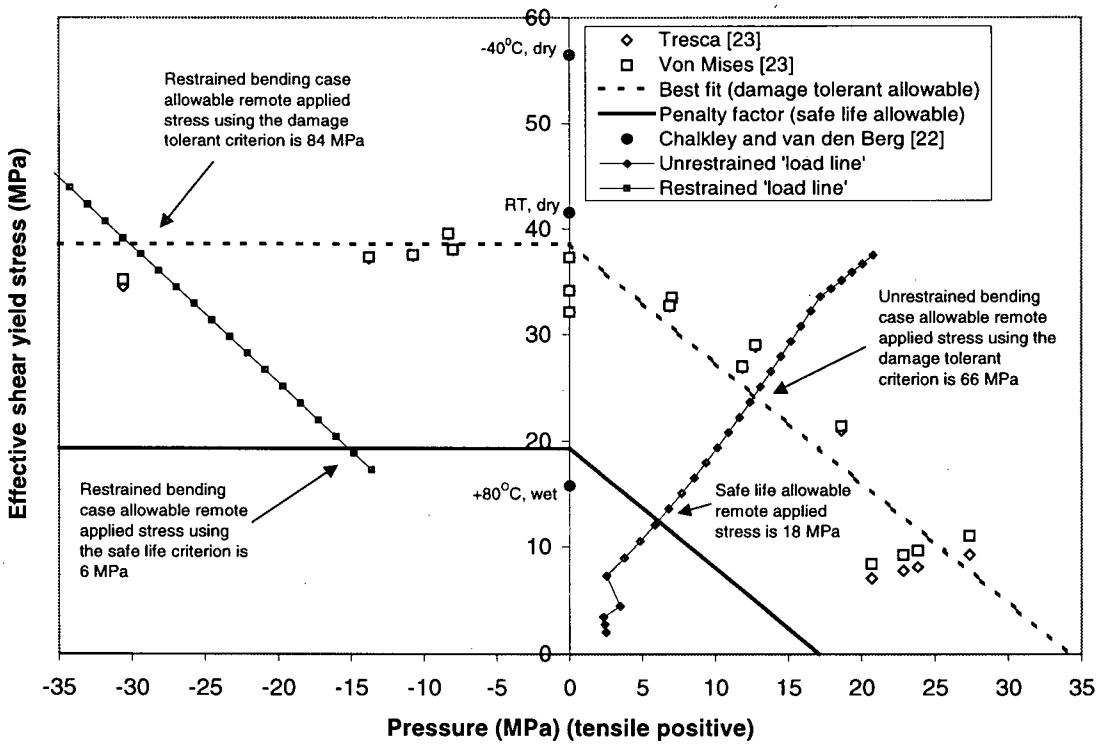

Figure 2-18: Adhesive yield criteria and finite element model adhesive stresses

The trace or 'load line' of the finite element model adhesive pressurization and shear stresses is plotted in Figure 2-18 for both the restrained bending and unrestrained bending cases. For restrained and unrestrained bending the adhesive should begin to yield under a remote applied stresses of 84 and 66 MPa, respectively. It is apparent that the adhesive was repeatedly loaded into the plastic range during the fatigue testing, and that without bending restraint, significant peel stresses and pressurization developed in the adhesive near the crack, explaining the rapid failure of the repair. Applying the safe life design criterion that includes factors to account for environmental effects, neither of the two cases would result in a useful load carrying capability. It is clear that the safe life allowable stress is very conservative and would be difficult to meet in the presence of a

long crack under a repair. It is an appropriate criterion, however, in the tapered region where good design can reduce the adhesive stresses. In the region near the crack, environmental concerns are less likely to be critical, and the damage tolerant allowable may be more suitable, perhaps with a reduction such as the 80% of allowable shear strain policy used by the RAAF.

One must also assess adhesive fracture and fatigue. Since adhesive strength and stiffness result from molecular and inter-molecular forces which exhibit strain-rate, moisture, and temperature sensitivity, damage tolerance substantiation must include both the detrimental effect of cold temperature on fracture toughness [27] and the effect of high temperatures that induce plasticity and accelerate fatigue crack growth. The use of energy-based fracture parameters is complicated by the dependence of the stress distribution on the joint loading type, geometry, and material composition. This violates the similarity criterion, whereby it is assumed that cracks have similarly-shaped stress distributions regardless of crack length, position, or geometry and thus explains why inconsistent results can arise when they are used to predict fracture and fatigue [8, 28]. A final complication is that either of two modes of cracking may occur, cohesive and adhesive. Cohesive failures occur when the adhesive fails by yielding and cracking, while adhesive failures occur at the bond line. There is debate over whether pure interfacial failure can occur or if it occurs by low-energy fracture of the weaker material due to constraint from the stiffer and (usually) stronger material present. But, it is generally agreed that for a well-designed joint, adhesive failures should not occur unless a bond surface has been poorly prepared, i.e. the principle forming the basis for quality assurance testing of bonded joints. These are significant challenges, and in practice test data from specimens with a similar composition, geometry, and loading is required. Many researchers in the bonded composite repair field have been critical of the strain-energy release rate approach to adhesive fatigue and fracture, and other options have been suggested including use of the Hart-Smith plastic strain energy density [29] or plastic strain range [8] approaches. In spite of this criticism, the use of strain energy release rates for specific geometries and loading conditions has provided some excellent results [30-37], and a body of literature exists for the Textron 2251 boron prepreg and Cytec FM73M patch system [e.g. 38-40] which includes information on fatigue threshold and environmental effects.

Here, the authors test the use of elastic adhesive stresses as a conservative criterion for fracture and fatigue assessment of the adhesive. In a previous round-robin test of bonded joint analysis methodologies for the cracked lap-shear specimen [41], Joseph and Erdogan demonstrated that the opening and shear mode strain energy release rates are related to the peak peel and shear adhesive stresses. This approach builds on the strain energy release rate arguments of Rice [42], an approach which is considered to provide

exact results for many fracture problems, and has been applied by other researchers [e.g. 8, 43]. The round-robin testing showed that this method of strain energy release rate calculation provides reasonable results when compared to other techniques such as modified crack-closure. Accordingly, the opening and sliding mode strain energy release rates may be calculated from the peel and shear adhesive stresses as follows:

$$G_I = \frac{t_a \sigma_p^2}{E_a}, \quad G_{II} = \frac{t_a \tau_p^2}{G_a} \tag{2a,b}$$

For a linear-elastic homogeneous material, the strain energy release rate may be converted to a stress intensity using the plane strain relationship, $K^2 = GE_a/(1-\nu_a^2)$. Thus the adhesive stresses, G, and K should be more or less equally capable of predicting fatigue and fracture in the elastic regime for joints of similar composition and loading. In the plastic regime, the elastic-plastic strain energy release rate, J, can be calculated by defining contours outside of the crack tip process zone and using energy arguments to determine the rate of work required for crack extension. J is effectively independent of the state of the process zone unless the plastic strains are sufficient to cause significant changes in the energy state of the elastic region of the specimen. In this case, the method of Erdogan and Joseph will still provide accurate results and the adhesive stresses, G (or J), and K based on an elastic analysis are still more or less equally capable of predicting fatigue and fracture. Similarly by the method of Erdogan and Joseph, the strain energy density and adhesive stresses are also simply related for a linear elastic material. Accordingly, while each of these various measures of the state of the adhesive has advantages concerning how it is calculated or assessed from a numerical model or experimental results, and some provide a better representation for an adhesive experiencing creep or gross plasticity, there is in many ways little to choose between them, particularly when one considers that the design criteria will essentially restrict the thickness-averaged adhesive stresses to the elastic range. The main difference is convention, whereby an analyst will understand a critical stress intensity to imply a material property whereas a strain energy release rate should be understood as a measure of the energy absorbed during the failure of a particular specimen under particular conditions. For repair and overhaul there is not the time, information, or expertise to perform sophisticated analysis, and even with conventional repairs, simple and conservative means are often preferred, even at the expense of increased operational burdens such as higher inspection frequency or early scrapping or rework. Accordingly, the authors will use the available experimental data to test the stress-based adhesive failure criteria.

As a comparison of adhesive failure criteria, Figure 2-19 plots experimental data from several sources against the yield criteria by assuming an adhesive thickness of 0.17 mm,

which is the value used by Butkus and Johnson [39]. The data has been converted from adhesive stresses and strain energy release rates to opening mode (K_I) and sliding mode (K_{II}) stress intensities as described above. Given the complex interactions between the boron fibres, matrix, and adhesive, this conversion does not imply that the actual stress intensity at the tip of a crack has been calculated. The plotted results indicate that the stress-based criteria are conservative in all cases, even when including environmental effects and matrix or interface cracking. It is also seen that, for this adhesive thickness, the yield criterion and room temperature fatigue threshold (including environmental effects) are similar and a criterion based upon the adhesive stresses should be adequate for both fracture and fatigue. Note that Butkus and Johnson used a threshold of $10^{-9} m/cycle$, whereas Chalkley and Baker used $6 \cdot 10^{-9} m/cycle$.

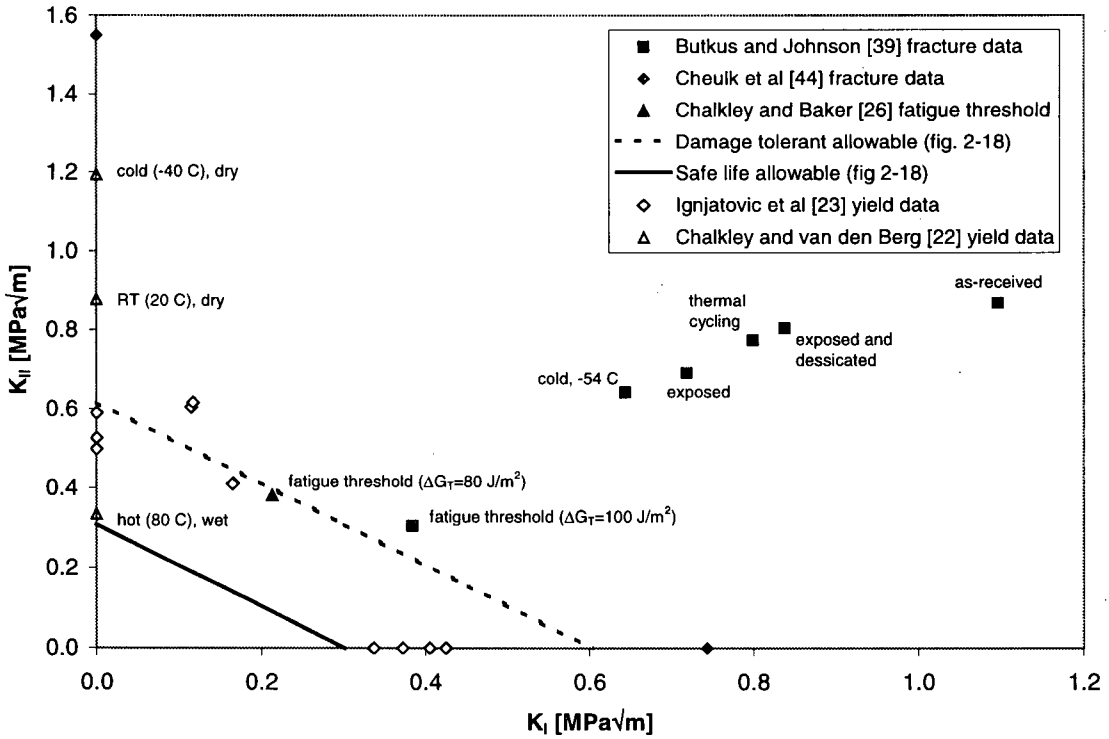

Figure 2-19: Comparison of adhesive fracture data and yield criteria

For fatigue assessment, it has been proposed by many [e.g. 8, 30, 36] that the adhesive stresses be low enough that disbond growth will not occur. Hart-Smith [45] has also emphasized that well designed bonded joints should designed for an infinite life, and that the locus of failure or weak link in the structure should not be the bond. This proposition arises because adhesive joints exhibit high disbond growth rates that increase very quickly with an increase in the applied fatigue load, and because through good design it is usually possible to reduce the adhesive stresses to the point where fatigue cracking is extremely unlikely. It is suggested that the unmodified adhesive failure criteria be

employed in the damage-tolerant region about the repaired crack, and that the safe life criteria (to account for environmental effects) be used for the safe-life region about the edges of the repair. This is in accordance with the definition of the safe life and damage tolerant regions of a repair as defined by Baker [46], but to some degree this runs counter to the advice of Chalkley et al [8], who have suggested that a stress-based approach for fatigue assessment may not be appropriate because in their experiments, the specimens with the highest stresses were not always the ones that failed first. However, given the experimental threshold data shown in Figure 2-19, which by nature accounts for the effects of local stress raisers (e.g. due to fibre geometry and lay-out, adhesive imperfection, etc.) that are not included in most repair models, it should be adequate to simply show that limit loads do not result in adhesive stresses that exceed these allowables. This is particularly true if one considers that the effective once-per-flight fatigue loads (the load that would be applied once per flight cycle to represent all the fatigue damage accrued by the actual fatigue spectrum) are typically well below limit load (usually below 60% of limit load) and that the fatigue threshold data applied is typically for room temperature testing while flight loads will tend to occur at high altitude where the lower temperatures enhance fatigue strength. Accordingly, the authors suggest that a stress-based approach, while imperfect, would still be applicable by the principle of compounded conservatism [47, sec 9.5]. Compounded conservatism is the practice of applying many 'worst-case' conservative assumptions together to ensure safety, and while it may lead to an inefficient design it does ensure safety in the face of a number of factors that are difficult to quantify (e.g. temperature and environmental effects, fatigue that may be dominated by very local structural details, or stochastic variations in properties or material processes).

2.5.3 Composite fracture and delamination

The textbook approach to composite failure analysis is to use interactive failure criteria such as the Tsai-Wu theory [e.g. 48]. These theories extend the energy-based failure criteria that have been successful for homogeneous anisotropic ductile solids to the analysis of heterogeneous fibre-polymer composites that exhibit fracture-dominated failure modes. Pioneering data on the application of the Tsai-Wu failure theory is available for boron fibres with an older matrix system [49, 50]. The other general class of failure criteria arise from mechanistic modelling, in which individual failure modes are analysed to form a set of equations that form a failure envelope based upon stresses or strains. The WWFE (World Wide Failure Exercise) [52] tested several composite failure criteria against a set of tests that are representative of design problems arising in different industries. Interactive theories were found to give good results in most cases, but caution was urged in their application to unidirectional lamina, where unconservative results could be obtained. Most criteria provided reasonable results for the types of problems for

which they were designed, including maximum stress or strain criteria that are often used for specific applications in codes and standards. It was emphasised that careful interpretation of the results is required, and that for large deformations or final failure strength, non-linearity and progressive damage are important considerations. Given that for a repair patch, weight optimization is not critical, simple criteria are preferable and adequate when supported by experimental data, and a mechanistic approach expressed in terms of simple stress or strain limits may be preferable.

Hart-Smith [51] has made a convincing case that the various constituents and failure modes of the composite should be treated separately, and that interaction should be handled by superposition of loads, allowing the strength of the composite to be assessed through separate analysis of the constituents (fibres, matrix, and interface) under the combined loads (including cure-induced thermal residual stresses in the matrix), leading to a failure envelope comprised of several individual criteria for each constituent. Micro-mechanical failure models are often only required for the development of engineering design allowables, and resulting individual failure criteria are often quite simple. Hart-Smith has catalogued the typical failure mechanisms, which after elimination of those that are not relevant to crack patching with a unidirectional patch, are summarized in Table 2-2.

Fracture of fibres at flaws and defects, and fibre failure under tensile loads
Fibre micro-instability and fibre shear failure under compressive loads
Ductile matrix failure under in-plane loads
Matrix cracking under transverse-tension (geometry dependent)
Interfacial failure between fibre and matrix
Interlaminar failure at edges and discontinuities
Delamination under impact or transverse shear loads

Table 2-2: Possible composite failure modes for unidirectional patch

Within FAA guidance documents and the crack-patching literature, it has been stressed that composite and adhesive failure modes must be addressed. As the technology has been used primarily in structures with significant bending restraint and primarily tensile loads, composite failure mechanisms other than progressive adhesive disbonding or delamination have rarely been observed. The requirement for fatigue test validation has also provided a definitive control on composite failure modes. With increasing interest in the use of single-sided repairs and wider application of generic repairs without specific tests, it will be necessary to specifically address each composite failure mode, especially considering that single-sided repairs are much more susceptible to composite failures and instability under compressive loads, as demonstrated by the testing carried out by the authors as described above.

Given that: a) for most boron-epoxy repairs the primary load path is in the primary direction of the patch, b) the aluminum substrate will support out-of-plane loads, c) crack closure will shield the composite patch from the worst of the compressive stresses, and d) the tensile strength of the boron patch is high compared to the underlying aluminum plate, it should generally not be necessary to perform a sophisticated analysis of the many possible failure modes to assess the strength of the composite patch. The margins against both matrix and fibre failure should generally be high, except in the presence of significant bending and peel stresses which may promote matrix cracking (due to transverse stresses) and the failure of fibers on the inner or outer surface of the repair. Transverse loading can result in matrix or interfacial failure as stiff fibers lead to stress concentrations in the matrix, causing it to fail before the nominal transverse stress exceeds the strength of the matrix. From testing and fractography, it has been shown that the exact geometrical distribution of the fibres has a significant role, and a strength reduction factor must be used to develop a failure criterion for the composite [48]. It is suggested that the adhesive stress allowables already cover this assessment of the composite matrix, including the temperature and environmental effects and the stress concentrations in the matrix due to the constraint of the fibres. The adhesive stresses are representative of the critical matrix transverse stresses and the Butkus and Johnson data [39] provides assurance that they will be held to an appropriate level.

Under axial loads, for a unidirectional polymer-reinforced composite such as boron-epoxy, failure occurs when the stress in the boron fibres reaches its maximum, corresponding to a nominal tensile stress in the orthotropic solid. This is the principal strength of the composite, and Textron product data [53] specifies a tensile strength of 1520 MPa at room temperature and 1450 MPa at elevated temperatures. Fatigue under such loading may be characterized by a stress-life (S-N) diagram, with small reductions in stiffness and strength occurring as the matrix cracks and delaminates near fibre breaks and stress concentrations. When compressive stresses occur (possibly due to bending), transverse stresses and interlaminar failure have a detrimental effect. Tensile interlaminar stresses develop due to the buckling of fibres, and transverse stresses may cause interlaminar failure. This form of fibre-buckling is controlled by the adhesive shear yield stress [48]. Textron product data provides a compressive strength of 2930 MPa at room temperature and a much lower 1250 MPa at elevated temperatures. As the compressive strength is controlled by the matrix shear stress, it is suggested that the lower value be used as a basis for a conservative design allowable.

In the experimental work described above, the composite repair was observed to have failed via partial delamination, and ultimately by fracture under combined bending and axial loads at the edge of the disbonded region. The composite stresses at point A of the finite element model are presented in Figure 2-20, where it can be seen that the sum of

the membrane and bending stresses is high but does not exceed the principal strength of the composite (as quoted in the paragraph above) for either restrained or unrestrained bending. Some fibre failure was observed in the experiments, and could be explained by either fatigue failure under these relatively high stresses, or due to the adhesive/matrix peel stresses. These adhesive/matrix peel stresses were shown by the authors to be very large after removal of the bending restraint and could act to break individual fibres that come free of the matrix due to delamination.

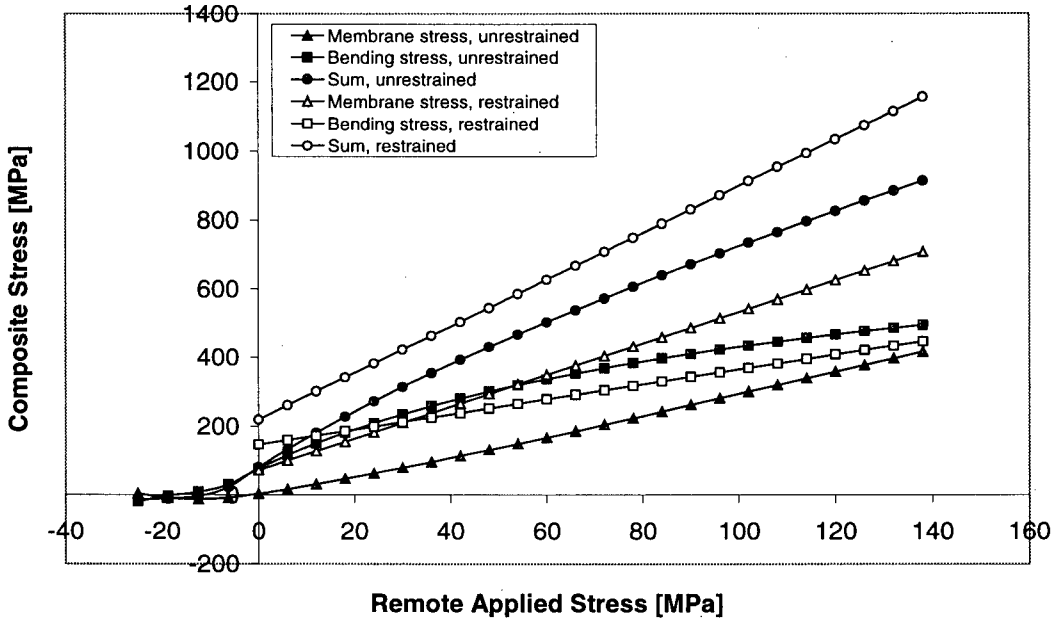

Figure 2-20: Composite stresses

Although comparison to the results of this single test is not definitive, it is likely that the principal strength design criteria are adequate for the composite patch itself, so long as the adhesive stress design criteria are adequate to rule out early failure due to transverse stresses. This can be confidently stated because the strength of the boron/epoxy patch is very high relative to the substrate. It may prove to be necessary, however, to develop a knock-down factor to account for fatigue (i.e. to keep the stresses low enough to prevent composite fatigue failures during the life of a patch), but there should generally be a sufficient margin to cover such a strength reduction.

Given that the adhesive design criteria adequately covers the possibility of early failure due to high transverse normal or shear stresses in the matrix, and the composite strength accounts for failure from tensile or compressive stresses, early patch failure should only be possible due to impact damage or manufacturing flaws. Currently, low-velocity impact tests are required to determine the susceptibility of a repair to such damage. As "best practices" and the proposed adhesive and composite design criteria will keep the stresses

low in the bulk of the repair through good design, only low rates of sub-critical damage growth should occur in the event of accidental flaws. One would not expect significant growth of inter-ply or impact damage unless it is accompanied by fiber damage or occurs in a region experiencing significant bending and through-thickness stresses, compressive loads, or very large transfers of load through shear (such as might exist near a repaired crack or about the edges of the patch). In practice, this has proven to be true, with experimental results suggesting that delamination growth from impact damage or manufacturing flaws away from load transfer regions is minimal [11]. Accordingly, damage growth should only occur in highly loaded regions such as about the crack and near the edges of the repair, where the stresses have already been controlled through the proposed design criteria.

2.5.4 Synergy of aluminum and composite/adhesive fracture criteria

The final failure of the patch as observed in the experimental investigation was via simultaneous fracture of the repair and plate due to the overload of the composite by local bending and axial loads at the edge of the disbond. For symmetric repairs or repairs with significant bending restraint, failure has been observed to occur by fracture of the repaired plate and simultaneous growth of an adhesive disbond through to the edge of the repair, typically with the composite patch itself otherwise being undamaged. It is possible to model either scenario using a detailed finite element analysis, using nodal release and element removal to model the growing crack and disbond, or by generating a new model for every increment in crack growth or disbond growth. The actual residual strength can then be determined by whatever ratio of cracking and disbonding led to a natural balance between the failure of the patch and the repair/adhesive [e.g. 54]. Simplified finite element techniques [e.g. 12, 13], boundary element models [e.g. 10], and crack-bridging models [55] have all been used to evaluate the life of a repair with a growing disbond and crack. The authors have recently developed a new crack-bridging model for coupled bending and extension [56] and geometrically non-linear coupled bending and extension [57], which should allow for rapid assessment of unbalanced repairs.

The concept of synergy between crack and disbond growth and a natural disbond size, when combined with the allowable stress criteria described above and effective models for combined crack and disbond growth, leads to a new opportunity to simplify the damage tolerance substantiation of a repair. Experience suggests that limited disbonding will often occur near a repaired crack in a highly loaded structure, and that additional analysis will be required to fulfill substantiation requirements and ensure that the patch is sufficiently large to provide adequate damage tolerance against disbonding. It is suggested that, in the absence of a fatigue test that demonstrates otherwise, one must assume that the adhesive has debonded about the repaired crack to the point where the

adhesive stresses drop to a threshold value (i.e. the damage tolerant allowable). This will, in effect, result in disbond growth that is controlled by growth of the repaired crack under fatigue loading, where both the crack and disbond size are determined by applying standard LEFM techniques to the crack alone using the as-reinforced stress intensity (i.e. K_{mod} as demonstrated above). As crack growth in the metal substrate is well characterized, the issue of fatigue crack growth rate prediction for the adhesive is avoided, allowing a rational determination of the inspection criteria.

2.6 Discussion

The experiments and the validated finite element analysis demonstrate the potential for early failure of a single-sided bonded composite repair due to induced bending. The tested geometry was initially designed to include bending restraint and did not have a sufficient overlap length to minimize bending loads and adhesive peel stresses. Without bending restraint, failure occurred very rapidly, illustrating the need for adherence to bonded joint design guidelines, particularly the use of sufficient overlap lengths. The observed failure modes included rapid disbonding of the adhesive at the adhesive-composite interface, fibre breaking, and ultimately simultaneous failure of both the repair and the underlying plate. It is shown that nonlinear analysis techniques are required for the accurate analysis of a repair, and that crack face contact must be modeled to evaluate a repair under compressive loads. These results show that composite and adhesive failure modes must be treated very seriously for single-sided repairs, and the specimen proves to be an extreme test for patch design methods.

In the second half of the paper, finite element results for the stress intensity in the underlying plate, the stresses in the adhesive layer, and the composite patch stresses were compared to failure criteria for fatigue, yielding, and fracture. It was shown that the underlying plate can be treated using LEFM, and that adhesive and composite stresses can be controlled to ensure integrity of the patch. Linear elastic analysis is used to determine the adhesive stresses and a failure criterion and a method for fatigue assessment is proposed that accounts for adhesive pressurization and places a large penalty on peel stresses. Most of the complications of fatigue and fracture assessment of bonded joints are encapsulated within the proposed allowable stresses, allowing for a relatively simple assessment of the joint. With more experimental work to justify the design allowables, and with appropriate closed-form tools for repair analysis, most repairs should be able to be certified using a simple analysis of this type.

The principal strength of the composite was also shown to be an adequate criterion for longitudinal tensile loads in the unidirectional patch. As the compressive strength of the composite is determined primarily by the shear strength of the matrix, the authors suggest that the high temperature compressive strength be used as the allowable stress in

compression. This corresponds to the approach developed by the authors for evaluation of the adhesive and of the composite matrix under transverse loads, whereby it was shown that a simple stress-based criterion is generally adequate for damage tolerance substantiation of a repair.

The stress-based adhesive failure criteria were achieved by directly comparing the adhesive yield criteria to fracture criteria via Joseph and Erdogan's definition of the strain energy release rate for a bonded joint. The technique is promising but needs further investigation to validate. Specifically, the adhesive yield criteria under combined peel and shear stresses need to be established under hot and wet conditions, and more fracture strength and fatigue threshold data needs to be generated for the aluminum/FM73M/boron-epoxy system considering the effects of adhesive thickness and environment. This would entail a detailed testing program, but would establish an authoritative stress-based design allowable for bonded repairs. As the practical working range of an adhesive in this application is only 0.125 to 0.250 mm [58], the scope of this additional testing should not be overly expensive or onerous. An additional problem that needs to be addressed is that, to ensure consistency in the comparison of the test results, Joseph and Erdogan's method should be used throughout. It is noted that the strain energy release rates reported by Butkus and Johnson were calculated using the virtual crack closure technique. Finally, the criteria should be tested against the working stresses in the many repairs that have been accepted for certification through a comprehensive damage tolerance substantiation process, to ensure that the proposed stress-based design criteria is sufficiently conservative when compared to established practice. The observation that the composite patch and the repaired plate fail in a synergistic manner, when combined with this simple stress-based design criteria that encapsulates the many complex damage mechanisms that can occur within a repair, leads to a new opportunity to evaluate the design life of a repair and the ability to assign an inspection interval without a detailed analysis of the fatigue response of the adhesive. In this proposed approach it should be assumed that an adhesive disbond will exist that is large enough to reduce the adhesive stresses to the threshold level. The fatigue assessment and damage tolerance substantiation can then be can carried out based on the crack length alone, with the ultrasonic or thermographic inspection of the repair being carried out at the same time as the eddy current inspection of the underlying crack.

Based upon the adhesive stress design criteria and the residual strength and fatigue life of the unrepaired crack, it is possible to divide repairs into four categories, as shown in Figure 2-21. By applying the principle of compounded conservatism and by applying a simple risk assessment to ensure that the safety of the repaired structure is higher than that established during the design of the original damage tolerant structure, it is possible

to develop acceptance criteria for bonded repairs applied to weakened or damaged structures.

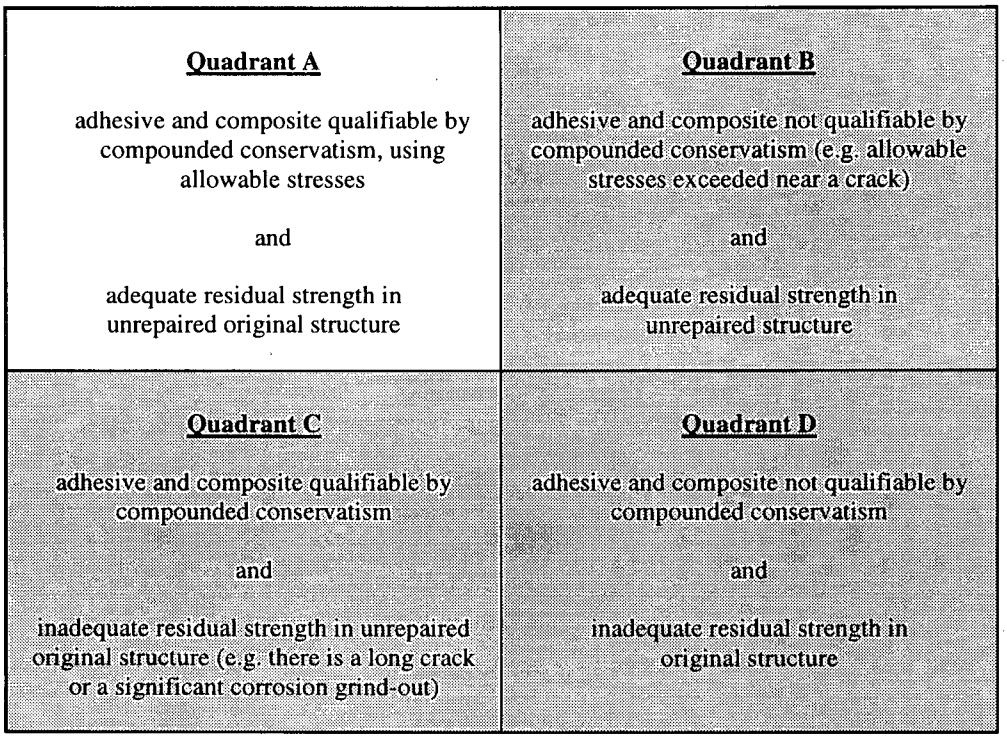

Figure 2-21: Proposed classification of repairs by DT substantiation requirements

Repair designs in Quadrant A have very low working stresses in the composite/adhesive and the underlying structure has adequate residual strength even without the repair. In practice, the working stresses in many transport airframe components are low and the structure can tolerate very long (e.g. bay-to-bay) cracks and still survive limit load due to other reinforcing structures such as stringers and frames. Under this scenario, for the repair of a relatively short crack, the authors suggest that the repair may be substantiated without much further work with inspections based on the crack growth predicted in the equivalent unrepaired structure. The only additional work required would be to ensure that load attraction to the patch does not result in early failure in regions about the edge of the repair or in surrounding structures.

In Quadrant B, the adhesive stresses are locally high, but the patch is not really required to establish inspection criteria for the underlying structure, as it has sufficient residual strength. This could occur in the event of a small flaw or corrosion grind-out in an area where due to geometric constraints it is not possible to reduce the stresses in the composite/adhesive sufficiently to meet the very stringent design criteria, or for a reinforcement used to strengthen an under-designed but undamaged structure with high working stresses. Here, the adhesive/composite interface is likely to fail in a progressive

manner, which could be addressed by re-examining the limit loads to see if they are due to flight or landing loads (i.e. a fatigue case such as a vertical gust), or whether hot and wet conditions are likely to exist during the limit load maneuver. In the event that such a re-evaluation of the loads is insufficient, then a damage-mechanics analysis of the patch or a static test may be required to demonstrate that the patch itself will have sufficient strength even in a highly damaged state.

Like in Quadrant A, repairs in Quadrant C have low working stresses, but the underlying structure has significant damage and the reinforcing effect of the patch is required. An example might be a large fatigue crack emanating from a stress concentration in an otherwise lightly stressed fuselage panel. Here, the primary concern is the possibility of an unpredictable early failure of the repair due to poor surface treatment of the aluminum surface for bonding. Quality assurance and bonding procedures minimize the probability of this type of failure, but cannot eliminate it, particularly for one-off repairs applied in the field. In this case, the authors propose the use of 'phenomenological risk assessment' [59] to assign a very conservative probability of failure to the patch and use this to redefine the limit load for the unrepaired structure. By this method, the repaired structure with an intact patch must be capable of carrying the full limit load, but in the unlikely event of a poorly bonded repair, the underlying structure must be shown to be capable of withstanding the reduced limit load without a patch. The resulting level of safety would still be much higher than the original design because a very conservative probability was used to generate the reduced limit load. By the tenets of phenomenological risk assessment, a conservative probability is assigned to the likelihood of failure based on expert opinion and regulatory acceptance. If it can be agreed upon that the likelihood of a bond lacking durability is much less than 1 in 100, then that is the likelihood that will be used. Whatever probability is chosen, service experience should be used as a basis for verification where possible. This probability can then be used to redefine the limit load for the unrepaired structure to give credit to the patch. If a gust load case were critical, this would lead to the critical case being defined as the gust that will occur 100 times during the life of the structure. This is consistent with providing a reasonable 'get home' ability to the unrepaired structure, and would work well with the requirement for once-per-flight visual check of the patch. This process of re-evaluation of the limit loads will be called Probabilistic Load Assessment (PLA) in the remainder of the chapter.

Quadrant D requires a more detailed assessment of a repair design according to the process shown in Figure 2-22.

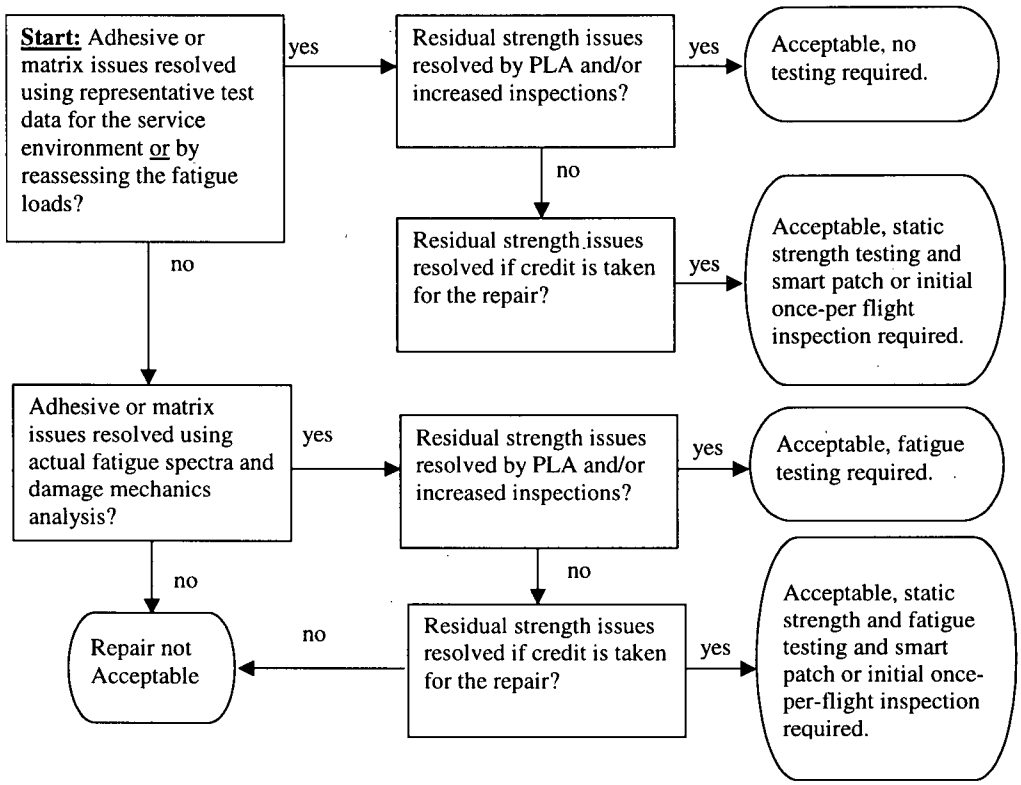

Figure 2-22: Process for 'Quadrant D' repairs

In Quadrant D, the adhesive/composite stresses exceed the stress-based design criteria and the damage in the underlying structure is sufficient to require that the patch be credited in some manner to establish a useful life for the repair. Here, the methods used for damage tolerance substantiation in Quadrants A, B, and C are extended and we find imposed additional requirements for static or fatigue testing, comprehensive damage tolerance analysis, and increased frequency and rigor in inspections, each depending on the particulars of the repair scenario. The use of the methodology and its rationale will be demonstrated by examining two scenarios.

The simplest scenario is one in which both the adhesive stresses and the residual strength of the structure may be addressed by the methods described for Quadrants B and C. Here, we allow the removal of only one of the many factors leading to the certification of the adhesive and composite by compounded conservatism (e.g. re-assessment of the fatigue loads or the environmental knock-down factor) with the understanding that the likelihood of a patch lacking durability is also very conservative and accordingly the resulting structure will still be much safer than the original design. If PLA is not sufficient and it is required to directly credit the patch to obtain an acceptable life, then additional testing and inspection requirements arise as shown.

A more complex scenario is one in which an accurate damage tolerance analysis of the repair is required to demonstrate adequate patch life. Here, we can no longer rely on simple stress-based criteria for the composite and adhesive, and a detailed fracture mechanics and fatigue analysis under the actual fatigue spectrum is required. Depending upon the residual strength of the structure, we find that a patch can be deemed to be outright unacceptable, or acceptable with possibly onerous inspection and testing requirements. In this case, we have essentially reverted to the full requirements for certification of composite structures, and detailed testing and analysis are required. Such a repair is likely to be uneconomical unless it is a fleet-wide repair, or is to be applied to an integral component of the aircraft that cannot be removed or replaced.

2.7 Concluding remarks

The experimental and finite element results clearly demonstrate the importance of both bending and cracked plate geometry on the mechanics of a bonded composite repair. As bending plays a critical role in the peel loading of the adhesive and failure of the fibres in the patch, it is critical to include bending effects in the damage tolerance and durability analysis of a repair. The authors have proposed an approach to damage tolerance assessment based on a conservative adhesive allowable stress that envelopes information regarding adhesive and composite matrix fatigue and fracture, including environmental effects. It is demonstrated that the hot and wet adhesive static strength represents the critical case for both the adhesive and the composite matrix, and accordingly provides adequate protection against fracture, fatigue, and other environmental effects. As the method also places a large penalty upon peel stresses, the new criteria should be adequate to protect against poor designs. The authors have also proposed a quadrant classification scheme for repairs, based upon the residual strength of the unrepaired structure and the calculated adhesive and composite stresses. Different damage tolerance analysis methods and requirements for substantiation are outlined for each class of repair. While more adhesive test data is required (ideally using a consistent method to determine the strain energy release rates), and the effects of adhesive thickness on fracture and fatigue thresholds needs to be assessed with rigor, a process has been established that is applicable to most day-to-day repairs of scratches, dents, oversized holes, and minor corrosion grind-outs which should fall within quadrant A, allowing for rapid design and certification without much more engineering effort than is required for conventional riveted repairs. For more significant repairs, requirements for in-service inspection and testing of representative specimens are assigned by applying probabilistic risk assessment and the principle of compounded conservatism.

2.8 References

[1] Baker, A.A., "Repair efficiency in fatigue-cracked aluminum components reinforced with boron/epoxy patches", Fatigue and Fracture of Engineering Structures, Vol. 16, Num. 7, 1993, pp. 753-765

[2] Baker, A.A., "Fiber composite repair of cracked metallic aircraft components - practical and basic aspects", Composites Vol. 18, Num. 4, 1987, pp. 293-308

[3] Baker, A.A., "Bonded composite repair of metallic aircraft components - overview of Australian activities", AGARD - 79th Structures and Materials Panel Meeting. Specialists Meeting: Composite Repairs of Military Aircraft Structures, 1994, pp. 1-14

[4] Baker, A.A., Roberts, J.D., Rose, L.R.F., "Experimental study of overlap joint parameters relevant to k reduction due to crack patching". 28th National SAMPE Symposium, 1983, pp. 627-639

[5] Raizenne, M.D., Benak, T.J., Heath, J.B.R., Simpson, D.L., Baker, A.A. "Bonded composite repair of thin metallic materials: variable load amplitude and temperature cycling effects", AGARD - 79th Structures and Materials Panel meeting. Specialists Meeting: Composite Repairs of Military Aircraft Structures, 1994, pp. 5-1

[6] Hucalek, P., Raizenne, M.D., Scott, R.F., "Influences of environment and stress history on the composite patch repair of cracked metallic structures", Canadian Aeronautics and Space Institute Journal. Vol. 34, Num. 2, 1988, pp. 85-91

[7] Albat A.M., Romilly, D.P., Raizenne, M.D., "Thermal residual strain measurement in a composite repair on a cracked aluminum structure", ICCM-11, Gold Coast, Australia, 14th to 18th July 1997, pp. VI-279-VI-288

[8] Chalkley,P.D., Wang, C.H., Baker, A.A.,"Fatigue testing of generic bonded joints". In: "Advances in the Bonded Composite Repair of Metallic Aircraft Structure", Volume 1, Baker AA, Rose LRF, Jones R, Eds. Elesvier, 2002, pp. 103-126.

[9] Sharp, P.K., Clayton, J.Q., Clark, G., "Retardation and repair of fatigue cracks by adhesive infiltration", Fatigue and Fracture of Engineering Materials and Structures, Vol. 20, Num. 4, 1997, pp. 605-614.

[10] Poole, P., Lock, D., Young, A., "Composite patch repair of thick aluminum sections", International Conference on Aircraft Damage Assessment and Repair, 1991, pp. 85-91.

[11] Denney, J., Mall, S., "Characterization of disbond effects on fatigue crack growth behavior in aluminum plate with bonded composite patch", Engineering Fracture Mechanics, Vol. 57, Num. 5, 1997, pp. 507-525.

[12] Denney, J., Mall, S., "Fatigue behaviour in thick aluminum panels with a composite repair", Collection of Technical Papers, 39th Annual AIAA-ASME-ASCE-AHS Structures, Structural Dynamics, and Materials Conference Vol. 3, 1998, pp. 2434-2443.

[13] Denney, J., Mall, S.,"Effect of disbond on fatigue behavior of cracked aluminum panel with bonded composite patch", Collection of Technical Papers – AIAA/ASME/ASCE/AHS/ASC Structures, Structural Dynamics & Materials Conferences, Vol. 1, 1996, pp. 14-21.

[14] Klug, J., Malley, S., Sun. C.T.,"Characterization of fatigue behavior of bonded composite repairs", Journal of Aircraft Vol. 36, Num. 6, 1999, pp. 1017-1022.

[15] Sabelkin, V., Mall, S., Avram, J.B., "fatigue crack growth analysis of stiffened cracked panel repaired with bonded composite patch", Engineerin Fracture Mechanics, 73, 2006, 1553-1567.

[16] Jones, R., Chiu, W.K., Smith, R.,"Airworthiness of composite repairs: failure mechanisms", Engineering Failure Analysis Vol. 2, 1995, pp. 117-128

[17] ANSYS 9.0 University Intermediate, Release 9.0, ANSYS,Inc, Canonsburg, PA, USA, 2004

[18] Clark, R.J. and Romilly, D.P., "Coupled bending and extension of bonded composite repairs", CANCOM 2005, August 2005, Vancouver, British Columbia, Canada, Paper No. 41.

[19] NASGRO 4.0, Southwest Research Institute, San Antonio, Texas, USA, 2002.

[20] Anon, "Metallic Materials Properties Development and Standardization Handbook" (formerly MIL-HDBK-5), Federal Aviation Administration Technical Report.

[21] Duong, C.N., Wang, C.H., "On the characterization of fatigue crack growth in a plate with a single-sided repair", Journal of Engineering Material and Technology, Vol. 126, April 2004, pp.192-198.

[22] Chalkley P., van den Berg, J., "On obtaining design allowables for adhesives used in the bonded composite repair of aircraft", Australian Department of Defense, Defense Science and Technology Organization, DSTO-TR-0608, 1998.

[23] Ignjatovic, M., Chalkley, P., Wang, C., "The yield behavior of a structural adhesive under complex loading", Australian Department of Defense, Defense Science and Technology Organization, DSTO-TR-0728, 1998.

[24] Wang, C.H., and Chalkley, P., "Plastic yielding of a film adhesive under multiaxial stresses", International Journal of Adhesion and Adhesives", Vol. 20, 2000, pp. 155-164.

[25] Chester, R.J., Walker, K. F., Chalkley, P.D., "Adhesively bonded repairs to primary aircraft structure", International journal of Adhesion and Adhesives, Vol. 19, 1999, pp. 1-8.

[26] Chalkley, P., and Baker A.A., "Adhesives characterization and database". Chapter 4 in: Advances in the Bonded Composite Repair of Metallic Aircraft Structure", Volume 1, A.A. Baker, Rose, L.R.F, Jones, R., Eds. Elesvier, 2002, pp. 87-102.

[27] Wilkins, D.J., Eisenmann, J.R., Camin, R.A., Margolis, W.S., Benson, R.A., "Characterizing delamination growth in graphite-epoxy", Damage in Composite Materials, ASTM STP 775, K.L. Reifsnider, Ed., American Society for Testing and Materials, 1982, pp. 168-183

[28] Lin , C., Liechti, K.M., "Similarity concepts in the fatigue fracture of adhesively bonded joints", Journal of adhesion, Vol. 21, Num. 1, 1987, pp.1-24.

[29] Hart-Smith, L.J., "Adhesively bonded double lap joints", NASA Langley Research Report, NASA CR-112235, January 1973.

[30] Mall, S., Johnson, W.S., Everett, R.A., "Cyclic debonding of adhesively bonded composites". Adhesive joints: formation, characterization and testing: proceedings of an international symposium. Plenum press, New York, 1982, pp. 639-658.

[31] Kinlock, A.J., Osiyemi, S.O., "Predicting the fatigue life of adhesively bonded joints", Journal of adhesion, Vol. 43, Num. 1, 1993, pp.79-90.

[32] Fernlund, G., Papini, M., McCammond, D., Spelt, J.K., "Fracture load predictions for adhesive joints", Composites Science and Technology, Vol. 51, 1994, 587-600.

[33] Williams, J.G., "On the calculation of energy release rates for cracked laminates", International Journal of Fracture, Vol. 36, 1988, pp. 101-119.

[34] Mall, S., Ramamurthy, G., Rezaizdeh, M.A., "Stress ratio effect on cyclic debonding in adhesively bonded composite joints", Composite Structures, Vol. 8, 1987, 31-45.

[35] Mall, S., Yun, K.T., "Effect of adhesive ductility on cyclic debond mechanism in composite-to-composite bonded joints", Journal of Adhesion, Vol. 23, 1987, pp. 215-231.

[36] Mall, S., Johnson, W.S., "Characterization of mode 1 and mixed-mode failure of adhesive bonds between composite adherends". Composite Materials: Testing and Design (Seventh Conference), ASTM STP 893, J.M. Whitney, Ed., American Society for Testing and Materials, Philadelpia, 1986, pp. 322-334.

[37] Hwu, C., Kao, C.J., Chang, L.E., "Delamination failure criteria for composite laminates", Journal of Composite Materials, Vol. 29, No. 15, 1995, pp. 1962-1985

[38] Valentin, R.V., Butkus, L.M., Johnson, W.S., "A finite element and experimental evaluation of boron-epoxy doublers bonded to an aluminum substrate", Journal of Composites Technology and Research, Vol. 20, No. 2, 1998, pp. 108-119.

[39] Butkus, L.M., Johnson, W.S., "Environmental effects on the opening mode fracture behavior of bonded boron-epoxy/aluminum joints", Proceedings of the American society for composites, 11th technical conference, October 7-9, 1996, Atlanta, Georgia, pp. 1039-1048.

[40] Lubke, K.A., Butkus, L.M., Johnson, W.S., "Effects of environment on fracture toughness and debond growth of aluminum/FM73/boron-epoxy adhesively bonded joints", Journal of Composites Technology and Research, Vol. 23, No. 1, 200, pp. 42-49.

[41] Joseph and Erdogan in: Johnson W.S., "Stress Analysis of the cracked-lap shear specimen: an ASTM round-robin", Journal of Testing and Evaluation, Vol. 6., 1987, pp. 303-324.

[42] Rice, J.C. "Stresses in an infinite strip containing a semi-infinite crack", Journal of Applied Mechanics - Transactions of the ASME, 1967, pp. 248-249

[43] Krenk, S., "Energy release rate of symmetric adhesive joints", Engineering Fracture Mechanics, Vol. 43, No. 4, 1992, pp. 549-559.

[44] Cheulk, P.T., Tong, L., Wang, C.H., Baker, A., Chalkley, P., "Fatigue crack growth in adhesively bonded composite-metal double-lap joints", Composite Structures, Vol. 57, 2002, pp. 109-115

[45] Hart-Smith, LJ, "Design and analysis of bonded repairs for metal aircraft structures". In: "Bonded repair of aircraft structures", Baker AA and Jones R, eds. Martinus Nijhoff Publishers, 1988, pp.31-47.

[46] Baker, A.A. "On the certification of bonded composite repairs to primary aircraft structure". Proceedings of ICCM-11, Gold Coast, Australia, 1997, I-1 to I-23.

[47] Anon., "Composite materials handbook volume 3. Polymer matrix composites materials usage design and analysis", MIL-HDBK-17-3F, U.S.A. Department of Defense, 2002.

[48] Hull, D., Cliyne, T.W., "An Introduction to Composite Materials", 2nd Edition, Cambridge University Press, 1996.

[49] Pipes, R.B.,"On the off-axis strength of anisotropic materials", Journal of Composite Materials, Vol. 7, 1973, pp. 248-256.

[50] Hashin, Z., "Failure criteria for unidirectional fiber composites", Journal of Applied Mechanics, Vol. 47, 1980, pp. 329-334.

[51] Hart-Smith, L.J., "What textbooks won't teach you about interactive composite failure criteria", Composite Structures: Theory and Practice, ASTM STP 1383. P. Grant and C.Q. Rousseau, Eds. American Society for Testing and Materials, West Conshohocken, P.A. 2000. pp. 413-436.

[52] Sodena P.D., Kaddourb, A.S., Hintonc, M.J., "Recommendations for designers and researchers resulting from the world-wide failure exercise". Composites Science and Technology, Vol. 64, 2004, pp. 589–604.

[53] Textron Specialty Materials, Boron Epoxy Prepreg Tape-5521 Product Data Sheet, 2 Industrial Avenue, Lowell, MA.

[54] Papikanos, P., Tserpes, K.I., Labeas, G., Pantelakis, Sp., "Progressive damage modeling of bonded composite repairs", Theoretical and Applied Fracture Mechanics, Vol. 43, 2005, pp. 189-198.

[55] Clark, R.J., Romilly, D.P., "Linear coupled bending and extension of an unbalanced bonded composite repair", International Journal of Solids and Structures. Vol. 44, 2007, pp. 3156–3176.

[56] Clark, R.J., Romilly, D.P., "Nonlinear mechanics of hybrid bonded joints and bonded composite repairs", International Journal of Nonlinear Mechanics. Submitted November 2006.

[57] Clark, R.J., Romilly, D.P., "Fatigue Damage Prediction for Bonded Composite Repairs Applied to Metallic Aircraft Structures", SAE Transactions - Journal of Aerospace, 2001.

[58] Okafor, A., Singh, N., Enemuoh, U.E., Rao, S.V., "Design, analysis and performance of adhesively bonded composite patch repair of cracked aluminum aircraft panels", Composite Structures, Vol. 71, 2005, pp. 258-270

[59] Theofanous, T.G., "On the proper formulation of safety goals and assessment of safety margins for rare and high-consequence hazards", Reliability Engineering & System Safety, Vol. 54, 1996, pp. 243-257

Chapter 3: Extension of generalized plane strain plates with reinforced cracks*

Randal J. Clark, Douglas P. Romilly

University of British Columbia, Department of Mechanical Engineering

3.1 Introduction

In this chapter, a line-spring model for a transversally isotropic generalized plane strain plate is developed and applied to the analysis of a reinforced crack under extensional loads. The generalized plane strain plate model of Mindlin and Kane, as refined by Kotousov and Wang, is applied to the analysis of a through crack in plates of arbitrary thickness and the governing equations are developed into a hyper-singular line-spring model by the application of Fourier transforms. This line-spring model is first used to develop standard linear-elastic fracture mechanics geometry correction factors to account for the effects of changes in the transverse modulus, Poisson's ratio, and plate thickness on the stress intensity and crack opening displacement. Next, the line-spring model is used to calculate the reinforcing effect of springs bridging the crack faces. In accordance with the Rose model for the analysis of reinforced cracks, the stress intensity and crack opening displacement are shown to become independent of crack length for long cracks, and an interpolation for the stress intensity and crack opening displacement is developed which employs the geometry correction factors developed in the first part of the chapter. This technique allows the inclusion of plate thickness effects in the fracture and fatigue analysis of reinforced cracks.

Reinforced cracks occur in a wide range of engineered structures. Examples in the aerospace field include cracking of filamentary composite structures, repair of damaged aluminum panels by the application of adhesively bonded composite repairs, and cracking in hybrid materials such as ARALL or GLARE. Crack-bridging is also a common occurrence in other fields. Examples include failure of natural fibrous materials such as wood and engineered wood laminates or bonded composite repair of concrete structures. Crack bridging analysis and line-spring models are also used to evaluate the stress intensity in part-through cracks and in the assessment of crack-tip plasticity. Past efforts to develop line-spring models have employed plane stress or plane strain plate

---

* A version of this chapter has been submitted for publication. R.J. Clark, D.P. Romilly, "Extension of generalized plane strain plates with reinforced cracks", Engineering Fracture Mechanics.

models, in which either the transverse stress or the transverse strain are assumed to vanish. This requires the analyst to assume that the plate is in one of these two limiting states, a problem which is particularly significant during the analysis of a crack bridged by springs, as the portion of the load carried by the reinforcing springs is determined by the ratio of the stiffness of the plate compared to the stiffness of the springs. A plane stress plate has a larger displacement and hence the springs will carry a larger portion of the stresses than in a plane strain plate. In reality, the plate exists in a state between the limiting cases of plane stress and plane strain. To obtain an accurate assessment of the fatigue and fracture resistance of a reinforced plate, this thickness effect must be included in the analysis.

In this chapter, the governing equations for a transversally isotropic generalized plane strain plate are presented and are developed into a line-spring model. The line-spring model is then used to develop linear-elastic fracture mechanics geometry correction factors to account for plate thickness effects and to determine the stress intensity and crack opening displacement for a reinforced crack. These results are used to extend the very successful Rose model for the extension of reinforced cracks to include plate-thickness effects. The result is a relatively simple set of closed-form equations that can be used to assess the fracture and fatigue performance of reinforced structures and materials without requiring the analyst to make assumptions regarding the transverse stresses in the cracked plate.

3.2 The generalized plane strain plate

Kane and Mindlin [1] introduced the generalized plane strain plate model for the analysis of extensional vibrations of plates, where plane stress and plane strain models respectively under and over predict the natural frequencies observed in experimental studies. More recently, Kotousov and Wang [2] have reformulated the model, decoupling the governing partial differential equations and developing fundamental solutions for in-plane loading, greatly simplifying its use. They also developed closed-form solutions for circular holes, approximate solutions for notches with circular tips, and a dislocation-based solution for a through-crack [3]. Generalised plane strain is one example out of the many approximate plate theories that exist in the engineering literature. Plate models are usually based on the selection of functions to represent the through-thickness variation of either stresses or strains. If the chosen functions are sufficiently general, the exact solution may result, but this is only practical for the simplest problems. Accordingly, the selection of a plate theory entails the selection of an appropriate form for the transverse strains or stresses. As an example, the plane stress model assumes vanishing through-thickness stresses and provides the exact result only for the simple case of a plate acting under a uniform or linearly varying stress field. Within the generalized plane strain plate

theory, it is assumed that the transverse strain is constant through the thickness of the plate, and the effects of transverse stresses and strains may be explicitly included in the analysis.

The development of the differential equation governing the displacement field for a generalized plane strain plate, as per Kotousov and Wang [2], is brief and is provided here to introduce the symbols and concepts used in subsequent sections. For a plate of thickness 2h, the displacement field in the plate may be approximated as follows.

$$u_x = u_x(x,y), \qquad u_y = u_y(x,y), \qquad u_z = \frac{z}{h} w(x,y) \tag{1}$$

This displacement field is illustrated in Figure 3-1, along with a depiction of typical stress distributions through the thickness of the plate.

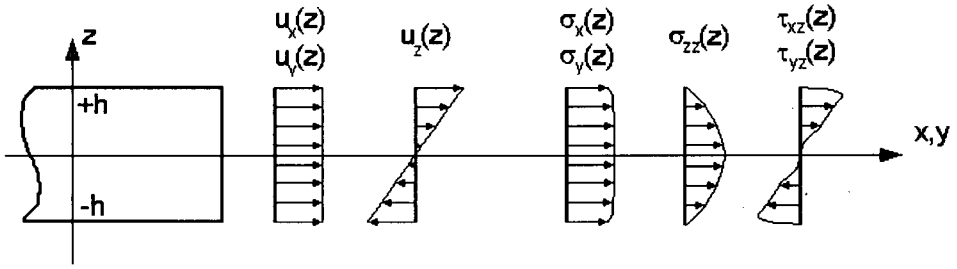

Figure 3-1: Distribution of plate displacements and stresses

In displacement-based plate theories, the stresses are expressed in terms of stress resultants or line-forces in the plate. These are obtained by integration through the thickness of the plate.

$$N_{xx} = \int_{-h}^{h} \sigma_{xx} dz, \qquad N_{yy} = \int_{-h}^{h} \sigma_{yy} dz, \qquad N_{xy} = \int_{-h}^{h} \tau_{xy} dz \tag{2}$$

The transverse normal and shear stresses may also be expressed as stress resultants. The transverse shear stress resultants are defined as the first moments of the shear stresses taken about the plate centre line, and represent a 'pinching' force. Curvatures in the in-plane stress fields lead to transverse shear stresses and the accompanying normal stresses.

$$N_{zz} = \int_{-h}^{h} \sigma_{zz} dz, \qquad R_x = \int_{-h}^{h} \tau_{xz} z dz, \qquad R_y = \int_{-h}^{h} \tau_{yz} z dz \tag{3}$$

Observing that the plate surfaces are stress free, the equilibrium equations may also be expressed in terms of stress resultants by integration through the thickness.

$$N_{xx,x} + N_{xy,y} = 0, \qquad N_{yy,y} + N_{xy,x} = 0, \qquad R_{x,x} + R_{y,y} = N_{zz} \tag{4}$$

The assumed displacement field satisfies all but one of the compatibility equations.

$$\varepsilon_{xx,yy} + \varepsilon_{yy,xx} = \gamma_{xy,xy} \tag{5}$$

The constitutive equations may also be expressed in terms of the stress resultants. For a transversally isotropic material $E_x = E_y = E$ and $\nu_x = \nu_y = \nu$, and the normal strains may be expressed as follows:

$$\varepsilon_{xx} = \frac{1}{2h}\left(\frac{N_{xx}}{E} - \nu\frac{N_{yy}}{E} - \nu_z\frac{N_{zz}}{E_z}\right) \tag{6a}$$

$$\varepsilon_{yy} = \frac{1}{2h}\left(\frac{N_{yy}}{E} - \nu\frac{N_{xx}}{E} - \nu_z\frac{N_{zz}}{E_z}\right) \tag{6b}$$

$$w = h\varepsilon_{zz} = \frac{1}{2E_z}\left(N_{zz} - \nu_z N_{xx} - \nu_z N_{yy}\right) \tag{6c}$$

The shear constitutive equations may be expressed as follows.

$$\varepsilon_{xy} = \frac{N_{xy}}{2hG}, \qquad w_{,x} = \frac{3}{2h^2}\frac{R_x}{G_z}, \qquad w_{,y} = \frac{3}{2h^2}\frac{R_y}{G_z} \tag{7}$$

The equilibrium equations in the plane of the plate have the same form as for plane stress and plane strain, and one may use an Airy stress function, ϕ, to satisfy equilibrium.

$$\phi_{,yy} = N_{xx}, \quad \phi_{,xx} = N_{yy}, \quad \phi_{,xy} = -N_{xy} \tag{8}$$

Using the average extensional stress in the plate, $2N = N_{xx} + N_{yy} = \nabla^2\phi$, the constitutive law for transverse strain (6c) yields an expression for pressurization of the plate.

$$N_{zz} = 2\nu_z N + 2E_z w \tag{9}$$

This result combined with equilibrium in the transverse direction (4) and the constitutive laws for transverse shear (7) lead to the following relationship between w and N.

$$\nabla^2 w - \frac{3}{h^2}\frac{E_z}{G_z}w = \frac{3}{h^2}\frac{\nu_z}{G_z}N \tag{10}$$

Defining $\eta = \nu_z\sqrt{E/E_z}$, a second condition for w and N arises from compatibility (5).

$$\nabla^2 N = \frac{\nu_z E}{1-\eta^2}\nabla^2 w \tag{11}$$

The governing differential equation arises by de-coupling equations (10) and (11).

$$\nabla^6\phi - k^2\nabla^4\phi = 0 \tag{12}$$

Here, k is a parameter characterizing the thickness and properties of the plate.

$$k^2 = \frac{3}{h^2}\frac{E_z}{G_z(1-\eta^2)} \tag{13}$$

The generalized plane strain plate requires three boundary conditions. These are the in-plane normal and shear stresses of the classical plane stress and plane strain plate models, and the transverse shear 'pinching' stress resultant. In the next section this work will be expanded and the problem of a crack in a plate will be solved using a Fourier integral transform, thus allowing the development of a line-spring model for a cracked plate.

3.2.1 A cracked plate

Given the governing differential equation, it is possible to develop a solution to the problem of a cracked plate. To achieve this, the authors use an integral transform technique in the manner of Erdogan and Joseph [4,5] in the development of a line-spring model for a Reissner plate [6]. The Fourier transform of a function and the inverse transform may be defined as follows.

$$\overline{f} = \overline{f}(x,\alpha) = \int_{-\infty}^{\infty} f(x,y)e^{i\alpha y}dy\,, \qquad f = f(x,y) = \frac{1}{2\pi}\int_{-\infty}^{\infty}\overline{f}(x,\alpha)e^{-i\alpha y}d\alpha \tag{14}$$

Applying this transform to the governing equation, it can be expressed as an ordinary differential equation.

$$\left(\overline{\phi}_{,xxxxxx} - 3\alpha^2\overline{\phi}_{,xxxx} + 3\alpha^4\overline{\phi}_{,xx} - \alpha^6\overline{\phi}\right) - k\left(\overline{\phi}_{,xxxx} - 2\alpha^2\overline{\phi}_{,xx} + \alpha^4\overline{\phi}\right) = 0 \tag{15}$$

Keeping only roots that vanish for $x \to \infty$, the solution is

$$\phi = \frac{1}{2\pi}\int_{-\infty}^{\infty}\left(A_1(\alpha)e^{-|\alpha|x} + A_2(\alpha)xe^{-|\alpha|x} + A_3(\alpha)e^{-Rx}\right)e^{-i\alpha y}d\alpha\,, \quad R^2 = \alpha^2 + k^2 \tag{16}$$

To simplify the notation α is assumed to be positive in the remainder of the development. To satisfy symmetry about the crack plane, the shear and pinching stress resultants must vanish.

$$N_{xy}(0,y) = -\phi_{,xy}(0,y) = 0 \tag{17}$$

$$R_x(0,y) = 0 \tag{18}$$

From (7), the pinching shear condition requires $w_{,x}(0,y)=0$. Using equations (10) and (11), w may be expressed in terms of the average in-plane stress.

$$w=\frac{\nu_z}{E_z}\left[\frac{1}{\eta^2 k^2}\nabla^2 N-N\right] \tag{19}$$

This leads to an additional symmetry condition.

$$\nabla^4\phi_{,x}(0,y)-\eta^2k^2\nabla^2\phi_{,x}(0,y)=0 \tag{20}$$

Using the two symmetry conditions (17, 20), two constants may be eliminated from (16), and the stress function takes the following form.

$$\bar{\phi}=\left[\left(\frac{1}{\alpha}-\frac{2\alpha}{\beta^2}+x\right)e^{-\alpha x}+\frac{2\alpha^2}{R\beta^2}e^{-Rx}\right]A_2(\alpha),\quad \beta^2=k^2\frac{\eta^2-1}{\eta^2} \tag{21}$$

To form the line-spring model, the remaining constant must be expressed in terms of the displacement of the crack faces. From compatibility (5) and the constitutive equations (6a,b,d).

$$\varepsilon_{xx,yy}=\frac{1}{2h}\left[\frac{N_{xy,xy}}{G}-\frac{N_{yy,xx}}{E}+\nu\frac{N_{xx,xx}}{E}+\nu_z\frac{N_{zz,xx}}{E_z}\right] \tag{22}$$

An expression for N_{zz} may be found from equations (9) and (19). This relationship shows that the pressurization of the plate arises due to curvatures in the in-plane stress field.

$$N_{zz}=2\frac{\nu_z}{\eta^2k^2}\nabla^2 N \tag{23}$$

Equation (22) may now be expressed as follows.

$$2hE\varepsilon_{xx,yy}=2(1+\nu)N_{xy,xy}-N_{yy,xx}+\nu N_{xx,xx}+\frac{2}{k^2}\nabla^2 N_{,xx} \tag{24}$$

Next we express the in-plane stresses in terms of ϕ, and integrate to find the displacement. As the displacement must vanish as $[x,y]\to\infty$, the integration constant must also vanish.

$$2hEu_{x,yy}=-2(1+\nu)\phi_{,xyy}-\phi_{,xxx}+\nu\phi_{,xyy}+\frac{1}{k^2}\nabla^4\phi_{,x} \tag{25}$$

Symmetry requires $\phi_{,xy}(0,y)=0$, and the first and third terms must vanish. Substituting for ϕ, the crack face displacement may be expressed as follows.

$$hEu_{x,yy}(0,y) = \frac{-1}{2\pi}\int_{-\infty}^{\infty}\alpha^2 A_2(\alpha)e^{-i\alpha y}d\alpha \tag{26}$$

Inverting the Fourier transform.

$$\frac{-\alpha^2}{hE}A_2(\alpha) = \int_{-\infty}^{\infty}u_{x,tt}(t)\ e^{i\alpha t}d\alpha \tag{27}$$

Integrating by parts twice, noting that again displacements must vanish as $[x,y]\to\infty$, and that the crack opening displacement exists only over the interval of the crack, L.

$$A_2(\alpha) = hE\int_L u_x(t)e^{i\alpha t}dt \tag{28}$$

An integral relating the crack opening displacement to N_{xx} may now be formed.

$$N_{xx}(0,y) = \frac{-hE}{2\pi}\int_L u_x(t)\int_{-\infty}^{\infty}\left[|\alpha| - 2\frac{|\alpha|\alpha^2}{\beta^2} + \frac{2\alpha^4}{\beta^2 R}\right]e^{i\alpha(t-y)}d\alpha dt \tag{29}$$

Note the following integral identities, where K_2 is the modified Bessel function of the second kind.

$$\int_0^{\infty}\alpha e^{i\alpha(t-y)}d\alpha = \frac{-1}{(t-y)^2} \tag{30a}$$

$$\int_0^{\infty}\alpha^3 e^{i\alpha(t-y)}d\alpha = \frac{6}{(t-y)^4} \tag{30b}$$

$$\int_0^{\infty}\frac{\alpha^4}{R}e^{i\alpha(t-y)}d\alpha = k^4\left[1+\frac{3}{k^2(t-y)^2}\right]K_2(k|t-y|) \tag{30c}$$

Defining a stress boundary condition $\bar{\sigma}(y) = -N_{xx}/2h$, equation (29) may be written as follows.

$$\bar{\sigma}(y) = \frac{E}{2\pi}\int_L u_x(t)\left\{\frac{-1}{(t-y)^2} - \frac{12}{\beta^2(t-y)^4} + \frac{2k^4}{\beta^2}\left[1+\frac{3}{k^2(t-y)^2}\right]K_2(k|t-y|)\right\}dt \tag{31}$$

Separating equation (31) into singular and regular parts in order to perform numerical integration, one finds the final form of the hyper-singular integral equation.

$$\bar{\sigma}(y) = \frac{-1}{2\pi}\frac{E}{1-\eta^2}\int_L u_x(t)\left\{\frac{1}{(t-y)^2} + \eta^2 k^2 L(k|t-y|)\right\}dt \tag{32}$$

Here, $L(z)$ includes the regular part of the integrand and a weak logarithmic singularity. The logarithmic singularity is embedded in the Bessel function.

$$L(z)=2\left[1+\frac{3}{z^2}\right]K_2(z)-\frac{12}{z^4}-\frac{1}{z^2} \tag{33}$$

Equation (32) may be compared to equations (34) and (35) for plane stress and plane strain respectively provided below.

$$\bar{\sigma}(y)=\frac{-E}{2\pi}\int_L\frac{u(t)}{(t-y)^2}dt \tag{34}$$

$$\bar{\sigma}(y)=\frac{-1}{2\pi}\left(\frac{E}{1-\eta^2}\right)\int_L\frac{u(t)}{(t-y)^2}dt \tag{35}$$

Note that the first term of the generalized plane strain solution given by equation (32) matches the plane strain solution given by equation (35). As the contribution of $L(z)$ vanishes (i.e. the crack interval reduces as in the case of a short crack), the plane strain solution is seen to dominate. The thickness effects causing deviations from the plane strain solution evolve from the contributions of $L(z)$. Failure to account for these effects can lead to inaccuracies in the cracked plate analysis.

3.2.2 Numerical solution

In this section, a collocation method and Chebyshev polynomial expansion are used to develop a line-spring model that will be used to generate geometry correction factors and a crack-bridging model for a reinforced cracked plate. While applied to a new application, this is similar to the technique used by Erdogan and Joseph to solve the Reissner plate bending problem [4,5], and proceeds as follows. By expressing the crack opening displacement as a series of Chebyshev polynomials of the second kind, equation (32) may be decomposed into a linear system, solvable for the displacements, and hence the stresses in the plane of the crack. The first step is to normalise the bounds and parameters in the integral equation. Normalising all dimensions with respect to the half-crack length, a, we define the following parameters.

$$u(r)=u_x(t)/a,\quad r=t/a,\quad s=y/a,\quad \kappa=ka \tag{36}$$

The hyper-singular integral equation then simplifies.

$$\bar{\sigma}(s)=\frac{-1}{2\pi}\frac{E}{1-\eta^2}\int_{-1}^{1}u(r)\left\{\frac{1}{(r-s)^2}+\eta^2\kappa^2L(\kappa|r-s|)\right\}dr \tag{37}$$

The crack face deflection may be expanded using Chebyshev polynomials of the second kind.

$$u(r) = W(r)\sum_{i=0}^{N} f_i U_i(r) \tag{38}$$

Here, $W(r) = \sqrt{1-r^2}$ is the weighting function, $U_i(r) = \sin((i+1)\cos^{-1}(r))/\sqrt{1-r^2}$, and the solution will be expressed in terms of the displacement coefficients, f_i. The hyper-singular part of the integral may now be evaluated analytically.

$$\frac{1}{\pi}\int_{-1}^{1}\frac{\sqrt{1-r^2}U_n(r)}{(s-r)^2}dt = \begin{cases} -(n+1)U_n(s) & |s|<1 \\ (n+1)\dfrac{\left(s-\sqrt{s^2-1}\right)^{n+1}}{\sqrt{s^2-1}} & |s|>1 \end{cases} \tag{39}$$

The integral equation may now be written in terms of the Chebyshev polynomials. The logarithmic term in $L(z)$ may be calculated analytically, but the regular part requires numerical integration.

$$\overline{\sigma}(s) = \frac{E}{1-\eta^2}\sum_{i=0}^{N} f_i\left(\frac{i+1}{2}U_i(s) - \frac{\eta^2\kappa^2}{2\pi}\int_{-1}^{1}L(\kappa|r-s|)W(r)U_i(r)dr\right) \tag{40}$$

By selecting a set of collocation points, s_i, a linear system of equations results, solvable for the coefficients, f_j. The linear system may be expressed in the following form.

$$\overline{\sigma} = A\overline{f}, \qquad A_{i,j} = \frac{E}{1-\eta^2}\left(\frac{i+1}{2}U_j(s_i) - \frac{\eta^2\kappa^2}{2\pi}L_{i,j}\right) \tag{41}$$

Here, $L_{i,j}$ has the following definition, where $V_{i,j}$ includes the logarithmic singularity, and may be solved analytically, as demonstrated by Erdogan and Joseph [4,5] and by Wang and Rose [7].

$$L_{i,j} = \int_{-1}^{1}\left[L(\kappa|r_i-s|) + \frac{3}{4}\ln(|r_i-s|)\right]W(s)U_j(s)ds - \frac{3}{4}V_{i,j} \tag{42}$$

$$V_{i,j} = \int_{-1}^{1}\ln|r_i-s|W(s)U_j(s)ds = \begin{cases} -\dfrac{\pi}{2}\left[-r_i^2 + \dfrac{1}{2} + \ln 2\right] & j=0 \\ -\dfrac{\pi}{2}\left[\dfrac{T_j(r_i)}{j} - \dfrac{T_{j+2}(r_i)}{j+2}\right] & j>0 \end{cases} \tag{43}$$

The regular part requires numerical integration. Any method is applicable, but for this problem, the authors chose to apply Gauss-Chebychev quadrature, as suggested by

Joseph and Erdogan. This method concentrates the integration points in the region of the crack tip, where the crack opening displacement has the greatest variability.

Equation (37) is valid anywhere along the line $x=0$, and hence may be used to examine the stresses near the crack tip and calculate the stress intensity. The only terms that contain a $\sqrt{r}$ singularity arise from the hyper-singular part of the equation. These terms may be found by examining equation (39) for the region outside of the domain of the crack. The result follows from the conventional definition of the stress intensity.

$$K = \lim_{r\to 1+} \sqrt{2\pi a(r-1)}\sigma_{xx}(0,r) = \frac{E\sqrt{\pi a}}{2(\eta^2-1)} \sum_{i=0}^{N} f_i U_i(1) = \frac{E\sqrt{\pi a}}{2(\eta^2-1)} \sum_{i=0}^{N} (i+1) f_i \qquad (44)$$

It is now possible to calculate the crack face deflection and the stress intensity for a crack in a generalised plane strain plate using a displacement-based solution.

3.2.3 Geometry correction factors for a cracked plate

The displacement-based solution of the cracked plate problem generated above is now available to calculate the stress intensity factor and crack face displacement for a transversally isotropic plate, such that the effects of plate thickness and the material properties through the thickness may be calculated. Table 3-1 shows the properties for some selected transversely isotropic materials that will be used to test the model and develop a set of geometry correction factors.

Material	E (GPa)	ν	E_z (GPa)	ν_z
(1) Isotropic	71.0	0.5	-	0.5
(2) Isotropic	71.0	0.33	-	0.33
(3) Isotropic	71.0	0.1	-	0.1
(4) Quasi-isotropic boron/epoxy	106	0.12	25	0.028
(5) Transversely loaded unidirectional boron/epoxy	25	0.019	210	0.21

Table 3-1: Material properties used to test the GPS model

Figure 3-2 shows the generalized plane strain stress intensity results normalized to the classical result, $K_0 = \sigma\sqrt{\pi a}$, and plotted against the crack length. The results match those found by Kotousov and Wang [3], who used a dislocation density method. In the limit, as the crack length increases, all of the materials obey the limit $K/K_0 = 1/\sqrt{1-\eta^2}$.

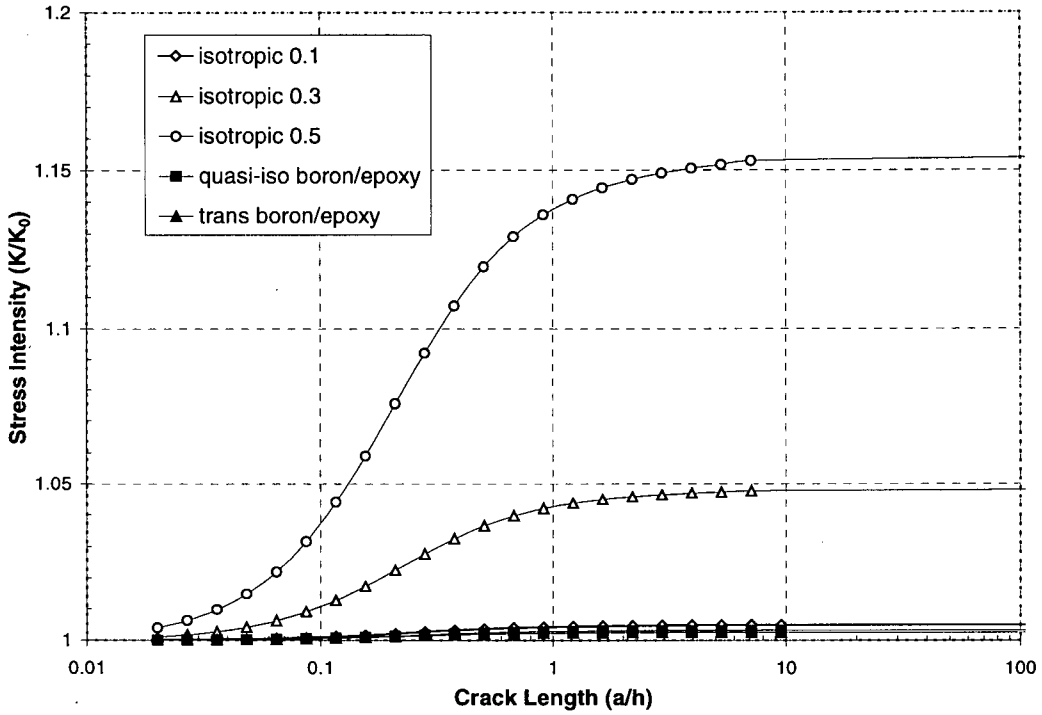

Figure 3-2: Stress intensity for a through crack

The stress intensity may also be plotted against a normalised crack-length, $c = \kappa\sqrt{1-\eta^2}$ as shown in Figure 3-3.

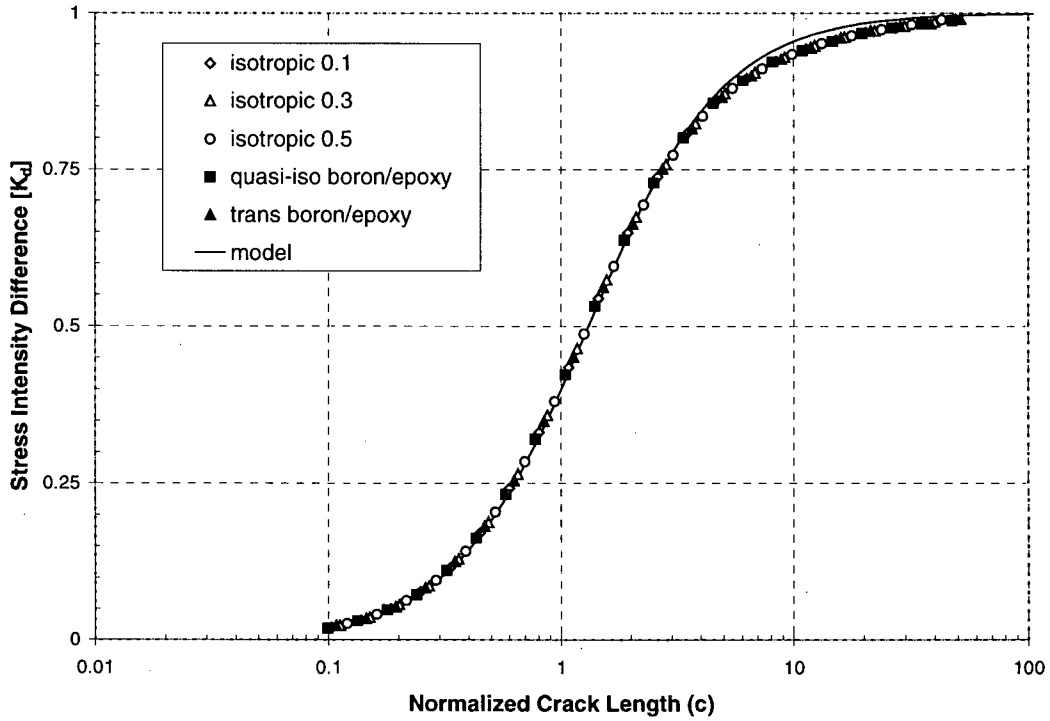

Figure 3-3: Stress intensity difference plotted against normalized crack length

Here, $c = 1$ corresponds to a crack length of approximately one-third of the thickness of the plate. It may be observed that with this normalization, and by taking into account the asymptotic behaviour for long cracks, the difference in stress intensity between the classical solution, K_0, and generalized plane strain plate, K_d, collapses onto one curve for all of the tested materials.

$$K_d = \frac{(K/K_0)-1}{\left(1/\sqrt{1-\eta^2}\right)-1} \tag{45}$$

This curve is well approximated by the simple interpolation of equation (46). As shown in Figure 3-3, this approximate model fits the data very well.

$$K_d = \frac{c^{1.5}}{c^{1.5}+1.5} \tag{46}$$

This relationship can be developed into an expression for a geometry correction factor.

$$Y_k = \frac{K}{K_0} = 1 + \left(\frac{c^{1.5}}{c^{1.5}+1.5}\right)\left(\frac{1}{\sqrt{1-\eta^2}}-1\right) \tag{47}$$

It is also useful to examine the variation in strain energy release rates. Within the classical plate theories, the strain energy release rate may be expressed in terms of the stress intensity.

$$G = \begin{cases} \dfrac{K^2}{E} & \text{plane stress} \\ (1-\eta^2)\dfrac{K^2}{E} & \text{plane strain} \end{cases} \tag{48}$$

Kotousov and Wang [2] have made the observation that all cracks are in a state of plane strain near the crack tip. This occurs because the large stress gradients near the tip of the crack will always pressurize the plate, regardless of the plate thickness. Thus, the plane stress assumption is not valid and only the plane strain relationship is required. As the crack length becomes very large, $Y_k \to 1/\sqrt{1-\eta^2}$, and the strain energy release rate may be expressed in terms of the nominal stress intensity as $G = K_0^2 / E$. Similar results may be developed for the crack face deflection. Figure 3-4 shows the deflection at the centre of the crack normalized to the plane strain result, $u_0 = 2a(1-\eta^2)\sigma_0 / E$.

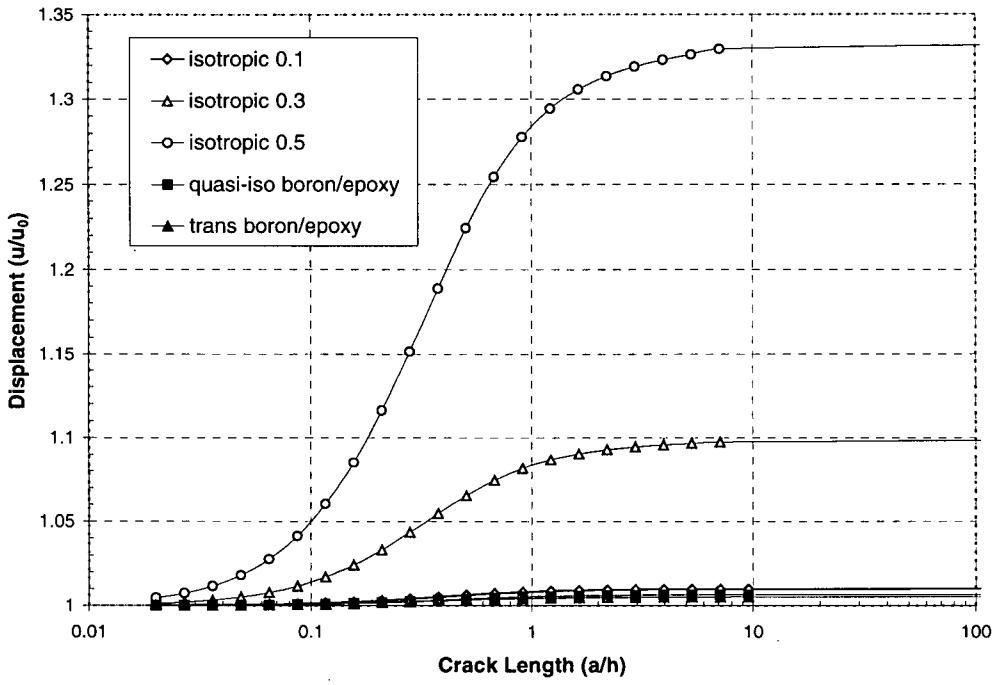

Figure 3-4: Crack face displacement plotted against crack length.

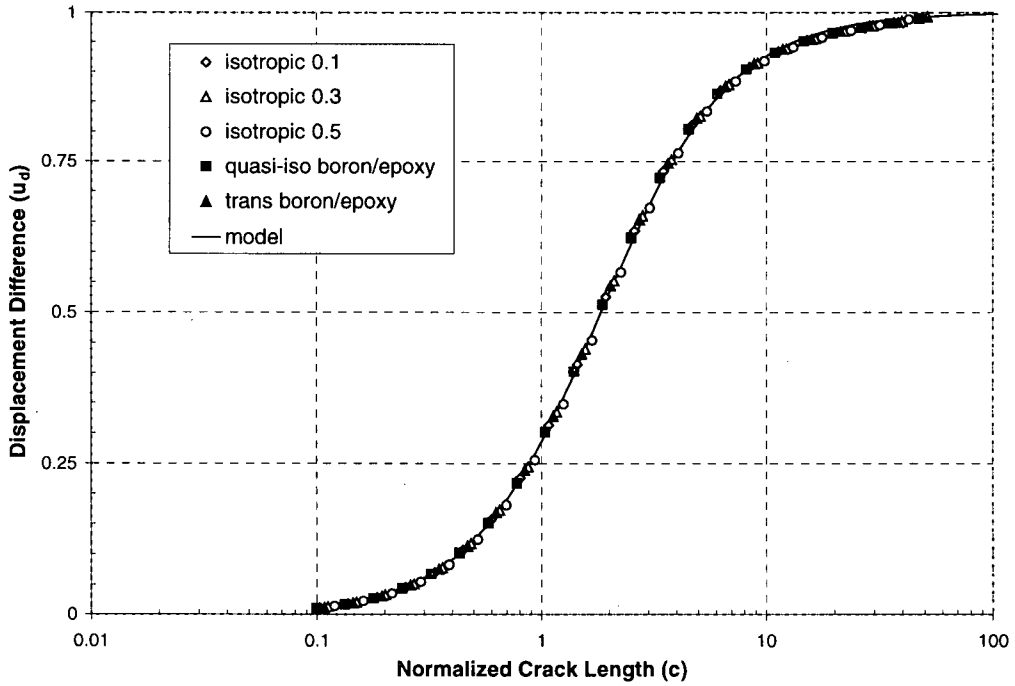

Figure 3-5: Difference in crack face displacement plotted against crack length.

In the long-crack limit, $u/u_0 = 1/(1-\eta^2)$, and the following normalization collapses the results for all of the materials onto one curve, as shown in Figure 3-5.

$$u_d = \frac{(u/u_0)-1}{(1/(1-\eta^2))-1} \tag{49}$$

Once again, it is possible to develop a simple model that fits the data remarkably well.

$$u_d = \frac{c^{1.5}}{c^{1.5}+2.5} \tag{50}$$

This relationship can be developed into a geometry correction factor, Y_d.

$$Y_d = \frac{u}{u_0} = 1+\left(\frac{c^{1.5}}{c^{1.5}+2.5}\right)\left(\frac{1}{1-\eta^2}-1\right) \tag{51}$$

The geometry correction factors derived in equations (47) and (51) provide a significant step forward towards the accurate closed-form engineering analysis of cracks in finite thickness plates.

3.3 Crack bridging: a line-spring model

This section describes the development of a numerical line-spring model, which is used to test closed-form design equations that utilize the new correction factors for stress intensity, strain energy release rate, and crack face displacement. For a reinforced crack, the springs bridging the crack faces will develop a force countering the applied stresses, acting to partially close the crack faces, as shown in Figure 3-6.

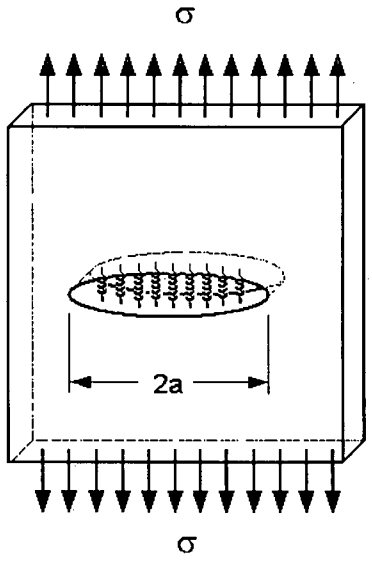

Figure 3-6: A reinforced crack in a plate.

Erdogan and Joseph [4,5] and Wang and Rose [7] have used the same technique to examine this phenomenon for the plane stress case. Including the effect of the springs,

equation (37) may be rewritten as follows, where k_s is the line-spring stiffness, or the stress generated by the springs per unit deflection of a crack face.

$$\overline{\sigma}(s) - ak_s u(s) = \frac{-1}{2\pi}\frac{E}{1-\eta^2}\int_{-1}^{1} u(r)\left\{\frac{1}{(r-s)^2} + \eta^2\kappa^2 L(\kappa|r-s|)\right\}dr \qquad (52)$$

By expanding $u(r)$ and choosing a set of collocation points, one may develop a linear system of equations, solvable for the crack face displacement.

$$\overline{\sigma} = A\overline{f}, \qquad A_{i,j} = \frac{E}{1-\eta^2}\left(\frac{i+1}{2}U_j(r_i) - \frac{\eta^2\kappa^2}{2\pi}L_{i,j}\right) + ak_s W(r_i)U_j(r_i) \qquad (53)$$

The stress intensity may be calculated using equation (44). Figure 3-7 shows the results for an isotropic plate with $\overline{\sigma} = 10\,MPa$, $\upsilon = 0.5$ and $E = 71.0\ GPa$. The results are shown for a wide range of spring stiffnesses, which are reported in the legend.

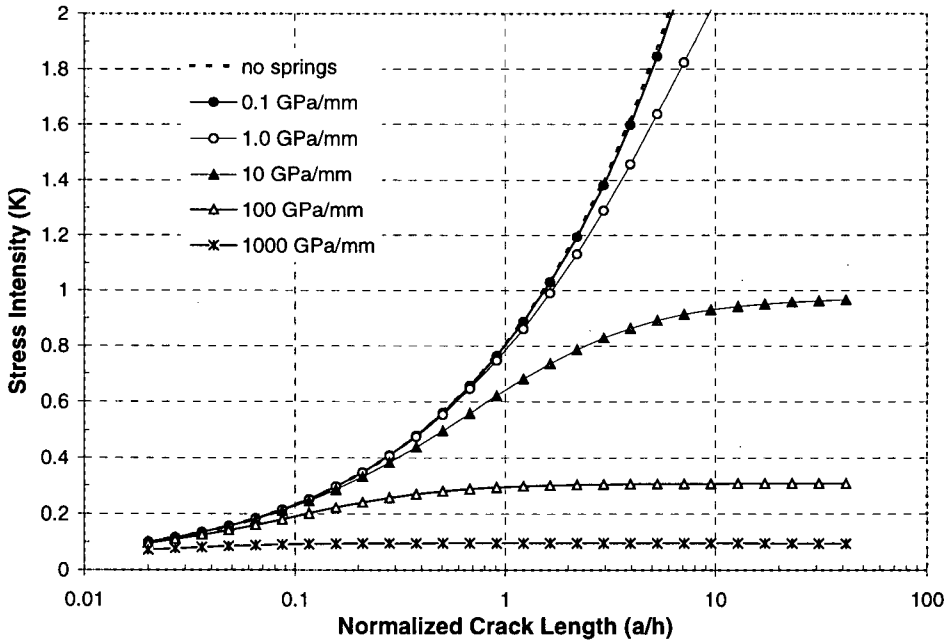

Figure 3-7: Stress intensity results from the line-spring model

It is apparent that stiffer springs lead to lower stress intensities, reaching a limit for long cracks. Applying the method of Rose [8,9], one may analytically determine the limit strain energy release rate for a very long crack. Rose observed that stresses near the crack tip become independent of crack length. Hence, for linear problems, the strain energy released with an increment of crack growth can be found from the difference in stored elastic energy between two strips of material far removed from the crack tip. One strip is located well away from the crack, is undisturbed by the singular stress field near the

crack, and has no stored strain energy. The other is over the middle of the long crack, has energy stored in the springs bridging the crack. The difference in stored energy is given solely by the energy stored in the springs bridging the crack, and the strain energy release rate may be expressed as follows:

$$G_\infty = 2\int_0^u \sigma \, dx = 2\int_0^u k_s x \, dx = k_s u^2 = \frac{\sigma_0^2}{k_s} \tag{54}$$

As the crack tip is in a plane strain state, the limit stress intensity (K_∞) and an effective crack length a_{eff} (for a correction factor of Y_k) for a long crack may now be defined.

$$K_\infty = \sqrt{\frac{G_\infty E}{1-\eta^2}} = \sigma_0 \sqrt{\frac{E}{k_s(1-\eta^2)}} \tag{55}$$

$$a_{eff} = \frac{E}{Y_k^2 \pi \, k_s (1-\eta^2)} \tag{56}$$

Figure 3-8 shows the generalized plane strain results normalized with respect to this limit stress intensity and effective crack length. As crack length increases, the theoretical limit is observed. Unfortunately, the polynomial expansion used in this study is limited in its ability to resolve this limit state in the case of a very long crack with very compliant springs. In this study, the authors used the first 128 even Chebyshev polynomials.

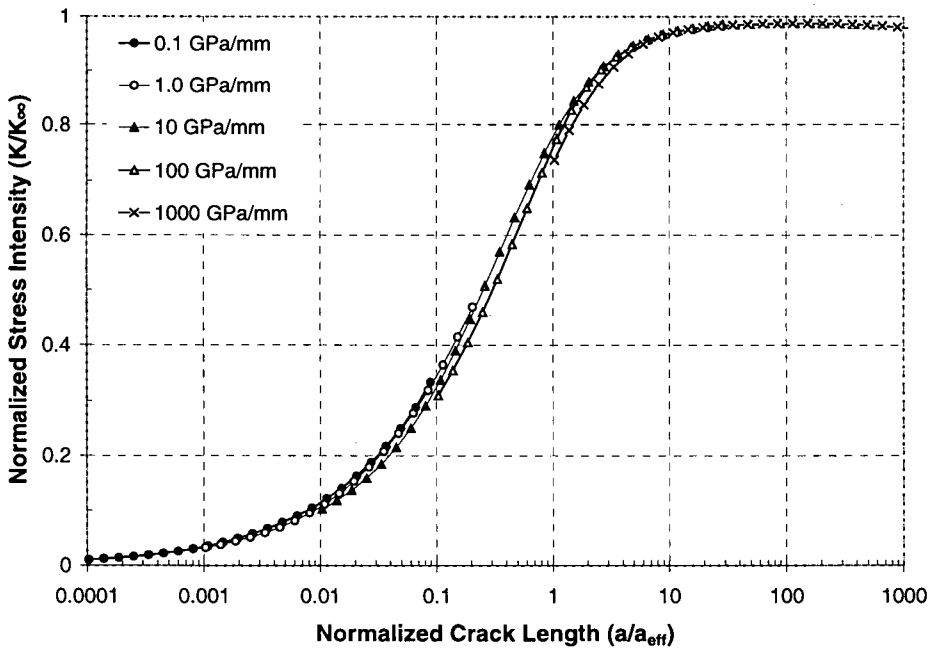

Figure 3-8: Normalized stress intensity plotted against crack length.

In addition to an expression for the limit stress intensity, Rose developed an interpolation for the stress intensity for an arbitrary length of crack. For the limiting state of a very short crack, the crack opening displacement is small, and the springs bridging the crack cannot develop a large stress to resist the applied load. The stress intensity will be that calculated by considering an un-reinforced crack, given by equation (45). In the long crack limit, the stress intensity will approach the limit given by equation (55). The stress intensity for an arbitrary crack length may then be approximated by a simple interpolation between these limiting states, expressed as follows.

$$K_r = Y_k \sigma_0 \sqrt{\frac{\pi \ aa_{eff}}{a + a_{eff}}} \tag{57}$$

Figure 3-9 shows the stress intensity values predicted by the interpolation model normalized to values obtained by numerical analysis. Equation (57) provides results that are low by up to 4%, an error that has also been observed when it is applied to plane stress or plane strain plates.

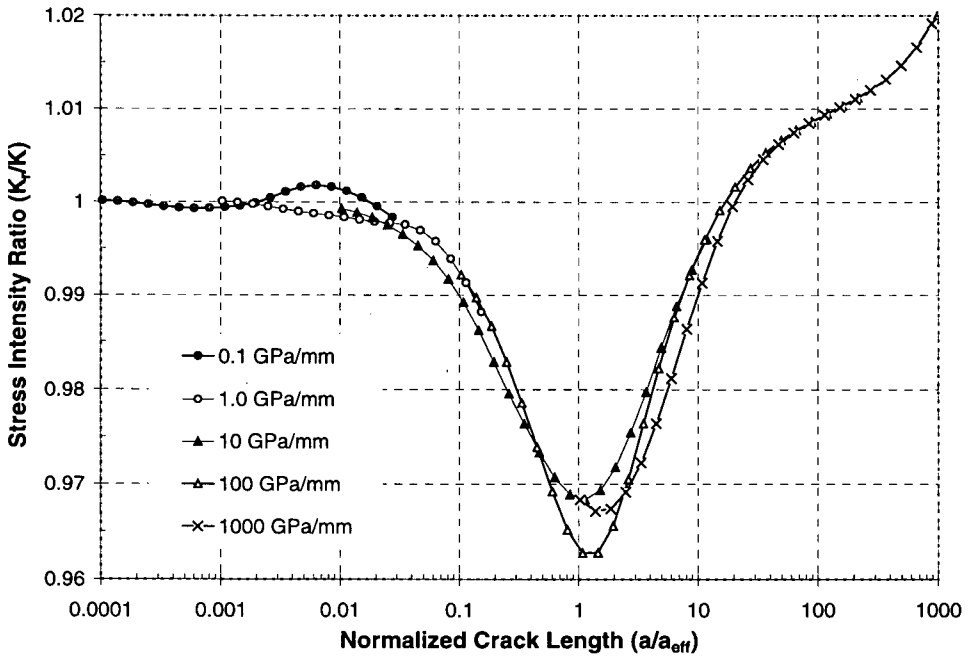

Figure 3-9: Comparison of stress intensity predictions.

The concepts used to develop expressions for the stress intensity may also be used to estimate the crack face displacements [10]. As the crack face displacement is proportional to the stretch and hence the maximum stress in the springs, the maximum crack face displacement is a valuable parameter for estimating the strength of the structure and its resilience to fatigue loading, where performance of the springs may degrade over time. Figure 3-10 shows the crack-face displacement results from the line-

spring model. Once again, for very weak springs, the results approach the nominal solution for an un-reinforced crack. The limiting behaviour for long cracks is evident in the results for cracks bridged by stiff springs.

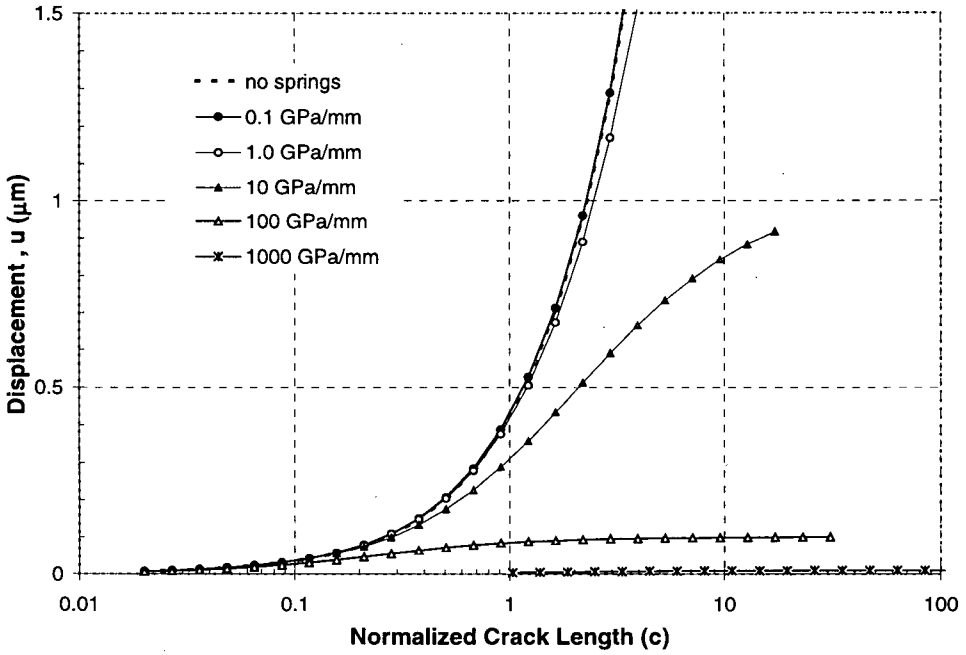

Figure 3-10: Crack face displacement for various spring stiffnesses.

The long-crack limit crack face displacement is given by $u_\infty = \sigma_0 / k_s$, and the behaviour for a short crack may be determined from equation (51). One may then develop a simple interpolation between these two limit states:

$$u_r = \frac{u_\infty u_0}{u_0 + u_\infty} = \sigma_0 \frac{\left(2Y_d(1-\eta^2)a/E\right)\left(1/k_s\right)}{\left(2Y_d(1-\eta^2)a/E\right)+\left(1/k_s\right)} = \frac{\sigma_0}{k_s + E/\left(2Y_d(1-\eta^2)a\right)} \qquad (58)$$

Figure 3-11 shows the ratio of the interpolation and line-spring model results for crack displacement. Once again, the interpolation model results in a reasonable error, in this case not exceeding 6%. The line-force in the springs is given by $N_{xx} = 2hk_s u_r$ and may be used to predict potential rupture or fatigue degradation of the springs bridging the crack faces.

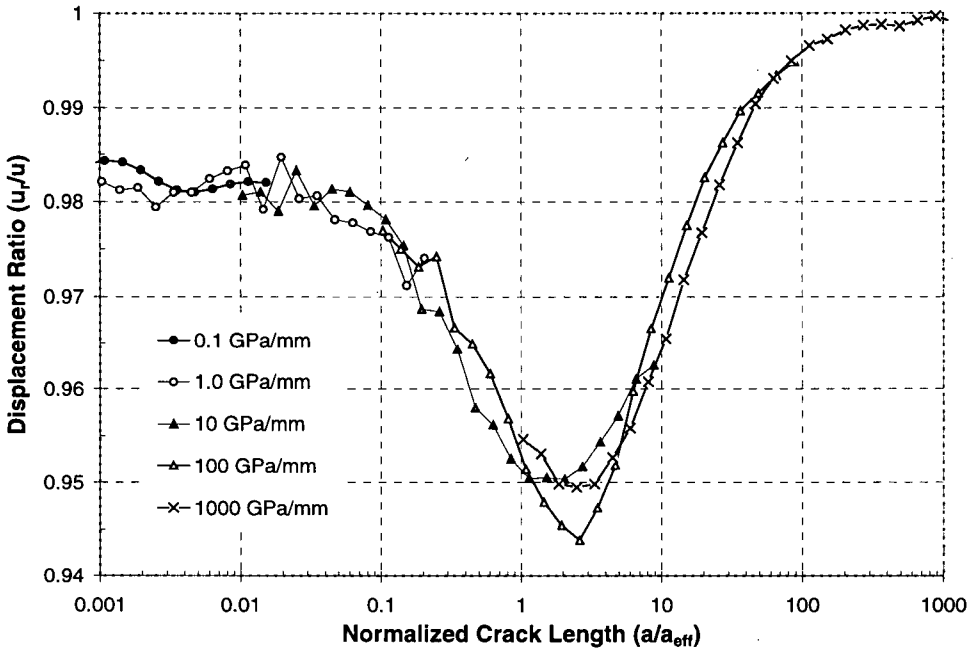

Figure 3-11: Comparison of crack face displacement predictions.

3.4 Discussion

The generalized plane strain plate model allows one to include the effects of finite plate thickness and transverse stresses caused by curvatures in the stress field in the plate. This is particularly important in the analysis of cracks, which arguably contain the largest stress gradients possible in a real structure. Accordingly, the first important result of the generalized plane strain model is that, at least in terms of the stress resultants, the base of a crack in a plate can always be assumed to be in a state of plane strain. This result is of particularly great importance for the analysis of bridged cracks, where strain energy release rate arguments are used to determine the stress intensity at the reinforced crack tip. This result is also consistent with the definition of the opening mode strain energy release rate as it is used in the analysis of cracks in three-dimensional bodies.

The asymptotic behaviour observed for un-reinforced long cracks can be explained as follows: away from the crack tip the stress gradients become small, and the plate is essentially in a state of plane stress. However, the crack tip is still in a state of plane strain, and the plate is effectively stiffened by the transverse pressures around the crack tip. For a long crack, subsequent increases in crack length lead to a dispersion of stresses that can be well-approximated by plane stress analysis, except in the region of the crack tip, where plane strain conditions exist and additional load transfer results due to the 'stiffened' region around the crack tip. The geometry correction factors developed in this paper are a simple extension of the geometry correction factors traditionally used in fracture mechanics, and are a very effective way to deal with this complication.

The long-crack limit stress intensity factor and the interpolation model developed by Rose offer a very effective method for the analysis of bridged cracks. The manner in which geometry correction factors are included in the model was first introduced by Rose [9]. This form of the interpolation model was shown to be accurate within 5%. This order of error is in line with what has been reported previously by the authors [10], and can be attributed to the approximate nature of the interpolation model, and not to the correction factors introduced in this paper. It is unfortunate that the Chebyshev expansion method is not more effective in dealing with weak springs or very long cracks. Most forms of expansion will result in the same difficulties, as the crack face displacement gradients will always be concentrated at the very tip of the crack under these conditions. This may be alleviated by considering the integral over an open domain (i.e. a semi-infinite crack) and using an appropriate orthogonal expansion, but as the existence of the long-crack limit is well accepted, there is little practical reason to expend effort in this direction.

3.5 Concluding remarks

The authors have developed the generalized plane strain plate model into a hyper-singular integral equation relating crack-face deflections to stresses along the plane of the crack. This numerical model has been solved using a collocation method, and the results have been used to develop simple and accurate geometry correction factors to account for the effects of plate thickness and Poisson's ratio on the fracture of through-cracked plates. These geometry correction factors were then used to improve the classical models for cracked plates reinforced by springs. The resulting closed-form equations were validated against the new line-spring model, and shown to be accurate to within 6%, an error which is mostly due to the approximate nature of the original interpolation model used for bridged cracks.

The generalized plane strain line-spring model is an improvement upon existing line-spring models, and may be used to refine the results for the calculation of stress intensity factors for surface cracks [e.g. 3,4], to include the effects of transverse stresses in Dugdale strip-yield models, and in the analysis of cracks partially reinforced by ligaments bridging the crack faces. The model is based on the assumption of a linear-elastic material and is not applicable to problems involving gross plasticity near the crack tip unless the plastic zone is explicitly included as a set of plastic springs or a superposed crack-closing stress applied in the region of the crack tip. The improvements to the Rose model for fracture and fatigue of reinforced cracks are easy to apply, and are useful in many fields including fracture analysis of layered structures, composites, and bonded aircraft repairs.

3.6 References

[1] Kane T.R., Mindlin R.D. High-frequency extensional vibrations of plates. Journal of Applied Mechanics, v. 55, p. 277-283, 1955.

[2] Kotousov A., Wang C.H., A generalized plane strain theory for transversally isotropic plates. Acta Mechanica, v. 161, p. 53-64, 2003.

[3] Kotousov A., Wang C.H. Fundamental solutions for the generalised plane strain theory. International Journal of Engineering Science, v. 40, p.1775-1790, 2002.

[4] Joseph P.F., Erdogan F. Surface crack problems in plates. International Journal of Fracture, v. 41, pp. 105-131, 1989.

[5] Joseph, P.F., Erdogan, F. Plates and shells containing a surface crack under general loading conditions. NASA CR 178232, NASA Langley Research Centre, 1987.

[6] Reissner E. The effect of transverse shear deformation on the bending of elastic plates. ASME Journal of Applied Mechanics v. 12, pp. A69-77, 1945.

[7] Wang, C.H., Rose, L.R.F. A crack bridging model for bonded plates subjected to tension and bending. International Journal of Solids and Structures, v. 36, pp. 1985-2014, 1999.

[8] Rose, L.R.F. A cracked plate repaired by bonded reinforcements. International Journal of Fracture, v.18, n.2, pp. 135-144, 1982.

[9] Rose, L.R.F. Theoretical Analysis of crack patching. In: Baker A.A., Jones R. Bonded Repair of Aircraft Structures. Martinus Nijhoff Publishers, pp. 77-105, 1988.

[10] Clark, R.J., Romilly, D.P. Fatigue damage prediction for bonded composite repairs applied to metallic aircraft structures. SAE Trans. - Journal of Aerospace, 2001, 10 p.

Chapter 4: Transverse shear and pressurization in the bending of reinforced cracks*

Randal J. Clark and Douglas P. Romilly

University of British Columbia Department of Mechanical Engineering

4.1 Introduction

The authors develop an 8^{th}-order model for bending of transversally isotropic plates and use integral transforms and a collocation method to form a line-spring model for a cracked plate. The 8^{th}-order model allows satisfaction of the three standard plate bending boundary conditions; the normal moment, twisting moment, and transverse shear force, and an additional shear stress resultant that allows analysis of transverse normal stresses near the crack tip. The line-spring model is used to develop geometry correction factors for bending of finite-thickness plates, accounting for transverse shear deformation and pressurization of the plate near the crack tip. The line-spring model is then applied to the problem of a plate with a reinforced crack, and the results are used to validate an interpolation solution based on an energy method. While not explicitly analysed, the models are applicable to many problems, including bending of bonded repairs, fracture and fatigue of composite and layered materials, surface cracks, crack tip plasticity and crack closure or crack face interaction.

Plates are important structural elements in applications ranging from aircraft and naval structures to building construction and infrastructure. When compared to the analysis of in-plane loading, plate bending is complicated by transverse shear deformations and transverse loads, leading to higher-order models that are more difficult to solve. For this reason, the construction and analysis of plate bending models has been an ongoing topic, with researchers seeking models that are easy to apply and yet capture the essential characteristics of the three-dimensional behaviour of the plate. Accordingly, a range of models exists for engineering analysis of plates. Selection of the correct model for an application depends upon many factors including the geometry and composition of the plate, whether large stress gradients are present, and on the accuracy required of the analysis.

---

* A version of this chapter has been accepted for publication. R.J. Clark, D.P. Romilly, "Transverse shear and pressurization effects in the bending of plates with reinforced cracks", International Journal of Fracture, v 142, 2006, p 81-102.

In the simplest models, transverse shear deformations are neglected and the Kirchoff boundary condition is used to combine the twisting moment and shear force boundary conditions. The result is a 4^{th}-order governing equation expressed in terms of the transverse deflection of the plate. This biharmonic problem is relatively easy to solve, and exact solutions exist for many geometries. More sophisticated models exist that explicitly include all three standard plate bending boundary conditions and account for shear deflections, the most accepted being the 6th-order Reissner [1] and Mindlin [2] models. The Reissner model follows from the assumption that the transverse stresses in a plate will assume the through-thickness distribution predicted by simple beam bending, and is an example of a stress-based solution, whereas the Mindlin model follows from the assumption of a plane strain form for the displacement field. More sophisticated models may be developed using higher-order functions to approximate the through-thickness variation of the stresses or strains, and require the adoption of extra boundary conditions to solve the arising differential equations. These models usually employ an infinite series expansion of the stresses or strains, and are of interest in the field of fracture mechanics as they allow an accurate assessment of the stresses near a crack tip [e.g. 3]. For most engineering problems, stress gradients are small, and the Reissner and Mindlin models are considered adequate. Other examples of applications requiring more advanced models are those involving large stress gradients (e.g. higher frequency vibrations), when failure is governed by through-thickness stresses, or if there is otherwise the need for very accurate solutions.

For plate extension, Kotousov and Wang [4,5] developed a dislocation-density solution for a crack in a generalized plane strain plate and found that, in terms of the stress resultant or average of the through-thickness stresses, the crack tip in plate extension is in a state of plane strain. This is contrary to the common belief that for very thin plates, the crack tip is effectively in a state of plane stress. This observation has consequences for the use of energy methods in fracture mechanics. The pertinent example is the analysis of reinforced cracks, where the strain energy release rate may be calculated analytically, but the conversion to stress intensity requires the assumption of either plane stress or plane strain conditions. Clark and Romilly [6] have used the generalized plane strain plate model to develop a line-spring model and geometry correction factors for extension of cracked plates. The line-spring model was then used to investigate the effects of reinforcing springs bridging the crack faces, and it was found that the geometry correction factors could be used to include the effects of plate thickness and transverse material properties on the stress intensity and crack-face deflection, leading to improved accuracy in the analysis of a reinforced crack. The problem of transverse stresses building up near the crack tip also exists for plate bending, but is not often recognized due to the already difficult problem of modelling the shear forces and shear deflections and

assessing the effects of crack face contact. Accordingly, the fracture mechanics of bending plates is less well understood than for extension.

In this chapter, the authors develop an 8^{th}-order plate bending model, which is effectively a generalized plane strain model for bending. This is the simplest model possible that includes the effects of both transverse normal stresses and shear deflections. The motivation for this work is to develop a practical line-spring model and corresponding engineering analysis methods that include these two plate thickness effects and allow the calculation of the thickness-averaged bending stress intensity factor. The goal is to expedite the design of bonded composite repairs where the repaired structure consists of plates containing reinforced cracks subjected to bending. The authors achieve this by using the integral transform method of Joseph and Erdorgan [7,8] whereby the new plate bending model is reduced to a hyper-singular integral expressed in terms of the bending stresses along the plane of the crack and the displacement of the crack faces. The line spring model is then used to develop equations suitable for the assessment of plates containing through-cracks and reinforced cracks subjected to bending. The resulting equations are accurate, easy to apply, and include both transverse shear deflection and transverse normal stresses effects.

4.2 Basic plate bending models and fracture

In this section, the authors describe four basic engineering plate bending models. These models are similar to the classical plate bending models available in the literature, and form the basis for the 8^{th}-order model developed in subsequent sections. The first two employ the Kirchoff or 'effective shear stress' boundary condition, and will be referred to as the **plane stress** and **plane strain** plate bending models. In their development, it is assumed that either the transverse stresses or the transverse strains vanish. The Kirchoff boundary condition allows the twisting moment and shear force acting along a cut to be combined, i.e. an artificial condition that satisfies equilibrium but does not allow for the explicit inclusion of the transverse shear forces. For crack problems, these models cannot be trusted. Errors in the range of 60% to 70% may exist, depending on the crack length and the thickness and elastic properties of the plate. Another problem is that while the governing equations are equivalent to those arising in the plane stress and plane strain plate extension models, the Kirchoff boundary condition causes inconsistencies between the stress and displacement based definitions of the stress intensity factor, as observed by Joseph and Erdogan [8]. This occurs because the crack tip is a region of large stress gradients, and hence it is important to properly account for the zero shear force boundary condition on the edge of the crack. For plane stress bending, the deflection of the crack face and the bending stress at the outer fibre are derived in Appendix D and may be expressed as follows.

$$u(y) = 2\frac{\bar{\sigma}}{E}\left(\frac{1+\nu}{3+\nu}\right)\sqrt{a^2 - y^2}, \qquad |y| < a \tag{1}$$

$$\sigma(y) = \bar{\sigma}\frac{y - \sqrt{y^2 - a^2}}{\sqrt{y^2 - a^2}}, \qquad |y| > a \tag{2}$$

For plane strain plate bending of transversally isotropic plates, where $\eta = \nu_z\sqrt{E/E_z}$ is an effective Poisson's ratio, the stresses are given by (2), and the crack face deflection is given by:

$$u(y) = 2\bar{\sigma}\left(\frac{1+\nu}{3+\nu-2\eta^2}\right)\left(\frac{1-\eta^2}{E}\right)\sqrt{a^2 - y^2}, \qquad |y| < a \tag{3}$$

The two remaining basic models will be referred to as the **plane stress shear deformable plate** and the **plane strain shear deformable plate**. These are formed by including the transverse shear deflection in the analysis. These 6th order bending models satisfy all three engineering stress resultants; the normal moment, twisting moment, and transverse shear force. While the Reissner model assumes that the transverse stresses take the form given by simple beam bending, the plane stress shear deformable plate is somewhat simplified, as the transverse normal stresses are assumed to vanish. The plane strain shear deformable plate is identical to the Mindlin plate, where it is assumed that the transverse strains vanish. The Reissner plate is usually considered to be more accurate than the Mindlin plate, as the assumed transverse stresses more closely model those found in an actual plate. In the presence of large stress gradients, both the Reissner and Mindlin models are far more accurate than the Kirchoff model, but their use in fracture mechanics is limited by assumptions regarding plane stress or strain, similar to the problem that exists for extension of cracked plates. For the limiting case of a very short crack in the plane stress shear deformable plate, the deflection of the crack face at the outer fibre has the same form as may be found for plane stress plate extension, as derived in Appendix D.

$$u(y) = \frac{2\bar{\sigma}}{E}\sqrt{a^2 - y^2}, \qquad |y| < a \tag{4}$$

Similarly, for a very short crack in the plane strain shear deformable plate, the crack face deflection takes the form for plane strain plate extension.

$$u(y) = \frac{2\bar{\sigma}(1-\eta^2)}{E}\sqrt{a^2 - y^2}, \qquad |y| < a \tag{5}$$

For both types of shear deformable plate, the stresses at the base of the crack assume the form given by equation (2). It will be shown in subsequent sections that these basic

models describe limits on the behaviour of the 8th-order, or **generalized plane strain** bending model.

4.3 An 8th-order plate bending model

Here, we develop an 8th-order plate bending model for a transversally isotropic plate, allowing the evaluation of both the transverse shear deflections and transverse normal stresses. For a plate of thickness 2h, the displacement field may be approximated by equations (6a,b,c) below. The series expansion of the transverse displacement is truncated to produce an engineering model that requires four boundary conditions and allows the evaluation of the effects of transverse pressurization at the crack tip.

$$u_x = \frac{z}{h}u_x(x,y), \qquad u_y = \frac{z}{h}u_y(x,y), \qquad u_z = w(x,y) + \frac{z^2}{h^2}u_z(x,y) \tag{6a,b,c}$$

The displacement field and the stresses in the plate are illustrated in Figure 4-1. The depicted stresses are a schematic representation intended to illustrate odd or even behaviour and the zero-stress boundary conditions at the edges of the plate.

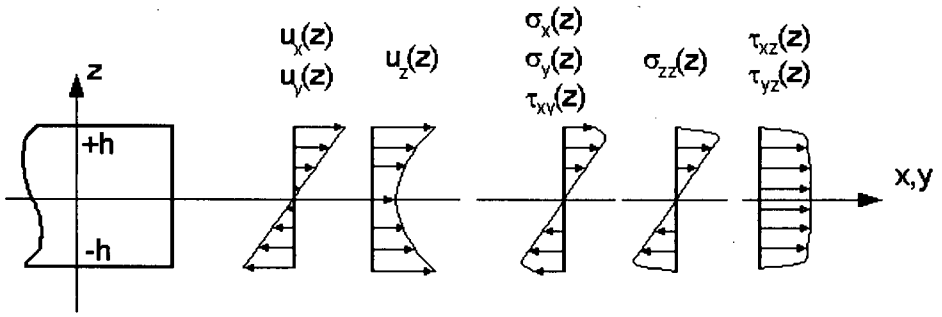

Figure 4-1: Displacements and stresses for the 8th-order plate bending model

For displacement-based theories, stresses are expressed as stress resultants or line-forces. Integrating through the thickness, we find expressions for the moments and shear forces.

$$M_{xx} = \int_{-h}^{h} \sigma_{xx} z dz, \qquad M_{yy} = \int_{-h}^{h} \sigma_{yy} z dz, \qquad M_{xy} = \int_{-h}^{h} \tau_{xy} z dz \tag{7a,b,c}$$

$$V_x = \int_{-h}^{h} \tau_{xz} dz, \qquad V_y = \int_{-h}^{h} \tau_{yz} dz \tag{7d}$$

These are the loads evaluated in the basic plate models. Pressurization of the plate may be modelled by integration of the transverse normal stress as shown below.

$$P_{zz} = \int_{-h}^{h} \sigma_{zz} z dz \tag{7e}$$

A final set of 'pinching shear' stress resultants arise from the transverse shear stresses (resulting from curvatures in the in-plane stress fields) and act to pressurize the plate.

$$R_x = \int_{-h}^{h} \tau_{xz} z^2 dz\,, \quad R_y = \int_{-h}^{h} \tau_{yz} z^2 dz \tag{7f,g}$$

The equilibrium equations may similarly be formulated in terms of stress resultants.

$$M_{xx,x} + M_{xy,y} = V_x\,, \qquad M_{yy,y} + M_{xy,x} = V_y\,, \qquad V_{x,x} + V_{y,y} = -q \tag{8a,b,c}$$

A final equilibrium condition arises from the second moment of the transverse equilibrium equations, relating the pressurization of the plate to transverse loads and 'pinching shear stress resultants'.

$$2P_{zz} = h^2 q + R_{x,x} + R_{y,y} \tag{8d}$$

The constitutive laws for a transversally isotropic material may also be integrated over the thickness, and the stress resultants may be expressed in terms of the plate displacements.

$$M_{xx} = D\left[u_{x,x} + \frac{\nu + \eta^2}{1-\eta^2} u_{y,y} + \frac{\nu_z(1+\nu)}{1-\eta^2}\frac{2}{h} u_z\right] \tag{9a}$$

$$M_{yy} = D\left[u_{y,y} + \frac{\nu + \eta^2}{1-\eta^2} u_{x,x} + \frac{\nu_z(1+\nu)}{1-\eta^2}\frac{2}{h} u_z\right] \tag{9b}$$

$$P_{zz} = D\left[\frac{1-\nu^2}{1-\eta^2}\left(\frac{\nu_z^2}{\eta^2}\right)\frac{2}{h} u_z + \frac{\nu_z(1+\nu)}{1-\eta^2}\left(u_{x,x} + u_{y,y}\right)\right] \tag{9c}$$

$$M_{xy} = \frac{2h^2 G}{3}\left[u_{x,y} + u_{y,x}\right] \tag{9d}$$

$$V_x = 2G_z\left[u_x + h w_{,x} + \frac{h}{3} u_{z,x}\right] \tag{9e}$$

$$V_y = 2G_z\left[u_y + h w_{,y} + \frac{h}{3} u_{z,y}\right] \tag{9f}$$

The second moment of the transverse shear stress constitutive equations results in expressions for the pinching shears.

$$R_x = \frac{2G_z h^2}{3}\left[u_x + hw_{,x} + \frac{3h}{5}u_{z,x}\right] \tag{9g}$$

$$R_y = \frac{2G_z h^2}{3}\left[u_y + hw_{,y} + \frac{3h}{5}u_{z,y}\right] \tag{9h}$$

The plate bending constant, D, takes the form for plane strain.

$$D = \frac{4h^2}{3}\left(\frac{1-\eta^2}{1-\nu-2\eta^2}\right)G \tag{10}$$

Substitution of the constitutive (9) into the equilibrium equations (8) will yield the governing equations for the plate. It proves useful to define the functions ϕ and ψ.

$$\phi = u_{x,x} + u_{y,y}, \qquad \psi = u_{x,y} - u_{y,x} \tag{11}$$

Eliminating q from the transverse equilibrium equations (8c,d) yields the following.

$$\phi + h\nabla^2 w + \frac{h}{3}\nabla^2 u_z = 0 \tag{12}$$

$$\frac{2}{h}u_z + \frac{\eta^2}{(1-\nu)\nu_z}\phi = \left(\frac{1-\nu-2\eta^2}{1-\nu^2}\right)\frac{\eta^2 G_z}{\nu_z^2 G}\frac{h}{15}\nabla^2 u_z \tag{13}$$

Adding the derivatives of equations (8a) and (8b), equilibrium in the plane of the plate, and using equation (8c) to cancel the shear stress resultants leads to the following:

$$\nabla^2\phi + \frac{(1+\nu)\nu_z}{1-\eta^2}\frac{2}{h}\nabla^2 u_z = 0 \tag{14}$$

Subtracting the derivatives of equations (8a) and (8b) leads to the following additional condition:

$$\nabla^2\psi - k_\psi^2\psi = 0, \qquad k_\psi^2 = \frac{3G_z}{h^2 G} \tag{15}$$

Decoupling equations (12) through (14), we find a fourth order governing equation for ϕ along with the second order equation for ψ given by equation (15).

$$\nabla^4\phi - k_\phi{}^2\nabla^2\phi = 0, \qquad k_\phi{}^2 = \left(\frac{1+\nu}{1-\eta^2}\right)\frac{30\nu_z^2 G}{h^2\eta^2 G_z} \tag{16}$$

The governing equation will be expressed in terms of the average deflection of the plate.

$$\overline{w} = \frac{1}{2h}\int_{-h}^{h}\left[w + \frac{z^2}{h^2}u_z\right]dz = w + \frac{1}{3}u_z \tag{17}$$

By equation (12), we note that $\phi = -h\nabla^2 \overline{w}$, and we find the following expression for $\overline{w}$.

$$\nabla^6 \overline{w} - k_w{}^2 \nabla^4 \overline{w} = 0, \text{ where } k_w{}^2 = k_\phi^2 \tag{18}$$

Equations (18) and (15) form an 8th-order system, requiring four boundary conditions. The first three are the normal and twisting moments and the shear force. The fourth is the 'pinching shear'. For ξ acting along a cut and ς along the outward normal, these are:

$$M_{\varsigma\varsigma} = \overline{M}_{\varsigma\varsigma}, \qquad M_{\xi\varsigma} = \overline{M}_{\xi\varsigma}, \qquad V_\varsigma = \overline{V}_\varsigma, \qquad R_\varsigma = \overline{R}_\varsigma \tag{19}$$

The functions ϕ and ψ describe the normal and shear deformations of the plate, and lead to a simple derivation of the governing equations, but are not convenient for calculating the moments or shear forces. For this purpose, one may define a stress function. From equilibrium, we note that a function χ must exist such that:

$$V_x = \chi_{,y}, \qquad V_y = -\chi_{,x}. \tag{20}$$

From the definition of ψ, and constitutive equations (9e,f), we find the following.

$$\nabla^2 \chi = 2G_z \psi \tag{21}$$

A differential equation for χ may now be found from equation (16).

$$\nabla^4 \chi - k_\psi^2 \nabla^2 \chi = 0 \tag{22}$$

Equations (18), (15), and (22) allow the analysis of transverse shear stresses and pressurization in plate bending.

4.4 Hyper-singular integral equations

In this section, the governing equations are reduced to a hyper-singular integral relating the crack face deflection to the bending stresses along the crack plane. The authors apply the integral transform method used by Erdogan and Joseph [7,8] to analyse a Reissner plate. The Fourier transform of a function and its inverse are defined as follows.

$$\overline{f} = \overline{f}(x,\alpha) = \int_{-\infty}^{\infty} f(x,y) e^{i\alpha y} dy, \qquad f = f(x,y) = \frac{1}{2\pi} \int_{-\infty}^{\infty} \overline{f}(x,\alpha) e^{-i\alpha y} d\alpha \tag{23}$$

Applying this transform, the governing equations may be written as ordinary differential equations.

$$\left(\overline{w}_{,xxxxx} - 3\alpha^2 \overline{w}_{,xxx} + 3\alpha^4 \overline{w}_{,x} - \alpha^6 \overline{w}\right) - k_w^2 \left(\overline{w}_{,xxx} - 2\alpha^2 \overline{w}_{,x} + \alpha^4 \overline{w}\right) = 0 \tag{24}$$

$$\left(\overline{\psi}_{,x} - \alpha^2 \overline{\psi}\right) - k_\psi^2 \overline{\psi} = 0 \tag{25}$$

Keeping only the roots that vanish as $x \to \infty$, one finds the following expressions for $\bar{w}$ and ψ.

$$\bar{w} = \frac{1}{2\pi}\int_{-\infty}^{\infty}\left(A_1(\alpha)e^{-|\alpha|x} + A_2(\alpha)xe^{-|\alpha|x} + A_3(\alpha)e^{-R_w x}\right)e^{-i\alpha y}d\alpha, \qquad R_w{}^2 = \alpha^2 + k_w^2 \tag{26}$$

$$\psi = \frac{1}{2\pi}\int_{-\infty}^{\infty}\left(B_1(\alpha)e^{-R_\psi x}\right)e^{-i\alpha y}d\alpha, \qquad R_\psi{}^2 = \alpha^2 + k_\psi^2 \tag{27}$$

Symmetry requires vanishing shear stresses along the line of the crack. Accordingly:

$$M_{xy}(0,y) = 0, \qquad V_x(0,y) = 0, \qquad R_x(0,y) = 0 \tag{28a,b,c}$$

From the constitutive equations, the deflections along the line of the crack are limited as follows:

$$u_{x,y} + u_{y,x} = 0, \qquad u_x + h\bar{w}_{,x} = 0, \qquad u_{z,x} = 0 \tag{29a,b,c}$$

One must express these in terms of $\bar{w}$ and ψ. The following arise from (29a):

$$u_{x,y} = \frac{1}{2}\psi, \quad u_{y,x} = -\frac{1}{2}\psi \tag{30}$$

The first symmetry condition arises from (29a) by substitution from (29b) and (30b).

$$\psi + 2h\bar{w}_{,xy} = 0 \tag{31}$$

To find the second symmetry condition, we require an expression for $M_{xx,x}(0,y)$ under the restrictions (29). The following may be obtained from constitutive equation (9a).

$$M_{xx,x}(0,y) = D\left[\phi_{,x} + \frac{1}{2}\left(\frac{1-\nu-2\eta^2}{1-\eta^2}\right)\psi_{,y}\right] \tag{32}$$

The second symmetry condition will then arise from equilibrium equation (8a).

$$\phi_{,x} + \frac{1}{2}\left(\frac{1-\nu-2\eta^2}{1-\eta^2}\right)\psi_{,y} = 0 \tag{33}$$

A general equation for the transverse displacement arises from equations 13 and 14.

$$\nu_z\frac{2}{h}u_z + \frac{\eta^2}{1-\nu}\phi + \frac{1}{k_w^2}\left(\frac{1-\nu-2\eta^2}{1-\nu^2}\right)\nabla^2\phi = 0 \tag{34}$$

After taking the derivative, the final symmetry condition may be found from (29c).

$$\nabla^2\phi_{,x} + k_w^2\eta^2\left(\frac{1+\nu}{1-\nu-2\eta^2}\right)\phi_{,x} = 0 \tag{35}$$

Substitution of (24) and (25) into symmetry conditions (31), (33), and (35) leads to the following restrictions on the integration constants.

$$B_1 + 2hi\left[A_1\alpha^2 - A_2\alpha + A_3 R_w\alpha\right] = 0 \tag{36a}$$

$$2A_2\alpha^2 - k_w^2 R_w A_3 + \frac{i\alpha}{2h}\left(\frac{1-\nu-2\eta^2}{1-\eta^2}\right)B_1 = 0 \tag{36b}$$

$$R_w A_3 = \frac{2\alpha^2}{k_w^2}\left(\frac{\eta^2}{1-\eta^2}\right)\left(\frac{1+\nu}{1-\nu}\right)A_2 \tag{36c}$$

After some manipulation, we find that A_1 and B_1 may be expressed as follows.

$$\alpha A_1 = -\left(\frac{1+\nu}{1-\nu}\right)A_2 - R_w A_3, \quad \frac{i}{2h}B_1 = \frac{-2\alpha}{1-\nu}A_2 \tag{37a,b}$$

The symmetry conditions eliminate all but one integration constant, and the crack face rotation, $\beta = -\overline{w}_{,x}(0,y)$, may now be written in terms of $A_2(\alpha)$.

$$\beta = \frac{-1}{2\pi}\int_{-\infty}^{\infty}\frac{2}{1-\nu}A_2 e^{-i\alpha y}d\alpha \tag{38}$$

The last integration constant arises from the boundary condition $M_{xx}(0,y) = -\overline{M}(y)$, but one must first find an expression for either $u_{x,x}(0,y)$ or $u_{y,y}(0,y)$. Transforming equation (22) and applying the symmetry conditions, the stress function χ is given by:

$$\chi = \frac{1}{2\pi}\int_{-\infty}^{\infty}\frac{-8ihG_z}{k_\psi^2(1-\nu)}\left(e^{-|\alpha|x} - e^{-R_\psi x}\right)e^{-i\alpha y}d\alpha \tag{39}$$

From constitutive equations (9e,f) we find expressions for $u_{x,x}(0,y)$ and $u_{y,y}(0,y)$.

$$u_{x,x} = \frac{\chi_{,xy}}{2G_z} - h\overline{w}_{,xx}, \qquad u_{y,y} = \frac{-\chi_{,xy}}{2G_z} - hw_{,yy} \tag{40}$$

From (9a), we now find an expression for the boundary condition $\overline{M}(y) = -M(0,y)$.

$$\overline{M}(y) = -\frac{4h^2G}{3}\left[u_{x,x} + \frac{\nu}{1-\nu}\phi - \frac{1}{k_w^2(1-\nu)}\nabla^2\phi\right] \tag{41}$$

An integral equation arises by substituting for $u_{x,x}$ and w.

$$\overline{M}(y) = -\frac{2h^3 G}{3\pi}\left(\frac{1+\nu}{1-\nu}\right)\int_{-\infty}^{\infty} f(\alpha) A_2 e^{-i\alpha y} d\alpha \tag{42}$$

Here, $f(\alpha)$ is given as follows.

$$f(\alpha) = \left(\frac{3+\nu}{1+\nu}\right)\alpha + \frac{4\alpha^2(\alpha - R_\psi)}{k_\psi^2(1+\nu)} + \frac{1}{k_w^2}\left(\frac{2\eta^2}{1-\eta^2}\right)\left(\alpha^3 - \frac{\alpha^4}{R_w}\right) \tag{43}$$

We may now form a hyper-singular equation for the crack face rotation. Inverting equation (38) we find an expression for integration constant A_2.

$$-\frac{2A_2}{1-\nu} = \int_{-\infty}^{\infty} \beta(t)\ e^{i\alpha t} d\alpha \tag{44}$$

By substitution, an integral arises relating the moment to the crack face rotation.

$$\overline{M}(y) = \frac{h^3 E}{6\pi}\int_L \beta(t) \int_{-\infty}^{\infty} f(\alpha) e^{i\alpha(t-y)} d\alpha\ dt \tag{45}$$

Note the following integral identities, where K_0 and K_2 are modified Bessel functions of the second kind.

$$\int_0^{\infty} \alpha e^{i\alpha(t-y)} d\alpha = \frac{-1}{(t-y)^2} \tag{46a}$$

$$\int_0^{\infty} \alpha^3 e^{i\alpha(t-y)} d\alpha = \frac{6}{(t-y)^4} \tag{46b}$$

$$\frac{1}{k^4}\int_0^{\infty} R\alpha^2 e^{i\alpha(t-y)} d\alpha = \frac{1}{2}\left(K_2(k|t-y|) - K_0(k|t-y|)\right) + \frac{3}{(k|t-y|)^2} K_2(k|t-y|) \tag{46c}$$

$$\frac{1}{k^4}\int_0^{\infty} \frac{\alpha^4}{R} e^{i\alpha(t-y)} d\alpha = \left(1 + \frac{3}{k^2(t-y)^2}\right) K_2(k|t-y|) \tag{46d}$$

Applying these identities, equation (45) may be written as a hyper-singular integral. The regular and weakly singular parts have been separated into the functions L_ψ and L_ϕ.

$$\overline{M}(y) = \frac{-h^3 E}{3\pi(1-\eta^2)}\int_L \beta(t)\left[\frac{1}{(t-y)^2} + \frac{k_\psi^2}{2}\frac{1-\eta^2}{1+\nu} L_\psi(k_\psi|t-y|) + k_w^2 \eta^2 L(k_w|t-y|)\right] dt \tag{47}$$

The function L_ψ describes the transverse shear deflections, and function L_ϕ is the same expression found by the authors [6] for generalized plane strain plate extension, and accounts for the effects of pressurization near the crack tip.

$$L_\psi(z) = -\frac{48}{z^4} + \frac{4}{z^2} + 4\left(K_2(z) - K_0(z)\right) + \frac{24}{z^2}K_2(z) \tag{48}$$

$$L(z) = 2\left[1 + \frac{3}{z^2}\right]K_2(z) - \frac{12}{z^4} - \frac{1}{z^2} \tag{49}$$

Equation (47) may be written in terms of the bending stress in the outer fibre as follows.

$$\overline{\sigma}(y) = \frac{-hE}{2\pi(1-\eta^2)}\int_L \beta(t)\left[\frac{1}{(t-y)^2} + \frac{k_\psi^2}{2}\frac{1-\eta^2}{1+\nu}L_\psi(k_\psi|t-y|) + k_w^2\eta^2 L(k_w|t-y|)\right]dt \tag{50}$$

The equivalent equations for the four basic bending models are derived in Appendix D.

4.5 Bending of a cracked plate

Here, the shear deformable plate models are solved by expanding the crack face deflection into a series of Chebychev polynomials. With this expansion, a set of collocation points may be chosen to form a linear system, solvable for the expansion coefficients. First one must normalize the bounds and parameters in the integral equations. We define the normalized quantities:

$$u(r) = \frac{h}{a}\beta(t), \quad r = t/a, \quad s = y/a, \quad \kappa_\psi = k_\psi a, \quad \kappa_w = k_w a \tag{51}$$

Equations (52) through (54) show the normalized form of the hyper-singular integrals for the plane stress shear deformable plate, the plane strain shear deformable plate, and the eighth order plate, respectively

$$\overline{\sigma_b}(s) = \frac{-E}{2\pi}\int_{-1}^{1} u(r)\left(\frac{1}{(r-s)^2} + \frac{\kappa_\psi^2}{2(1+\nu)}L_\psi(\kappa_\psi|r-s|)\right)dr \tag{52}$$

$$\overline{\sigma_b}(s) = \frac{-E}{2\pi(1-\eta^2)}\int_{-1}^{1} u(r)\left(\frac{1}{(r-s)^2} + \frac{\kappa_\psi^2}{2}\left(\frac{1-\eta^2}{1+\nu}\right)L_\psi(\kappa_\psi|r-s|)\right)dr \tag{53}$$

$$\overline{\sigma_b}(s) = \frac{-E}{2\pi(1-\eta^2)}\int_{-1}^{1} u(r)\left(\frac{1}{(r-s)^2} + \frac{\kappa_\psi^2}{2}\frac{1-\eta^2}{1+\nu}L_\psi(\kappa_\psi|r-s|) + \kappa_w^2\eta^2 L(\kappa_w|r-s|)\right)dr \tag{54}$$

The crack face deflection may be expanded into Chebyshev polynomials of the second kind, $U_i(r) = \sin((i+1)\cos^{-1}(r))/\sqrt{1-r^2}$, with the weight function $W(r) = \sqrt{1-r^2}$.

$$u(r) = W(r)\sum_{i=0}^{N} g_i U_i(r) \tag{55}$$

The hyper-singular part may be evaluated analytically.

$$\frac{1}{\pi}\int_{-1}^{1}\frac{\sqrt{1-r^2}U_n(r)}{(s-r)^2}dr = \begin{cases} -(n+1)U_n(s) & |s|<1 \\ (n+1)\dfrac{\left(s-\sqrt{s^2-1}\right)^{n+1}}{\sqrt{s^2-1}} & s>1 \end{cases} \tag{56}$$

Equations (52), (53), and (54) may now be written in terms of the expansion.

$$\overline{\sigma_b}(s) = E\sum_{i=0}^{N} g_i\left(\frac{i+1}{2}U_i(s) - \frac{\kappa_\psi^2}{4\pi(1+\nu)}\int_{-1}^{1}L_\psi(\kappa_\psi|r-s|)W(r)U_i(r)dr\right) \tag{57}$$

$$\overline{\sigma_b}(s) = \frac{E}{1-\eta^2}\sum_{i=0}^{N} g_i\left(\frac{i+1}{2}U_i(s) - \frac{\kappa_\psi^2}{4\pi}\left(\frac{1-\eta^2}{1+\nu}\right)\int_{-1}^{1}L_\psi(\kappa_\psi|r-s|)W(r)U_i(r)dr\right) \tag{58}$$

$$\overline{\sigma_b}(s) = \frac{E}{1-\eta^2}\sum_{i=0}^{N} g_i\left(\begin{array}{c}\dfrac{i+1}{2}U_i(s) - \dfrac{\kappa_\psi^2}{4\pi}\left(\dfrac{1-\eta^2}{1+\nu}\right)\displaystyle\int_{-1}^{1}L_\psi(\kappa_\psi|r-s|)W(r)U_i(r)dr \\ -\dfrac{\kappa_w^2\eta^2}{2\pi}\displaystyle\int_{-1}^{1}L_w(\kappa_w|r-s|)W(r)U_i(r)dr\end{array}\right) \tag{59}$$

Analytical solutions exist for the logarithmic parts of $L_\psi(z)$ and $L_w(z)$, but the regular parts require numerical integration. The term $V_{i,j}$ includes the logarithmic singularity and may be solved analytically, as demonstrated by Joseph and Erdogan [7] and by Wang and Rose [9]. To evaluate the regular part, the authors used Gauss-Chebychev quadrature, as suggested by Joseph and Erdogan.

$$L_{i,j}^{\psi} = \int_{-1}^{1}\left[L_\psi(\kappa_\psi|r_i-s|) - \ln(|r_i-s|)\right]W(s)U_j(s)ds + V_{i,j} \tag{60}$$

$$L_{i,j}^{w} = \int_{-1}^{1}\left[L_w(\kappa_w|r_i-s|) + \frac{3}{4}\ln(|r_i-s|)\right]W(s)U_j(s)ds - \frac{3}{4}V_{i,j} \tag{61}$$

$$V_{i,j} = \int_{-1}^{1} \ln|r_i - s| W(s) U_j(s) ds = \begin{cases} -\frac{\pi}{2}\left[-r_i^2 + \frac{1}{2} + \ln 2\right] & j = 0 \\ -\frac{\pi}{2}\left[\frac{T_j(r_i)}{j} - \frac{T_{j+2}(r_i)}{j+2}\right] & j > 0 \end{cases} \tag{62}$$

Selecting collocation points s_i, a linear system arises, solvable for the coefficients, g_j.

$$\overline{\sigma_b} = A\overline{g} \tag{63}$$

For the three bending models, the coefficient matrix may be expressed as follows.

$$A_{i,j} = E\left(\frac{i+1}{2} U_j(s_i) - \frac{\kappa_\psi^2}{4\pi(1+\nu)} L_{i,j}^{\psi}\right) \tag{64}$$

$$A_{i,j} = \frac{E}{1-\eta^2}\left(\frac{i+1}{2} U_j(s_i) - \frac{\kappa_\psi^2}{4\pi}\left(\frac{1-\eta^2}{1+\nu}\right) L_{i,j}^{\psi}\right) \tag{65}$$

$$A_{i,j} = \frac{E}{1-\eta^2}\left(\frac{i+1}{2} U_j(s_i) - \frac{\kappa_\psi^2}{4\pi}\left(\frac{1-\eta^2}{1+\nu}\right) L_{i,j}^{\psi} - \frac{\kappa_w^2 \eta^2}{2\pi} L_{i,j}^{w}\right) \tag{66}$$

Equations (57), (58), and (59) are valid along the entire line $x = 0$, and allow the evaluation of the stresses near the crack tip. As for plate extension, the only terms containing a $\sqrt{r}$ singularity arise from the hyper-singular part of the equation. These terms may be found by examining integral identity equation (56) for the region outside of the crack domain. The results for plane stress and plane strain bending (equations (67) and (68) respectively) follow from the stress-based definition of the stress intensity. The result reported is for the stress intensity in the outer fibre of the plate.

$$K = \lim_{r \to 1+} \sqrt{2\pi a(r-1)}\,\sigma_{xx}(0,r) = \frac{E\sqrt{\pi a}}{2} \sum_{i=0}^{N} g_i U_i(1) = \frac{E\sqrt{\pi a}}{2} \sum_{i=0}^{N} (i+1) g_i \tag{67}$$

$$K = \lim_{r \to 1+} \sqrt{2\pi a(r-1)}\,\sigma_{xx}(0,r) = \frac{E\sqrt{\pi a}}{2(\eta^2-1)} \sum_{i=0}^{N} g_i U_i(1) = \frac{E\sqrt{\pi a}}{2(\eta^2-1)} \sum_{i=0}^{N} (i+1) g_i \tag{68}$$

For the 8th-order model, in the evaluation of the part of the stress field containing the $\sqrt{r}$ singularity, the stresses and crack face displacements are related by the equations that arise in the analysis of plane strain plate extension, meaning that the crack tip singular stress field exists in a state of plane strain. This is analogous to the result of Kotousov and Wang [5] for extension of cracked plates. Equations (67) and (68) allow the evaluation of the stress intensity for the various plate bending models. Table 4-1 shows properties for selected transversely isotropic materials that will be used to evaluate them.

Material	E (GPa)	ν	E_z (GPa)	ν_z
(1) Isotropic	71.0	0.5	-	0.5
(2) Isotropic	71.0	0.33	-	0.33
(3) Isotropic	71.0	0.1	-	0.1
(4) Quasi-isotropic boron/epoxy	106	0.12	25	0.028
(5) Transversely loaded unidirectional boron/epoxy	25	0.019	210	0.21

Table 4-1: Material properties used to test the GPS model

Figure 4-2 shows stress intensity results for the plane stress shear deformable bending model, which are normalized to the nominal result $K_0 = \sigma_b \sqrt{\pi a}$ and plotted against the crack length.

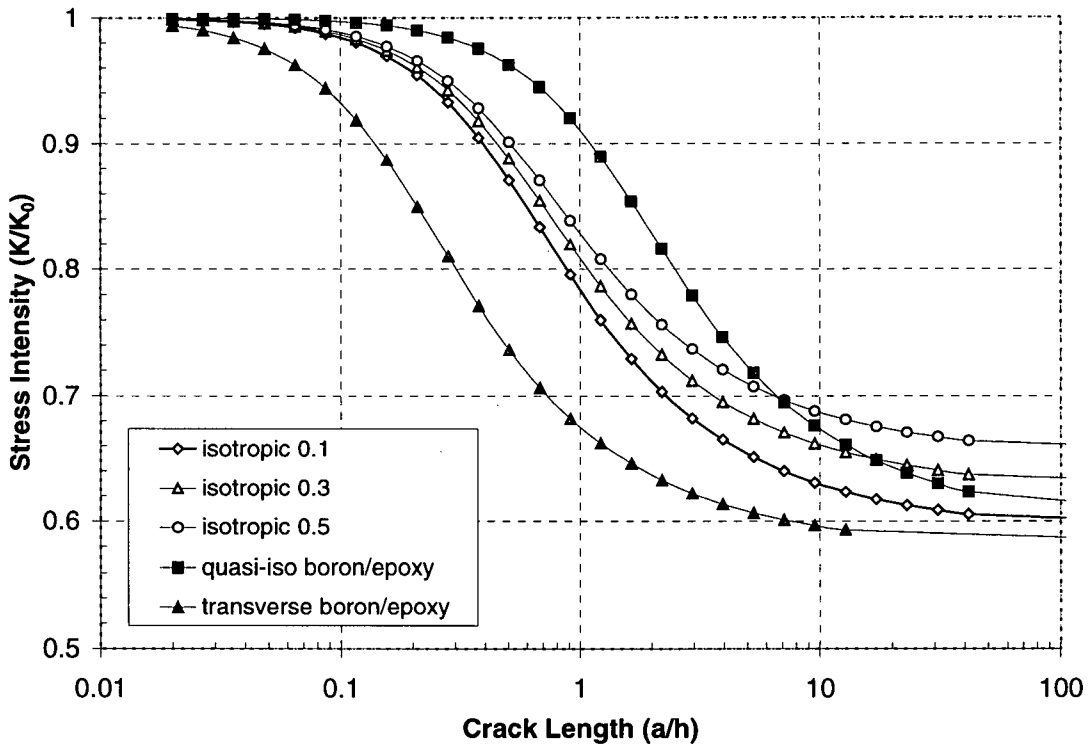

Figure 4-2: Stress intensities for shear deformable plane stress bending

For a very long crack, the stress intensity reaches a limit that can be calculated according to the following argument. Large stress gradients and hence large shear forces only exist near the crack tip. Thus, for a long crack, shear deflections have a vanishing contribution to the deflection well away from the crack tip, and the plane stress plate model gives the correct result. The strain energy release rate for an increment in crack growth is proportional to the work done by the applied stress on the crack face, which may be calculated considering the deflection given by equation (1). For the plane stress

shear-deformable plate, the crack tip is in plane stress, and the limit stress intensity follows.

$$K_\infty = \sqrt{g_\infty E} = \sqrt{\frac{1+\nu}{3+\nu}} K_0 \tag{69}$$

The stress intensity result may be plotted against a normalized crack-length, defined as:

$$c_\psi = \kappa_\psi \sqrt{\frac{3+\nu}{1+\nu}}. \tag{70}$$

Applying the normalized crack length and the long crack limit stress intensity, the difference between the plane stress and the plane stress shear deformable plate solutions for stress intensity (i.e. denoted K_d) collapses onto one curve for all of the tested materials.

$$K_d = \frac{(K/K_0)-1}{\sqrt{\frac{1+\nu}{3+\nu}}-1} \tag{71}$$

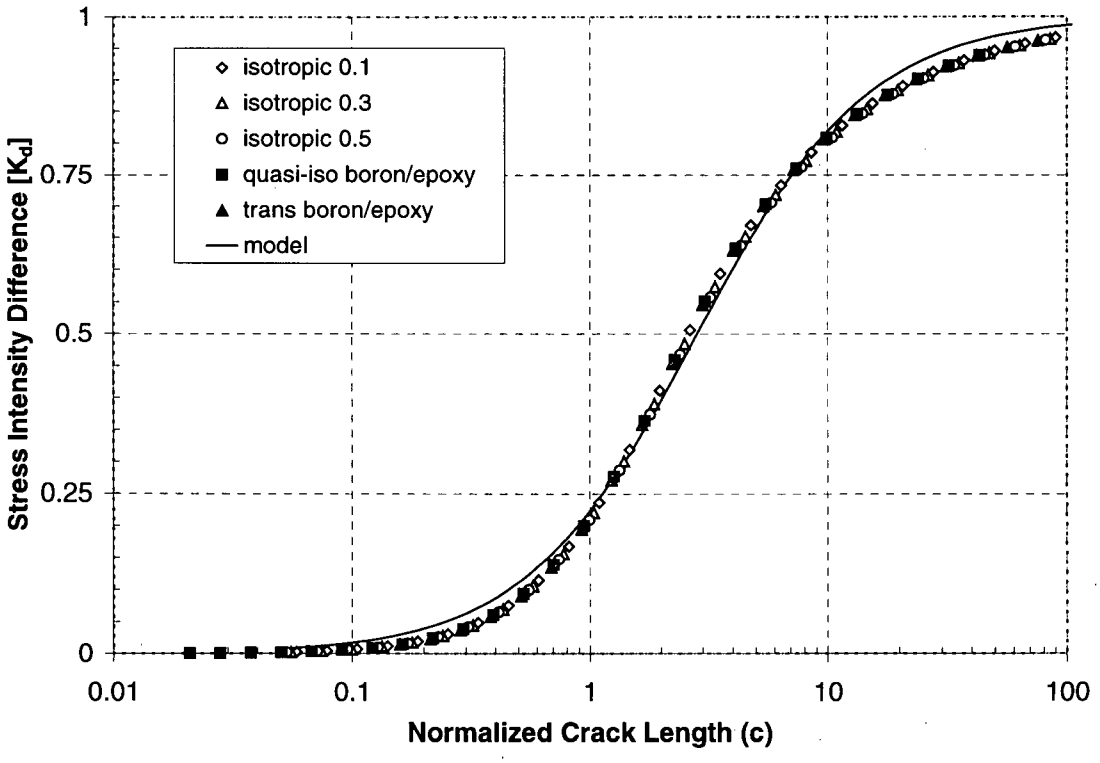

Figure 4-3: Stress intensity difference plotted against normalized crack length

Using a statistical analysis package, equation (72) was fit to K_d. Figure 4-3 shows that this approximate model fits the data reasonably well, with an error not exceeding 2.5% .

$$K_d = \frac{c_\psi^{1.2}}{c_\psi^{1.2} + 3.5} \tag{72}$$

This relationship can be developed into an expression for a geometry correction factor.

$$Y_k = \frac{K}{K_0} = 1 - \left(\frac{c_\psi^{1.2}}{c_\psi^{1.2} + 3.5} \right) \left(1 - \sqrt{\frac{1+\nu}{3+\nu}} \right) \tag{73}$$

Similar results may be found for the crack face displacement at the outer fibre of the plate and the centre of the crack. Figure 4-4 shows this displacement normalized to the result for plane stress bending, $u_0 = 2\sigma_b a / Eh$.

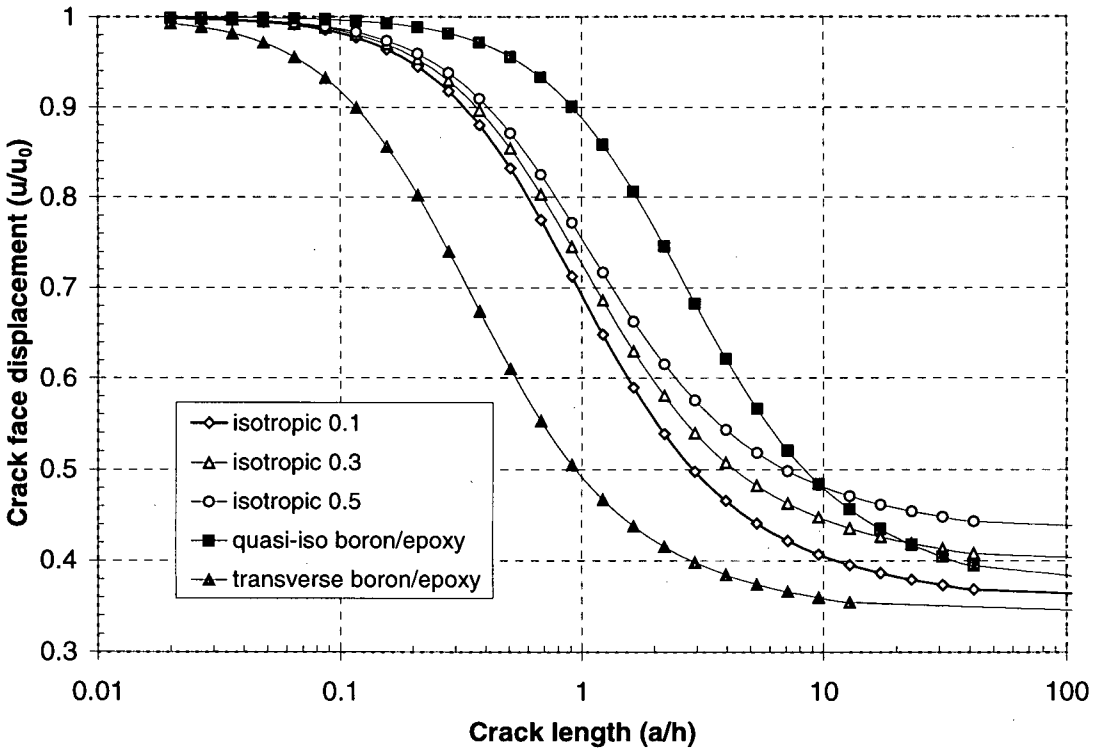

Figure 4-4: Crack face displacements for shear-deformable plane stress bending

The following normalization collapses these results onto one curve (Figure 4-5).

$$u_d = \frac{(u/u_0) - 1}{\frac{1+\nu}{3+\nu} - 1} \tag{74}$$

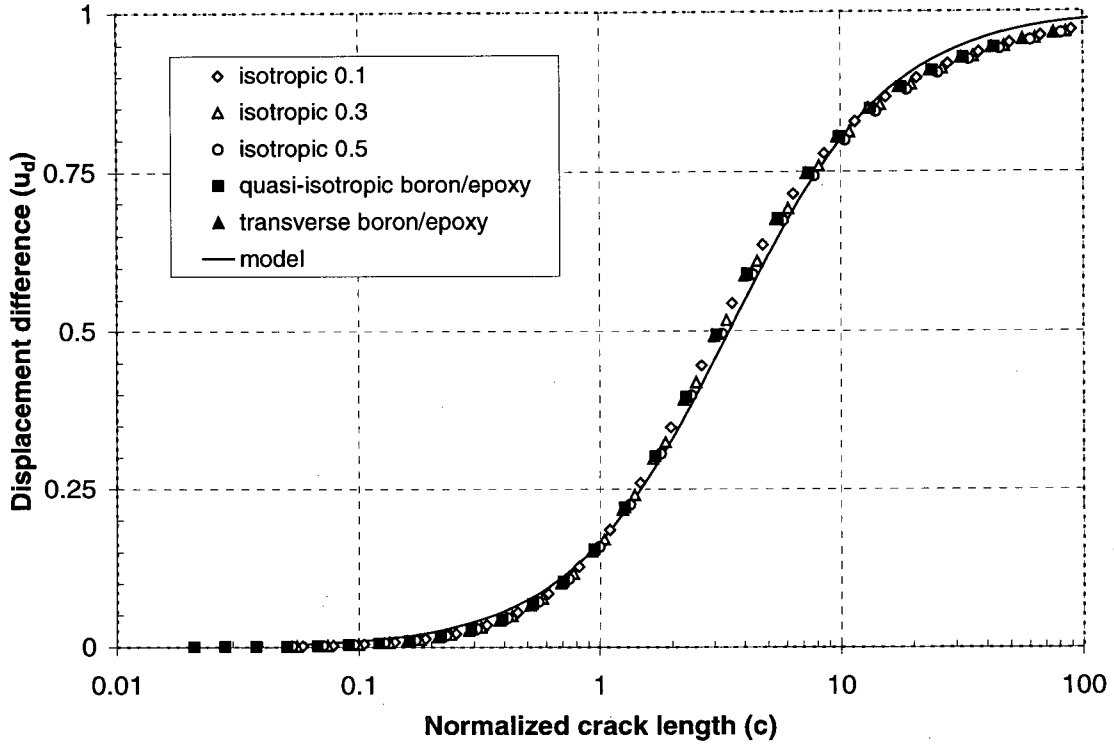

Figure 4-5: Difference in crack face displacements plotted against crack length

Once again, one may develop a simple model that fits the data remarkably well.

$$u_d = \frac{c_\psi^{1.3}}{c_\psi^{1.3} + 5} \tag{75}$$

This relationship can be developed into a geometry correction factor, Y_d.

$$Y_d = \frac{u}{u_0} = 1 - \left(\frac{c_\psi^{1.3}}{c_\psi^{1.3} + 5} \right) \left(1 - \frac{1+\nu}{3+\nu} \right) \tag{76}$$

Very similar results are found for the plane strain shear deformable plate. The limit stress intensity factor, crack length normalization, and geometry correction factors follow.

$$K_0 = \sigma_b \sqrt{\pi a}\,, \qquad u_0 = 2\frac{\sigma_b a\left(1-\eta^2\right)}{E} \tag{77a,b}$$

$$K_\infty = \sqrt{\frac{g_\infty E}{1-\eta^2}} = \sqrt{\frac{1+\nu}{3+\nu-2\eta^2}} K_0, \qquad u_\infty = \left(\frac{1+\nu}{3+\nu-2\eta^2} \right) u_0 \tag{78a,b}$$

$$c_\psi = \kappa_\psi \sqrt{\frac{3+\nu-2\eta^2}{1+\nu}} \tag{79}$$

$$Y_k = \frac{K}{K_0} = 1 - \left(\frac{c^{1.2}}{c^{1.2}+3.5}\right)\left(1 - \sqrt{\frac{1+\nu}{3+\nu-2\eta^2}}\right) \tag{80}$$

$$Y_d = \frac{u}{u_0} = 1 - \left(\frac{c^{1.3}}{c^{1.3}+5}\right)\left(1 - \frac{1+\nu}{3+\nu-2\eta^2}\right) \tag{81}$$

It was found above that the crack tip is effectively in a state of plane strain, and that the crack face displacement away from the crack tip will approach the displacement given by the plane stress model as the crack length gets very large. The developed 8th-order bending formulation allows one to investigate this varying effect of shear and transverse deformations on bending of a cracked plate. Figure 4-6 shows the stress intensity results obtained for the five trial materials analysed. The solid lines are the values obtained from the approximate model that will be developed over the next few pages. The points are data generated by solution of the hyper-singular equation for generalized plane strain plate bending. The nominal solutions follow:

$$K_0 = \sigma_b \sqrt{\pi a}\,, \qquad u_0 = 2\frac{\sigma_b a\left(1-\eta^2\right)}{E} \tag{82}$$

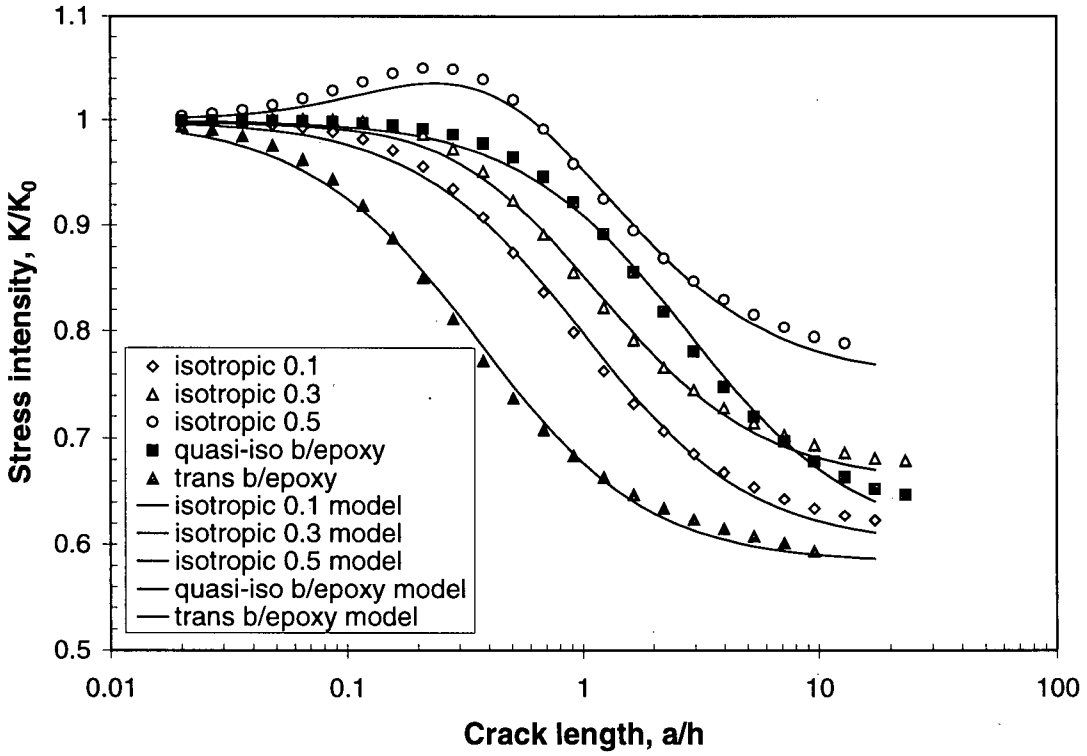

Figure 4-6: Stress intensity for 8th-order plate bending formulation

Transverse deformations (the difference between plane stress and plane strain) result in larger stress intensities, whereas shear deflections decrease the stress intensity and ultimately have a larger effect as crack length increases. The true stress intensity arises as a result of the combination of these effects. For an isotropic plate with a large Poisson's ratio, the increase in stress intensity is large enough and occurs at a short enough crack length that it results in a net increase in stress intensity for cracks somewhat smaller than the thickness of the plate. Figure 4-7 shows similar results for the crack face displacement.

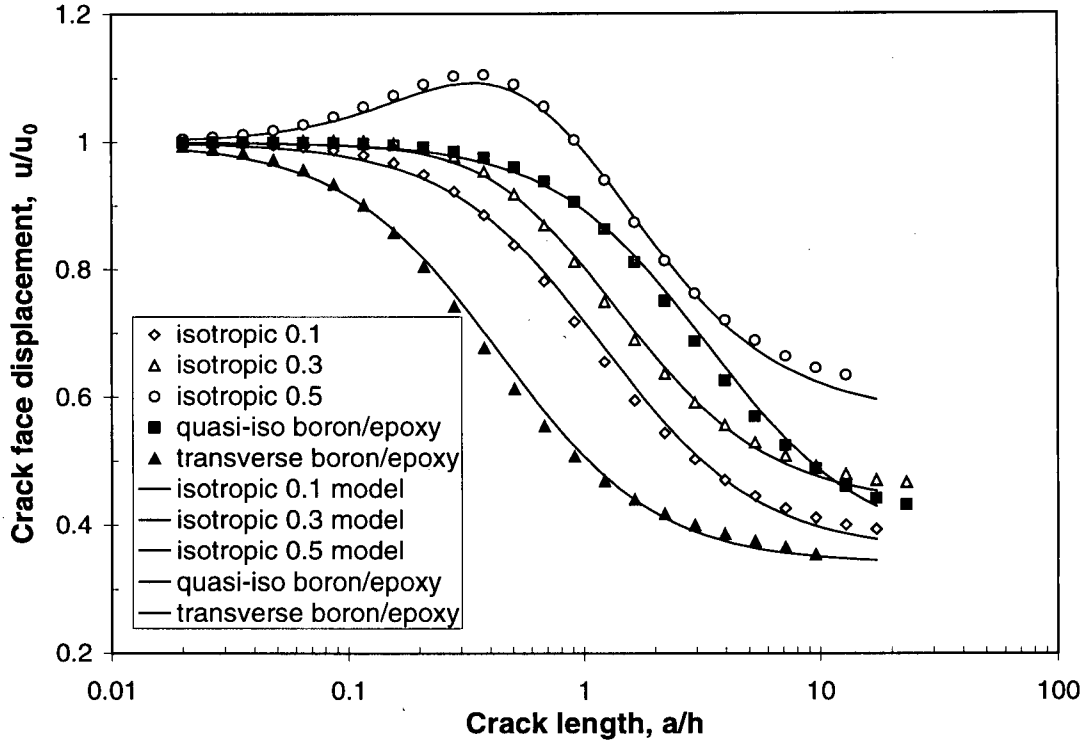

Figure 4-7: Crack face displacement for 8th-order plate bending formulation

No convenient normalization exists to collapse these results, but they do approach a limit as crack length increases. The stress intensity and crack face displacement for a long crack follow.

$$K_\infty = \sqrt{\frac{g_\infty E}{1-\eta^2}} = \sqrt{\frac{1+\nu}{3+\nu}}\frac{K_0}{\sqrt{1-\eta^2}}, \qquad u_\infty = \left(\frac{1+\nu}{3+\nu}\right)\frac{u_0}{1-\eta^2} \tag{83a,b}$$

Figures 4-8 and 4-9 show the generalized plane strain model results normalized to these limit values. The results are plotted against a normalized crack length.

$$c_\psi = \kappa_\psi \sqrt{\frac{3+\nu}{1+\nu}}\sqrt{1-\eta^2} \tag{84}$$

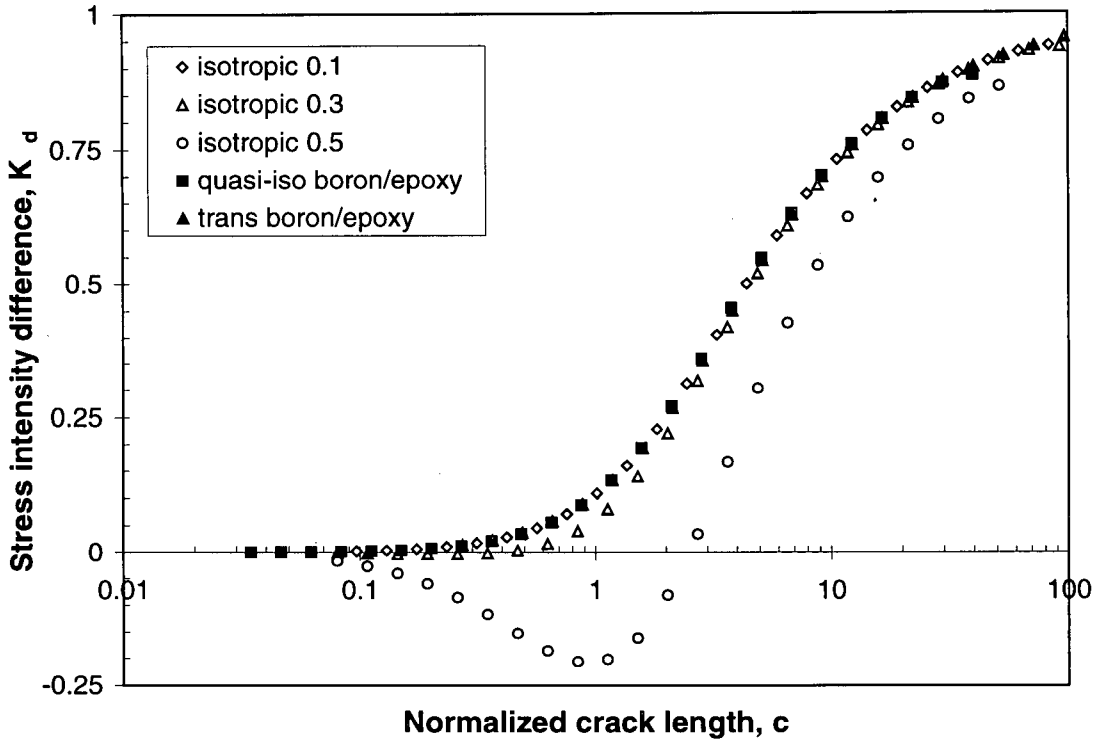

Figure 4-8: Stress intensity difference plotted against normalized crack length

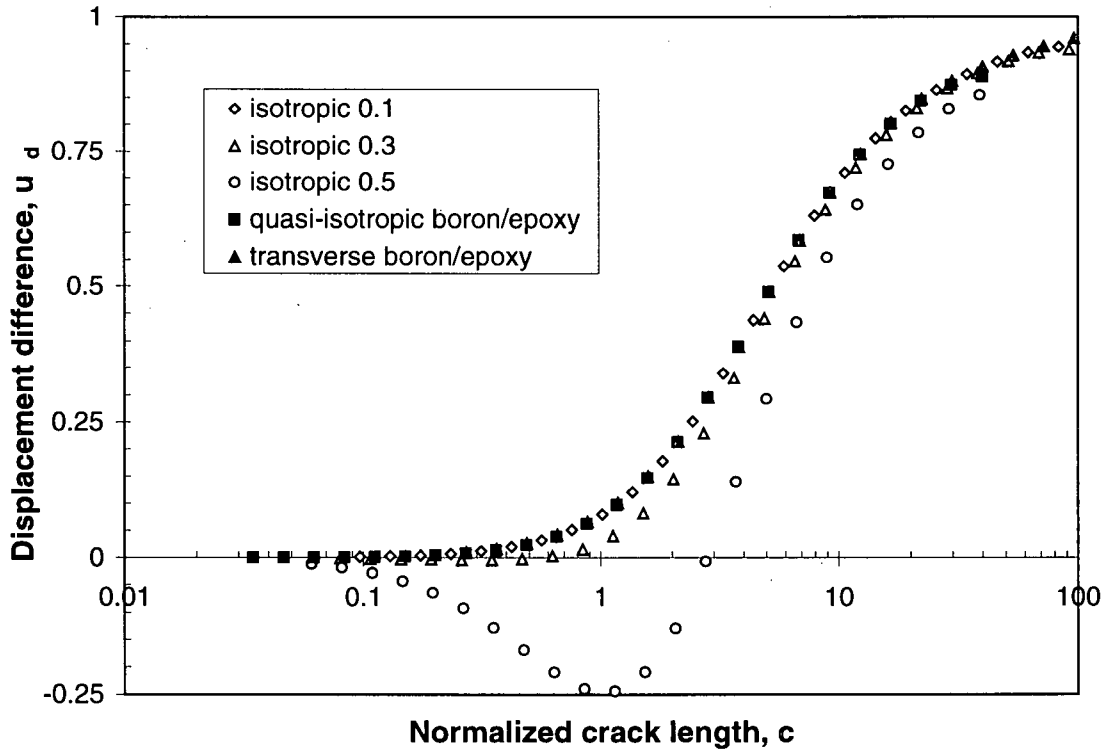

Figure 4-9: Crack face displacement plotted against normalized crack length

Correction factors for the generalized plane strain plate arise by multiplication of the correction factors for shear and transverse deformation. This is indicated by the form of equations (83a,b). For stress intensity, the correction factor is given by the following:

$$Y_k^{\psi} = 1 - \left(\frac{c_{\psi}^{1.2}}{c_{\psi}^{1.2} + 3.5} \right) \left(1 - \sqrt{\frac{1+\nu}{3+\nu}} \right) \tag{85}$$

$$Y_k^{w} = 1 + \left(\frac{c_{w}^{1.5}}{c_{w}^{1.5} + 1.5} \right) \left(1 - \frac{1}{\sqrt{1-\eta^2}} \right) \tag{86}$$

$$K = Y_k^{\psi} Y_k^{w} K_0 \tag{87}$$

A similar result may be found for the crack face displacement as shown below.

$$Y_d^{\psi} = 1 - \left(\frac{c_{\psi}^{1.3}}{c_{\psi}^{1.3} + 5} \right) \left(1 - \frac{1+\nu}{3+\nu} \right) \tag{88}$$

$$Y_d^{w} = 1 + \left(\frac{c_{w}^{1.5}}{c_{w}^{1.5} + 2.5} \right) \left(1 - \frac{1}{1-\eta^2} \right) \tag{89}$$

$$u = Y_d^{\psi} Y_d^{w} u_0 \tag{90}$$

Equations (85) and (88) only account for transverse shear deformations, and hence one should use the normalized crack length given by $c_{\psi} = \kappa_{\psi} \sqrt{\frac{3+\nu}{1+\nu}}$. Note that this should not be confused with the normalization given by equation (84) which includes a term to account for pressurization.

Figures 4-8 and 4-9 show the results obtained by this method. Equations (87) and (90) allow for a simple engineering analysis for bending of cracked finite thickness plates. An additional result is that the crack tip is observed to be in a state of plane strain, regardless of plate thickness. In the next section, we will develop a model for a crack bridged by springs, and use these newly developed correction factors for stress intensity, strain energy release rate, and crack face displacement to develop design equations for bridged cracks in plates of arbitrary thickness.

4.6 Comparison to three dimensional finite element results

In this section, the thickness-averaged stress intensity and the crack face displacement are compared to the results of a three-dimensional finite element model. The ANSYS finite element software package was used to analyse bending of a 20 mm crack in an isotropic plate with a Poisson's ratio of 0.495. The plate thickness was varied from 1 mm

to 64 mm, and both the width and height of a quarter-section of the plate were set at 600 mm, sufficient to minimize the effects finite plate dimensions on the through-thickness averaged bending stress intensity. A coarse model of the plate employs 4 elements through the thickness of the plate, with a finer sub-model employing 10 elements being used in the region of the crack tip. Figure 4-10 shows the planar element distribution for both the coarse model and fine sub-model.

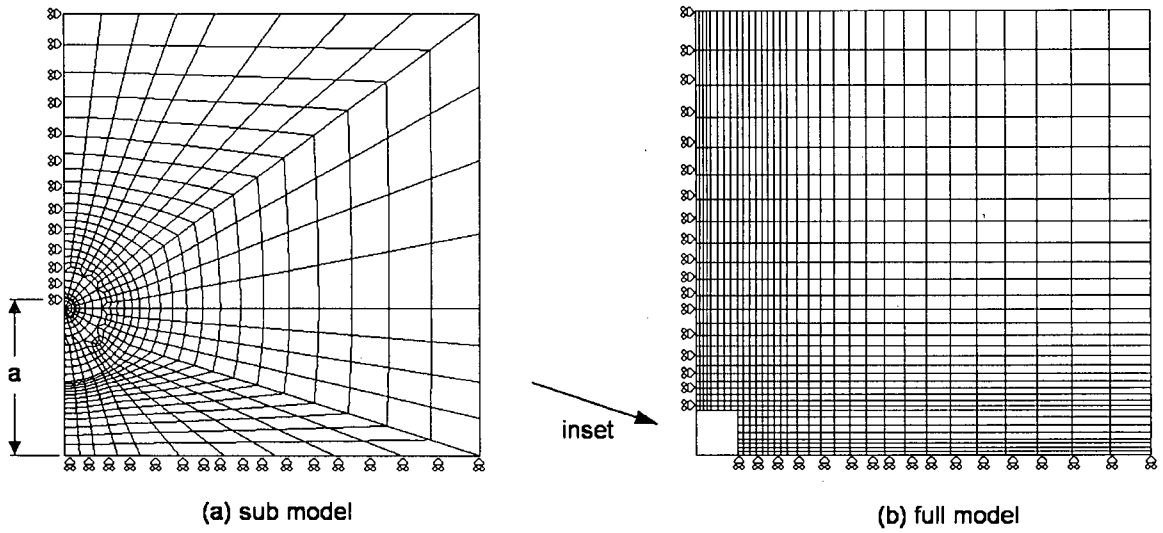

Figure 4-10: Finite element map showing boundary conditions

The crack tip elements are 20-noded solid brick elements collapsed into quarter-point singular wedges. These elements have an edge length of 1.0 mm, which by numerical experimentation was determined to be the smallest element size that could be reasonably used for this crack length. In the numerical experiments, the finite element stress intensity factor results with different sized crack tip elements were compared to the exact plane strain results. The 1 mm crack tip elements lead to an underestimate of the stress intensity of 2.8%. The results presented below were corrected to account for this error. During this verification process, the nodes of the three-dimensional finite element model were constrained in the thickness direction, and a membrane stress was applied to the edge of the model.

The stress intensity factor was calculated by the displacement-interpolation method using the displacement of the crack face nodes nearest the crack tip [10, equation 2]. A stress-based method was not used because of problems with oscillations occurring through the thickness of the plate, a problem that has been observed by others. Note that in the displacement-interpolation method, as is common in the three-dimensional analysis of cracks, the crack tip is assumed to be in a state of plane strain and the stress intensity is calculated based upon the theoretical plane-strain solution of the displacement of the crack faces. The plate-averaged bending stress intensity factor was calculated by least-

squares regression to results for each plane of nodes through the thickness of the plate at the crack tip. In this calculation, the nodes at the surface of the plate were given one half the weighting of interior nodes. Figure 4-11 shows the through-thickness variation of the stress-intensity factor for a selected set of the finite element results.

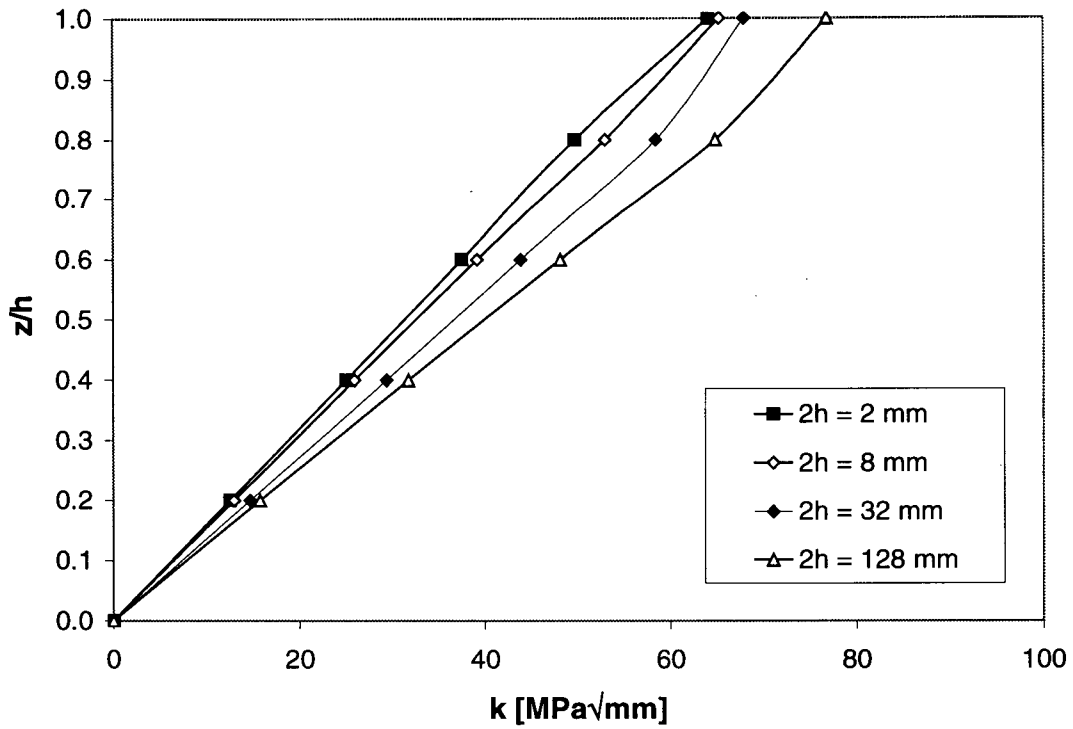

Figure 4-11: Through-thickness variation of the stress intensity

Note that the effect of the free edge is apparent at the edge of the plate, resulting in a somewhat reduced stress intensity factor at this location. This effect has been noted by many others [e.g. 3], and its characterization requires a higher order analysis than that presented in this chapter. It is also well known that at the intersection of the crack and the free edge of the plate, the singular stress field does not observe the classical $1/\sqrt{r}$ singularity except for the special case of $\nu = 0$. Figure 4-12 shows the bending stress intensity factor at the edge of the plate as determined by a least-squared fit to the slope of the through-thickness finite element results. The result is compared to the bending stress intensity factor determined by the geometry correction factors for the sixth- and eighth-order models described above. For comparison, additional displacement-interpolation method finite element results are shown in which the crack tip is assumed to exist in a state of plane stress.

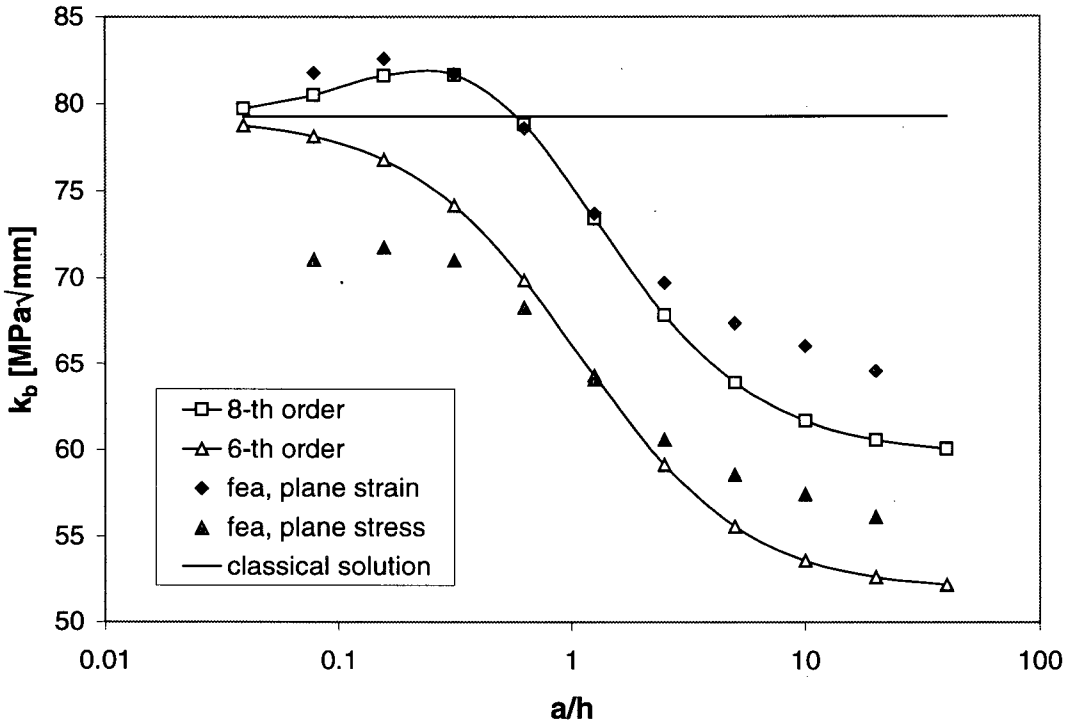

Figure 4-12: Theoretical and finite element bending stress intensities

It is readily apparent that the new eighth-order model provides a significant improvement for short cracks in thick plates. For long cracks in thin plates, the results are more difficult to explain and the accuracy of the proposed model is difficult to verify. When comparing the plane stress based displacement-interpolation finite element method to the 6^{th}-order model results, the finite element model predicts a higher stress intensity. This demonstrates that some degree of local stiffening and load attraction is occurring that is not predicted by the 6-th order models. Comparing the plane strain based finite element results to the 8^{th}-order model, the finite element results are also seen to be higher. The reason for this is that the displacement field predicted using a plane strain model is not identical to that predicted using the 8^{th}-order model except for very short cracks in thick plates, particularly as regards the regular and weakly-singular terms in the generalized plane strain formulation. Here, the finite element results must be seen to be in error, as the 8^{th}-order results represent an upper-bound on the actual stress intensity. The true solution should lie between the plane-stress based finite element results and the results predicted by the 8^{th}-order model.

It is possible to show that, as regards the generalized plane strain plate bending singular stress field, the crack tip is in a state of plane strain regardless of the thickness of the plate. Beginning with either of equations (8d) or (9c), it is possible to show that:

$$P_{zz} = \frac{4h^3 G \nu_z}{3k_w^2 \eta^2} \nabla^4 \overline{w} \tag{91}$$

By the method used to determine $\overline{M}(y)$ in section 4.4, it can also be shown that:

$$P_{zz}(y) = \frac{4h^3 G \nu_z}{3\pi(1-\eta^2)} \int_L \left(\frac{\beta(t)}{(t-y)^2} + \text{weakly singular} + \text{ reg. terms} \right) dt \tag{92}$$

Comparing with (47) and noting that $M_{xx}(y) = -\overline{M}(y)$, the singular stresses at the crack tip are found to obey the following relationship:

$$\frac{P_{zz}}{M_{xx}} = 2\nu_z \tag{93}$$

At the crack tip the singular parts of σ_{xx} and σ_{yy} are equal in magnitude, and accordingly the generalized plane strain model predicts that, in terms of the plate-averaged quantities P_{zz} and M_{xx}, the singular stresses at the crack tip exist in a state of plane strain. This is only true as regards the singular stresses in a small region close to the crack tip, and is in accord with the exact eigenfunction expansion results of Hartranft and Sih [11].

Significant differences between the finite element and the generalized plane strain plate bending model results were noted above which would not be expected if the crack tip were in a state of pure plane strain. It is possible that the finite element method used is sensitive to the lower-order terms. It is also possible that for very thin plates, the boundary layer at the plate edges begins to become large when compared to the dimensions of the singular region at the crack tip and the region dominated by purely plane strain conditions decreases in size. For the purposes of this chapter, it is unfortunate that the standard finite element approaches to stress intensity factor determination are built upon the assumption of the validity of the plane stress or plane strain states (i.e. classical models) and that a significant amount of engineering judgement is required in order to interpret the results.

Figure 4-13 shows a similar improvement in the prediction of the crack face displacement at the centre of the crack. Note that the results are very good for both short cracks in thick plates and long cracks in thin plates. Here, the results for the deflection of the crack face at the outer fibre of the plate are also fitted to the slope of the finite element results. Unlike the determination of the stress intensity factor, these results are not subject to interpretation.

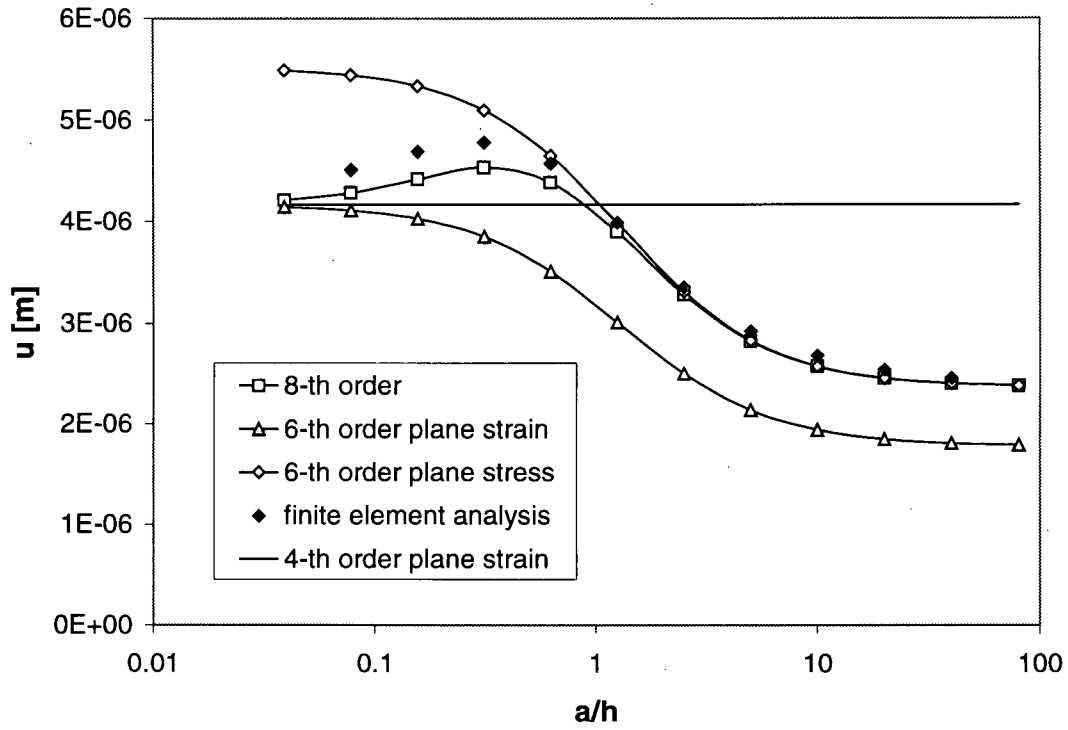

Figure 4-13: Theoretical and finite element model crack face deflections

4.7 Bending of reinforced cracked plates

Here we consider the action of springs bridging the crack, developing a line-spring model for a generalized plane strain plate under bending. Figure 4-14 shows a cracked plate in bending reinforced by springs. The goal here is to determine the bending stress intensity for the reinforced crack and to calculate the moment carried by the springs bridging the crack, such that the strength of the plate can be determined.

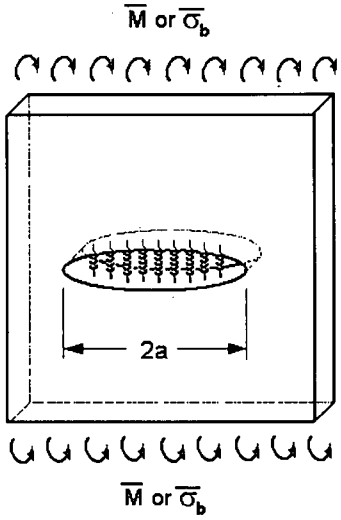

Figure 4-14: A bending crack reinforced by springs

To account for crack bridging, equation (59) may be modified to include a stress due to the reinforcing springs, which acts to restrict the motion of the crack faces. Here, k_s is the line-spring stiffness, or stress generated by the springs on the outer fibre of the plate per unit deflection of the crack surfaces. This definition of the bending spring stiffness leads to line-spring equations with a similar form to that found by Clark and Romilly for plate extension [6].

$$\overline{\sigma_b}(s) - ak_s u(s) = \frac{-E}{2\pi(1-\eta^2)} \int_{-1}^{1} u(r) \left(\frac{1}{(r-s)^2} + \frac{\kappa_\psi^2}{2} \frac{1-\eta^2}{1+\nu} L_\psi(\kappa_\psi |r-s|) + \kappa_w^2 \eta^2 L(\kappa_w |r-s|) \right) dr \tag{94}$$

Expanding $u(r)$ and choosing a set of collocation points, equation (94) will reduce to the linear system $\overline{\sigma_b} = A\overline{g}$. Here, A is expressed as follows, and includes a term to account for the springs.

$$A_{i,j} = \frac{E}{1-\eta^2} \left(\frac{i+1}{2} U_j(s_i) - \frac{\kappa_\psi^2}{4\pi} \left(\frac{1-\eta^2}{1+\nu} \right) L_{i,j}^{\psi} - \frac{\kappa_w^2 \eta^2}{2\pi} L_{i,j}^{w} \right) + ak_s W(s_i) U_j(s_i) \tag{95}$$

The generalized plane strain plate bending problem may now be solved for the case of a cracked plate bridged by springs. The stress intensity may be calculated from the expansion coefficients using equation (68). Figure 4-15 shows results for a cracked isotropic plate with $\sigma_b = 10\ MPa$, $\upsilon = 0.5$ and $E = 72.4\ GPa$. The results are plotted for a wide range of spring stiffnesses, as shown in the legend.

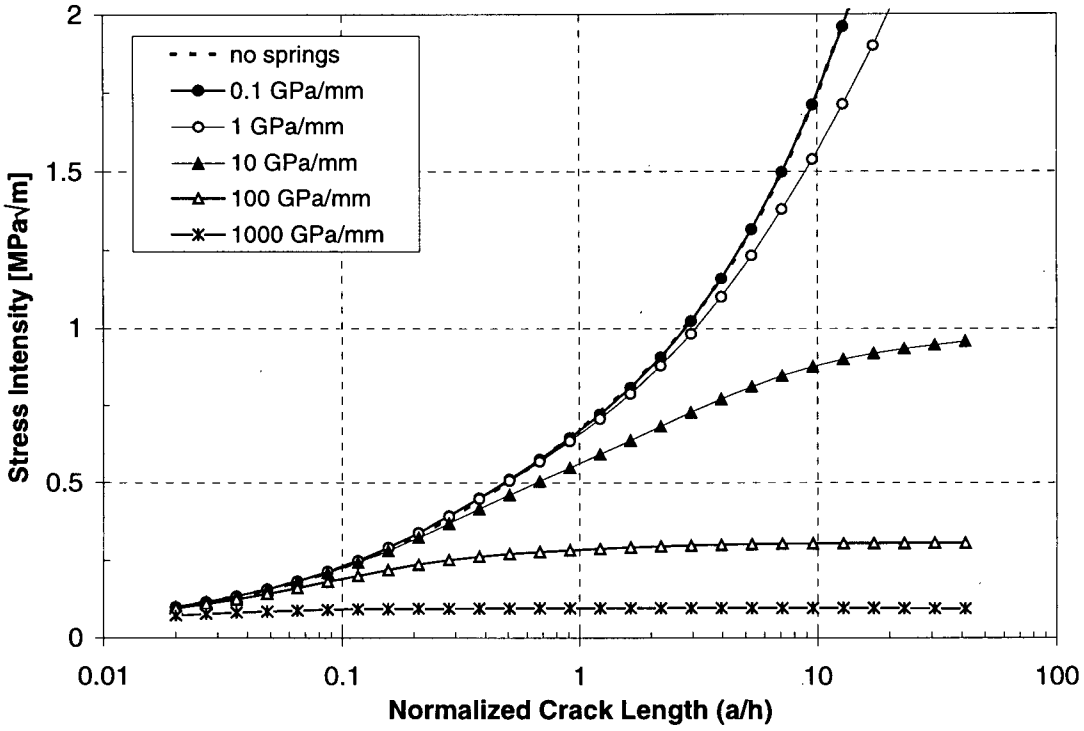

Figure 4-15: Stress intensity from the line spring model

As was the case for plate extension, it is apparent that stiffer springs lead to lower stress intensities, reaching a limit for long cracks. Applying the method of Rose [12,13], one may analytically determine the limit strain energy release rate for a very long crack. In this case, we examine the strain energy release rate at the outer fibre of the plate. In the limit of a very long crack reinforced by springs, the energy available for crack growth is given solely by considering the energy balance in the springs bridging the crack under the applied (nominal) bending stresses. The strain energy release rate may be expressed as follows:

$$G_\infty = 2\int_0^u \sigma_b \, dx = 2\int_0^u k_s x \, dx = k_s u^2 = \frac{\sigma_b^2}{k_s} \tag{96}$$

The equations governing bending are identical to those found for extension. As the crack tip has been shown to exist in a state of plane strain, the limit stress intensity may now be found.

$$K_\infty = \sqrt{\frac{G_\infty E}{1-\eta^2}} = \sigma_b \sqrt{\frac{E}{k_s(1-\eta^2)}} \tag{97}$$

An effective crack length may also be defined, including factors to correct for plate geometry.

$$a_{eff} = \frac{E}{(Y_k^w Y_k^\psi)^2 \pi \; k_s (1-\eta^2)} \tag{98}$$

Figure 16 shows the generalized plane strain results normalised with respect to these two theoretical limits. Note that as the crack becomes longer, the stress intensity limit is obeyed. Based on equation 97, the use of the 6th-order Riessner formulation would lead to an error in the determination of the long-crack limit stress intensity analogous to the difference between plane stress and plane strain, i.e. on the order of a 5% to 10% increase for most metals.

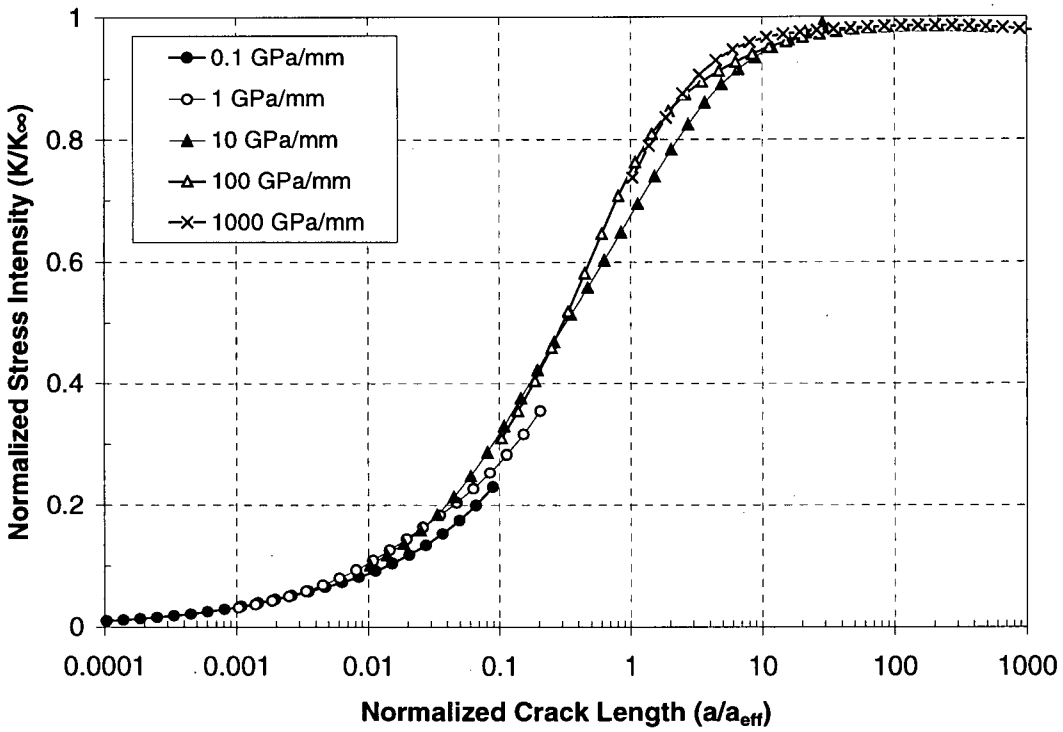

Figure 4-16: Normalized stress intensity plotted against crack length

It is also possible to define an interpolation for stress intensity between the limit states of a very short and a very long crack. For a short crack one may use equation (87), developed for an un-reinforced crack. In the long crack limit, the stress intensity will approach that determined by equation (97). The stress intensity for an arbitrary crack length follows.

$$K_r = Y_k^w Y_k^\psi \sigma_b \sqrt{\frac{\pi \; a a_{eff}}{a + a_{eff}}} \tag{99}$$

From equations (98) and (99), the transverse shear correction factor (based on the 6th-order models) will have a large role for moderately short cracks reinforced by relatively weak springs. In this case, based upon the previous analysis of an unreinforced crack, the

inclusion of the correction factor may improve the accuracy of the interpolation model by as much as 60%.

The effectiveness of the interpolation model for bending may be tested against the line spring model. Figure 4-17 compares the stress intensity predicted by equation (99) normalized with respect to values determined by numerical analysis. The interpolation model is observed to lead- to results that are low by up to 5%, a difference that has also been found for extension of reinforced plates. This over-riding trend in the error is principally due to the form of the interpolation model, but other trends may be noted that result from the interaction of the geometry correction factors and the numerical line-spring model. For long cracks, the numerical model cannot accurately model the crack tip and tends to over-predict the stress intensity. At the same time, shear effects (modelled by the shear correction factor) act to reduce the stress intensity at the crack tip. The observed oscillations are due to the interaction between these effects.

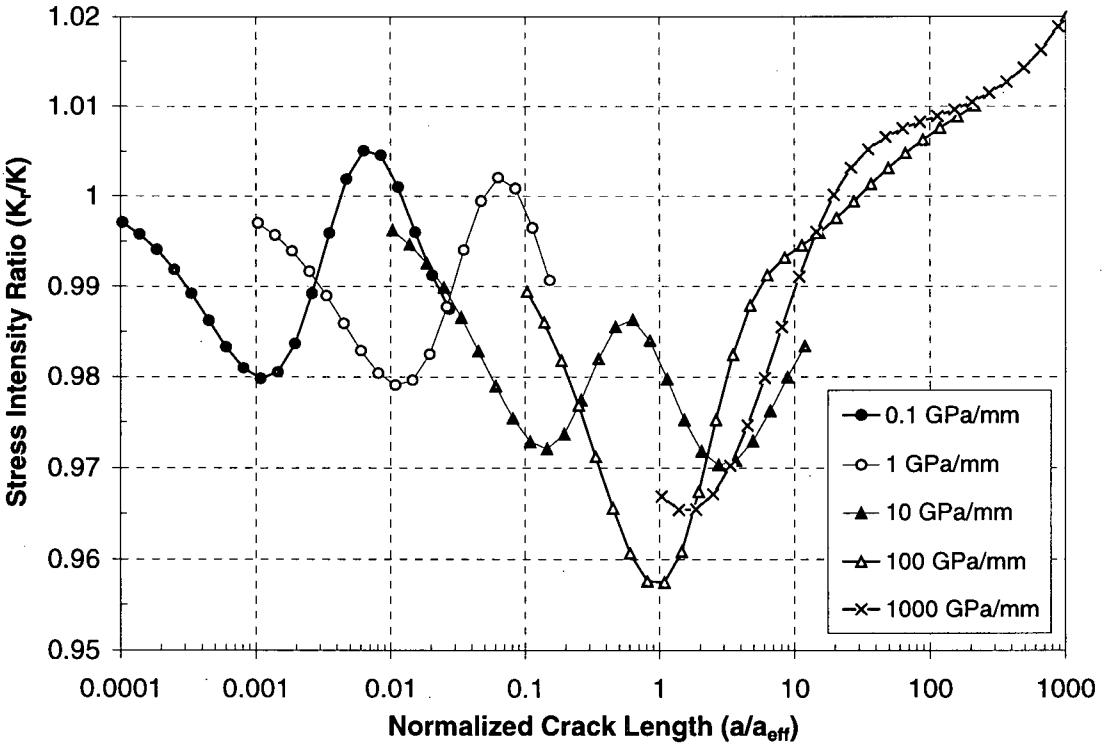

Figure 4-17: Stress intensity predicted by line-spring and interpolation models

One may apply the same methods to the crack face displacements. Figure 4-18 shows crack-face displacements from the line-spring model. For weak springs, they approach the nominal solution for an un-reinforced crack. The long crack limit is evident for cracks bridged by stiff springs.

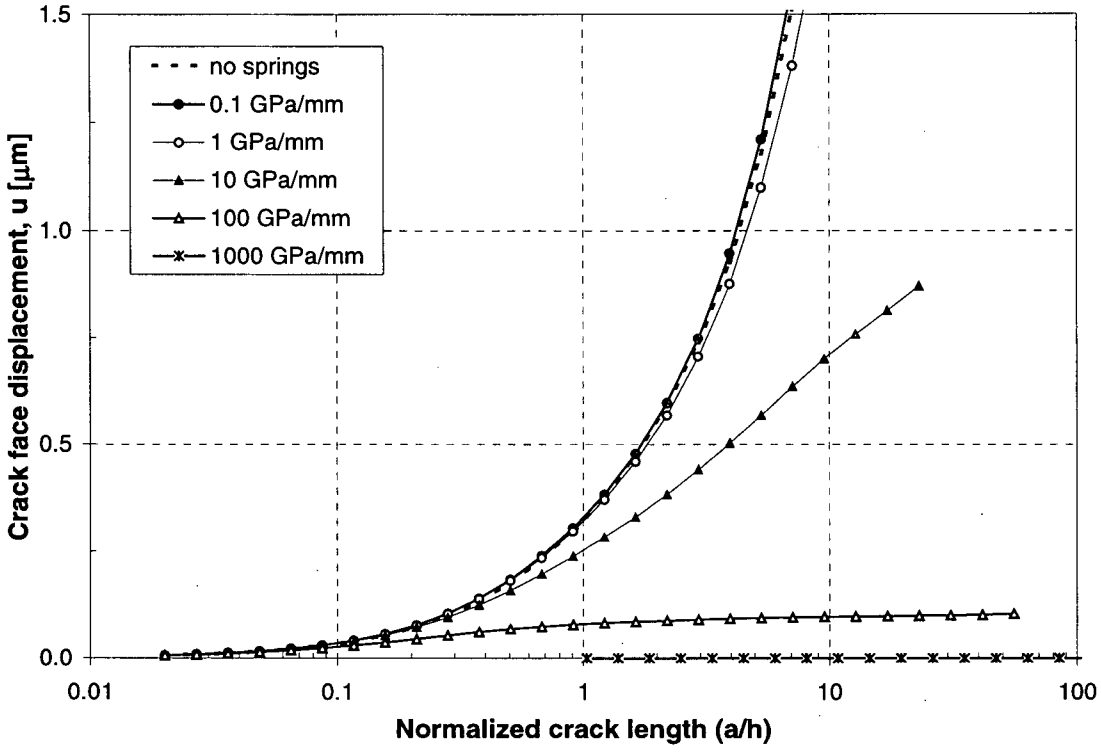

Figure 4-18: Crack face displacement for various spring stiffnesses

The long-crack limit crack face deflection is $u_\infty = \sigma_b / k_s$. The displacement for short cracks is given by equation (90). A simple interpolation between these limits is given by:

$$u_r = \frac{u_\infty u_0}{u_0 + u_\infty} = \sigma_b \frac{\left(2Y_d^w Y_d^\psi (1-\eta^2) a/E\right)(1/k_s)}{\left(2Y_d^w Y_d^\psi (1-\eta^2) a/E\right) + (1/k_s)} = \frac{\sigma_b}{k_s + E/\left(2Y_d^w Y_d^\psi (1-\eta^2) a\right)} \qquad (100)$$

Figure 4-19 shows the ratio of the interpolation model and line-spring model results for crack displacement. This simple interpolation results in an error not exceeding 7%.

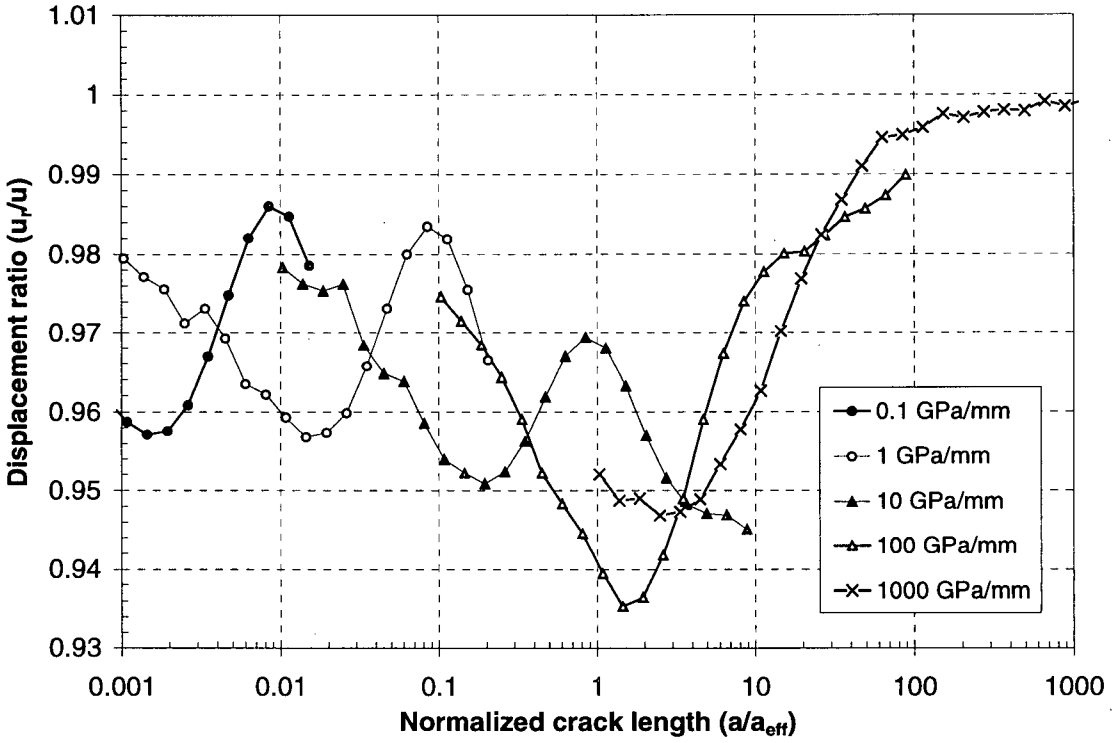

Figure 4-19: Crack face displacement from line-spring and interpolation models

The maximum moment carried by the springs is given by equation (101).

$$M_{xx} = \frac{2}{3} h^3 k_s u_r \tag{101}$$

Knowledge of this moment can be used to predict rupture or fatigue degradation of the spring materials (e.g. patch repair materials) bridging the crack faces.

4.8 Discussion

Similar to the case for extension of cracked plates, for plates in bending the crack tip is subject to very large stress gradients that induce pressurization of the plate near the crack. As for extension, this pressurization stiffens the plate locally in the region of the crack tip, effectively increasing the local stresses and reducing the overall crack face deflections from what would be predicted by models that neglect the build-up of transverse stresses. Different from the case of extension of cracked plates, in the solution of plate bending problems, the transverse shear stresses enter into the equilibrium equations and are accompanied by shear deflections. This additional set of loads and deflections requires the adoption of a higher-order plate model to obtain an accurate solution, particularly for thick plates and plates experiencing large stress gradients. The 8^{th}-order plate model developed in this chapter is the simplest possible model that can

include both of these effects, and has been used to develop a line-spring model which may now be used anywhere that line-spring models based on classical plate models have been applied, for example in the analysis of bonded composite repairs, surface cracks, crack tip plasticity, and crack closure.

The stresses at the base of a crack in bending, expressed in terms of the moment stress resultant, have been shown to exist in generalized plane strain conditions. This study has developed a set of standard engineering geometry correction factors to describe the effects of plate thickness and transverse material properties on the stress intensity and crack face deflection, allowing for a simple and accurate analysis of through-cracks in finite thickness plates. The correction factors account for transverse shear deflections and the effects of transverse stresses caused by curvatures in the stress field in the plane of the plate. This is an important phenomenon in the analysis of cracks, which contain very large stress gradients. These results are of particular significance for the analysis of bridged cracks, where strain energy release rate arguments are used to determine the stress intensity at the reinforced crack tip, and an appropriate conversion factor is required to determine the stress intensity. These results are in accord with the exact eigenfunction expansion results of Hartranft and Sih [11] and Hartranft [14], who found that the through-thickness stresses are singular and that plane strain conditions should exist at the crack tip, a property which is not possessed by many other approximate theories. Lower-order plate bending theories are also not capable of modelling the local 'stiffening' effect caused by this region of generalized plane strain, and the authors see the 8^{th}-order model as an excellent engineering approach due to its relative ease of application and the ability to capture the relevant phenomena in a conservative but reasonably accurate manner.

As for extension, the long-crack limit stress intensity factor and the interpolation model developed by Rose offer a very effective method for the analysis of bending of bridged cracks. The interpolation model for the stress intensity in a repaired crack has been shown to be accurate within 5%, a similar result to that found for extension of reinforced cracks [15,16]. This error is principally attributed to the approximate nature of the interpolation model, and not to the correction factors introduced in this chapter. At its worst, the interpolation model result for the crack face deflection is low by approximately 7%, a difference which should be accounted for when using the model to predict rupture or fatigue degradation of the spring materials bridging the crack.

It is important to note that this study has not addressed the subject of crack closure and crack face interaction, a limitation that is general to any basic cracked-plate plate bending theory. It is widely known that such an interaction will act to reduce the bending stress intensity factor at the tension side of the plate [e.g. 17]. The study of this effect requires the superposition of extensional and bending models for cracked plates, and nonlinear

analysis is required to determine the area of contact of the crack surfaces. Several approaches exist to address this problem, including the use of line-spring models [8]. The authors have applied the 8^{th}-order plate bending model to the analysis of linear coupled bending and extension of reinforced cracks in a recently accepted paper [15] that could easily be extended to such a nonlinear analysis.

4.9 Concluding remarks

The authors have developed a high-order plate model and by the method of integral transforms have developed a hyper-singular integral equation useful for the bending analysis of plates containing cracks. The model allows for the inclusion of both shear deformations of the plate and pressurization of the crack tip under the extreme stress gradients induced by the presence of a crack. The resulting line-spring model and engineering analysis equations for through-cracks and reinforced cracks are applicable to a wide range of plate fracture problems and provide a significant improvement in accuracy over models based on the classical plate models, and thus should be should be widely adopted.

4.10 References

[1] Reissner E. The effect of transverse shear deformation on the bending of elastic plates. Journal of Applied Mechanics 12, 1945, A69-77

[2] Mindlin R.D. Influence of rotary inertia and shear on flexural motions of isotropic, elastic plates. Journal of Applied Mechanics 18, 1951, 31-38

[3] Sih G.C. A review of the three-dimensional stress problem for a cracked plate, International Journal of Fracture 7, 1971, 39-61

[4] Kotousov A. and Wang C.H. Fundamental solutions for the generalised plane strain theory. International Journal of Engineering Science 40, 2002, 1775-1790

[5] Kotousov A. and Wang C.H. A generalized plane strain theory for transversally isotropic plates. Acta Mechanica 161, 2003, 53-64

[6] Clark R.J. and Romilly D.P. Reinforced cracks in transversally isotropic generalized pane strain plates. To be submitted to: Engineering Fracture Mechanics.

[7] Joseph P.F. and Erdogan F. Plates and shells containing a surface crack under general loading conditions. NASA contractor report 178232, NASA Langley Research Centre, 1987.

[8] Joseph P.F. and Erdogan F. Surface crack problems in plates. International Journal of Fracture 41, 1989, 105-131

[9] Wang C.H. and Rose L.R.F. A crack bridging model for bonded plates subjected to tension and bending. International Journal of Solids and Structures 36, 1999, 1985-201

[10] He W.J., Lin Y., and Ding H.J. A three-dimensional formula for determining stress intensity factors in finite element analysis of cracked bodies. Engineering Fracture Mechanics 57, 1997, 409-415

[11] Hartranft R.J. and Sih G.C. The use of eigenfunction expansions in the general solution of three-dimensional crack problems. Journal of mathematics and mechanics. 19, 1969, 123-138.

[12] Rose L.R.F. A cracked plate repaired by bonded reinforcements. International Journal of Fracture 18, 1982, 135-144

[13] Rose L.R.F. Theoretical Analysis of crack patching. In: A.A. Baker and R. Jones (eds.) Bonded Repair of Aircraft Structures. Martinus Nijhoff, 1988, 77-105

[14] Hartranft R.J. Improved approximate theories of the bending and extension of flat plates. In: G.C. Sih (ed.), Mechanics of Facture 3 - Plates and Shells with Cracks, Noordhoff, 1977, 45-83.

[15] Clark R.J. and Romilly D.P. Linear coupled bending and extension of an unbalanced bonded repair. Accepted by: International Journal of Solids and Structures, 2006.

[16] Clark R.J. and Romilly D.P. Fatigue damage prediction for bonded composite repairs applied to metallic aircraft structures. SAE Transactions - Journal of Aerospace, paper # 2001-01-26, 2001

[17] Liu R., Zhang T., Wu X.J., Wang C.H. Determination of stress intensity factors for a cracked shell under bending with improved shell theories. Journal of Aerospace Engineering, ASCE, 19(1), 2006, 21-28

Chapter 5: Linear coupled bending and extension of a bonded repair*

R.J. Clark and D.P. Romilly

University of British Columbia Department of Mechanical Engineering

5.1 Introduction

An unbalanced repair is a composite patch bonded to one side of a cracked structure for the purpose of preventing or reducing damage growth in the substrate. A single-sided repair offsets the load path within the structure, inducing out-of-plane bending. This bending increases the stress intensity of the underlying crack and causes adhesive peel stresses and bending of the repair which can, relative to a repair that is restrained against bending, lead to early failure. In this chapter the authors correct the analysis of Wang and Rose [1], developed by using an energy analysis of a single-sided or unbalanced repair applied to a very long crack, to comply with Maxwell's reciprocal theorem and to account for transverse normal and shear stresses at the crack tip and the accompanying shear deflections. The authors then develop closed-form equations useful for bonded composite repair design and damage tolerance assessment of cracks of arbitrary length by developing a new method for interpolation between this long-crack limit and a short-crack limit based on the stress intensity and crack face displacements for an unreinforced crack. The interpolation method is then tested against an advanced line-spring model that has been created by using a 6^{th} order generalized plane strain plate formulation in extension and a new 8^{th} order formulation in bending, thus allowing for the inclusion of transverse shear and normal stresses. The closed-form equations are found to be accurate when compared to the line-spring model, and to provide reasonable results when compared to a three-dimensional finite element model of a bonded repair. Inaccuracies are shown to exist principally in the determination of the nominal stresses in the vicinity of the crack.

A bonded composite repair consists of a filamentary composite reinforcement that is bonded to a damaged or weakened structure to reduce stresses and prevent or reduce continuing damage growth. Such repairs are an effective method by which to extend the

---

* A version of this chapter has been published. R.J. Clark, D.P. Romilly, "Linear coupled bending and extension of an unbalanced bonded repair", International Journal of Solids and Structures, v 44, 2007, p 3156–3176.

life of aircraft structures, offering advantages in effectiveness, weight, profile, application time, cost, and inspectability when compared to mechanically fastened repairs. Bonded composite repairs have seen significant use in military applications but limited use in civil aviation, primarily due to certification issues. Repairs to primary or structurally significant aircraft structures are required to meet Damage Tolerance (DT) requirements, which are outlined in FAA Circular 25.571-1C (1998), effectively requiring an assessment of the residual life of the part and the development of an inspection schedule suitable for the detection of damage before the failure of the structure. Accordingly, models are required for the prediction of the fatigue life and residual strength of repaired structures. In this chapter, the authors develop closed-form equations for the analysis of an unbalanced repair, where the patch is bonded to only one side of a cracked structure, and induces out-of-plane bending by offsetting the load path. Bending increases the stress intensity in the underlying crack and causes adhesive peel stresses and bending of the repair that, if not properly accounted for in the analysis, could lead to premature failure.

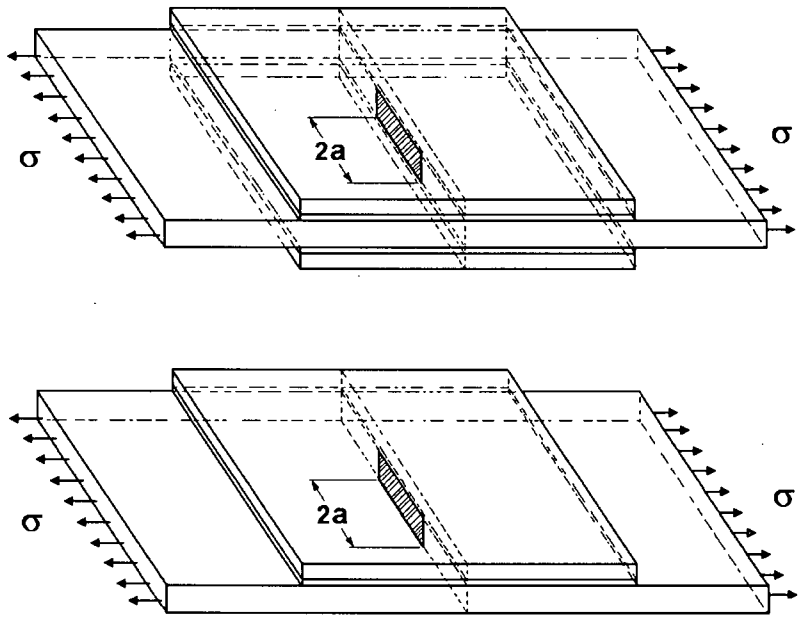

Figure 5-1: Repair configurations: balanced (top) and unbalanced (bottom)

A significant body of work exists for the analysis of bonded composite repairs, which can be separated into two broad classes, balanced or double-sided repairs and unbalanced or single-sided repairs (Figure 5-1). Closed-form equations useful for composite repair design and damage tolerance analysis have existed for some time for balanced repairs, in which patches are applied to both sides of a cracked plate or in which the repaired plate exhibits a large degree of bending restraint due to underlying structure. The most significant contributions have been from Rose [2-4], who established an upper limit on

the stress intensity for a very long reinforced crack by means of an energy analysis. By using this long-crack solution as an upper limit and the nominal, or unreinforced solution as a short-crack limit, Rose developed a very effective interpolation for cracks of arbitrary length. Wang and Rose [5] have demonstrated that for extension of reinforced plates the long-crack limit needs to be modified to account for the plane strain conditions present at the crack tip. Clark and Romilly [6] have developed a generalized plane strain line-spring model for plate extension and developed a set of geometry correction factors for finite thickness plates which allows for accurate determination of both the stress intensity and crack opening displacement in balanced repairs. The closed-form equations of Rose have been adapted to the analysis of repairs with finite planar dimensions via the inclusion analogy [2], with significant shear lag in the composite patch [7,8], for partially disbonded repairs [9,10], and for tapered repairs [11]. These closed-form methods allow for simplified damage tolerance analysis, reliability assessment, and design optimization of repairs.

There is much interest in the application of unbalanced repairs, as often only one face of a structure is exposed. Often the interior structure of the aircraft does not provide restraint against bending, and application of the repair will result in significant out-of plane loading due to a shift in the neutral axis. For balanced repairs, failure typically occurs by progressive cracking and adhesive disbonding. Composite fibre and matrix failures are rare except in the presence of compressive loading or bending induced by geometric details or lack of restraint. For unbalanced repairs, composite failure mechanisms such as interply delamination and fracture are more likely to occur in conjunction with cracking and disbonding. Jones, Chiu, and Smith [12] have reviewed the failure modes and damage locations observed in both laboratory and in-service military use of bonded repairs. They conclude that, besides substrate cracking and cohesive disbonding, damage tolerance assessment should include fibre failure, adhesive failure, cohesive failure at the patch-adhesive interface, adhesive failure at the adhesive-substrate interface, plus inter-laminar failure and delamination. These aspects are reflected in the FAA circular, which requires the assessment of the repaired structure, adhesive, and composite repair, including impact damage, inter-ply delamination, and adhesive disbonding. To streamline the design and certification of repairs, particularly single-sided repairs, closed-form methods are needed to assess the effects of bending on the rate of failure of the repaired structure, but perhaps more importantly, methods are required to assess the life and strength of the repair itself under bending and transverse normal (peel) stresses.

Many studies have been carried out in an effort to characterize the effect of bending. The first result is due to Ratwani [13] who developed a bending correction factor by adding the bending stress expected in the outer fibre of the plate to the nominal stresses in the crack plane, allowing the results for a symmetric repair to be applied to a one-sided

repair. Early finite element studies by Jones [e.g. 7,8] set out the framework by which two-dimensional finite element models of plates can be extended to the analysis of adhesively bonded layered plates. Several studies have focussed on producing numerical methods such as three-layer finite element analyses [14,15], boundary element methods [16], or automated damage growth in fully three-dimensional models [e.g. 17] in order to predict the life of a repaired structure. The focus of this chapter is the development of closed-form methods that are easily adaptable to damage tolerance or reliability analysis and design optimization. As for the analysis of balanced repairs, Australian researchers have led the field in the development of closed-form methods. Rose [4] developed a bending correction factor for the long-crack case that includes geometrically nonlinear (stress-stiffening) effects by considering the adhesive as providing a rigid bond and applying an energy analysis to determine the strain energy release rate for a very long crack. More recently, Wang and Rose [18] have developed an expression for the total strain energy release rate for a long crack bridged by coupled bending and extensional springs, and a method for separation of this strain energy release rate into the membrane and bending stress intensity components. Unfortunately, by comparison to a three-dimensional finite element analysis, they concluded that their energy method significantly over-predicts the bending stress intensity and thus was not valid or useful for the design of a repair. Wang, Rose, and Calinan [19] went on to develop an analytical approach for separation of the strain energy release rate (expressed as the root-mean-square stress intensity) by assuming that the bending and membrane components act in the same ratio regardless of the length of the crack. By considering the short-crack limit, where the springs bridging the crack faces do not provide any constraint to the motion of the crack faces, the membrane and bending stress intensity components are linearly related to the membrane and bending stresses in the substrate in the plane of the crack, and this ratio could easily be determined. They continued by developing an interpolation between the long-and short-crack limit solutions for the root-mean-square stress intensity, allowing the membrane and bending stress intensity to be calculated for a crack of arbitrary length. Unfortunately, as this approach assumes that the membrane and bending stress intensities act in the same proportion for any crack length, the validity of the approach must be assessed on a case-by-case basis, particularly if it is to be extended to non-linear analysis of a repair or to new repair geometries. This approach also provides no information regarding the stresses in the adhesive or the composite patch near the crack.

Through the work of Australian researchers (primarily Rose and Wang), closed-form equations exist that establish a conservative upper limit on the root-mean-square stress intensity at the crack tip. Unfortunately, the energy methods that have been very successful for the analysis of tensile loading of double-sided repairs, have otherwise been

abandoned in favour of line-spring models for analyzing the case of coupled bending and extension [20]. In a recent conference paper, Romilly and Clark [21] stated that a corrected form of the energy method of Wang and Rose [18], which establishes long-crack limits for the membrane and bending stress intensity in a repair, is in fact very accurate when compared to the predictions of generalized plane strain line-spring models which capture the three-dimensional behaviour of the plate near the crack tip. In this chapter, the authors continue by fully describing the line-spring model and using it to validate an interpolation approach that is valid for cracks of arbitrary length. This methodology and the resulting analysis are then tested against a three-dimensional finite element model, demonstrating very accurate results for both the membrane and bending stress intensity and the crack face displacements, which may be related to the stresses in the adhesive and in the composite patch.

5.2 A methodology for damage tolerance assessment

In keeping with the two-step approach introduced by Rose [2,3], several elements are required to complete the analysis of a bonded composite repair. The first step is to determine the stresses in the plane of the crack for the prospective repair. Due to load transfer from the plate to the patch, this stress will normally be reduced from the stress in the plate before application of the repair. The second step is to perform an analysis to determine the stress intensity and the stresses in the repair in the region of the crack. To achieve this, it is first necessary to characterize the stiffness of the repair as it acts to restrain the opening of the crack. Once these two steps are completed, a crack-bridging model is used to predict the stress intensity in the plate and the stresses in the adhesive and the composite repair. This is usually achieved by interpolation between limit states developed from an energy analysis of a very long crack bridged by springs and a very short crack without reinforcement. The resulting interpolation solution is applicable to a crack of arbitrary length.

5.2.1 Stress in the crack plane

The work of Wang and Rose [1] provides a set of useful expressions for the plate stresses in the vicinity of the crack. By their analysis one can consider that the shear and peel stresses in the adhesive bond joining the repair patch to the plate will vanish in areas remote from the edges of the repair, the plate and repair may be considered to be rigidly bonded, and that the membrane and bending stresses in the plate may be calculated by considering the structure to be a simple composite beam. The neutral axis of the combined structure is offset from the centreline of the repaired plate by a distance $\bar{z}$, calculated as follows.

$$\bar{z} = \frac{S(t_p + t_r)}{2(1+S)} \tag{1}$$

The moment of inertia of the reinforced plate is then calculated from:

$$I_t = \frac{t_p^3}{12} + t_p \bar{z}^2 + \frac{E_r}{E_p}\left[\frac{t_r^3}{12} + t_r\left(\frac{t_p}{2} + \frac{t_r}{2} - \bar{z}\right)^2\right] \tag{2}$$

With these two quantities defined, the membrane and bending stress under a remote applied extensional stress, σ^a, are given as follows:

$$\sigma_m^0 = \sigma^a\left(\frac{1}{1+S} + \frac{t_p^2 \bar{z}^2}{I_t}\right) \tag{3}$$

$$\sigma_b^0 = \sigma_a \frac{t_p^2 \bar{z}}{2I_t} \tag{4}$$

For nonlinear bending of a repair of large planar extent with low bending restraint, the neutral axis will move to the load line upon the first instance of loading and the moment carried by the patched structure at the crack plane will vanish. In this case, the stresses on the crack plane simplify to $\sigma_m^0 = \sigma^a/(1+S)$ and $\sigma_b^0 = 0$.

5.2.2 Characterization of crack-bridging springs

To perform the crack-bridging analysis of a repair, it is necessary to model the patch as a set of springs bridging the crack faces. The desired result is a set of spring constants relating the crack-opening stresses to the displacement of the crack face:

$$\begin{pmatrix}\sigma_m \\ \sigma_b\end{pmatrix} = \begin{bmatrix}k_{mm} & k_{mb} \\ k_{bm} & k_{bb}\end{bmatrix}\begin{pmatrix}u_m \\ u_b\end{pmatrix} \tag{5}$$

By inversion of equation (5), the springs may also be characterized using a compliance matrix, as shown below.

$$\begin{pmatrix}u_m \\ u_b\end{pmatrix} = \begin{bmatrix}c_{mm} & c_{mb} \\ c_{bm} & c_{bb}\end{bmatrix}\begin{pmatrix}\sigma_m \\ \sigma_b\end{pmatrix} \tag{6}$$

The spring compliance coefficients are determined by the analysis of a bonded lap joint that is equivalent in geometry and composition to the cross-section of the repair taken in the region of the crack. The governing equations for a bonded joint under tension and bending are originally from Volkerson [22] and from Goland and Reissner [23], and may be expressed in terms of the adhesive stresses as:

$$\tau_a'''(x) - \kappa_m^2 \tau_a'(x) = 0 \tag{7}$$

$$\sigma_a''''(x) + 4\kappa_b^4 \sigma_a(x) = 0 \tag{8}$$

The two characteristic parameters κ_m and κ_b describe the shear and bending response of the joint, and are given as follows:

$$\kappa_m^2 = \frac{4G_a}{t_a}\left(\frac{1}{E_p t_p} + \frac{1}{E_r t_r}\right) \tag{9}$$

$$\kappa_b^4 = \frac{E_a}{t_a}\left(\frac{1}{D_p} + \frac{1}{D_r}\right) \tag{10}$$

By applying the boundary conditions at the crack face, the compliance of the springs bridging the crack faces may be calculated as follows. First, the general solutions to equations (7) and (8), considering only those parts that vanish as $x \to \infty$, are given by:

$$\tau_a(x) = Ae^{-\kappa_m x} \tag{11}$$

$$\sigma_a(x) = [B\cos(\kappa_b x) + C\sin(\kappa_b x)]e^{-\kappa_b x} \tag{12}$$

The derivation then follows the method of Wang and Rose [18] with the exception of the treatment of the adhesive shear stress boundary condition. The integration constants are determined by the boundary conditions of the joint. Of interest are the displacements under the action of an applied force and moment acting on the plate.

$$N_p(0) = -\sigma_m^0 t_p \tag{13}$$

$$M_p(0) = -\sigma_b^0 t_p^2 / 6 \tag{14}$$

The force and moment acting on the reinforcement are determined considering equilibrium.

$$N_r(0) = \sigma_m^0 t_p \tag{15}$$

$$M_r(0) = \sigma_b^0 t_p^2 / 6 + \sigma_m^0 t_p (t_p + t_r)/2 \tag{16}$$

The final condition is symmetry, which requires the transverse shear forces to vanish.

$$V_p(0) = V_r(0) = 0 \tag{17}$$

The stresses may be expressed in terms of the boundary conditions using the adhesive constitutive equations. The process is identical to that of Wang and Rose [1], with the

exception that here the shear forces are made to vanish according to (17). Wang and Rose included an extra term to balance the shear stress at the edge of the adhesive layer, $\tau_a(0)$, which is of minor consequence and will vanish in a real joint. Equation (17) requires $C = -B$, and the remaining constants are found to be:

$$A\frac{\kappa_m t_a}{G_a} = \left[\frac{1}{E_r t_r} + \frac{1}{E_p t_p} + \frac{3(t_r + t_p)}{E_r t_r^2}\right]\sigma_m^o t_p + \left[\frac{1}{E_r t_r^2} - \frac{1}{E_p t_p^2}\right]\sigma_b^0 t_p^2 \tag{18}$$

$$B\frac{\kappa_b^2 D_r t_a}{E_a} = \left(\frac{t_r + t_p}{2}\right)\sigma_m^0 t_p + \frac{1}{6}\left(1 + \frac{D_r}{D_p}\right)\sigma_b^0 t_p^2 \tag{19}$$

The displacements of the plate are then given by equations (20) and (21).

$$u_b(0) = \frac{t_p}{2}\left(w_p'(0) - w_r'(0)\right) = -\frac{t_p t_a}{2E_a}\sigma_a'(0) = \kappa_b \frac{t_p t_a}{2E_a} B \tag{20}$$

$$u_m(0) = t_a\left(u_p(0) - u_r(0)\right) + u_b(0) = \frac{t_a}{G_a}A + \kappa_b \frac{t_p t_a}{2E_a} B \tag{21}$$

At this point, the spring compliance coefficients may easily be found, and are given by equations (22) through (25).

$$c_{mm} = \frac{t_p}{\kappa_m}\left(\frac{1}{E_r t_r} + \frac{1}{E_p t_p} + \frac{3(t_r + t_p)}{E_r t_r^2}\right) + \frac{t_p^2}{2\kappa_b D_r}\left(\frac{t_r + t_p}{2}\right) \tag{22}$$

$$c_{mb} = \frac{t_p^2}{\kappa_m}\left(\frac{1}{E_r t_r^2} - \frac{1}{E_p t_p^2}\right) + \frac{t_p^3}{12\kappa_b}\left(\frac{1}{D_r} + \frac{1}{D_p}\right) \tag{23}$$

$$c_{bb} = \frac{t_p^3}{12\kappa_b}\left(\frac{1}{D_r} + \frac{1}{D_p}\right) \tag{24}$$

$$c_{bm} = \frac{t_p^2}{2D_r\kappa_b}\left(\frac{t_r + t_p}{2}\right) \cong 3c_{mb} \tag{25}$$

As found by Wang and Rose, c is asymmetric. This asymmetry is required to satisfy Maxwell's reciprocal theorem, whereby it can be shown that the compliance matrix must obey the relationship $c_{bm} = 3c_{mb}$. For a linear system, a set of forces is related to a set of displacements at the points of application of the forces by a symmetric compliance matrix, denoted here as C.

$$u = [C]F \tag{26}$$

For a moment acting on a plate, the moment may be equivalently expressed as a pair of forces as shown in Figure 5-2.

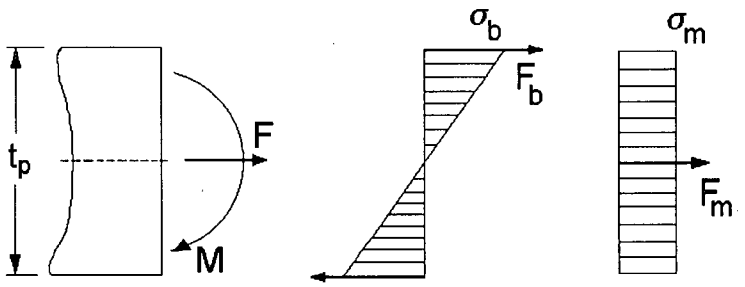

Figure 5-2: Equivalency of forces and moments

For the bending and membrane stress distributions shown in Figure 5-2, the equivalent forces are given as follows:

$$F_b = \frac{M}{t_p} = \frac{t_p \sigma_b}{6} \tag{27}$$

$$F_m = t_p \sigma_m \tag{28}$$

The compliance matrix may now be expressed in terms of the bending and membrane stresses and displacements.

$$\begin{pmatrix} u_m \\ u_b \end{pmatrix} = \begin{bmatrix} C_{mm} & C_{mb} \\ C_{bm} & C_{bb} \end{bmatrix} \begin{pmatrix} F_m \\ 2F_b \end{pmatrix} = t_p \begin{bmatrix} C_{mm} & \frac{C_{mb}}{3} \\ C_{bm} & \frac{C_{bb}}{3} \end{bmatrix} \begin{pmatrix} \sigma_m \\ \sigma_b \end{pmatrix} \tag{29}$$

By Maxwell's reciprocal theorem, $C_{mb} = C_{bm}$. Comparison with equation (6) shows that for the spring compliances, $c_{bm} = 3c_{mb}$. Small variations from this relationship will also result from approximations made during the derivation of the bonded joint model. For example, the simple analytical models described by equations (7) and (8) do not include bending moments in the adherends caused by adhesive shear stresses acting at the adherend/adhesive interface. Coupling of extension and bending results only from equilibrium and compatibility requirements employed during the application of the boundary conditions, and small errors will result because the bonded joint model and boundary conditions are inconsistent. Additional minor errors will arise if the adhesive thickness is ignored during derivation of the bonded joint model but included when one determines the boundary conditions.

5.2.3 Long-crack limit behaviour

Within the crack-bridging analysis, the long-crack limit behaviour of a repair may be determined by energy analysis [3,18], providing a limiting value for the stress intensity in the plate. To analyze linear coupled bending and extension of a repair, Wang and Rose [18] have developed an energy method for the separation of the membrane and bending components of the stress intensity in the repaired structure. In this paper, the authors have corrected their method to account for asymmetry of the compliance matrix and the presence of plane strain conditions at the crack tip, as found by Kotousov and Wang [24] for extension of cracked plates, and by Clark and Romilly [25] for plate bending. For consistency with line-spring models developed by Clark and Romilly [6,25], the line-forces acting on the crack faces are expressed in terms of the membrane and bending stresses in the plane of the crack.

Rose [2-4] observed that for a very long reinforced crack, the stresses near the crack tip become independent of crack length. The strain energy released with an increment of crack growth may then be found from the difference in stored elastic energy between strips of material far removed from the crack tip. One strip is located over the middle of the long crack, and its displacement is governed by the stretch of the springs bridging the crack. The other is well away from the crack and is undisturbed by the singular stress field near the crack. The difference in stored energy between the two strips is given by the energy stored in the springs bridging the crack. For a very long reinforced crack, the energy available to drive crack growth will then be equal to the strain energy stored in the springs, and is evaluated as follows [18].

$$\begin{aligned} G_\infty &= \frac{1}{t_p}\int_{-t_p/2}^{t_p/2}\sigma\ (z)u(z)dz \\ &= \frac{1}{t_p}\int_{-t_p/2}^{t_p/2}\left(\sigma_m+\sigma_b\frac{2z}{t_p}\right)\left(u_m+u_b\frac{2z}{t_p}\right)dz \\ &= c_{mm}\sigma_m^2+2c_{mb}\sigma_m\sigma_b+\frac{1}{3}c_{bb}\sigma_b^2 \end{aligned} \tag{30}$$

Based on the results of the generalized plane strain models for extension [24] and bending [25] of plates, the crack tip must be in a state of plane strain. The strain energy release rate at the outer fibre of the plate will have two components, one for bending and one for extension. Here, K_b and G_b are the stress intensity and strain energy release rate at the outer fibre.

$$G_\infty = G_m+\frac{1}{3}G_b=\frac{1-\eta^2}{E_p}\left(K_m^2+\frac{1}{3}K_b^2\right) \tag{31}$$

The applied stresses are linearly related to the membrane and bending stress intensities.

$$\begin{pmatrix} K_m^{\infty} \\ K_b^{\infty} \end{pmatrix} = \begin{bmatrix} d_{mm} & d_{mb} \\ d_{bm} & d_{bb} \end{bmatrix} \begin{pmatrix} \sigma_m \\ \sigma_b \end{pmatrix} \tag{32}$$

As for the spring compliance matrix, by Maxwell's reciprocal theorem, the authors will demonstrate that $d_{bm} = 3d_{mb}$. This is a significant correction to the method of Wang and Rose [18]. Since 1997, it has also been shown that plane strain conditions always exist at the crack tip, and the stress intensity at any point along the crack front can be related to the crack face displacement as follows, where r is the distance from the crack tip.

$$K = \lim_{r \to 0} \frac{E_p}{4(1-\eta^2)} \sqrt{\frac{2\pi}{r}} u(r) \tag{33}$$

In the region of the crack tip, equation (33) can be rewritten as follows:

$$\lim_{r \to 0} \frac{E_p}{4(1-\eta^2)} \sqrt{\frac{2\pi}{r}} \begin{pmatrix} u_m(r) \\ u_b(r) \end{pmatrix} = \begin{bmatrix} d_{mm} & d_{mb} \\ d_{bm} & d_{bb} \end{bmatrix} \begin{pmatrix} \sigma_m \\ \sigma_b \end{pmatrix} \tag{34}$$

By the same argument used for the spring compliances (comparison with equation 29) it can be stated that $d_{bm} = 3d_{mb}$. Substitution of (32) into (31) provides a second expression for G_{∞}, which is a corrected version of that given by Rose and Wang [18].

$$\begin{aligned} \frac{E_p G_{\infty}}{1-\eta^2} = & \left(d_{mm}^2 + 3d_{mb}^2\right)\sigma_m^2 \\ & + 2d_{mb}\left(d_{mm} + d_{bb}\right)\sigma_m \sigma_b \\ & + \left(d_{mb}^2 + d_{bb}^2/3\right)\sigma_b^2 \end{aligned} \tag{35}$$

Repeated differentiation of equations (30) and (35) with respect to the applied stresses will lead to a set of equations solvable for the coefficients of matrix d, as follows:

$$\left(d_{mm}^2 + 3d_{mb}^2\right) = c_{mb} \frac{E_p}{1-\eta^2} \tag{36}$$

$$d_{mb}\left(d_{mm} + d_{bb}\right) = c_{mb} \frac{E_p}{1-\eta^2} \tag{37}$$

$$d_{mb}^2 + d_{bb}^2/3 = \frac{1}{3} c_{bb} \frac{E_p}{1-\eta^2} \tag{38}$$

A unique solution can be found by noting that d_m, d_b must be positive and non-zero, leading to a system of equations solvable for the coefficients of matrix d. It is convenient to define three intermediate variables.

$$A = c_{mm}\frac{E_p}{1-\eta^2}, \qquad B = c_{mb}\frac{E_p}{1-\eta^2}, \qquad C = c_{bb}\frac{E_p}{1-\eta^2} \tag{39}$$

Equations (36) through (38) may then be decoupled to form a single equation for d_{mm}.

$$\left(d_{mm} + \sqrt{C - A + d_{mm}^2}\right)\sqrt{A - d_{mm}^2} = \sqrt{3}B \tag{40}$$

Equation (40) has one positive real root, bounded by upper and lower limits given by $\sqrt{A}$ and $\sqrt{A-C}$. The correct value of d_{mm} may be found in this interval using a simple root finding procedure. The remaining coefficients of the d matrix follow:

$$d_{bb} = \sqrt{C - A + d_{mm}^2} \tag{41}$$

$$d_{mb} = \frac{B}{d_{mm} + d_{bb}} \tag{42}$$

The resulting long-crack limit membrane and bending stress intensities follow from equation (32), and the limit spring displacements are given by equation (6). These corrected quantities define the effectiveness of a repair and are essential for the development of an interpolation applicable to repaired cracks of arbitrary length.

5.2.4 Interpolation for arbitrary crack lengths

This section describes the development of a new engineering model for the stress intensity and crack opening displacement for bridged cracks of arbitrary length. These quantities may be estimated by developing an interpolation between the long-crack limit solutions given by equations (32) and (6), and the nominal solutions for an unreinforced crack. In both cases, the stresses given by equations (3) and (4) are assumed to act to open the crack. The first step is to establish the short-crack limit, or nominal solutions for a through-thickness crack without reinforcing springs. For finite thickness plates, Clark and Romilly [6,25] have developed a set of geometry correction factors by using generalized plane strain models for extension and bending of plates. These correction factors account for the through-thickness material properties and the thickness of the plate. For the stress intensity, they take the following form:

$$Y_k^{pres.}(\alpha) = 1 + \left(\frac{\alpha^{1.5}}{\alpha^{1.5} + 1.5}\right)\left(\frac{1}{\sqrt{1-\eta_p^2}} - 1\right) \tag{43}$$

$$Y_k^{shear}(\alpha) = 1 - \left(\frac{\alpha^{1.2}}{\alpha^{1.2} + 3.5}\right)\left(1 - \sqrt{\frac{1+\nu_p}{3+\nu_p}}\right) \tag{44}$$

Using these correction factors, the nominal membrane and bending stress intensity follow:

$$K_m^0 = Y_k^{pres.}\left(\alpha_m^{pres.}\right)\sigma_m^0\sqrt{\pi\, a} = Y_{km}\sigma_m^0\sqrt{\pi\, a} \tag{45}$$

$$K_b^0 = Y_k^{pres.}\left(\alpha_b^{pres.}\right)Y_k^{shear}\left(\alpha_b^{shear}\right)\sigma_b^0\sqrt{\pi\, a} = Y_{kb}\sigma_b^0\sqrt{\pi\, a} \tag{46}$$

Equations (47) and (48) provide the necessary geometry correction factors for the maximum displacement of the crack faces, which occurs at the centre of the crack.

$$Y_d^{pres.}(\alpha) = 1+\left(\frac{\alpha^{1.5}}{\alpha^{1.5}+2.5}\right)\left(\frac{1}{1-\eta_p^2}-1\right) \tag{47}$$

$$Y_d^{shear}(a) = 1-\left(\frac{\alpha^{1.3}}{\alpha^{1.3}+5}\right)\left(1-\frac{1+\nu_p}{3+\nu_p}\right) \tag{48}$$

Without any crack-bridging springs, the extensional and bending displacements of the crack faces under the action of the crack-opening stresses, σ_m^0 and σ_b^0, will then be:

$$u_m^0 = 2Y_d^{pres.}(\alpha_m^{pres.})\frac{\sigma_m^0(1-\eta_p^2)}{E_p}a = 2Y_{dm}\frac{\sigma_m^0(1-\eta_p^2)}{E_p}a \tag{49}$$

$$u_b^0 = 2Y_d^{pres.}(\alpha_b^{pres.})Y_d^{shear}(\alpha_b^{shear})\frac{\sigma_m^0(1-\eta_p^2)}{E_p}a = 2Y_{db}\frac{\sigma_m^0(1-\eta_p^2)}{E_p}a \tag{50}$$

Each of the correction factors is a function of α, a normalized crack length that accounts for the effects of the transverse properties and thickness of the plate. The three normalized crack lengths characterize the effects of transverse normal stresses in extension, transverse normal stresses in bending, and transverse shear in bending, respectively.

$$\alpha_m^{pres.} = \frac{2a}{t_p}\sqrt{3\left(1+\nu_p^z\right)} \tag{51}$$

$$\alpha_b^{pres.} = \frac{2a}{t_p}\frac{\nu_p^z}{\eta}\sqrt{\frac{15E_p}{G_p^z}} \tag{52}$$

$$\alpha_b^{shear} = \frac{2a}{t_p}\sqrt{\frac{6G_p^z(3+\nu_p)}{E_p}} \tag{53}$$

These nominal solutions for the stress intensities and displacements provide the short-crack limit solution. The long-crack limit stress intensities may be calculated using

equation (32), and the corresponding long-crack limit displacements are given by equation (6). At this point the authors propose a new method of interpolation between these limits to establish the state of a reinforced crack of arbitrary length. For the case of coupled extension and bending, a very effective interpolation may be achieved by considering the stiffness of both the cracked plate and the crack-bridging springs. Equations (49) and (50) may be inverted to develop expressions for the stiffness of the cracked plate.

$$k_m^p = \frac{\sigma_m^0}{u_m^0} = \left(\frac{E_p}{1-\eta_p^2}\right)\frac{1}{2Y_{dm}a} \tag{54}$$

$$k_b^p = \frac{\sigma_m^0}{u_b^0} = \left(\frac{E_p}{1-\eta_p^2}\right)\frac{1}{2Y_{db}a} \tag{55}$$

A stiffness matrix for the as-reinforced crack may now be developed by considering the crack and the patch as a set of springs acting in parallel. The result is an as-reinforced stiffness matrix applicable to repaired cracks of arbitrary length.

$$\begin{pmatrix}\sigma_m^0\\ \sigma_b^0\end{pmatrix} = \begin{bmatrix}k_{mm}+k_m^p & k_{mb}\\ k_{bm} & k_{bb}+k_b^p\end{bmatrix}\begin{pmatrix}u_m^r\\ u_b^r\end{pmatrix} \tag{56}$$

By inverting the combined stiffness matrix of equation (56), a new compliance matrix may be generated for any particular crack length that accounts for the stiffness of the cracked pate:

$$\begin{pmatrix}u_m^r\\ u_b^r\end{pmatrix} = \begin{bmatrix}c_{mm}^r & c_{mb}^r\\ c_{bm}^r & c_{bb}^r\end{bmatrix}\begin{pmatrix}\sigma_m^0\\ \sigma_b^0\end{pmatrix} \tag{57}$$

The as-reinforced crack face displacements can now be calculated directly, and the as-reinforced membrane and bending stress intensity may be calculated by the applying the new compliance matrix to the energy method described in Section 5.2.3. This is a new application of the energy method, which has in the past only been used to calculate long-crack limit solutions. This method of interpolation does not require any assumptions regarding the ratio of the membrane and bending components, overcoming a significant problem with the method of Wang, Rose and Calinan [19].

This new approach to the interpolation allows for the simplified analysis of linear coupled bending and extension of a repair and includes the effects of transverse normal and shear stresses and accompanying shear deflections. It is a valuable tool for patch design and damage tolerance. In subsequent sections, this new interpolation model will be validated against a numerical line-spring model for generalized plane strain plates and against a three-dimensional finite element model of a bonded composite repair.

5.3 A line-spring model for crack-bridging

In this section we combine the generalized plane strain crack-bridging models for extension and bending [6,25] to address the problem of a crack bridged by coupled springs. The results will be used to validate the closed-form equations developed in Section 5.2 above. The springs bridging the crack are characterized by equation (5), i.e. the stiffness matrix relating the membrane and bending stresses to the crack face displacements. Using an approach similar to that of Wang and Rose [1], the line-spring models for extension and bending may be combined to include the effect of the coupling springs. The significant differences in the current approach are the use of the generalized plane strain plate models and the choice to express the bending moment and displacement in terms of the crack face displacement and the bending stress in the outer fibre of the plate. The generalized plane strain plate models lead to additional terms that account for pressurization and transverse shear about the crack tip. This leads to the following set of coupled Fredholm integral equations with hyper-singular integrands that are solvable for the crack face displacements. The left side of the equation is the net crack opening stress along the crack face, and the right side describes the reaction of the plate.

$$\begin{matrix}\sigma_m^0(y)-k_{mm}u_m(y)\\ -k_{mb}u_b(y)\end{matrix}=\frac{-1}{2\pi}\int_{-a}^{a}\frac{E_p u_m(t)}{1-\eta^2}\left(\begin{matrix}\dfrac{1}{(t-y)^2}\\ +\eta^2\left(\kappa_m^{pres.}\right)^2 L^{pres.}\left(\kappa_m^{pres.}|t-y|\right)\end{matrix}\right)dt \tag{58}$$

$$\begin{matrix}\sigma_b^0(y)-k_{bb}u_b(y)\\ -k_{bm}u_m(y)\end{matrix}=\frac{-1}{2\pi}\int_{-a}^{a}\frac{E_p u_b(t)}{1-\eta^2}\left(\begin{matrix}\dfrac{1}{(t-y)^2}\\ +\dfrac{\left(\kappa_b^{shear}\right)^2}{2}\dfrac{1-\eta^2}{1+\nu}L^{shear}\left(\kappa_b^{shear}|t-y|\right)\\ +\left(\kappa_b^{pres.}\right)^2\eta^2 L^{pres.}\left(\kappa_b^{pres.}|t-y|\right)\end{matrix}\right)dt \tag{59}$$

In equations (58) and (59), the following parameters characterize the through-thickness properties of the plate.

$$\kappa_m^{pres.}=\frac{2}{t_p}\sqrt{\frac{3E_z}{G_z(1-\eta_p^2)}} \tag{60}$$

$$\kappa_b^{pres.}=\frac{2\nu_p^z}{t_p\eta_p}\sqrt{\frac{15E}{G_z(1-\eta_p^2)}} \tag{61}$$

$$\kappa_b^{shear}=\frac{2}{t_p}\sqrt{\frac{3G_z}{G}} \tag{62}$$

The functions $L^{pres.}(z)$ and $L^{shear}(z)$ describe the effects of pressurization and transverse shear stresses near the crack tip. If the $L^{pres.}(z)$ functions are neglected, the line-spring model will take the forms for classical plane strain extension and plane strain plate bending with shear deflections (i.e. plate bending according to the Mindlin formulation). If the term $L^{shear}(z)$ is also removed, then the effects of transverse shear stresses and the accompanying shear deflections will be removed. The formulation of Wang and Rose [1] can be recovered by neglecting the pressurization terms, removing the plane-strain modification of the Young's modulus, and using isotropic rather than transversely isotropic material properties. The functions $L^{pres.}(z)$ and $L^{shear}(z)$ have the following form, where K_n are various orders of modified Bessel functions of the second kind.

$$L^{pres.}(z) = 2\left[1+\frac{3}{z^2}\right]K_2(z) - \frac{12}{z^4} - \frac{1}{z^2} \tag{63}$$

$$L^{shear}(z) = -\frac{48}{z^4} + \frac{4}{z^2} + 4\left(K_2(z) - K_0(z)\right) + \frac{24}{z^2}K_2(z) \tag{64}$$

The domain of the integration in equations (58) and (59) may be normalized with respect to the half-crack length, a, and the displacements expanded using Chebyshev polynomials of the second kind:

$$U_i(r) = \sin((i+1)\cos^{-1}(r))/\sqrt{1-r^2} \tag{65}$$

For this set of orthogonal polynomials, the weight function is given by:

$$W(r) = \sqrt{1-r^2} \tag{66}$$

Given this expansion, the crack face displacements may now be decomposed as follows:

$$u_m(r) = \sum_i W(r)U_i(r)f_i \tag{67}$$

$$u_b(r) = \sum_i W(r)U_i(r)g_i \tag{68}$$

Choosing a set of collocation points, a coupled linear system may now be defined from equations (58) and (59), which may be solved for the expansion coefficients.

$$\begin{Bmatrix} \bar{\sigma}_m \\ \bar{\sigma}_b \end{Bmatrix} = \begin{bmatrix} A & B \\ C & D \end{bmatrix} \begin{Bmatrix} f \\ g \end{Bmatrix} \tag{69}$$

In this system, the matrix coefficients have the following definitions.

$$A_{i,j} = \frac{E_p}{1-\eta^2}\left(\frac{i+1}{2}U_j(r_i) - \frac{\eta^2\left(a\kappa_m^{pres.}\right)^2}{2\pi}L_{i,j}^{pres.}\right) + ak_{mm}W(r_i)U_j(r_i) \tag{70}$$

$$B_{i,j} = ak_{mb}W(r_i)U_j(r_i) \tag{71}$$

$$C_{i,j} = \frac{E_p}{1-\eta^2}\left(\frac{i+1}{2}U_j(s_i) - \frac{\left(a\kappa_b^{shear}\right)^2}{4\pi}\left(\frac{1-\eta^2}{1+\nu}\right)L_{i,j}^{shear} - \frac{\left(a\kappa_b^{pres.}\right)^2\eta^2}{2\pi}L_{i,j}^{pres.}\right) + ak_{bb}W(s_i)U_j(s_i) \tag{72}$$

$$D_{i,j} = ak_{bm}W(r_i)U_j(r_i) \tag{73}$$

Analytical solutions exist for the logarithmic parts of $L^{shear}(z)$ and $L^{pres.}(z)$, but the regular parts require numerical integration. The term $V_{i,j}$ arises from the logarithmic singularity, and may be solved analytically, as demonstrated by Joseph and Erdogan [26,27] and by Wang and Rose [1]. To evaluate the regular part, the authors used Gauss-Chebyshev quadrature, as suggested by Joseph and Erdogan.

$$L_{i,j}^{shear} = \int_{-1}^{1}\left[L^{shear}\left(a\kappa^{shear}\left|r_i - s\right|\right) - \ln\left(\left|r_i - s\right|\right)\right]W(s)U_j(s)ds + V_{i,j} \tag{74}$$

$$L_{i,j}^{pres.} = \int_{-1}^{1}\left[L^{pres.}\left(a\kappa^{pres.}\left|r_i - s\right|\right) + \frac{3}{4}\ln\left(\left|r_i - s\right|\right)\right]W(s)U_j(s)ds - \frac{3}{4}V_{i,j} \tag{75}$$

$$V_{i,j} = \int_{-1}^{1}\ln\left|r_i - s\right|W(s)U_j(s)ds = \begin{cases} -\frac{\pi}{2}\left[-r_i^2 + \frac{1}{2} + \ln 2\right] & j = 0 \\ -\frac{\pi}{2}\left[\frac{T_j(r_i)}{j} - \frac{T_{j+2}(r_i)}{j+2}\right] & j > 0 \end{cases} \tag{76}$$

For the generalized plane strain plate models, the stress intensities in extension and bending may be found from the expansion coefficients in the following manner.

$$K_m^n = \frac{E\sqrt{\pi a}}{2(1-\eta^2)}\sum_{i=0}^{N}(i+1)f_i \tag{77}$$

$$K_b^n = \frac{E\sqrt{\pi a}}{2(1-\eta^2)}\sum_{i=0}^{N}(i+1)g_i \tag{78}$$

These stress intensity results will be compared to the interpolation model results and finite element results in Section 5.4.1.

Equation (5) relates the displacement of the crack faces to the line-forces carried by the springs. Expressing the membrane and bending stresses as their line-force equivalents:

$$N_x(y) = 2h\left(k_{mm}u_m(y) + k_{mb}u_b(y)\right) \tag{79}$$

$$M_x(y) = \frac{2}{3}h^3\left(k_{bm}u_m(y) + k_{bb}u_b(y)\right) \tag{80}$$

Given the crack face displacements, these expressions for loading may be used to predict fatigue cracking and/or rupture of the springs (i.e. the patch materials) bridging the crack faces as required for patch design and/or damage tolerance assessment.

5.4 Comparison to finite element models

In this section, finite element models are used to determine the capability of the closed-form equations. The stress intensities and crack face displacement results from the closed-form equations and the line-spring model are compared to a three-dimensional bonded repair model, and the nominal stresses in the substrate and compliance of the repair as it bridges the crack are investigated using two-dimensional bonded joint models.

5.4.1 Stress intensity and crack face displacements

The authors have developed three-dimensional solid finite element models representing the AMRL (Australian Maritime Research Laboratory) specimen, a specimen type that has been widely adopted for the investigation of bonded repairs [e.g. 9]. The models have been validated against mechanical testing of an instrumented specimen, during which strains were measured at nearly 100 positions on the patch and repaired plate, including 40 strain gauges applied to the face of the repair as it bridges the crack [28]. Figure 5-3(a) shows the model in a large-plate configuration for a crack length of 160 mm. With the appropriate boundary conditions, symmetry allows the use of a one-quarter plate model. The large-plate model is designed to test the closed-form equations and line-spring model for the idealized case from which they where derived. Figure 5-3(b) shows a close-up of the elements near the crack tip, with elements removed to show the repair patch, epoxy, and plate layers. The crack face is identified by the cross-hatched region.

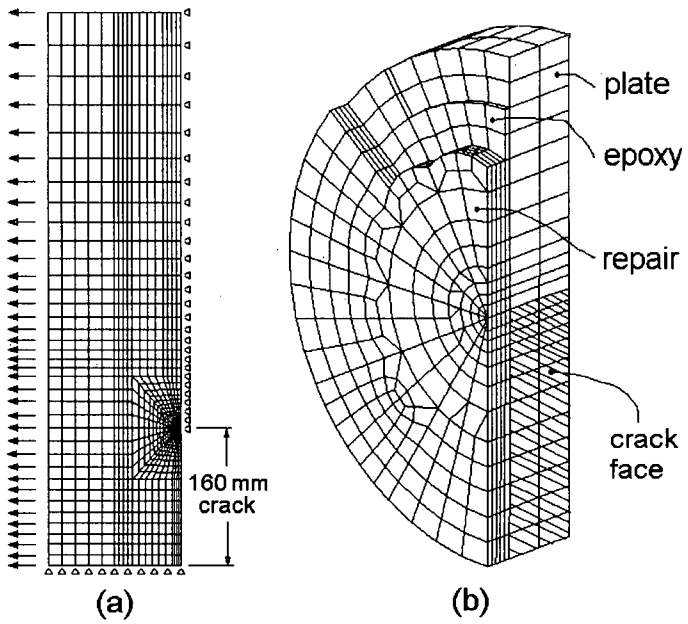

Figure 5-3: Three-dimensional finite element model of a repair

The finite element models were developed in ANSYS, utilizing three-dimensional 20-node brick elements and 15-node wedges. The wedge elements use quarter-point mid-side nodes to model the singularity at the crack tip, from which the stress intensity was calculated using the stresses at three integration points in the wedges ahead of the crack tip. This stress-based approach allowed an accurate evaluation of the stress intensity as it varied through the thickness of the plate. Validation models demonstrated stress intensities accurate to within 2% compared to theoretical models corrected for through-thickness effects. Table 5-1 shows the material properties and dimensions used in the finite element models. For the purposes of this chapter, the patch was modelled as an isotropic solid to remove the complicating effects of transverse shear and peel deformations as would otherwise exist in an orthotropic composite.

Property	Boron/Epoxy Patch	FM-73M Adhesive	2024-T3 Aluminum Plate
Elastic Modulus, E	210 GPa	2.14 GPa	72.4 GPa
Shear Modulus, G	7.24 GPa	0.805 GPa	27.2 GPa
Poisson's Ratio, υ	0.21	0.33	0.33
Thermal Expansion, α	4.61 $\mu\varepsilon$ /^{0}C	50.0 $\mu\varepsilon$ /^{0}C	23.45 $\mu\varepsilon$ /^{0}C
Thickness, t	0.924 mm	0.25 mm	3.125 mm

Table 5-1: Material properties and dimensions

The membrane and bending stress intensities are the average stress intensity and the stress intensity at the outer fibre of the plate, respectively, as found from the average and the first moment of the stress intensity taken through the thickness of the plate. These

quantities were calculated using a linear least-squares fit to the stress intensities found at the integration points through the thickness of the plate. To determine the actual transverse variation of the stress intensity through the thickness of the plate would require the use of many elements, as a thin boundary layer exists at the top and bottom surfaces. However, convergence studies have shown that few elements are required to obtain accurate values for the plate-averaged quantities, K_m and K_b. The three-dimensional finite element models employ two elements through the thickness of the plate, enough to ensure that errors due to through-thickness mesh refinement are much smaller than the 2% error resulting from stress intensity determination.

Figures 5-4 and 5-5 show the membrane and bending stress intensities predicted by the interpolation model and by the line-spring model when compared to the large plate finite element model, under a remote applied stress of 1 MPa. The nominal results are the membrane and bending stress intensities that would arise if the patch only acted to reduce the stresses in the underlying plate but did not act to restrict the opening of the crack. For both the interpolation model and the line-spring model, the nominal stresses were calculated using plane strain results from a two-dimensional finite element model (described in Section 5.4.2) and the spring stiffnesses were calculated using the plane strain analytical results from Section 5.2.2.

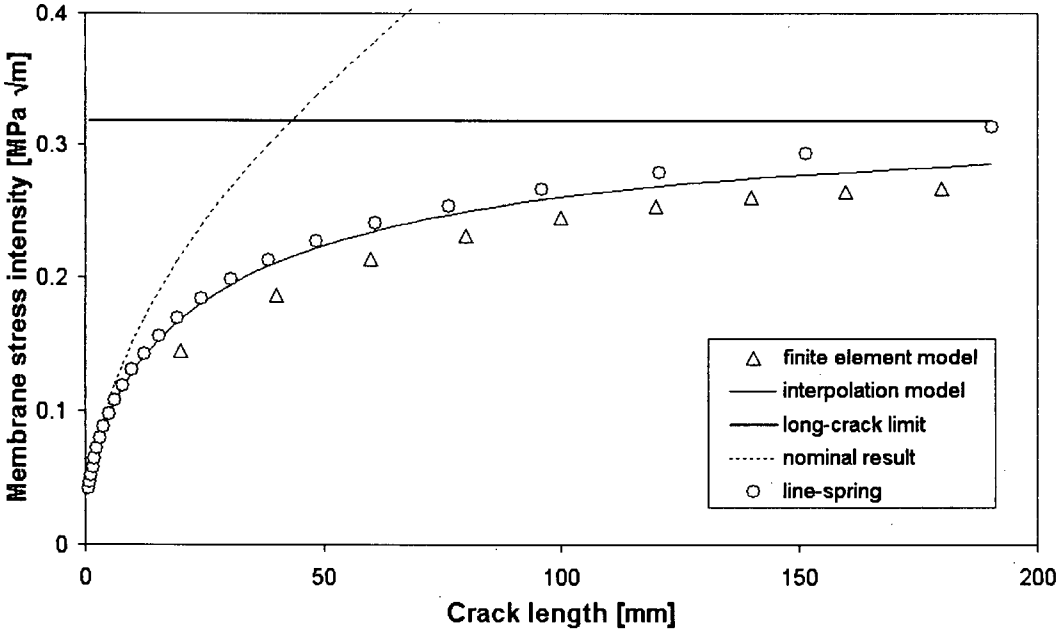

Figure 5-4: Membrane stress intensity

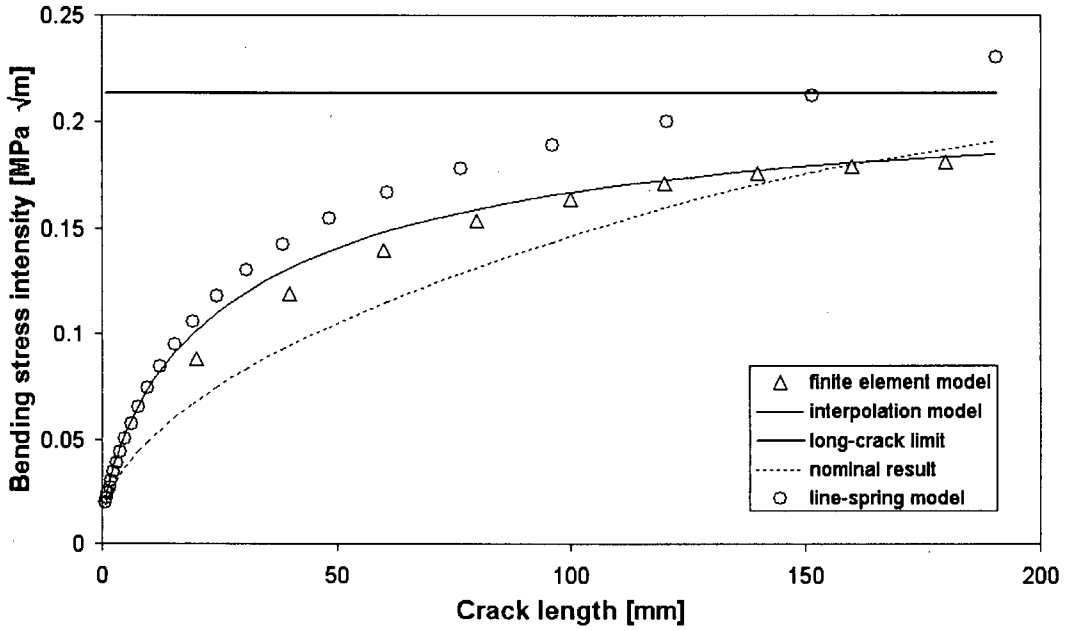

Figure 5-5: Bending stress intensity

The interpolation and line-spring models provide very similar results for short cracks but diverge when the crack length becomes large. For long cracks, the line-spring model develops errors due to the increasing importance of the higher order Chebychev polynomials and the errors arising from numerical integration of the regular parts of the hyper-singular integrals. For relatively short cracks with $a < 50\,mm$, the interpolation model membrane stress intensity is lower by less than 2% and the interpolation model bending stress intensity is higher by as much as 10% when compared to the FEM results. This 10% error can be attributed in roughly equal parts to three sources. First, equation (31) slightly over-predicts the nominal stress intensity for this plate, next, very small variations from Maxwell's reciprocal theorem that arise due to simplifications made during the development of the spring compliance matrix lead to disproportionately large errors for this crack length and last, the interpolation method is approximate and errors of up to 5% should be expected. The finite element results are generally lower than those calculated using either analytical model, a difference that could arise from a number of sources. Using the limited academic version of ANSYS, it is difficult to include enough elements in the adhesive layer near the crack, and at the same time model a repaired plate of large planar extent. An insufficiently dense mesh would cause the repair to appear to be overly stiff and artificially reduce the stress intensity and crack face displacement.

Figures 5-6 and 5-7 compare the membrane and bending crack face displacements calculated using the interpolation model and the line-spring model to the results of the large-plate finite element model.

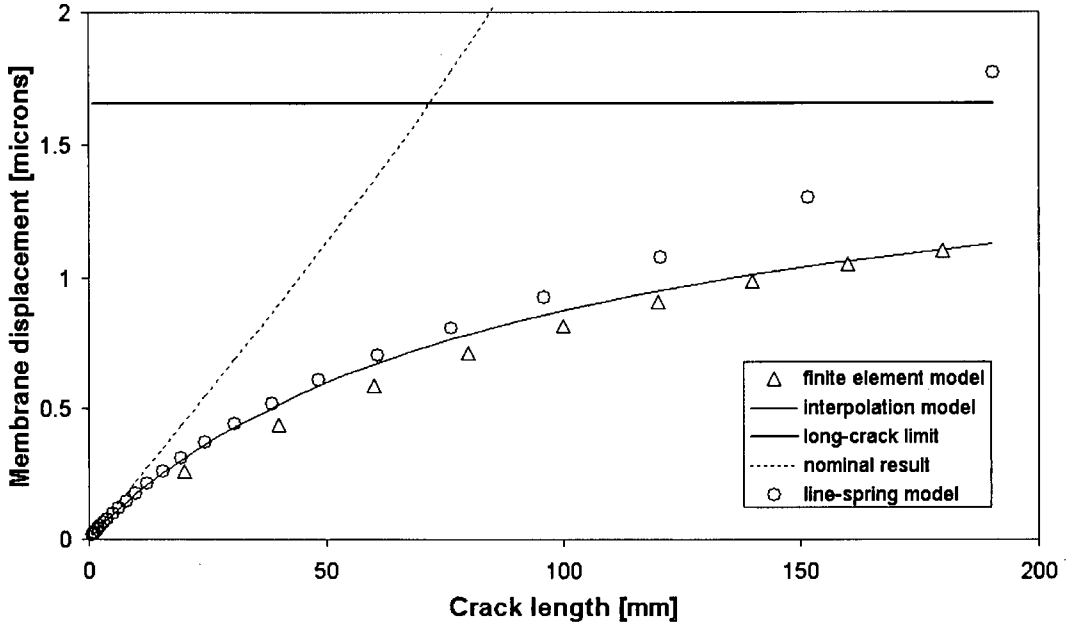

Figure 5-6: Membrane crack face displacement

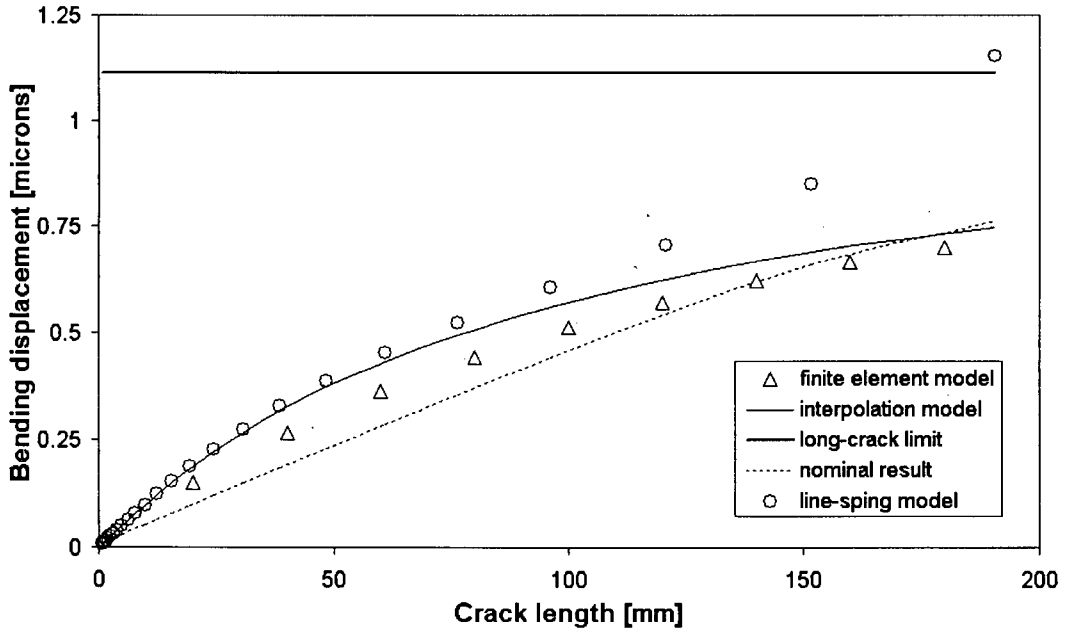

Figure 5-7: Bending crack face displacement

The crack displacement results follow a similar trend to that observed for the stress intensities. For short cracks with $a < 50\,mm$, both the interpolation model membrane and bending displacements are lower by less than 4% when compared to the FEM results. For long cracks the interpolation and line-spring model results diverge for the same reasons as stated above. In both cases, interpolation provides reasonable results, and the long-

crack limits established by the energy analysis are obeyed. This contradicts the findings of Wang and Rose [18], who, by comparison to a three-dimensional finite element model, observed that the energy method significantly over-predicts the bending stress intensity and is not a useful approach. This supports the validity of the modifications described in Section 5.2, i.e. that the crack tip must be considered to be in a state of plane strain and that Maxwell's reciprocal theorem must be satisfied in the manner shown. In the next section, a two-dimensional finite element model will be used to examine the effectiveness of the means used to calculate the crack opening pressures and the definition of the spring constants.

5.4.2 Spring stiffness and nominal stress determination

The composite beam model used to calculate the nominal stresses under a repair is, strictly speaking, only applicable to a very large patch without boundary conditions that lead to restraint against bending. The effect of a finite patch applied to a plate with rotational constraints at the grips can be estimated using finite element analysis. Using the same materials and geometry as were used for the large plate finite element model, a two-dimensional finite element model has been developed for this purpose and to calculate the compliance of the repair as it bridges the crack. This model has been validated against load-deflection curves, strain gauge data, and lateral deflections from experiments [29]. Figure 5-8 shows the finite element mesh and boundary conditions for two configurations of the model, one with a crack under the patch (top), and an uncracked version used to calculate the nominal stresses under the repair (bottom).

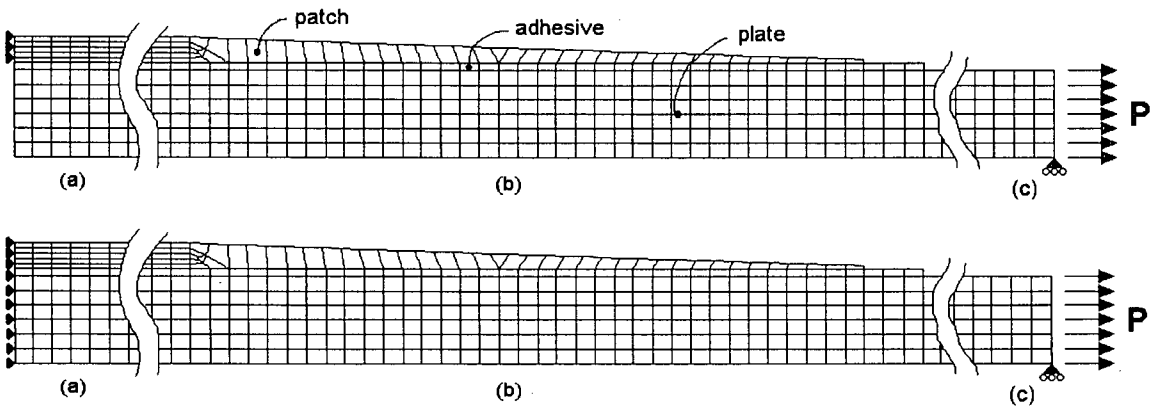

Figure 5-8: FE mesh showing the (a) cracked, (b) tapered, and (c) grip regions

In this particular analysis, the bonded repair is assumed to be isotropic to eliminate composite deformations that cannot be predicted using the bonded joint equations presented in this chapter. Figure 5-9 shows the nominal stresses predicted by the closed-form equations for a remote applied stress of 1 MPa. Both the finite element and closed-

form equation results are shown for two cases: plane stress and plane strain. It is likely that the correct case is the intermediate one of generalized plane strain, where the structure is allowed to deform uniformly in the transverse direction. For the AMRL geometry, it is seen that the closed-form equations provide reasonable results, but that there are sufficient differences to account for the errors observed in the comparison of the line-spring and interpolation model results to the three-dimensional finite element results. The closed-form equations are seen to generally over-predict the nominal stresses, which would lead to an over-estimate of the stress intensities and crack face displacements.

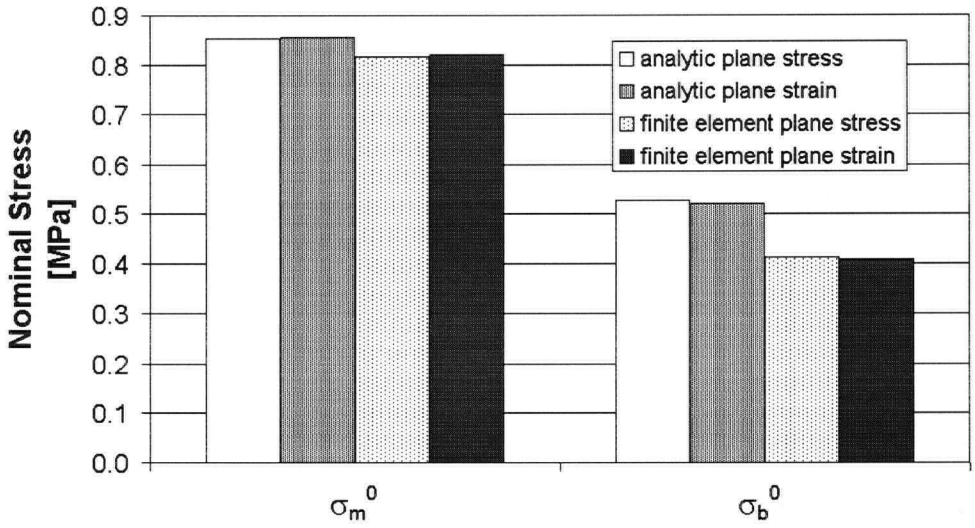

Figure 5-9: Nominal stresses

The other factor that would affect the interpolation results is the calculation of the spring compliances. Figure 5-10 shows a comparison of the spring compliances predicted by the closed-form equations and the finite element model. These displacements were derived by separately applying a uniform membrane stress and a linearly varying bending stress to the face of the crack in the two-dimensional finite element model shown above. Again, the results are shown for two cases, plane stress and plane strain.

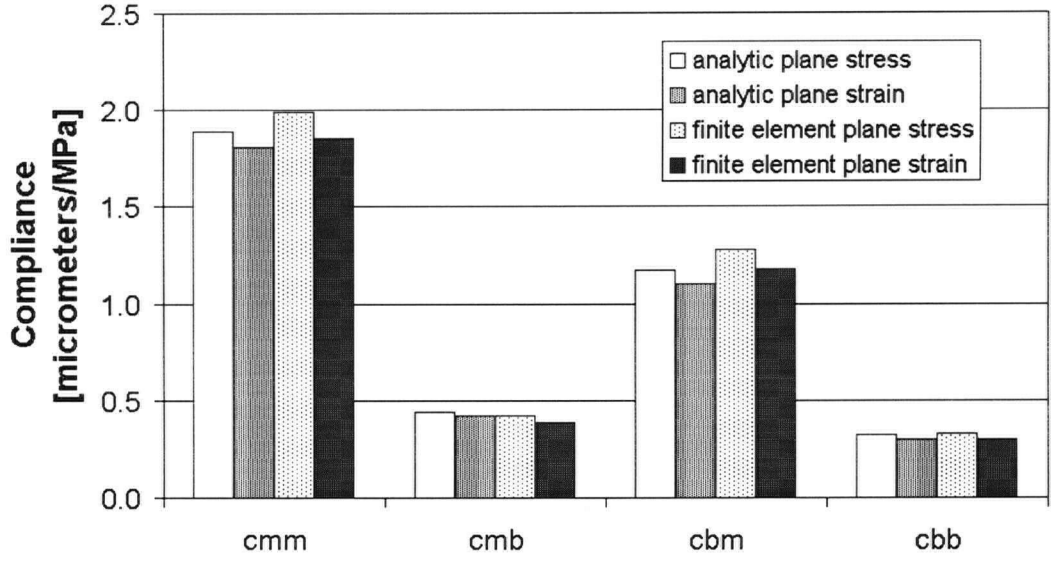

Figure 5-10: Spring compliances

The closed-form equations are shown to provide very reasonable results, generally slightly under-estimating the stiffness of the patch when compared to finite elements. In the generation of Figures 5-4 to 5-7, the plane stress closed-form equations were used, which when compared to the plane strain results, may demonstrate a slight over-estimate of the compliance of the repair. As in the determination of the nominal stresses, the actual state of the repair in the idealized large plate case is likely to be one of generalized plane strain, and intermediate to the plane stress and plane strain results. Accordingly, it is difficult to precisely determine what role the spring stiffness equations might contribute to the differences observed between the three-dimensional finite element models and the interpolation and line-spring models.

5.5 Results and discussion

Through comparison with three-dimensional finite element results, it has been shown that the line-spring and new interpolation models capture the crack-bridging behaviour of a repair. Also through comparison with finite element analysis, it has been shown that the composite beam model may lead to some inaccuracies in the determination of the nominal stresses acting under the repair. Factors affecting its applicability include the length of the repair, the support conditions, and the planar stress state assumed to exist in the repair (i.e. plane stress or plane strain conditions). Some additional complicating effects that have not been investigated for the case of linear coupled bending and extension are the shape of the patch (whereby patches of finite planar geometry are known to generally increase the stresses in the region of the repair) and the effects of a highly anisotropic composite patch. Another pressing issue is that, while the common

bonded joint model presented in this paper proved adequate in the case of an isotropic repair, the composite nature of a real repair is a complicating factor in the determination of the compliance of the repair as it bridges the crack. The modelling of such a hybrid bonded joint is complicated by many secondary effects such as shear and peel (transverse normal) deformations that act to increase the compliance of the repair, pressurization of the adhesive due to peel stresses, the plane state of the adherends and the adhesive, and the complementary shear deformations resulting from the rapidly changing bending stresses in the patch and plate. These effects can be particularly important in the prediction of failure of the repair by disbonding, where the peel and shear stresses in the adhesive must be known. The alternative to accurately determining the adhesive stresses is to calculate the strain energy release rate of the bonded joint system, which may be safely compared to experimental results for a similar specimen under similar loading conditions to predict fracture and fatigue, but is not directly comparable to any adhesive material property. This would necessitate a significant amount of testing for each new combination of materials or for new loading combinations, which is currently the norm in the development of composite airframe structures.

An additional issue that has not been addressed is the crack closure phenomenon that occurs on the compressive side of the bending plate when the applied tensile loads are not sufficient to prevent closure. This has been identified by Duong and Wang [30] as one of the principal impediments to the prediction of the rate of failure of a cracked plate under tensile and bending loads. They have proposed an effective or modified stress intensity to account for combined bending and tensile loads, but admit that their technique requires further work before it can be used generally. The authors hope that the development of the generalized plane strain plate line-spring models will prove useful in the analysis of this phenomenon. Crack closure would pose a nonlinear contact problem, which could be examined by using a one-dimensional finite element mesh along the crack face instead of using Chebychev polynomials to obtain a numerical solution. Without a method to address this issue, experimental verification or very conservative means should be employed in the prediction of failure, such as simply adding the membrane and bending stress intensities and comparing them to the critical stress intensity for the material or by using them together in the Paris equation. This approach should prove to be conservative, as it will effectively over-predict the energy available for fracture.

5.6 Concluding remarks

In this chapter, the authors have, based on a corrected form of the energy method of Wang and Rose, developed a new interpolation model applicable to the analysis of bridged cracks under combined tension and bending. The interpolation model has been tested against a line-spring model of for a generalized plane strain cracked plate and a full

three-dimensional analysis of a repaired plate, and proven to be very accurate for the AMRL specimen geometry. Some deficiencies have been noted in the methods used to determine the nominal stresses acting in the regions of the repair and in the extension of linear crack-bridging models to the analysis of unbalanced repairs experiencing stress stiffening, and accordingly the authors urge bonded repair designers to verify their results against finite element models or experiments when thick plates or repairs of limited planar dimensions are analysed. It has also been noted that for an anisotropic composite repair, standard bonded joint models may not be adequate for the determination of the spring compliances or the prediction of disbonding and fracture. Prediction of the rate of failure or ultimate load of the structure is also complicated by the lack of an adequate and widely accepted means of translating the stress intensities or adhesive stresses into crack or disbond fracture or growth rates, which will continue to require the structural testing of repairs (and composite structures in general) to determine their suitability for service.

5.7 References

[1] Wang C.H., Rose L.R.F. A crack-bridging model for bonded plates subjected to tension and bending. International Journal of Solids and Structures 36, 1999, 1985-2014.

[2] Rose L.R.F. An application of the inclusion analogy for bonded reinforcements. International Journal of Solids and Structures 17, 1981, 827-838.

[3] Rose L.R.F. A cracked plate repaired by bonded reinforcements. International Journal of Fracture 18(2), 1982, 135-144.

[4] Rose L.R.F. Theoretical Analysis of crack patching. In: A.A. Baker and R. Jones (eds.) Bonded Repair of Aircraft Structures. Martinus Nijhoff, 1988, 77-105.

[5] Wang C.H., Rose L.R.F. Bonded repair of cracks under mixed-mode loading. International Journal of Solids and Structures 35(21), 1998, 2749-2773.

[6] Clark R.J., Romilly D.P. Reinforced cracks in transversally isotropic generalized pane strain plates. To be submitted to Engineering Fracture Mechanics.

[7] Jones R. Neutral axis offset effects due to crack patching. Composite Structures 1, 1983, 163-174.

[8] Jones R., Callinan R.J., Aggarwal K.C. Analysis of bonded repairs to damaged fibre composite structures. Engineering Fracture Mechanics 17(1), 1983, 37-46.

[9] Baker A.A. Repair efficiency in fatigue-cracked aluminum components reinforced with boron/epoxy patches. Fatigue and Fracture of Engineering Materials and Structures 16(7), 1993, 753-765.

[10] Clark R.J., Romilly D.P. Fatigue damage prediction for bonded composite repairs applied to metallic aircraft structures. SAE Journal of Aerospace, paper # 2001-01-26, 2001.

[11] Albat A.M., Romilly D.P. A direct linear-elastic analysis of double-symmetric bonded joints and reinforcements. Composites Science and Technology 59, 1999, 1127-1137.

[12] Jones R., Chiu W.K., Smith R. Airworthiness of Composite Repairs: Failure Mechanisms. Engineering Failure Analysis 2(2), 1995, 117-128.

[13] Ratwani M.M. Cracked, adhesively bonded laminated structures. AIAA Journal 17(9), 1979, 988-994.

[14] Arendt C., Sun C.T. Bending effects of asymmetric adhesively bonded composite repairs on cracked aluminum panels. Proceedings of the FAA/NASA International Symposium on Advanced Structural integrity for Airframe Durability and Damage Tolerance, NASA conference publication 3274, Part1, 1994, 33-48.

[15] Schubbe, J.J, Mall, S.S. Modelling of cracked thick metallic structure with bonded composite patch repair using three-layer technique. Composite Structures 45(3), 1999, 185-193.

[16] Wen P.H., Aliabadi, M.H., Young, A. Boundary element analysis of flat cracked panels with adhesively bonded patches. Engineering Fracture Mechanics 69, 2002, 2129-2147

[17] Papanikos P., Tserpes K.I., Labeas G., Pantelakis Sp. Progressive damage modelling of bonded composite repairs. Theoretical and Applied Fracture Mechanics 43, 2005, 189-198.

[18] Wang C.H., Rose L.R.F. On the design of bonded patches for one-sided repair. Proceedings of the 11th Int Conference on Composite materials, Gold Coast, Australia, 5, 1997, 347-356.

[19] Wang C.H., Callinan R.J., Rose L.R.F. Analysis of out-of-plane bending of a one-sided repair. International Journal of Solids and Structures 35(14), 1998, 1653-1675.

[20] Rose L.R.F. and Wang C.H. Analytical methods for designing composite repairs. Chapter 7 in Advances in the bonded composite repair of metallic aircraft structure. Baker A.A., Rose L.R.F, Jones R., eds. Elsevier, 2002.

[21] Romilly D.P., Clark R.J. Damage tolerance analysis and testing of unbalanced bonded composite repairs for aluminum airframes. SAE 05-AMT-41, 2005.

[22] Volkersen O. Rivet strength distribution in tensile-stressed rivet joints with constant cross-section. Luftfahrforschung 15(1), 1938, 41-47

[23] Goland M., Reissner E. The stresses in cemented joints. Journal of Applied Mechanics – Transactions of the ASME 66, 1949, A17-A27.

[24] Kotousov A., Wang C.H. Fundamental solutions for the generalized plane strain theory. International Journal of Engineering Science 40, 2002, 1775-1790.

[25] Clark R.J., Romilly D.P. Bending of transversally isotropic generalized plane strain plates with reinforced cracks. Accepted by The International Journal of Fracture, 2006.

[26] Joseph P.F., Erdogan F. Surface crack problems in plates. International Journal of Fracture 41, 1989, 105-131.

[27] Joseph P.F., Erdogan F. Plates and shells containing a surface crack under general loading conditions. NASA contractor report 178232, NASA Langley Research Center, 1987.

[28] Clark R.J., Romilly D.P. Experimental study of a bonded composite repair. 2002 CSME Forum, May 21-24, Kingston, Ontario, Canada, 2002.

[29] Clark R.J., Romilly D.P. Non-linear bending study of hybrid aluminum and boron-epoxy bonded joints. CANCOM 2003, Ottawa, Ontario, Canada, 2003.

[30] Duong C.N., Wang C.H. On the characterization of fatigue crack growth in a plate with a single-sided repair. Transactions of the ASME 126, 2004, 192-198.

Chapter 6: Elastic analysis of hybrid bonded joints and bonded composite repairs*

D.P. Romilly and R.J. Clark

University of British Columbia Department of Mechanical Engineering

6.1 Introduction

In this chapter, the authors extend the closed-form bonded joint linear elastic analysis method of Delale et al [15] and Bigwood and Crocrombie [7] to include the composite deformation mechanisms and the thermal residual strains that arise in hybrid metal-composite joints such as those presented by bonded composite repairs applied to metallic aircraft structures. The analytical predictions for the adhesive stresses and the compliance are compared to the results of a linear elastic finite element model that has itself been validated by comparison with experimental results. The results are applied to the problem of coupled linear extension and bending of a bonded composite repair applied to a cracked aluminum substrate. The resulting stress intensity factor and crack opening displacement in the repaired plate are compared to the results of a three-dimensional finite element analysis, and also exhibit excellent results. Throughout the text, observations are made regarding the practical application of the results to failure prediction in hybrid joints, whereby the authors demonstrate the need for consistency in the analytical methods used to determine the fatigue and failure of composites from the coupon level to the analysis of the final structural details.

A bonded composite aircraft repair consists of a composite patch that is adhesively bonded to an underlying aluminum plate. The result is a hybrid structure with significantly mismatched adherends that will exhibit significant thermal residual strains and nonlinear deformation (stress stiffening) under applied tensile loads. In the damage tolerance analysis of such a repair, the stiffness of the structure and the stresses in the adhesive and the composite patch all require accurate evaluation. Accordingly, improved methods are required to analyse hybrid bonded joints with mismatched adherends and account for secondary effects such as coupled extensional and bending response, shear deformation, and axial adhesive stresses. In this paper, the authors extend and enhance the elastic analysis of Delale et al. [15] and Bigwood and Crocombe [7] to include the

---

* A version of this chapter has been accepted for publication. D.P. Romilly, R.J. Clark, "Elastic analysis of hybrid bonded joints and bonded composite repairs", Composite Structures.

effects of orthotropic adherends, adherend lateral shear deflection, transverse (through-thickness) adherend shear deformation caused by adhesive shear stresses (often termed adherend shear lag), transverse deformation of the adherends caused by adhesive peel stresses (peel lag), adhesive longitudinal stresses, and thermal stresses resulting from coefficient of thermal expansion mismatches, all of which may be included within their analysis method without raising the order of the governing equations. The enhanced hybrid bonded joint analysis method uses a linear elastic analysis to calculate the strength and compliance of the repair in the region of the underlying crack. The strain energy release rate and stress intensity values in the adhesive are then calculated from the stresses in the adhesive using the method of Joseph and Erdogan [9], and the results are verified against finite element model results for a single-lap joint geometry. The results are then applied to the linear analysis of a bonded repair to show the effectiveness of the resulting design equations.

The elastic analysis of bonded joints is an important subject, particularly in the design of aircraft structures. The accurate evaluation of adhesive stresses has been critical to the application of safe-life and damage tolerance methodologies to the airworthiness certification of such structures. In practice, four general methods are available to reduce the adhesive stresses in a joint: adherend tapering, increasing the adhesive thickness, decreasing the adhesive modulus, and the choice of an adequate overlap length. Also, due to the relatively high rate of crack growth in an adhesive joint, it is generally desired to keep the working stresses below a fatigue threshold. In the bonding of metal sheets, failure criteria for the sheets are usually easy to obtain and the elastic response of the isotropic adherends is easily modelled. In addition, the plates are often matched in stiffness, reducing the complexity of the analysis. For composite-composite bonded joints, the failure criteria and analysis requirements of the joint become complex as low-energy composite failure modes (such as interply delamination and fibre-buckling) become factors in the life of the structure, and the composite sheets require modeling as orthotropic materials to reflect the composition of the plates. For a composite repair applied to a metal plate, the panels being joined are often well matched in terms of extensional stiffness, but poorly matched in terms of bending stiffness. In addition, composite failure modes are a major concern, and physical testing or reference to physical tests is required to rule them out. For most applications of bonded joining during original manufacture, whether metal-metal or composite-composite, designers take significant measures to reduce peel stresses (e.g. adherend tapering), thus reducing or eliminating the risk of peel-induced failures. The result is that the original structure can generally be designed according to fail-safe principles. In the application of bonded composite repairs to metal structures, in the region around the repaired crack, the joint cannot be tapered, and it is typically not desirable to increase the thickness or compliance

of the adhesive to reduce the stresses as this will reduce the crack-stopping ability of the repair. Accordingly, composite delamination or adhesive disbonding may result near the repaired crack. Damage tolerance analysis is therefore necessary, and a method is required to predict the rate of damage progression and the load at failure. Finally, since the joint is typically a hybrid of aluminum and composite materials, the thermal expansion properties of the adherends are mismatched and the joint experiences large thermal residual strains from both patch application and temperature changes in service. In this paper, the authors develop a methodology to allow the accurate evaluation of stresses in hybrid bonded joints. To demonstrate the utility of the method, the results are applied to the analysis of a bonded composite repair. The methods developed should also be of use in the analysis of other composite-metal joints such as metal inserts for fastening of composite structures.

6.2 Background

Bonded joints are widely used in many industries, and accordingly much effort has been expended on characterizing their mechanics. The first effective analyses of the stresses in bonded joints are due to Volkersen [1] and to Goland and Reissner [2], by which the tensile and bending response are assumed to be linear and independent, and second and fourth order ordinary differential equations may be formed and solved for the shear and peel (transverse normal) stresses in the adhesive. In these analyses, the adhesive is assumed to act as a series of shear and tension springs, and the adherends are modelled as simple beams in tension and bending. These models have proven effective in the analysis and understanding of the mechanics of bonded joints. Models based on these equations have been adapted to many applications, usually by examining the boundary conditions specific to the particular application. For composite-composite joints, Renton and Vinson [5] have modified the equations to account for the lay-up of the adherends, and Jones et al. [16] have developed modifications to account for the relatively low in-plane shear stiffness and transverse or peel stiffness of composite adherends. For aluminum aircraft structures, Hart-Smith [e.g. 3] has used the basic bonded joint models to develop widely used design equations and failure criteria considering both elastic and perfectly plastic adhesive response. In the field of bonded composite repair of aluminum aircraft structures, Australian researchers have used the methods of Hart-Smith to characterize the strength and stiffness of the repair as it bridges the underlying crack [e.g. 14, 11].

Improved models for bonded joints have been developed to account for secondary effects that lead to coupling of the tensile and bending responses of the structure, to explicitly consider the equilibrium and stress-free boundary condition of the adhesive, and to include variations in the distribution of adhesive stresses through the thickness of the adhesive. Equilibrium requires the shear and bending response of the joint to be

coupled, as the adhesive shear stresses act on the face of the adherends and therefore must induce bending. Renton and Vinson [4] have developed a higher-order analytical model to examine the effects of adhesive equilibrium and the stress-free boundary condition, and predicted that the actual peak adhesive shear stress was shifted inboard from the edge of the joint and reduced when compared to the value found by traditional analysis methods. It should be noted that their method did not include coupling of the shear and bending responses of the joint, which has a significant effect on the stress distribution. Using an alternate approach, Allman [6] has expressed the stresses in the joint as a set of stress functions, and, by minimizing the strain energy in the joint, developed solutions that satisfied the adhesive stress free boundary condition and allowed the satisfaction of the full equilibrium equations for the adherends. Adams and Mallick [13] used this approach to develop a simple one-dimensional finite element solution that is easier to apply and to extend to nonlinear or viscoelastic adhesive response than closed-form bonded joint formulations. They found that, while the energy minimization method predicts the vanishing stresses at the edge and the stresses in the bulk of the joint, it generally under-predicts the peak stresses. In other work, Delale et al [15] extended the classical analysis of a bonded joint to include coupling between bending and extension, which resulted in modified constitutive equations for the adhesive that include the longitudinal stresses in the adhesive, derived from the average extensional strains in the adherends. Their results were shown to be accurate when compared to detailed finite element results for the adhesive stresses at the edge of a bonded joint. This allowed them to make the significant observation that it is not important to impose a stress-free boundary condition at the edge of the adhesive, since it is well known that the peak stresses occur at the singularity at the interface of the adherend and adhesive at the extreme edge of the joint. Bigwood and Crocombe [7] subsequently used an equivalent approach to test and develop design equations for bonded joints, but did not include the effects of mismatched adherend thermal expansion coefficients or the presence of adhesive axial stresses in their analysis.

In this paper, the authors modify the analysis techniques of Delale et. al., and Bigwood and Crocrombe to characterize the performance of bonded composite repairs. A bonded composite repair consists of a filamentary composite reinforcement that is bonded to a damaged or weakened structure to reduce stresses and prevent or reduce continuing damage growth, as shown in Figure 6-1. When the repair patch is bonded to only one side of a cracked structure, its presence induces significant out-of-plane bending by offsetting the load path. Bending increases the stress intensity in the underlying crack and causes adhesive peel stresses and bending of the repair that, if not accounted for in the design of the bonded structural repair, could lead to rapid failure.

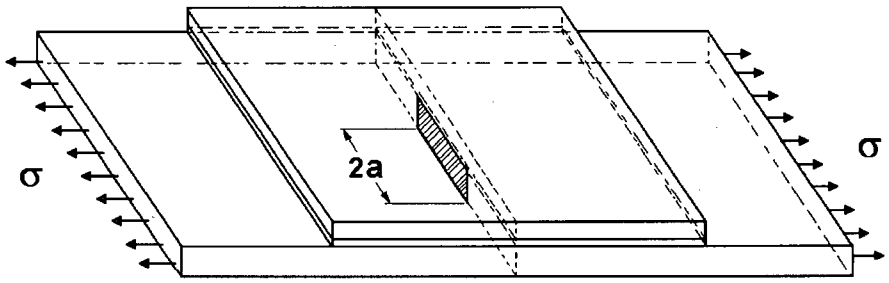

Figure 6-1: An unbalanced repair

There is much interest in the application of unbalanced repairs, as often only one face of a structure is exposed. In many cases the interior structure of the aircraft does not provide significant restraint against bending, potentially leading to rapid disbonding and composite and/or composite matrix failures. To design and certify single-sided repairs, closed-form methods are needed to assess the effects of bending on the rate of failure of the repaired structure, but perhaps more importantly, methods are required to assess the life and strength of the repair itself under bending and transverse normal (peel) stresses. Accordingly, the authors seek to develop closed-form solutions for the compliance of the bonded joint (characterizing its ability to stop the growth of the underlying crack) and the stress distribution in the adhesive and the composite repair.

6.3 Linear bonded joint formulation

In this section, the elastic analysis of Delale et. al. [15] and Bigwood and Crocombe [7] is extended to include phenomena that are critical to the understanding of the mechanics of hybrid composite-metal joints. These phenomena include: shear and peel deformation of the adherends, complementary shear of the adherends caused by the large bending stress gradients near the ends of the joint, pressurization of the adhesive due to out-of-plane and longitudinal constraint, and thermal residual strains. We begin with the definition of an element of the adherend/adhesive sandwich, the external loads that act upon it, and the internal (adhesive) stresses that hold it together. Figure 6-2 illustrates such an element.

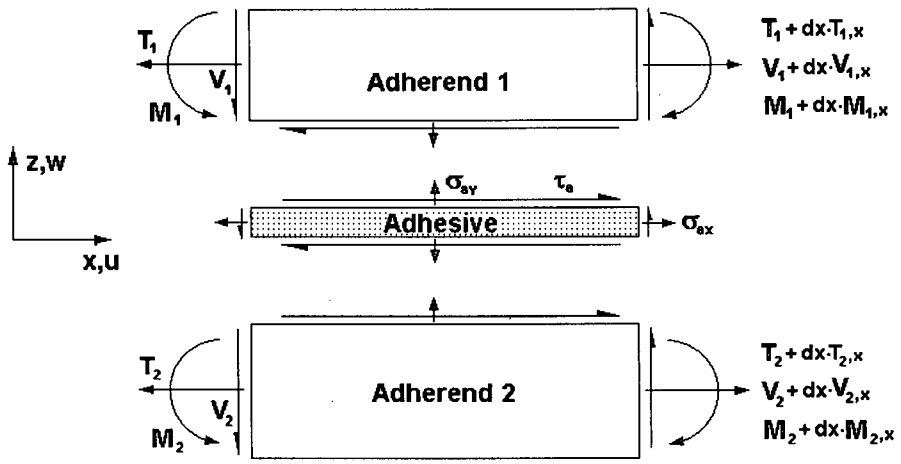

Figure 6-2: Hybrid bonded joint element

In the analysis that follows, the joint can be analysed in either plane stress or plane strain by choosing 'effective' elastic properties for the adherends and adhesive. The derivation will be carried out assuming that plane stress conditions exist. A simple substitution as follows will produce a plane strain analysis for an orthotropic material. For the plane strain case, it is assumed that the adherends are specially orthotropic, with vanishing through-thickness stresses.

$$E_i = \begin{cases} E_L & plane\ stress \\ \dfrac{E_L}{1-\nu_{TL}\nu_{LT}} & plane\ strain' \end{cases} \qquad E_a = \begin{cases} E_a & plane\ stress \\ \dfrac{E_a}{1-\nu_a^2} & plane\ strain \end{cases} \tag{1 a,b}$$

Similarly, the shear and transverse modulus for the adherends are expressed as follows.

$$G_i = G_{LT}, \qquad E_{Ti} \tag{2 a,b}$$

For adherends of thickness h, the plate bending stiffness may now be defined.

$$D_1 = \frac{E_1 h_1^3}{12}, \qquad D_2 = \frac{E_2 h_2^3}{12} \tag{3 a,b}$$

The strain at the interfaces between adhesive and adherends is given by the following. The third term in each of the equations accounts for 'shear lag', the deformation of the adherend caused by the adhesive shear stresses acting on the inner surface. The fourth term accounts for the lateral deformations caused by the shear force in each adherend.

$$u_{1,x} = \frac{T_1}{E_1 h_1} - \frac{h_1}{2}\frac{M_1}{D_1} - \frac{3h_1}{8}\frac{\tau_{,x}}{G_1} - \frac{V_{1,x}}{2G_1} \tag{4 a}$$

$$u_{2,x} = \frac{T_2}{E_2 h_2} + \frac{h_2}{2}\frac{M_2}{D_2} + \frac{3h_2}{8}\frac{\tau_{,x}}{G_2} - \frac{V_{2,x}}{2G_2} \qquad (4\text{ b})$$

The curvature at the interfaces between adhesive and adherends has been separated into two parts to include bending and shear deflections. A term has been included to account for deformation caused by peel stresses, or peel lag. These peel deformations should be accompanied by lateral deformations due to the Poisson effect, leading to some additional degree of coupling between the shear and peel responses of the joint. This has been neglected since the inclusion of the primary 'peel lag' term is already very much a secondary effect.

$$w^b_{1,xx} = -\frac{M_1}{D_1}, \qquad w^b_{2,xx} = -\frac{M_2}{D_2} \qquad (5\text{ a,b})$$

$$w^s_{1,x} = \frac{6V_1}{5G_1 h_1} - \frac{3h_1}{8}\frac{\sigma_{a,x}}{E_1}, \qquad w^s_{2,x} = \frac{6V_2}{5G_2 h_2} + \frac{3h_2}{8}\frac{\sigma_{a,x}}{E_2} \qquad (6\text{ a,b})$$

The shear and peel lag terms are found by assuming a linear variation of stresses in the adherends, as shown in Figure 6-3, and the shear strain will be:

$$u_{,z}(x,z) = \frac{\tau(x,z)}{G_i} = \frac{\tau_a}{G_i}\left(1 - \frac{z}{h_i}\right) \qquad (7)$$

The shear contribution to (4 a,b) follows by integration through the thickness. The peel lag terms in (6) follow by assuming a linear variation of transverse stresses. This method is due to Jones et. al. [16] who originally applied it to finite element analysis of repairs.

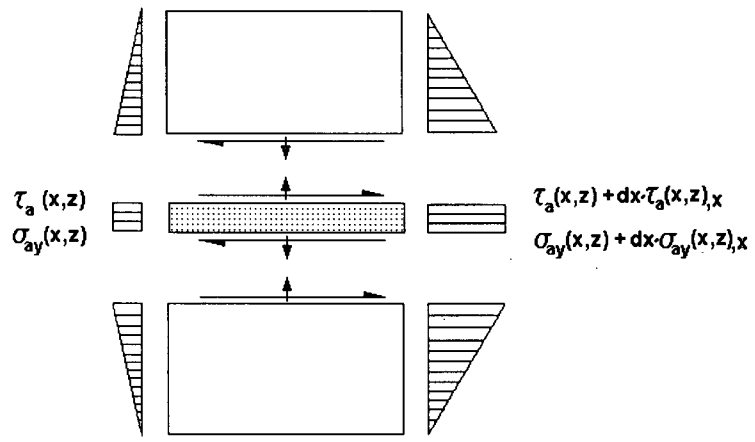

Figure 6-3: Assumed variation of transverse adherend stresses

Equations (4-6) describe the behaviour of the adherends. The adhesive is often modelled as independent shear and extensional springs, but one may instead model the adhesive by

employing the full form of the constitutive laws to relate the adhesive stresses to the relative displacements of the adherends.

$$\tau_a = \frac{G_a}{t_a}(u_1 - u_2), \qquad \sigma_{ax} = E_a\left(\frac{u_{1,x} + u_{2,x}}{2}\right) + \nu_a \sigma_{ay} \tag{8 a,b}$$

$$\sigma_{ay} = \frac{E_a}{t_a}\left(w_1^s - w_2^s + w_1^b - w_2^b\right) + \nu_a \sigma_{ax} \tag{8 c}$$

The last set of equations required to perform the analysis arise from adherend equilibrium.

$$T_{1,x} = \tau_a, \qquad T_{2,x} = -\tau_a \tag{9 a,b}$$

$$V_{1,x} = \sigma_a, \qquad V_{2,x} = -\sigma_a \tag{9 c,d}$$

$$M_{1,x} = V_1 - \frac{h_1 + t_a}{2}\tau_a, \qquad M_{2,x} = V_2 - \frac{h_2 + t_a}{2}\tau_a \tag{9 e,f}$$

To develop the governing equations, it proves convenient to introduce two functions.

$$\phi = \int \tau_a dx, \qquad \psi = \iint \sigma_a dx dx \tag{10 a,b}$$

The governing equations may be found as follows. First, eliminate σ_{ax} from (8 b,c) and then substitute ϕ, ψ for the peel and shear stresses in (4), (6), (8), and (9). Eliminate the displacements from (8) using (4), (6), and (8), and then eliminate the forces and moments using the equilibrium equations (9). The following ordinary differential equations arise:

$$K_0 \phi_{,xx} - K_1 \phi = -K_2 \psi - K_3 \psi_{,xx} \tag{11 a}$$

$$K_4 \psi_{,xxxx} - K_5 \psi_{,xx} + K_6 \psi = -K_7 \phi_{,xxxx} + K_8 \phi_{,xx} + K_9 \phi \tag{11 b}$$

The constants for the shear equation are given as follows, and account for shear lag of the adhesive and adherends, the extensional stiffness of the adherends, shear stresses caused by rotation of the adherends, and shear deformation of the adherends.

$$K_0 = \frac{h_1}{2G_1} + \frac{t_a}{G_a} + \frac{h_2}{2G_2} \tag{12 a}$$

$$K_1 = \frac{1}{E_1 h_1} + \frac{1}{E_2 h_2} + \frac{h_1(h_1 + t_a)}{4D_1} + \frac{h_2(h_2 + t_a)}{4D_2} \tag{12 b}$$

$$K_2 = \frac{6}{E_1 h_1^2} + \frac{6}{E_2 h_2^2} \tag{12 c}$$

$$K_3 = \frac{1}{2G_1} - \frac{1}{2G_2} \tag{12 d}$$

The constants for the peel equation follow and account for peel lag of the adherends and adhesive, adherend shear deflections, bending deflection, transverse adhesive stresses, and moments resulting from adhesive shear acting on the edge of the adherend. All terms that include ν_a arise from the inclusion of the longitudinal adhesive stress, σ_{ax}.

$$K_4 = \frac{h_1}{2E_{T1}} + \frac{t_a\left(1-\nu_a^2\right)}{E_a} + \frac{h_2}{2E_{T2}} + \frac{\nu_a t_a}{4}\left(\frac{h_1}{D_1} + \frac{h_2}{D_2}\right) \tag{12 e}$$

$$K_5 = \frac{6}{5}\left(\frac{1}{G_1 h_1} + \frac{1}{G_2 h_2}\right) - \frac{\nu_a t_a}{4}\left(\frac{h_1}{D_1} + \frac{h_2}{D_2}\right) \tag{12 f}$$

$$K_6 = \frac{1}{D_1} + \frac{1}{D_2} \tag{12 g}$$

$$K_7 = \frac{\nu_a t_a}{4}\left(\frac{h_1}{G_1} - \frac{h_2}{G_2}\right) \tag{12 h}$$

$$K_8 = 2\nu_a t_a\left(\frac{1}{E_1 h_1} - \frac{1}{E_2 h_2}\right) \tag{12 i}$$

$$K_9 = \frac{1}{2}\left(\frac{h_1 + t_a}{D_1} - \frac{h_2 + t_a}{D_2}\right) \tag{12 j}$$

These defined constants are now available for use in quantifying the parameters of the characteristic equation for the system as developed in the following section.

6.3.1 Solution and boundary conditions

Introducing the trial functions $\phi = Ae^{\lambda x}$ and $\psi = Be^{\lambda x}$, the characteristic equation for the system may be found from (11 a) and (11 b).

$$\lambda^6 - b\lambda^4 + c\lambda^2 - d = 0 \tag{13}$$

The coefficients follow.

$$b = \frac{K_1 K_4 + K_0 K_5 + K_2 K_7 - K_3 K_8}{K_0 K_4 - K_3 K_7} \tag{14 a}$$

$$c = \frac{K_0 K_6 + K_2 K_8 + K_1 K_5 + K_3 K_9}{K_0 K_4 - K_3 K_7} \tag{14b}$$

$$d = \frac{K_1 K_6 - K_2 K_9}{K_0 K_4 - K_3 K_7} \tag{14 c}$$

Setting $\lambda^2 = \theta + b/3$, the equation (13) may be expressed as a 'depressed' cubic.

$$\theta^3 + m\theta = n, \quad m = c - \frac{b^2}{3}, \quad n = d - \frac{bc}{3} + \frac{2b^3}{27} \tag{15}$$

The roots of the depressed cubic may be found as follows. Note that q is complex.

$$q = \left(\frac{n}{2} + \frac{\sqrt{3}}{18} \sqrt{4m^3 + 27n^2} \right)^{\frac{1}{3}} \tag{16}$$

$$\theta = \left\{ \begin{array}{c} q - \dfrac{m}{3q} \\ -\dfrac{1}{2}\left[q - \dfrac{m}{3q} + i\sqrt{3}\left(q + \dfrac{m}{3q} \right) \right] \\ -\dfrac{1}{2}\left[q - \dfrac{m}{3q} - i\sqrt{3}\left(q + \dfrac{m}{3q} \right) \right] \end{array} \right\} \tag{17}$$

The roots of (13) are given by $\lambda = \pm\sqrt{\theta + b/3}$. The solutions for ϕ and ψ follow.

$$\phi = \sum_i A_i e^{\lambda_i x} \tag{18 a}$$

$$\psi = a\phi_{,xxxx} + b\phi_{,xx} + c\phi \tag{18 b}$$

The constants in (18 b) arise from the governing equations (11 a,b).

$$a = \frac{K_4 K_0 - K_7 K_3}{K_3 K_6 + \dfrac{K_2}{K_3}(K_3 K_5 + K_2 K_4)} \tag{19 a}$$

$$b = \frac{K_3 K_8 - K_1 K_4 - \dfrac{K_0}{K_3}(K_3 K_5 + K_2 K_4)}{K_3 K_6 + \dfrac{K_2}{K_3}(K_3 K_5 + K_2 K_4)} \tag{19 b}$$

$$c = \frac{K_3 K_9 + \dfrac{K_1}{K_3}(K_3 K_5 + K_2 K_4)}{K_3 K_6 + \dfrac{K_2}{K_3}(K_3 K_5 + K_2 K_4)} \tag{19 c}$$

The adhesive stresses follow easily from the definitions (10 a,b).

$$\tau_a = \phi_{,x}, \qquad \sigma_a = \psi_{,xx} \tag{20 a,b}$$

The axial adhesive stress may be calculated from (8 b).

$$\sigma_{ax} = \frac{E_a}{\nu_a t_a}\left[K_8\phi - K_7\phi_{,xx}\right] - \frac{E_a}{4}\left[\left(\frac{h_1}{D_1}+\frac{h_2}{D_2}\right)\psi + \left(\frac{1}{G_1}+\frac{1}{G_2}\right)\psi_{,xx}\right] + \nu_a\psi_{,xx} \tag{21}$$

It remains to calculate the constants A_i given the forces applied to each end of each adherend. Here, we will examine the case of a very long joint, by keeping only those roots that vanish as $x \to \infty$. To obtain the solution for a finite length of joint, one must retain all of the eigenvalues and consider the forces at the far end of the joint. For the very long joint, the boundary conditions may be expressed as follows.

$$T_1(0) = T_1, \qquad T_2(0) = T_2, \qquad T(\infty) = T_1 + T_2 \tag{22 a}$$

$$V_1(0) = V_1, \qquad V_2(0) = V_2, \qquad V(\infty) = V_1 + V_2 \tag{22 b}$$

$$M_1(0) = M_1, \quad M_2(0) = M_2, \quad M(\infty) = M_1 + M_2 + \delta(T_1 - T_2) + x(V_1 + V_2) \tag{22c}$$

The method of Bigwood and Crocombe will be used to find the integration constants, thus developing the expressions relating the adhesive stresses to the applied loads. From the derivative of the adhesive shear constitutive equation (8 a), with substitution for the adherend deflections from equations (4 a,b), the first equation is obtained as

$$K_0\phi_{,xx} + K_3\psi_{,xx} = \frac{T_1}{E_1 h_1} - \frac{T_2}{E_2 h_2} - \frac{M_1 h_1}{2D_1} - \frac{M_2 h_2}{2D_2}. \tag{23}$$

From the second derivative of the adhesive peel constitutive equation (8 c), with substitution of the adherend shear and bending deflections from equations (5,6) the second equation is obtained as

$$K_4\psi_{,xxxx} - K_5\psi_{,xx} - K_8\phi_{,xx} + K_7\phi_{,xxxx} = -\frac{M_1}{D_1} + \frac{M_2}{D_2}. \tag{24}$$

From the third derivative of the adhesive peel constitutive equation (8 c), with substitution of the adherend deflections from equations (5) and (6), and equilibrium equation (9), the final equation is obtained. For a very long joint with boundary conditions that satisfy equilibrium at $x = 0$, equations (23)-(25) allow the definition of a set of three linear equations that may be solved for the integration constants. For a finite-length joint, equations (23)-(25) must also be defined for the far end, increasing the number of equations from three to six.

$$K_4\psi_{,xxxx} - K_5\psi_{,xx} - K_9\phi - K_8\phi_{,xx} + K_7\phi_{,xxxx} = -\frac{V_1}{D_1} + \frac{V_2}{D_2} \tag{25}$$

For loading systems that require the existence of forces or moments acting at a remote part of the joint (i.e. as $x \to \infty$), a complimentary solution is required to satisfy the far-field boundary conditions. For the unbalanced shear condition ($V_1 - V_2 \neq 0$), the limit solution has little physical meaning. Accordingly the complementary solution will be examined in the absence of the shear forces. As $x \to \infty$, the loads carried by the adherends do not vary and adherend equilibrium (8) requires the shear and peel stresses to vanish. The adherend deformations simplify as follows.

$$u_{1,x} = \frac{T_1}{E_1 h_1} - \frac{h_1}{2}\frac{M_1}{D_1}, \qquad u_{2,x} = \frac{T_2}{E_2 h_2} + \frac{h_2}{2}\frac{M_2}{D_2} \tag{26 a,b}$$

$$w^b_{1,xx} = -\frac{M_1}{D_1}, \qquad w^b_{2,xx} = -\frac{M_2}{D_2} \tag{27 a,b}$$

Vanishing stresses force the adhesive constitutive equations to take the following form.

$$u_1 - u_2 = 0, \quad w^b_1 - w^b_2 + \nu_a t_a \left(\frac{u_{1,x} + u_{2,x}}{2}\right) = 0 \tag{28 a,b}$$

These may be expressed in terms of the forces by substitution from (26) and (27).

$$\frac{T_1}{E_1 h_1} - \frac{T_2}{E_2 h_2} = \frac{h_1}{2}\frac{M_1}{D_1} + \frac{h_2}{2}\frac{M_2}{D_2}, \qquad \frac{M_1}{D_1} - \frac{M_2}{D_2} = 0 \tag{29 a,b}$$

Equations (29 a,b) and the third parts of equations (22 a,b) form a set of equations from which the force and moment in the adherends may be determined. The results follow.

$$T_1 = \frac{\frac{1}{2}\left(\frac{h_2 + h_1}{D_1 + D_2}\right)\left(\delta T(\infty) + M(\infty)\right) + \frac{T(\infty)}{E_2 h_2}}{\frac{1}{E_1 h_1} + \frac{1}{E_2 h_2} + \left(\frac{h_1 + h_2}{D_1 + D_2}\right)\delta} \tag{30 a}$$

$$T_2 = T(\infty) - T_1 \tag{30 b}$$

$$M_1 = \left(\frac{D_1}{D_1 + D_2}\right)\left(M(\infty) - \delta(T_1 - T_2)\right) \tag{30 c}$$

$$M_2 = \frac{D_2}{D_1} M_1 \tag{30 d}$$

Where $\delta = \frac{h_1}{2} + t_a + \frac{h_2}{2}$. The adhesive axial stress is given as follows:

$$\sigma_{ax} = \frac{E_a}{2}\left(\frac{T_1}{E_1 h_1} + \frac{T_2}{E_2 h_2} - \frac{h_1 M_1}{2D_1} + \frac{h_2 M_2}{2D_2} \right) \tag{31}$$

6.3.2 Thermal strains

Thermal strains often arise in hybrid composite joints due to the elevated temperature required to cure the adhesive, and due to thermal loading during service. During the cooling phase of the cure cycle for thermally activated adhesives, the temperature will drop below the adhesive glass-transition temperature, T_g, and residual strains will develop. As creep occurs near T_g, it is common practice to use an effective stress free temperature, T_{sf}, to assist in the analysis of a joint. The effective stress free temperature T_{sf} may be determined from experiments in which a specimen is heated until the warping due to thermal strains is eliminated. Thermal strains may be calculated by adding an additional complementary solution to the homogeneous solution from previous sections. The thermal load, ΔT, is the difference between T_{sf} and the service temperature. One may calculate the interfacial adherend strains as follows.

$$u_{1,x} = \frac{T_1}{E_1 h_1} - \frac{h_1}{2}\frac{M_1}{D_1} - \frac{3h_1}{8}\frac{\tau_{,x}}{G_1} + \alpha_1 \Delta T \tag{32 a}$$

$$u_{2,x} = \frac{T_2}{E_2 h_2} + \frac{h_2}{2}\frac{M_2}{D_2} + \frac{3h_2}{8}\frac{\tau_{,x}}{G_2} + \alpha_2 \Delta T \tag{32 b}$$

Using this new definition of the extensional strains, the governing equations follow:

$$K_0 \phi_{,xx} - K_1 \phi = -K_2 \psi - K_3 \psi_{,xx} + (\alpha_1 - \alpha_2)\Delta T \tag{33 a}$$

$$K_4 \psi_{,xxxx} - K_5 \psi_{,xx} + K_6 \psi = -K_7 \phi_{,xxxx} + K_8 \phi_{,xx} + K_9 \phi \tag{33 b}$$

The complementary solution requires consideration of polynomials of sufficient order to satisfy the forcing function. As the temperature is uniform, it is sufficient for ϕ, ψ to be constant, and the adhesive stresses will vanish. The method used in the previous section for the remote loading case is applicable, with the adherend deformations described by (32 a,b). The forces are required to obey the following relationships.

$$\left(\frac{T_1}{E_1 h_1} - \frac{T_2}{E_2 h_2} \right) - \frac{1}{2}\left(h_1 \frac{M_1}{D_1} + h_2 \frac{M_2}{D_2} \right) + (\alpha_1 - \alpha_2)\Delta T = 0 \tag{34 a}$$

$$\frac{M_1}{D_1} - \frac{M_2}{D_2} = 0 \tag{34 b}$$

The remaining consideration is equilibrium. For unrestrained thermal expansion, the net force and moment acting on a cut through the joint must both vanish.

$$T_1 + T_2 = 0, \quad M_1 + M_2 + (T_1 - T_2)\delta = 0 \tag{35 a,b}$$

As in the previous section, equations (34) and (35) may be solved for the forces and moments in the adherends.

$$T_1 = -T_2 = -\frac{\alpha_1 - \alpha_2}{\frac{1}{E_1 h_1} - \frac{1}{E_2 h_2} + \delta \frac{h_1 + h_2}{D_1 + D_2}} \Delta T \tag{36 a}$$

$$M_1 = \frac{-2D_1}{D_1 + D_2} T_1, \qquad M_2 = \frac{D_2}{D_1} M_1 \tag{36 b,c}$$

The axial adhesive stress may be determined from the axial strains.

$$\sigma_{ax} = \frac{E_a}{2}\left(\frac{T_1}{E_1 h_1} + \frac{T_2}{E_2 h_2} - \frac{h_1 M_1}{2D_1} + \frac{h_2 M_2}{2D_2} + (\alpha_1 + a_2 - 2\alpha_a)\Delta T \right) \tag{37}$$

The thermal strains will result in adhesive stresses and accompanying adherend deflections at the ends of a finite length joint, where the thermal forces and moments on the adherends are required to vanish. These stresses and deflections can be calculated by applying the thermal loads in equations (36 a-c) as boundary conditions in equations (23-25). The complete solution will then arise by superposition of the homogeneous and complementary (thermal) solution.

6.3.3 Joint failure

Given the techniques presented above, it is possible to calculate the strain energy release rate and stress intensity in the adhesive layer near the end of the joint. The total strain energy release rate is defined as follows, where dA is an increment in the area of the disbond or crack front.

$$G_T = \frac{d}{dA}(W - U) \tag{38}$$

Here, W is the potential of the externally applied loads, and U is the change in stored elastic energy. The standard calculation of G_T for a very long bonded joint is easily accomplished. Noting that the state of the joint is self-similar for an increment in disbond length, the energy released by crack extension may be determined by comparing a part of

the joint remote from the loaded end to the newly disbonded part. The segment far removed from the loaded end typically has no internal energy or loading, except in the presence of thermal residual strains, and the strain energy stored in the adhesive in the disbonded part is normally very small. G_T is then given by the energy balance in the disbonded part of the adherends.

$$G_T = \frac{1}{2}\left(\frac{T_1^2}{E_1 h_1} + \frac{T_2^2}{E_2 h_2}\right) + \frac{1}{2}\left(\frac{V_1^2}{G_1 h_1} + \frac{V_2^2}{G_2 h_2}\right) + \frac{1}{2}\left(\frac{M_1^2}{D_1} + \frac{M_2^2}{D_2}\right) \tag{39}$$

Calculation of G_T allows prediction of fracture or fatigue given test data for a joint with a very similar composition and loading. In practice, bonded joints are sensitive to loading mode, i.e. the relative proportions of energy associated with adhesive shear or peel. Consideration of mixed mode loading allows extrapolation of test data to different load cases, but not between joints of differing geometry or composition, even if the same adhesive is used. The reasoning is that the actual stresses and hence the stress intensity in the disbonding process zone are dependent upon the composition and geometry of the joint, including the adhesive thickness. Joint geometry plays a strong role in determining the actual stresses present in the part given a particular strain energy release rate. Accordingly, it is useful to partition the total strain energy release rate into opening and shear components.

$$G_T = G_I + G_{II} \tag{40}$$

The peel and shear strain energy release rates may be calculated using the method of Joseph and Erdogan [9], which is very convenient for this type of closed-form analysis. In round-robin testing for the Cracked Lap Shear (CLS) specimen, this method has been shown to provide results comparable to those obtained by other means, such as finite element analysis employing crack-closure techniques. The CLS specimen exhibits mixed-mode loading and non-linearity, and as such is a good test of the validity of the method. A description of the method and its application to this particular problem follows.

The strain energy release rate is identical under 'fixed-grip' and 'constant load' conditions for an elastic structure, and hence may be calculated by considering the change in stored elastic energy under 'fixed grip' conditions, where the external loads do no work and $dW = 0$. The strain energy release rate is then equal to the change in elastic strain energy for an increment in disbond size. The change in strain energy may be calculated by relaxing the adhesive stresses over an area $dA = wdb$, where w is the width of the joint and db is an increment in the length of the crack. It may be shown that for this condition, the change in strain energy in the adherends does not provide a contribution. As an example, consider an adherend acting under a shear stress, τ_a with 'fixed grips' at $x = 0$. The force, tensile stress, and strain in the adherend are:

$$T_1(x) = \tau_a w x, \qquad \sigma_1(x) = \tau_a \frac{x}{h_1}, \qquad \varepsilon_1(x) = \tau_a \frac{x}{h_1 E_1} \tag{41}$$

The change in strain energy in an adherend for an increment in crack growth follows.

$$\frac{dU_1}{dA} = -\frac{1}{2}\frac{d}{dA}\int_V \sigma_1(x)\varepsilon_1(x)dV = \frac{1}{2}\frac{\tau_a^2 db^2}{h_1 E_1} \tag{42}$$

In the limit, this quantity will vanish and only the strain energy released by the adhesive need be considered. The same result occurs for peel stresses and bending of the adherends. From the adhesive constitutive equations (8 a,b), we find the following.

$$G_T = -\frac{dU_a}{dA} = \frac{1}{2}\frac{d}{dA}\int_V \sigma_a(x)\varepsilon_a(x)dV = \frac{t_a}{2}\left(\frac{\sigma_{ay}^2 - 2\nu_a\sigma_{ay}\sigma_{ax} + \sigma_{ax}^2}{E_a} + \frac{\tau_a^2}{G_a}\right) \tag{43}$$

The separation of the peel and shear components follows by consideration of only the first term or the second term. This is essentially identical to the result found by Rice [12] for the strain energy release rate in an infinite strip containing a semi-infinite crack. In Rice's analysis, the deflection of the edges of the strip (i.e. the adherend/adhesive interface) is fixed at a constant value, and the energy released with a unit of crack growth is calculated based on the strain energy stored in a section of the strip well away from the crack. In Rice's analysis, the strain energy release rate is converted into stress intensity by applying the appropriate relationship to account for the degree of constraint through the width of the joint, i.e. by assuming a plane stress or a plane strain state. In fracture handbooks, this calculation is considered to be an exact, analytical result. The resulting opening and shear mode stress intensities are:

$$K_1^2 = \frac{t_a}{2}\left(\sigma_{ay}^2 - 2\nu_a\sigma_{ay}\sigma_{ax} + \sigma_{ax}^2\right), \qquad K_2^2 = \frac{t_a E_a}{2G_a}\tau_a^2 \tag{44 a,b}$$

In practice, the orientation and location of the crack within the adhesive layer, and the inelastic, environmental, and stress history dependent behaviour of the adhesive make it difficult to determine the precise state of the crack tip process zone. In addition, joints with a thin adhesive layer will experience elastic constraint in the process zone, resulting in a lower energy failure mode than a joint with a thicker adhesive layer. As this technique is a direct extension of the practice of using strain energy release rates, the same limitations on its use will apply, and it will only be applicable when test data is available for similar joints under similar environmental and loading conditions. When failure occurs along or near the adherend/adhesive interface, other issues such as stress concentrations around fibres and the compliance of the adherend may affect the crack tip stress field, and also result in a lower energy failure mechanism. These facts demonstrate the importance of applying a consistent analysis method from the coupon level through to

the analysis of structural details on in-service structures, and ensuring that the actual applied loading, geometry, and observed failure modes are also consistent with those input or predicted using the applied analysis.

6.4 Analysis of a bonded composite repair

Clark and Romilly [10] have developed design equations for the single-sided repair of cracked plates. The equations extend the analytical methods developed by Rose [14] for repair of cracked plates via double-sided repairs, and are based on a corrected form of the energy method of Wang and Rose [11] for determining the stress intensity for a crack repaired on one side. By this method, the efficiency of the repair is characterized by determining the stresses present in the reinforced plate in the vicinity of the crack, and then applying these stresses as crack-opening pressures in a crack-bridging analysis to determine the stress intensity for the repaired crack. The inputs to the crack bridging analysis are the stresses under the repair and the compliance of the repair as it bridges the crack. Here, the bonded joint analysis provided in Section 6.3 will be used to determine these quantities and the results will be tested against a two-dimensional finite element model. With these quantities in hand, the crack-bridging models described in [10] will be tested against a three-dimensional finite element model of a repair.

The AMRL (Australian Maritime Research Laboratory) specimen will be used to test the effectiveness of the models. This repair test article has been used by the Canadian National Research Council Institute for Aerospace Research (NRC-IAR) to evaluate environmental and load spectrum effects and by the authors to investigate thermal loading and structural mechanics. The specimens consist of boron-epoxy composite repairs applied to two cracked panels separated by a honeycomb core, and applied using Cytec FM-73M film adhesive. The authors have built bonded joint specimens to match the specifications of the AMRL specimen. Figure 6-4 shows the single lap joint specimen, which does not include a honeycomb bending restraint.

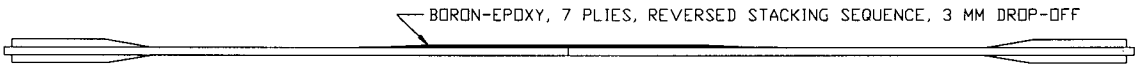

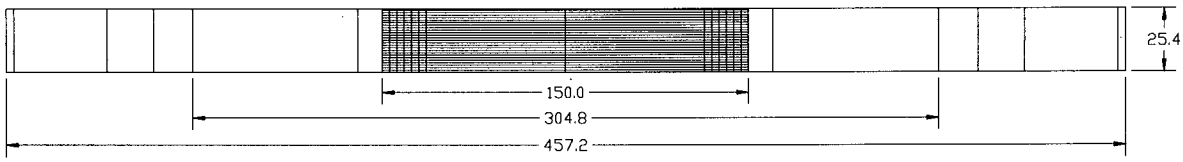

Figure 6-4: Single sided lap joint specimen

The material properties for the AMRL and lap joint specimens are summarized in Table 6-1, and will be used throughout the analyses presented below. The repair is made from layers of boron/epoxy. The result is a joint comprised of adherends that are balanced in extensional stiffness but not in bending. Differing thermal expansion coefficients also result in large thermal residual strains.

Property	Boron/Epoxy	FM-73M Adhesive	Aluminum Plate
Elastic Modulus (GPa)	$E_L = 210$ $E_T = 2.5$	$E = 2.14$	$E = 72.4$
Shear Modulus (GPa)	$G_L = 7.24$ $G_T = 1.0$	$G = 0.805$	$G = 27.2$
Poisson's Ratio	$\upsilon_L = 0.21$ $\upsilon_T = 0.019$	$\upsilon = 0.33$	$\upsilon = 0.33$
Thermal Expansion ($\mu\varepsilon/^0C$)	$\alpha_L = 4.61$ $\alpha_T = 25.87$	$\alpha = 50.0$	$\alpha = 23.45$
Thickness (mm)	t = 0.924	t = 0.25	t = 3.125

Table 6-1: Material properties and dimensions

The chosen adhesive thickness is near the high end of a practical working range of 0.125 to 0.25 mm [17]. This working range has been established because adhesive layers thinner than 0.125 mm tend to result in joints that are not very damage tolerant, while adhesive layers thicker than 0.25 mm are prone to the development of porosity during curing. Figure 6-5 is an illustration of a two-dimensional finite element model that will be used to test the analytical results from Section 6.3. Three parts of the structure are shown; (a) the cracked region of the lap joint, (b) the tapered region of the repair, and (c) the point of application of the load. This model has been validated against load-defection curves, strain gauge results, and lateral deflections obtained from experiments [21].

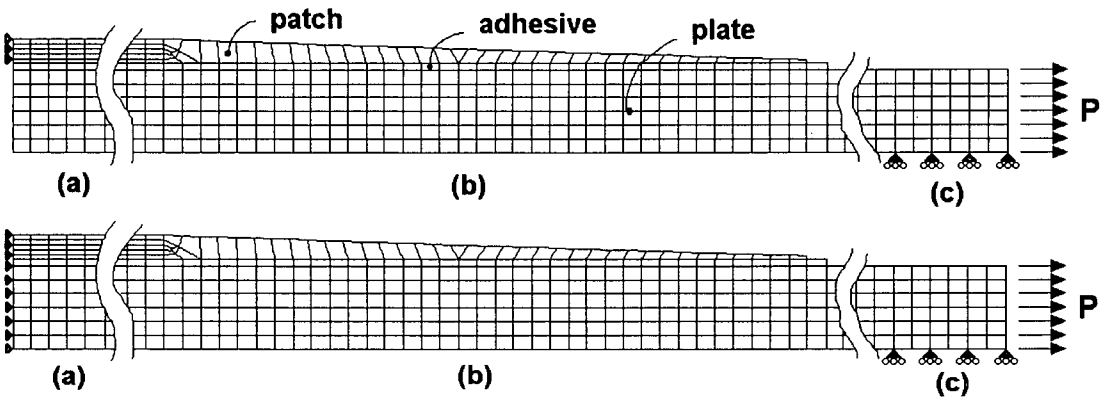

Figure 6-5: Lap joint finite element model

Results are reported for two versions of the model, the first including a crack under the repair, and the second, an uncracked version used to calculate the stresses under the repair. The model shown at the top of Figure 6-5 shows the cracked configuration, while the model on the bottom shows the uncracked configuration. Removal of the constraints on the left edge of the aluminum plate allows the crack to be modelled. The cracked configuration allows the investigation of the compliance of the repair and the adhesive stress as the repair bridges the crack.

6.4.1 Nominal stresses

The stresses in the repaired plate may be estimated using the two complementary solutions presented in Section 6-3, one for the applied loading, and one for the thermal stresses arising during the curing of the adhesive or thermal loading during service. The solution for remote loading is not significantly different from the bi-metallic strip model of Timoshenko [20], which has been used by Wang and Rose [11] to determine the stresses in the substrate under a repair. Figure 6-6 shows the nominal stresses for a $1\ MPa$ remote applied stress in the aluminum plate. This applied load is offset from the neutral axis of the repaired plate by a distance z_{na}, resulting in a moment that must also be included. The loads are given as follows:

$$T(\infty) = \sigma_{applied} h_2 \qquad M(\infty) = -2 z_{na} T(\infty) = \frac{-2S\delta}{1+S} \sigma_{applied} h_2 \qquad (45\ \text{a,b})$$

In Figure 6-6, finite element and closed-form equation results are shown for two cases: plane stress and plane strain. The difference is observed to be slight, as the composite patch is very compliant through both the width and thickness of the repair. The closed-form equations provide reasonable results, but there are significant differences due to the bending restraint at the grips of the specimen, which prevent it from bending as freely as the idealized geometry described by the theoretical model.

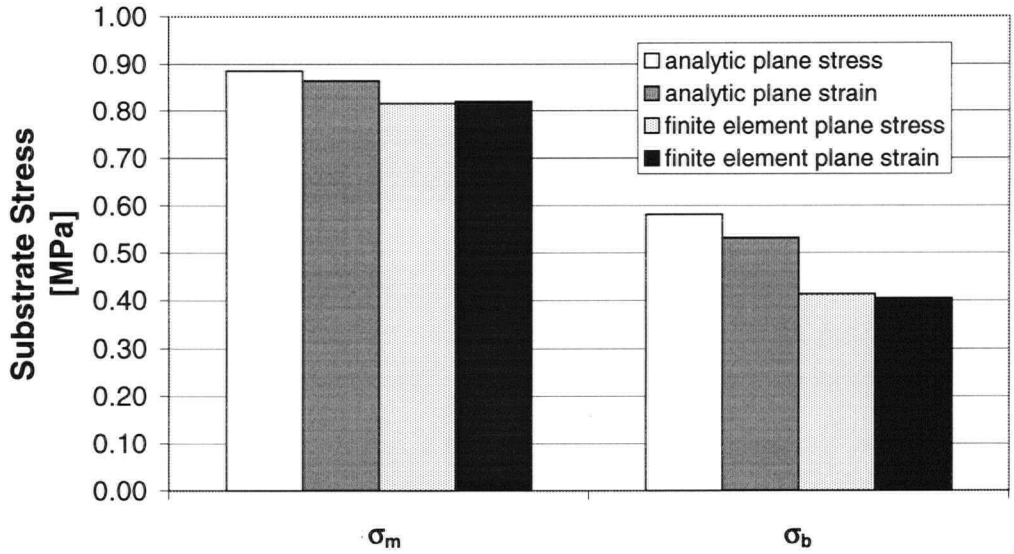

Figure 6-6: Substrate membrane and bending stresses under remote applied tension

The thermal stresses under the repair may be calculated by the methods of Section 6.3.2 using a stress-free temperature of $81^{o}C$ for the AMRL specimen [21]. Figure 6.7 shows the magnitude of the membrane and bending stresses in the substrate under the repair at an operating temperature of $20^{o}C$ when cured at $121^{o}C$. There are significant differences between the analytic and finite element model predictions, which arise due to two effects: 1) the rotational bending constraints included in the finite element model that simulate the effect of the mechanical grips on the actual test specimen, and 2) the effects of a finite patch and underlying plate. This highlights the importance of careful modelling of the bending effects and the influence of finite geometries.

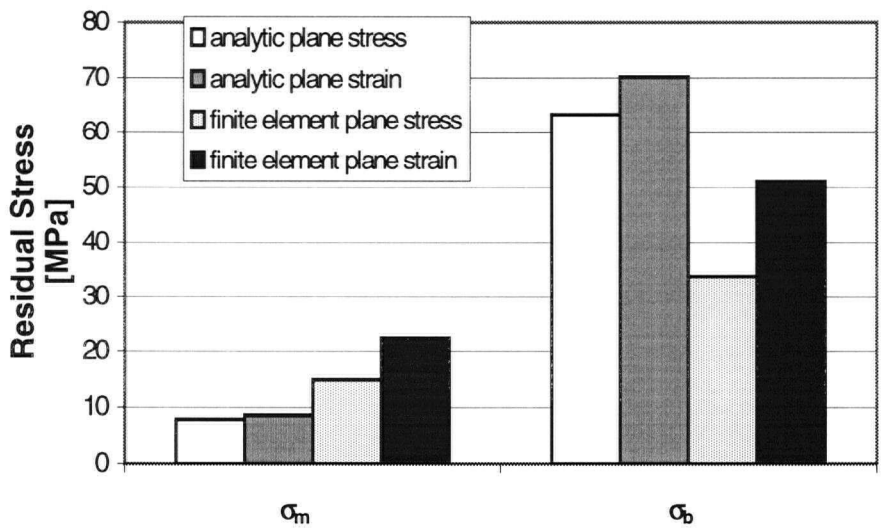

Figure 6-7: Substrate residual stresses at $20^{o}C$ for a $120^{o}C$ adhesive cure cycle

To determine the effectiveness of a repair, these stresses are assumed to act as crack opening pressures, and the repair is modelled as a set of springs bridging the crack faces.

6.4.2 Spring compliance and adhesive stresses

In this section the authors characterize the repair as it acts to bridge the crack in the underlying aluminum plate. The configuration analysed, shown in Figure 6-8, is a single-sided joint in which both adherends are free to bend. To model the symmetry condition at the centreline of the specimen, the composite repair is constrained in both bending and extension where it bridges the crack (i.e. at $x = 0$). The quantities of interest for the analysis include: the compliance of the structure under applied tensile and bending loads, the adhesive stresses, the accompanying adhesive strain energy release rates or stress intensity factors, and the stresses in the composite patch as it bridges the crack. The crack face loading shown in Figure 6-8 is a crack opening pressure that arises when the stresses determined in Section 6.4.1 are applied to any cracks that might exist under a repair.

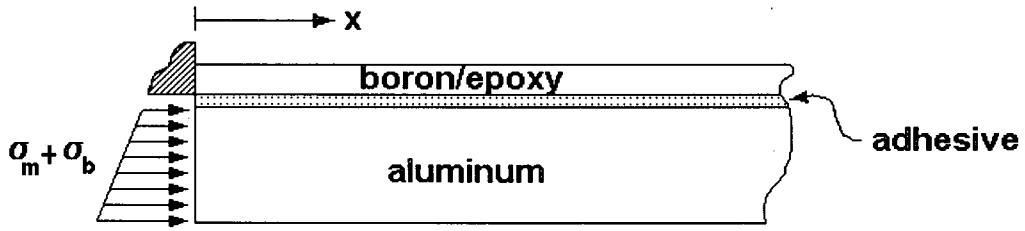

Figure 6-8: Model configuration for spring compliances

Two different loads will be applied to the aluminum plate, membrane and bending stresses of $1\,MPa$. Figures 6-9 and 6-10 compare the analytical results of Section 6.3 to adhesive stresses determined by finite element analysis for these two loading configurations, respectively. The plotted results generally illustrate good agreement between predicted adhesive stresses using both the analytical and FEA methods. The notable differences are a small over-prediction of the adhesive peel stresses and a corresponding small under-prediction of the peak shear stresses. There are two likely sources for this error: first, the analytical model does not include the stress-free adhesive boundary condition at x = 0, and second, the through-thickness variation of the adhesive and adherend stresses are assumed to act in a simple manner as shown in Figure 6.3. As per Delale et al [15] and Joseph and Erdogan [9] this does not preclude the use of this analytical method for the prediction of the failure of the bonded joint. Upon more global comparison of the results presented in the two figures, it is apparent that the stress distribution is dependent on the type of load applied, as well as the geometry and composition of the joint, thus making it difficult to apply fracture mechanics principles to bonded joints in a general manner.

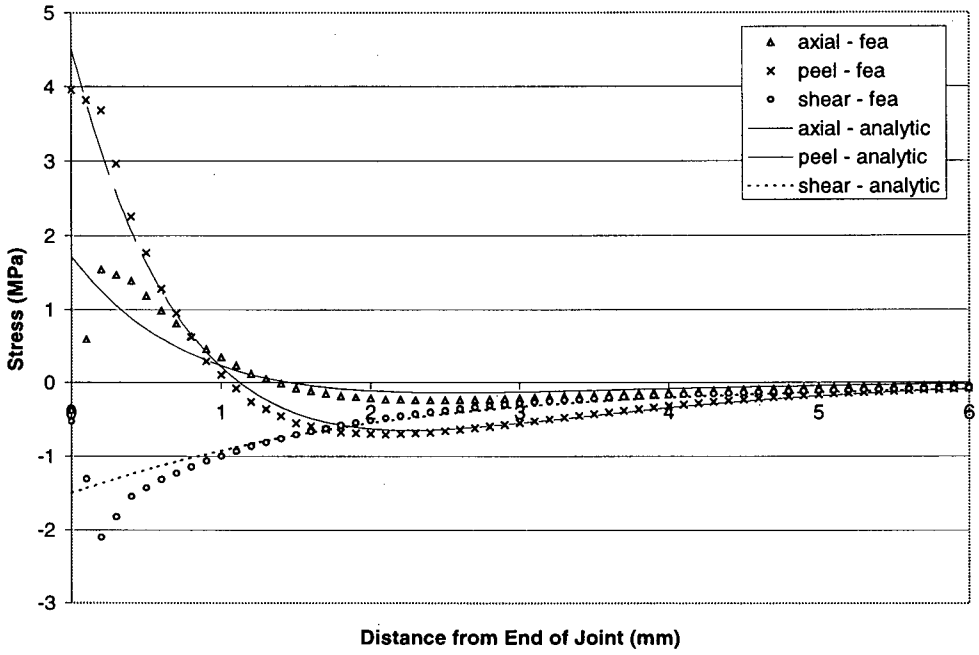

Figure 6-9: Adhesive stresses developed by an applied membrane load

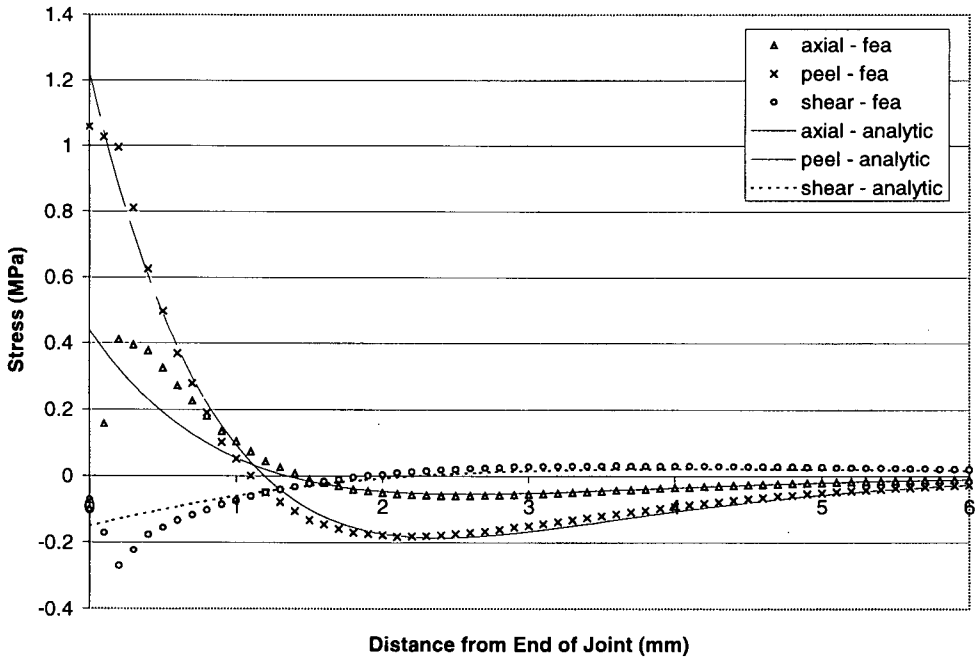

Figure 6-10: Adhesive stresses developed by an applied bending load

The adhesive stresses resulting from thermal loading with a service temperature of $20^0 C$, a cure temperature of $121^0 C$, and an effective stress-free temperature of $81^0 C$ may also be estimated by the methods of Section 6.3, and are shown in Figure 6-11.

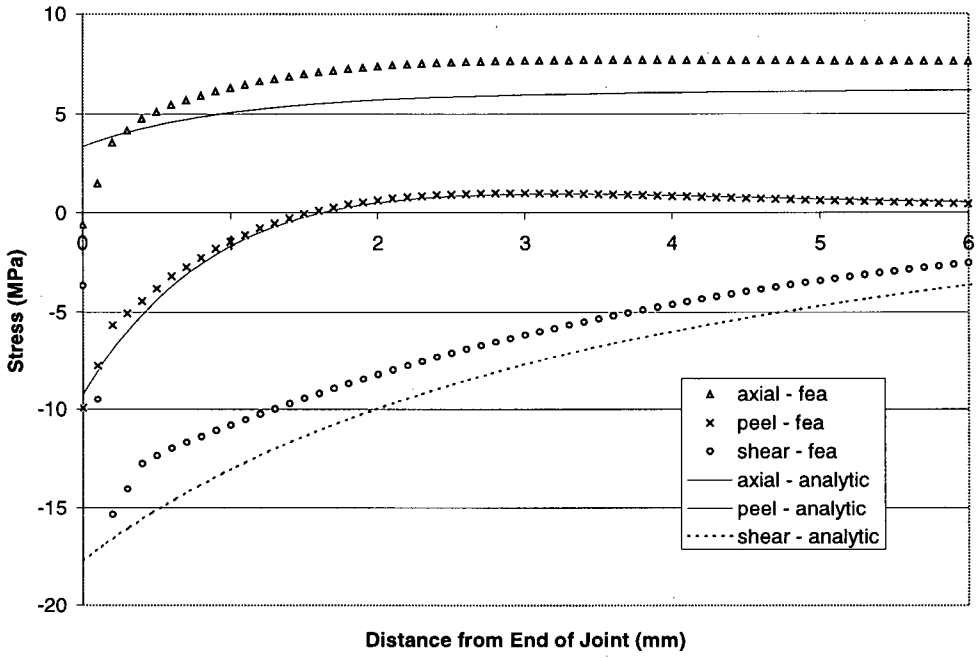

Figure 6-11: Adhesive thermal residual stresses

For these two configurations, the peel and shear strain energy release rates may be calculated from equation (48), and the resulting stress intensity in the cracking adhesive may be estimated from equation (49).

The compliance of the joint as it deflects under membrane and bending loads is calculated from the deflection and rotation of the aluminum plate at the point of application of the loads. It may be characterized according to the following matrix representation, where u_m is the membrane displacement of the crack face and u_b is the bending displacement at the outer fibre.

$$\begin{pmatrix} u_m \\ u_b \end{pmatrix} = \begin{bmatrix} c_{mm} & c_{mb} \\ c_{bm} & c_{bb} \end{bmatrix} \begin{pmatrix} \sigma_m \\ \sigma_b \end{pmatrix} \tag{46}$$

The relative deflections of the adherend/adhesive interface may be determined from the adhesive constitutive equations (8 a,b), however additional terms are required to account for both shear lag and peel lag terms, and the offset between the adhesive/adherend interface and the centreline of the adherends. Considering these effects, the rotation and deflection of the aluminum plate follow.

$$\overline{w}_{2,x} = -\frac{h_2}{2}\left[K_4 \psi_{,xxx} - K_8 \phi_{,x} - K_7 \phi_{,xxx} - \frac{\nu_a t_a}{4}\left(\frac{h_1}{D_1} + \frac{h_2}{D_2}\right)\psi_{,x} \right] \tag{47 a}$$

$$\bar{u}_2 = \bar{w}_{2,x}\left(1+\frac{2t_a}{h_2}\right) - K_0\phi_{,x} \qquad (47\ b)$$

In Figure 6-12, the compliances calculated using equations (47 a,b) are compared to those calculated using finite element analysis, and are expressed in terms of the crack face displacement per MPa of applied stress. It can be seen that the difference between plane stress and plane strain is small. Again, this is due to the low transverse stiffness of the patch material. In all cases, the analytical model was found to agree within 2% of the FEA results, thus verifying the accuracy and demonstrating the utility of the developed closed-form equations.

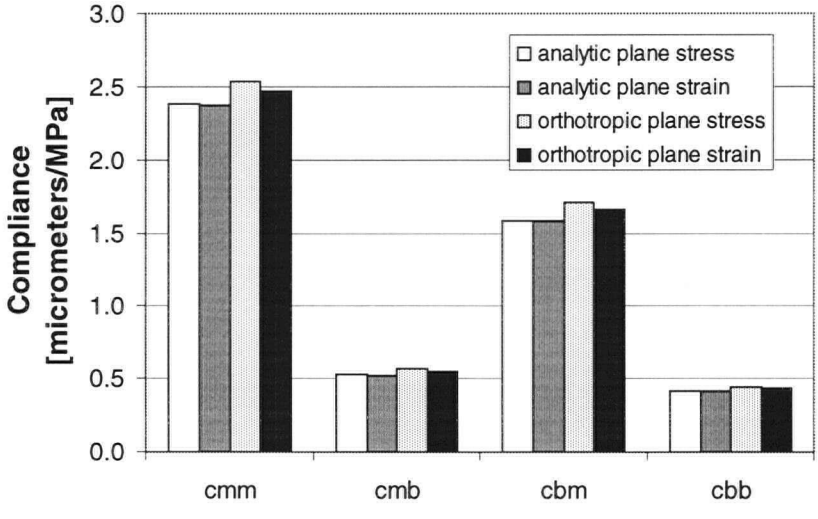

Figure 6-12: Repair compliance under membrane and bending loading

6.4.3 Crack bridging analysis

Once the crack-opening stresses and spring compliances have been determined for the repair, a crack-bridging analysis may be used to determine both the stress intensity for the repaired crack, and the stresses carried by the adhesive and adherends as the applied patch acts to reinforce the crack. For balanced repairs, Rose [14] observed that for a very long reinforced crack, the stresses near the crack tip become independent of crack length. Here, the strain energy released with an increment of crack growth may be calculated from the difference in stored elastic energy between strips of material far removed from the crack tip. One strip is located over the middle of the long crack, and its deflection is governed by the stretch of the springs bridging the crack. The other is well away from the crack and is undisturbed by the singular stress field near the crack. The difference in stored energy between the two strips is given by the energy stored in the springs bridging the crack, defining a limit value for the stress intensity. Wang and Rose [11] have adapted this method to the case of linear coupled bending and extension, separating the

membrane and bending components of the stress intensity. Clark and Romilly [10] have corrected the method to account for asymmetry of the crack-bridging spring compliance matrix, and for the presence of plane strain conditions at the crack tip. Plane strain conditions have been shown by Kotousov and Wang [18] to exist at the crack tip for the extension of cracked plates, and by Clark and Romilly [19] to exist for plate bending. The energy available for cracking is the energy stored in the crack bridging springs far from the crack tip, given as follows.

$$G_\infty = c_m \sigma_m^2 + 2c_{mb}\sigma_m\sigma_b + \frac{1}{3}c_b\sigma_b^2 \tag{48}$$

The strain energy release rate for the plate outer fibre has two components, one for bending and one for extension. Here, K_b and G_b are the stress intensity and strain energy release rate associated with bending at the outer fibre of the plate.

$$G_\infty = G_m + \frac{1}{3}G_b = \frac{1-\nu_p^2}{E_p}\left(K_m^2 + \frac{1}{3}K_b^2\right) \tag{49}$$

The applied stresses are linearly related to the membrane and bending stress intensities through the matrix expression below.

$$\begin{pmatrix} K_m^\infty \\ K_b^\infty \end{pmatrix} = \begin{bmatrix} d_m & d_{mb} \\ 3d_{mb} & d_b \end{bmatrix} \begin{pmatrix} \sigma_m \\ \sigma_b \end{pmatrix} \tag{50}$$

Substitution of (50) into (49) provides a second expression for G_∞.

$$\frac{E_p G_\infty}{1-\nu_p^2} = \begin{matrix} \left(d_m^2 + 3d_{mb}^2\right)\sigma_m^2 \\ + 2d_{mb}\left(d_m + d_b\right)\sigma_m\sigma_b \\ + \left(d_{mb}^2 + d_b^2/3\right)\sigma_b^2 \end{matrix} \tag{51}$$

Differentiation of (48) and (51) with respect to the applied stresses results in a set of equations solvable for d, allowing the calculation of the membrane and bending stress intensities for the case of a very long crack. For cracks of arbitrary length, the authors have developed a closed-form model to predict these values which utilizes an interpolation approach between this long-crack limit and a short-crack limit found by applying the crack opening stresses to an unreinforced crack [10]. The authors have also developed a three-dimensional finite element model of a repair that has been validated against strain data from mechanical tests of repairs with and without bending restraint. Figures 6-13 and 6-14 compare the three-dimensional finite element results to the long-crack limit stress intensity and the interpolation model stress intensity for the AMRL specimen, using the crack-opening stresses and spring compliances from the analytical models described in Section 6.3.

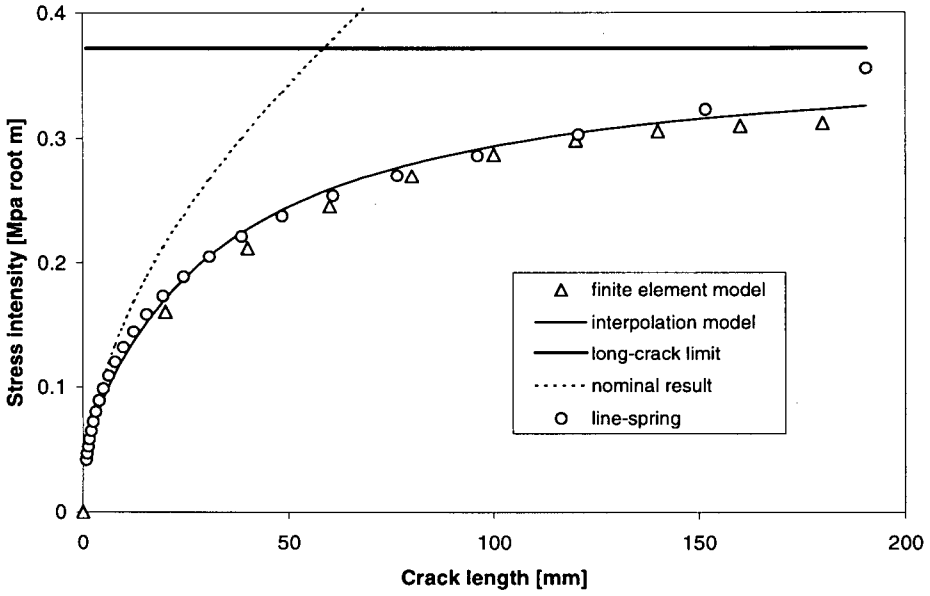

Figure 6-13: Comparison of membrane stress intensity predictions

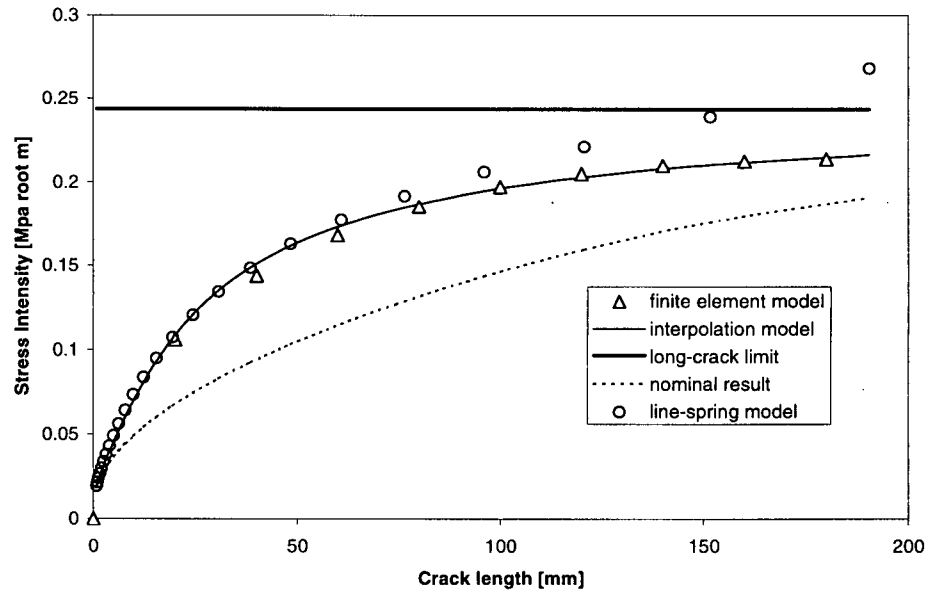

Figure 6-14: Comparison of bending stress intensity predictions

Similarly, it is possible to compare the crack face deflection (and hence the spring stretch) from the analytical and finite element models, allowing the calculation of the predicted stresses in the adhesive and in the repair as it bridges the crack.

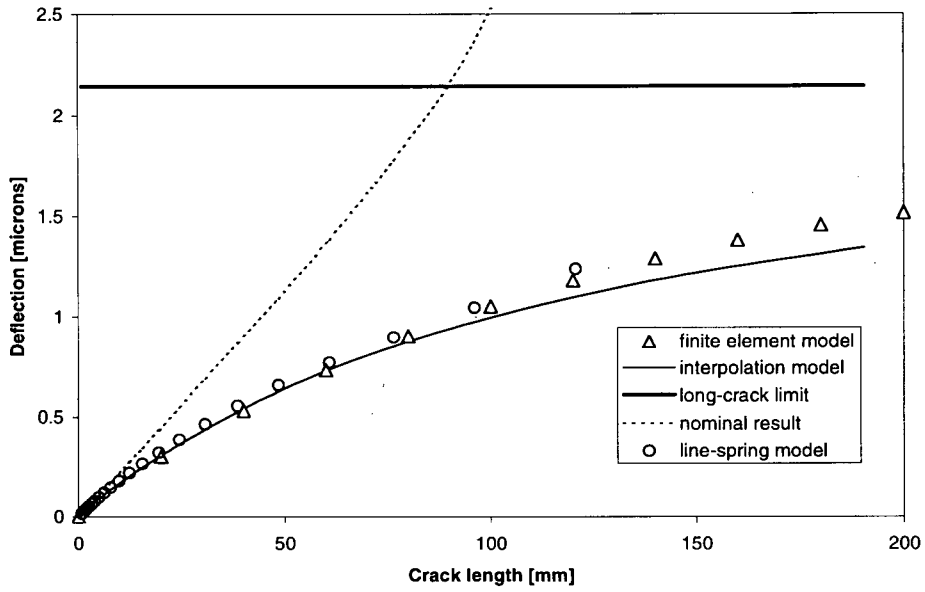

Figure 6-15: Membrane deflection results

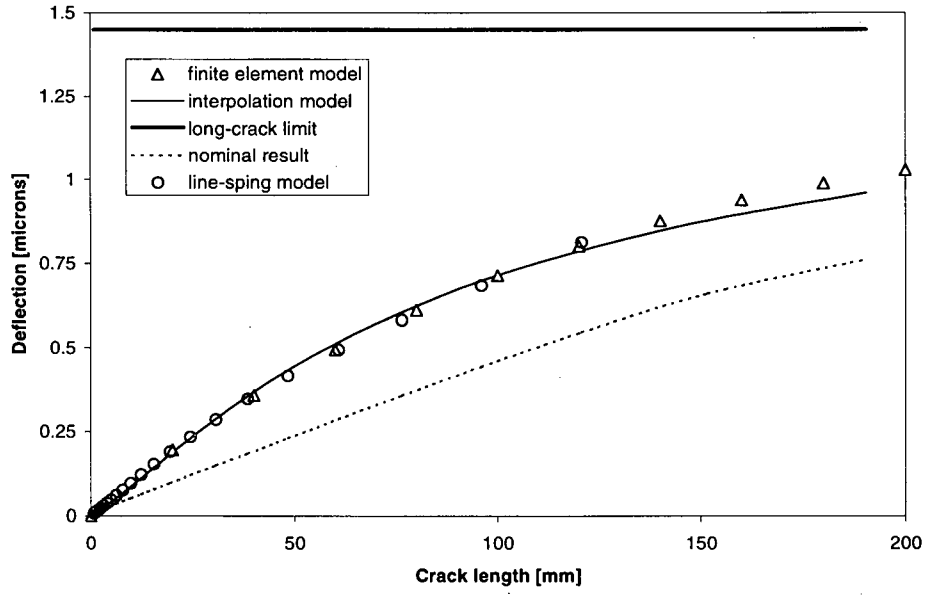

Figure 6-16: Bending deflection results

The stress intensity is an important parameter for assessing the efficiency of a repair in preventing or reducing crack growth, but the deflection of the aluminum plate is also an important parameter as it can be used to estimate the strength and life of the repair itself. Composite and adhesive failure mechanisms have proven to be active failure modes for single-sided repairs. The loads carried by the repair as it bridges the crack may be calculated from the crack face displacements as follows.

$$N = h_2\left(k_m u_m + k_{mb} u_b\right), \qquad M = \frac{h_2^3}{6}\left(k_{bm} u_m + k_{bb} u_b\right) \tag{52 a,b}$$

Given these loads, the adhesive stresses, strain energy release rate and stress intensity may be calculated by the methods of Section 6.3. Care must be taken to include all of the applicable stresses when evaluating the stresses in the composite repair as it bridges the crack. The composite repair must bear the thermal and mechanical loads determined by the complimentary solutions presented in Section 6.3.3, the force and moment determined from equations (52 a,b), and the adhesive stresses acting on the patch/adhesive interface. The adhesive peel stress is particularly important, as it acts to pull apart the fibres of the repair in the weaker through-thickness direction.

6.5 Results and discussion

When compared to finite element models, the developed closed-form analysis methods for a hybrid joint have been proven effective in characterizing the compliance of the repair as it acts to restrict the opening of a repaired crack. The improved model is necessary as the hybrid joint exhibits composite deformation modes, such as shear and peel lag, which are not critical for the analysis of metallic joints, and which significantly affect the stress distribution and compliance of the joint. This more complex model is also required due to the unbalanced nature of the joint, which results in additional forms of coupling between the bending and extensional responses that are not accounted for by previous simpler models. The closed-form models also provide a reasonable estimate of the peak stresses in the adhesive. When combined with the repair design equations presented by Clark and Romilly [10], the result is an enhanced, accurate and easily applied damage tolerance assessment approach for hybrid joints and repairs to cracked structures which allows an assessment of both the stress intensity in the underlying plate and the stresses in the adhesive and the composite in the region of the crack. The incorporated closed-form damage tolerance model is very useful for design optimization, life assessment, and probabilistic analysis to determine the effectiveness of various inspection regimes.

To properly utilize the developed damage tolerance approach, several aspects of the analysis require special attention. Examples include the determination of the nominal stresses acting under the repair for realistic repair geometries, the potential for geometry-related non-linear response of the hybrid structure, and development of appropriate failure criteria for the repair. The determination of the nominal stresses acting under the repair is often complicated by the need for an accurate assessment of the effects of the boundary conditions and the finite dimensions of the patch and underlying plate. In the practice, this requires the use of finite element modelling or the explicit inclusion of the mechanical boundary conditions and the finite repair geometry within composite beam

models such as the one presented in this paper. Another concern is geometrical non-linear coupling of the extensional loads and bending deflections of the repaired structure. Significant lateral deflections will typically occur due to moments induced by the neutral axis offset from the single-sided repair (particularly in regions of repaired structure where bending restraint is limited), and more locally due to the crack itself. Moments will develop in the structure to counteract any lateral deflections away from the load line of the membrane stresses (tensile loads) about the repair. This non-linear response can have a significant effect on the response of the repair as demonstrated in previous work by the authors [10]. Note that the analysis presented in this paper is applicable only to the linear case, analysis of the non-linear case will require special attention, including the definition of a new long-crack limit strain energy release rate, as first demonstrated by Rose [14].

Additional concerns involve the determination of adequate failure criteria. For bonded joints (as discussed in Section 6.3) there are no adequate means of generally predicting the strength of the repair based on adhesive or matrix material properties without considering the details of its particular application, including such factors such as the composition of the composite, the adhesive thickness, the type of loading and the environmental conditions. The result is that empirical data from testing of the specific joint composition under consideration, under similar loading and environmental conditions, must be used to evaluate the static and fatigue strength of the joint. Uncertainty can also be introduced as a result of the type of analysis used [9] (e.g. linear versus non-linear, three-dimensional versus two-dimensional, analytical versus finite element). For consistency and validation purposes, the same type of analysis should be used to determine the strain energy release rate (or the stress intensity) for the test configuration and for the damage tolerance analysis of the actual structure.

Composite-specific failure modes have proven to be very important in the damage tolerance assessment of unbalanced bonded composite repairs and hybrid joints. These failure modes are based on specific failure mechanisms that are typically less understood and thus less certain in their evaluation than is the case for metal-metal joints. There are several components to the stresses in the composite repair as it acts to bridge the crack. The critical location is the adhesive-adherend interface, where both the adhesive peel and shear stresses, and the composite reinforcement plate extension and bending stresses act. Several failure modes are possible for a composite laminate including; a) matrix or matrix/fibre interface failure due to excessive through-thickness stresses, b) reinforcement failure due to compression and buckling, extension and/or bending, and c) general composite failure due to gross overload or fatigue. In the analysis presented in this paper, it was assumed to be sufficient to characterize and control the stresses acting on the composite without considering these separate failure modes. To properly account for composite failures, significant additional work would be required to determine fatigue

thresholds for the composite acting under these stresses or to determine the rate of failure at applied loading levels above threshold values.

6.6 Concluding remarks

The authors have developed an enhanced, verified, and effective set of closed-form analysis equations for the damage tolerance analysis of metal, composite and hybrid joints and repairs to cracked structure. Utilizing as a basis the previous analyses of Delale [15], and Bigwood and Crocombe [7], the authors have extended the work to the analysis of a lap joint specimen analogous to a bonded composite repair applied to an aluminum aircraft structure. The enhanced closed-form analysis developed in this paper now accounts properly for many secondary effects, including coupling of the membrane and bending responses of the joint and deformation mechanisms that are particularly important to analysis of bonded joints with composite adherends. While several challenges have been identified which must be addressed before the damage tolerance analysis of bonded composite repairs can be carried out in a general manner, these new analysis tools, when combined with design equations previously developed by the authors, provide an effective, verified and relatively easily applied methodology to perform an accurate linear analysis of a bonded joint or repaired cracked structure experiencing bending and extensional loads. The enhanced closed-form equations developed in this research work provide another major tool in the structural designer's arsenal for the stress and failure analysis of hybrid structures.

6.7 References

[1] Volkersen O. Rivet strength distribution in tensile-stresses rivet joints with constant cross-section. Luftfahrforschung 1938;15(1):41-47

[2] Goland M and Reissner E. The stresses in cemented lap joints. Journal of Applied Mechanics, Transactions of the ASME 1944;66:A17-A27

[3] Hart-Smith LJ. Stress analysis: a continuum mechanics approach. In: developments in Adhesives, 1973.

[4] Renton WJ and Vinson JR. The efficient design of adhesive bonded joints. Journal of Adhesion 1975;():175-193

[5] Renton WJ and Vinson JR. Analysis of adhesively bonded joints between panels of composite materials. Journal of Applied Mechanics, Transactions of the ASME 1977: 44;101-106

[6] Allman DJ. A theory for the elastic stresses in adhesive bonded lap joints. Quarterly Journal of Mechanics and Applied Mathematics. 1977;30(4):415-436

[7] Bigwood DA and Crocombe AD. Elastic analysis and engineering design formulae for bonded joints. International Journal of Adhesion and Adhesives 1989;9(4):229-242

[8] Bigwood DA and Crocombe AD. Nonlinear adhesive bonded joint design analysis. International Journal of Adhesion and Adhesives 1990;10(1):31-41

[9] Joseph and Erdogan in: Johnson WS. Stress Analysis of the cracked-lap shear specimen: an ASTM round-robin. Journal of testing and Evaluation 1987;6:303-324

[10] Clark RJ and Romilly DP. Linear coupled extension and bending of an unbalanced bonded repair. International Journal of Solids and Structures. Accepted September 2006.

[11] Wang CH and Rose LRF. A crack bridging model for bonded plates subjected to tension and bending. International Journal of Solids and Structures 1999;36:1985-2014

[12] Rice JC. Stresses in an infinite strip containing a semi-infinite crack. Journal of Applied Mechanics - Transactions of the ASME, 1967;248-249

[13] Adams RD and Mallick V. A method for the stress analysis of lap joints. Journal of Adhesion, 1992;38:199-217

[14] Rose LRF. Theoretical analysis of crack patching. In: A.A. Baker and R. Jones (eds.) Bonded Repair of Aircraft Structures. Martinus Nijhoff, 1988;77-105

[15] Delale F, Erdogan F, Aydinoglu MN. Stresses in adhesively bonded joints: a closed-form solution. Journal of Composite Materials, 1981;15:249-271

[16] Jones R, Callinan RJ, Aggarwal KC. Analysis of bonded repairs to damaged fibre composite structures. Engineering Fracture Mechanics 1983;17(1):37-46

[17] Okafor A, Singh N, Enemuoh UE, Rao SV. Design, analysis and performance of adhesively bonded composite patch repair of cracked aluminum aircraft panels. Composite Structures. 2005:71:258-270

[18] Kotousov A, Wang CH. Fundamental solutions for the generalized plane strain theory. International Journal of Engineering Science 2002;40:1775-1790.

[19] Clark RJ, Romilly DP. Bending of transversally isotropic generalized plane strain plates with reinforced cracks. International Journal of Fracture. Accepted November 2006.

[20] Timoshenko SP. Analysis of bi-metal thermostats. Journal of the Optical Society of America. 1925:11;233-242

[21] Albat AM, Romilly DP, Raizenne MD. Thermal residual strain measurement in a composite repair on a cracked aluminum structure. ICCM-11, Gold Coast, Australia, 14th to 18th July 1997:VI:279-288

Chapter 7: Nonlinear mechanics of hybrid bonded joints and composite repairs*

D. P. Romilly and R. J. Clark

University of British Columbia Department of Mechanical Engineering

7.1 Introduction

An experimental investigation of the nonlinear mechanics of a hybrid joint (that is representative of a bonded composite repair) is used to validate a developed two-dimensional small strain/large displacement Finite Element (FE) model useful for repair design and Damage Tolerance Analysis (DTA). By testing the hybrid joint in both the cracked and uncracked configurations under an applied load, the energy available for growth of a long crack in the substrate under a repair can be directly assessed, and is calculated using the Rose model. Based on these results, the developed two-dimensional FE model is shown to provide excellent predictions of the strain energy release rate while further comparison with three-dimensional finite element results also demonstrates the model's ability to provide excellent results for the root-mean-square crack tip stress intensity. Using this validated tool, the authors then develop a nonlinear crack-bridging model and use it to predict the membrane and bending stress intensity, adhesive peel and shear stresses, and composite plate stresses for a repair applied to a crack of arbitrary length. The crack-bridging model is shown to provide reasonable results when compared to the three-dimensional finite element model.

A bonded composite repair is illustrated in Figure 7-1, and consists of a fibre-reinforced epoxy patch bonded to a cracked or weakened aircraft structure, offering improvements in life, cost, weight, and inspectability when compared to mechanically fastened repairs. A bonded repair exhibits smoother load transfer, and acts both to reduce stresses in the underlying structure, and to restrict the opening of any cracks. This advanced repair technology is a very valuable addition to the standard methods of aircraft structural repair, often allowing the refurbishment of structures that would otherwise not be repairable. The principal barrier to the widespread use of bonded repairs is the difficulty of performing a comprehensive damage tolerance analysis, particularly under excessive bending, where composite and adhesive failure modes can lead to rapid failure. In previous work [3], the authors have performed a full-scale bonded repair fatigue test which showed that, even for repairs reinforced against bending by an underlying

---

* A version of this chapter has been submitted for publication. D.P. Romilly, R.J. Clark, "Nonlinear mechanics of hybrid bonded joints and bonded composite repairs", International Journal of Nonlinear Mechanics.

structure, bending strains in the patch and plate are significant and can even exceed those caused by axial loads. For single-sided repairs, geometrically non-linear bending proved to dominate the mechanical response, leading to rapid failure.

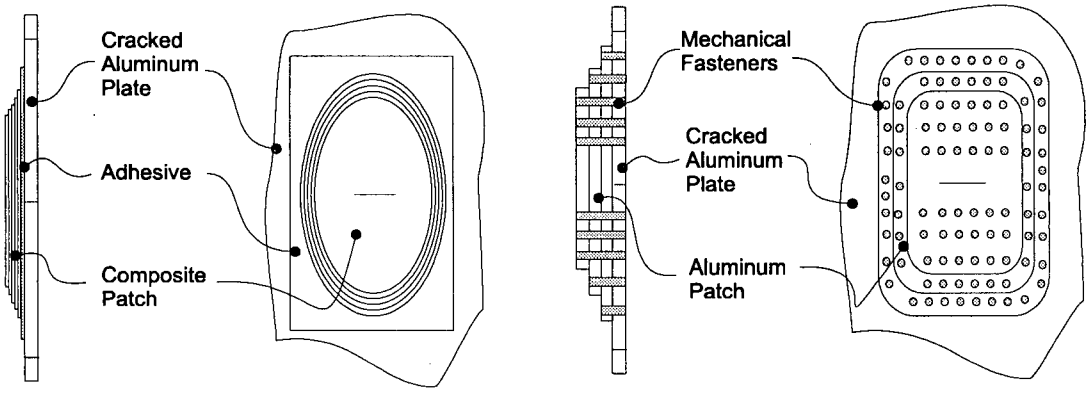

Figure 7-1: A bonded repair and a mechanically fastened repair

Early in the history of the bonded composite repair technology, Australian researchers [12] used double-lap joint specimens modelled after a bonded composite repair to evaluate bonded joint models, to investigate the effects of patch composition on the compliance of the repair as it acts to reinforce the crack, and to determine the mode and rate of failure of a repair in a simplified geometry. Here, the authors seek to achieve similar goals, but will examine the effects of nonlinear coupled bending and extension on the performance of a repair.

In this chapter, the authors investigate the mechanics of hybrid boron/epoxy and aluminum bonded lap joints that are representative of bonded composite repairs. The first half of the paper describes the experimental hybrid joint specimen testing and evaluation, which was used to validate a two-dimensional FE model of the hybrid joint. The specimens were tested with varying degrees of bending restraint and equipped with strain gauges both applied to the surface of the structure and embedded within the boron-epoxy patch, allowing the calculation of bending and tensile loads both near the grips and near the repaired crack at the centre of the specimen. Plots of load versus displacement recorded during pseudo-static loading of the specimens allow the investigators to determine the extent to which non-linearity governs the overall behaviour of the joint. Strain-energy considerations then allow the authors to evaluate the effectiveness of each type of joint in stopping or slowing crack growth in a repaired structure. These results, combined with lateral displacements measured using a contacting displacement probe and a linear scanner, illustrate the effectiveness of the FE models of hybrid bonded joints and repairs. The results also illustrate the capability of the Rose model [4], which allows the accurate calculation of the energy available for crack growth for a long crack embedded in the substrate under a repair.

In the second half of the paper, the authors address two problems: 1) separation of the energy available for cracking into membrane and bending components, and 2) determination of the adhesive and composite stresses in the vicinity of the repaired crack. This is achieved using a new nonlinear crack-bridging model. Past approaches to nonlinear analysis of repaired cracks have either employed numerical means such as three-dimensional finite element analysis [e.g. 13,14], or have employed a linear crack-bridging model and superposition to arrive at very conservative estimates of the membrane and bending stress intensity factor [7]. Few studies have comprehensively examined the adhesive or composite stresses about a repaired crack under geometrically nonlinear bending and extension, and to the author's knowledge, none have done so using a crack-bridging model. Closed-form models and simple crack-bridging models are highly desirable for the rapid design and damage tolerance evaluation of a bonded repair, as this newer technology must compete against conventional repairs that are generally well-understood and can be designed and assessed with relative ease using well-established methods.

7.2 Lap joint experiments

The mechanics of hybrid bonded lap joints with varying degrees of bending restraint were investigated by pseudo-statically loading several different types of bonded joint specimens in tension and compression. The tests were carried out using an MTS-810 servo-hydraulic loading frame with wedge grips. The remotely applied stress ranged between 0 and 68 MPa, which is about one half of the load range applied during previous fatigue testing of a complete bonded repair [3]. The applied loads were kept low to prevent premature damage to the specimens. The loading was applied slowly, such that the response of the joint could be considered static.

The hybrid specimens tested were of three different types, and each type was tested in both a cracked and uncracked configuration. They are illustrated in Figures 7-2 and 7-3. The Single Lap Joint (SLJ) specimen models a single-sided repair, and exhibits no bending restraint. For this specimen, thermal residual strains and the step change in neutral axis position near the crack can be expected to induce significant bending strains. The Double Lap Joint (DLJ) specimen models a symmetric double-sided repair, and is fully restrained against bending. The Honeycomb-Separated Double Lap Joint (HS-DLJ) specimen experiences partial bending restraint due to a compliant aluminum honeycomb separator bonded between the opposing patched plates. The details of the construction of the specimens are provided in Appendix A.

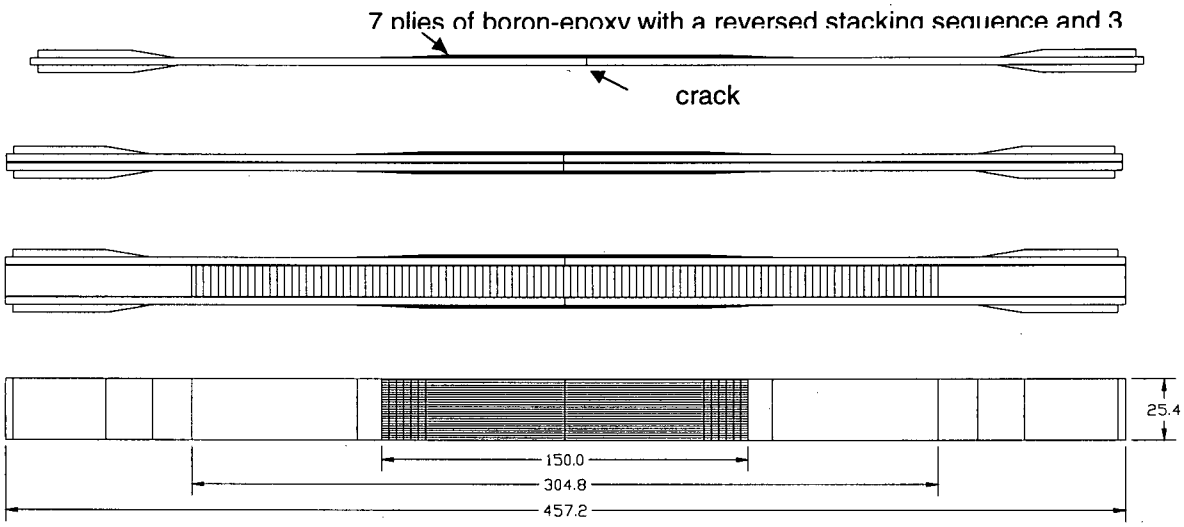

Figure 7-2: Lap joint specimens. From the top: SLJ, DLJ, and HS-DLJ specimens

The SLJ specimen was instrumented with five strain gauges in the cracked configuration and four gauges in the uncracked configuration. The strain gauges were applied in the region of the grips (location A), and near the crack (location B). Figure 7-3 shows the locations of these gauges. The gauges are placed on opposite sides of the structure to assess both axial loads and bending moments. The extra gauge on the cracked specimen is embedded in the composite at location B, one ply from the adhesive interface.

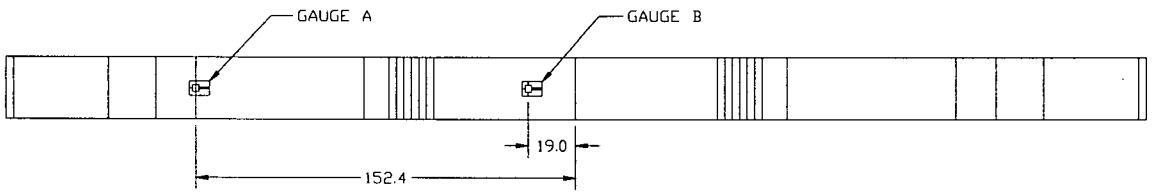

Figure 7-3: Strain gauge locations

In accord with practice in the field of bonded repairs, the loads applied to the specimens are reported in terms of a remote applied stress. During these tests, a remote tensile stress was applied to the specimens in increments of 0.74 MPa. For each increment, the displacement (stretch), load, and strains were recorded. The load was obtained from the average of the strains recorded at location A. Displacements were measured on each side of the specimen using an MTS-632 displacement transducer and a custom-built displacement transducer, each with a gauge length of 304.8 mm.

For remote applied stresses of 0, 22.7, 45.3 and 68 MPa, the load was held constant while a custom-built contact displacement probe and scanner were used to measured the

lateral deflection of the specimens. The developed probe consists of a cantilevered spring clip instrumented with two strain gauges. Calibration tests show this sensor to be linear to within 1% full-scale over a working range of ~5 mm displacement. The scanner incorporated a stepper motor and belts from a dot-matrix printer to move the probe along the deflected specimen surface. This configuration allowed 400 measurements to be taken along the length of a specimen during each scan.

After static testing of the specimens, the authors conducted a set of fatigue experiments to examine the effect of varying degrees of bending restraint on fatigue life and failure mode. Disbond growth was monitored both by the compliance drop method and by ultrasonic inspection. Figure 7-4 shows the rates of failure of the DLJ specimen for various cyclic load ranges. In all cases the load ratio was R = 0. This figure shows results measured via the compliance drop method. An initial period of relatively high crack growth is observed under the initial 280,000 cycles of constant-amplitude fatigue loading with a maximum applied stress of 68 MPa. This change in compliance was primarily due to failure of the adhesive bridging the crack faces, rather than by disbonding of the repair itself. For the next 280,000 cycles (with a maximum applied stress of 100 MPa), no change in compliance and hence no disbond growth is observed and significant disbonding was only observed when the reversing load exceeded 100 MPa, at which point the rate of disbonding increased rapidly with increasing applied loads.

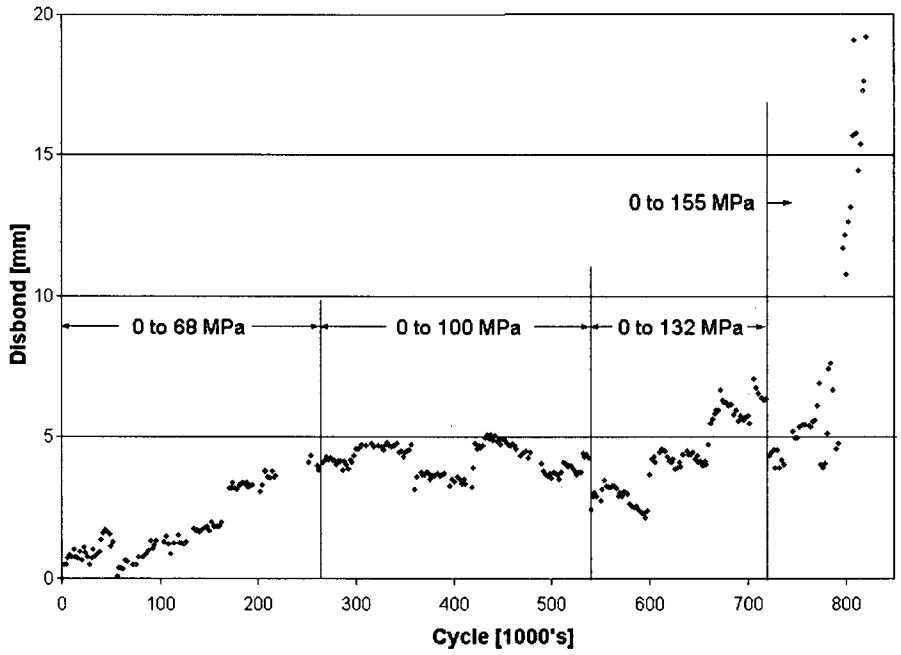

Figure 7-4: Disbonding of the DLJ specimen

Figure 7-5 shows the failure surface of the SLJ specimen, which was not constrained against bending. In this test, the adhesive bridge over the crack faces and the innermost

layer of fibers fractured upon the first cycle of loading, after which the delamination grew through the matrix of the patch. Marks left by dye penetrant indicate the amount of disbonding after an initial 36,000 cycles, and also at 48,000 cycles (i.e. 36,000 + 12,000 cycles) of fatigue loading. Under small applied stresses (see figure labels for values) the delamination grew more than 50 *mm* in only 60,000 cycles. Another interesting feature of the SLJ failure is that significant delamination occurred in only one direction, even though the SLJ specimen is symmetric about the crack. This shows that disbonding of unbalanced joints can happen in an unstable manner, i.e. once one part of the joint disbonds, bending strains concentrate and failure can occur more quickly.

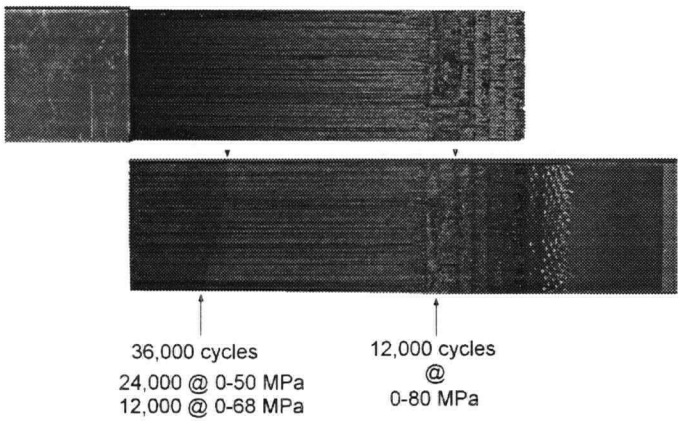

Figure 7-5: Failure surface of the SLJ specimen

It is apparent that different damage mechanisms and higher disbond growth rates occur in repairs with significantly higher degrees of bending. In these cases, composite patch fatigue and fracture enter into the picture. These composite failure mechanisms require special attention. Certification of one-sided repairs may necessitate additional testing and analysis, possibly resulting in more stringent restrictions on operation and shorter inspection intervals than would be required for two-sided repairs.

7.3 Bonded joint finite element model

The authors have constructed a Finite Element Model (FEM) of the lap joint specimens using an ANSYS script. The script allows one to specify the geometry, loading, bending constraint, and amount of disbonding of the joint, and constructs a mesh with a specified base element size. The script performs a non-linear solution and writes strain, lateral displacement, load-displacement, and strain-energy results to a comma-separated variable file. The model uses SOLID80 2D 8-node solid elements in plane stress or plane strain, with the honeycomb bending restraint being modelled using MATRIX27 elements applied to the bottom edge of the plate. The script calculates the stiffness of each MATRIX27 element in proportion to the size of the adjacent elements. The DLJ

specimen was modelled by fixing the bottom edge. Figure 7-6 shows the details of the mesh generated by the script for the uncracked single lap joint. An underlying crack can be modelled by removing the symmetry constraint on the edge of the plate.

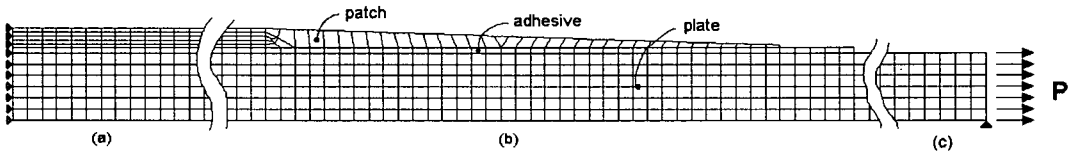

Figure 7-6: FE mesh showing the (a) cracked, (b) tapered, and (c) grip regions

The script applies the specified load in a series of steps, which were solved using the full Newton-Raphson method applying adaptive descent, stress stiffening, large displacements, and small strain theory. The patch was modelled as an orthotropic elastic solid, the adhesive as an isotropic elastic/perfectly plastic solid, and the aluminum plate as an isotropic elastic solid. The thermal residual stresses imparted by the patch bonding process were modelled using an effective stress-free temperature of 81°C. Table 7-1 lists the material properties used in the analysis. The script has also been designed to model a specified length of disbond propagating from the left edge of the model.

Property	Boron/Epoxy Patch	Adhesive	Aluminum Plate
Elastic Modulus (GPa)	$E_{longitudinal} = 210$ $E_{transverse} = 2.5$	E = 2.14	E = 72.4
Shear Modulus (GPa)	$G_{longitudinal} = 7.24$ $G_{transverse} = 1.0$	G = 0.805	G = 27.2
Poisson's Ratio	$\upsilon_{longitudinal} = 0.21$ $\upsilon_{transverse} = 0.019$	$\upsilon = 0.33$	$\upsilon = 0.33$
Thermal Expansion ($\mu\varepsilon$ /°C)	$\alpha_{longitudinal} = 4.61$ $\alpha_{longitudinal} = 25.87$	$\alpha = 50.0$	$\alpha = 50.0$
Thickness	7 plys, t = 0.924 mm	t = 0.25 mm	t = 3.125 mm
Yield Strain	N/A	0.0739	N/A

Table 7-1: Material properties and dimensions

Figures 7-7 and 7-8 compare strain gauge data for the SLJ specimens with strains predicted by the FEM. This specimen is free to bend, and the nonlinear nature of this bending is evident in these figures. Large elastic strains were generated for small loads, followed by more linear behaviour once the specimen's neutral axis had shifted toward the load line. There are several possible sources for the differences between the experimental and FEM results. By numerical experimentation it was found that the compliance of the fibreglass end tabs (modelled with rigid boundary conditions) has

some effect on the amount of bending, that the finite thickness of the strain gauges tends to amplify the observed bending strains by a small but tangible amount, and that the results are also dependant upon the initial curvature of the specimen. It should also be noted that the specimens had sat for some time before testing, and that a number of static tests had to be performed to set up the apparatus, so creep may have somewhat reduced the residual strains and hence the effective stress-free temperature used in the analysis (based upon results for an unloaded and un-aged specimen [5]) may have been somewhat unrepresentative. For these reasons, it is not possible to achieve as high a high level of correspondence between experimental and numerical results in a nonlinear analysis of this type as one would expect for a monolithic elastic material experiencing small strains and small displacements. The results for location B (at the centre of the specimen) are generally better than the results at location A (near the end tabs). This can be attributed to the sensitivity to the end conditions at location A, whereas the strains at location B are more dependant on the global mechanics of the joint and the behaviour about the embedded crack. Despite these observed differences, the overall trends match quite well, and as will be shown, the lateral deflections and the load-displacement curves obtained from the finite element model and the experimental results prove to match well enough to test some energy methods for bonded composite repair design.

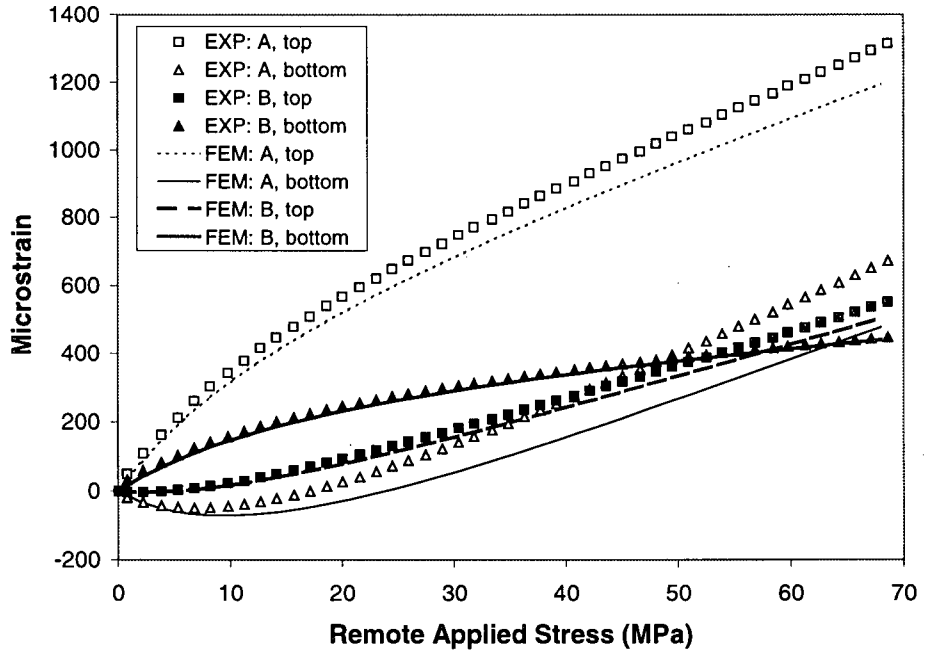

Figure 7-7: Strains for the cracked SLJ specimen

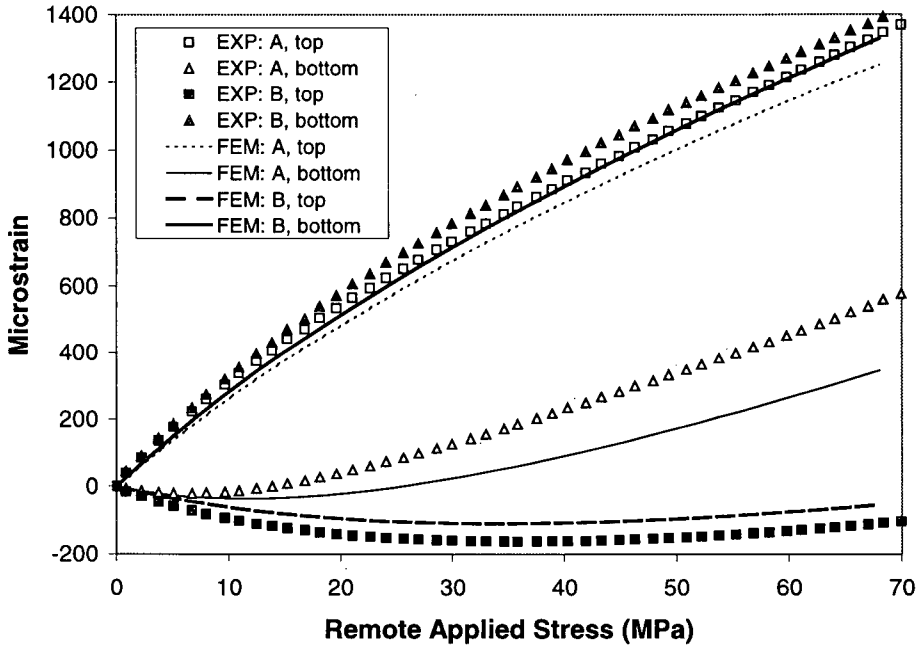

Figure 7-8: Strains for the uncracked SLJ specimen

Figures 7-9 and 7-10 plot the scanned position of the outer face of the patch and the deflections predicted by the FEM. The scanner also reads the thickness of the patch and adhesive, explaining the difference between the results. The specimen deflections after correction for the thickness of the patch is presented in Figures 7-11 and 7-12.

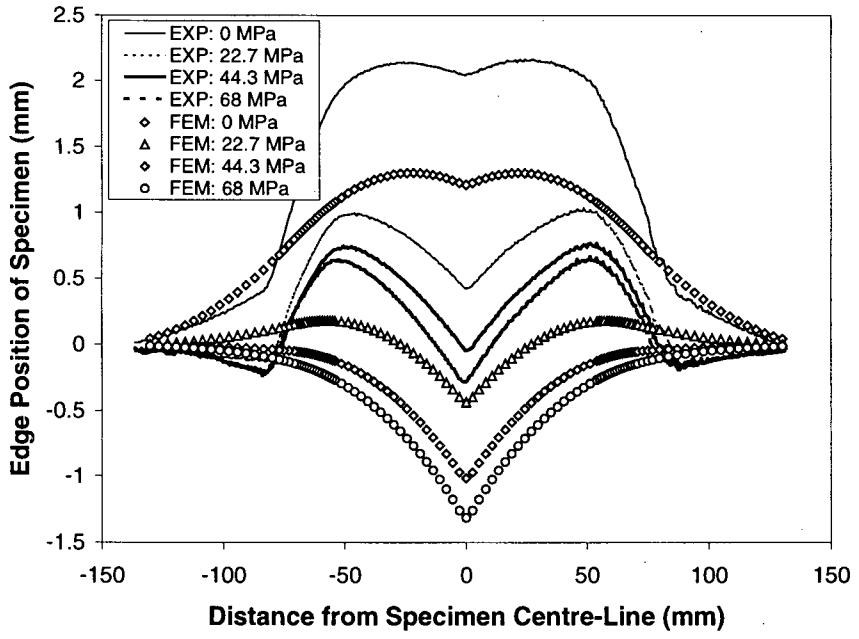

Figure 7-9: Edge position of cracked SLJ

Two important features should be noted from these figures: 1) the cracked specimen exhibits a sharp bend over the crack, and 2) the change in deflection induced by the applied load markedly decreases with each load increment. The bending over the crack is indicative of the lost bending stiffness due to the underlying crack. This effect has been shown to dramatically accelerate the rate of failure of single-sided bonded repairs [3].

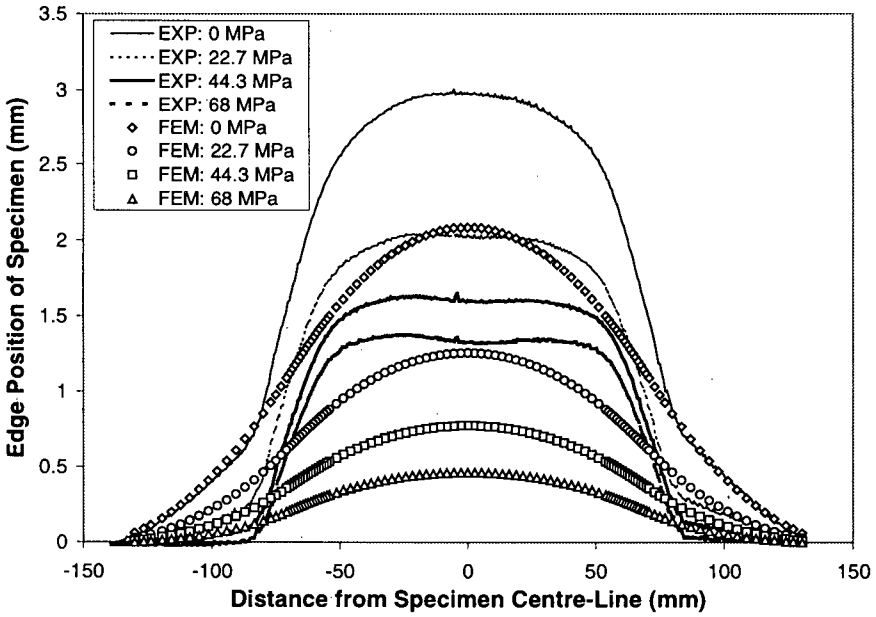

Figure 7-10: Edge position of uncracked SLJ

Figures 7-11 and 7-12 plot the lateral deflections of the SLJ specimens by subtracting the position at particular loads from the initial, unloaded position.

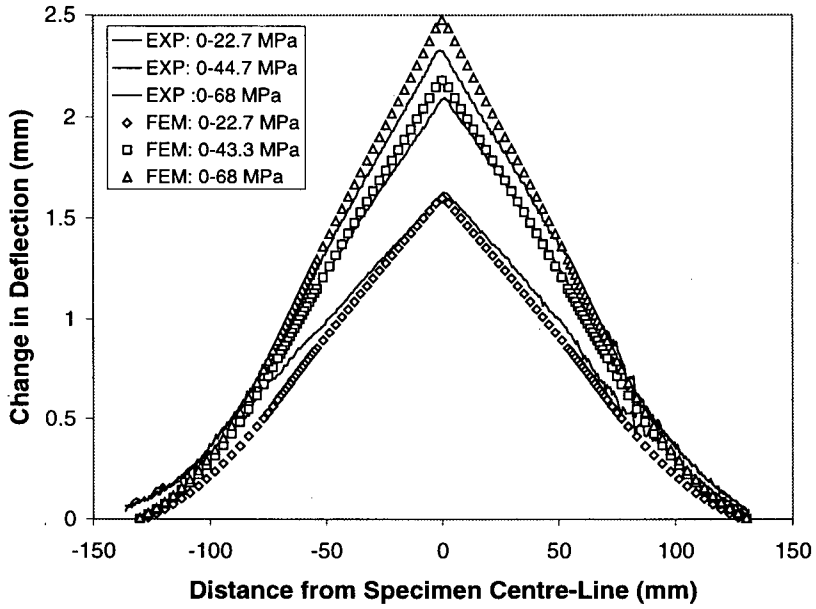

Figure 7-11: Cracked SLJ lateral deflection

There is reasonably good agreement (generally within 10%) between the experiments and the FEM in these results, and again, the dramatic effect of the crack is evident in the cracked specimen. The change in lateral deflection is proportional to the moments applied to the structure when it is loaded, so this good agreement between the finite element and experimental results indicates that the model is accurate in its depiction of the bending of the lap joint, and hence should provide excellent results for analysing the effects of mixed-mode loading.

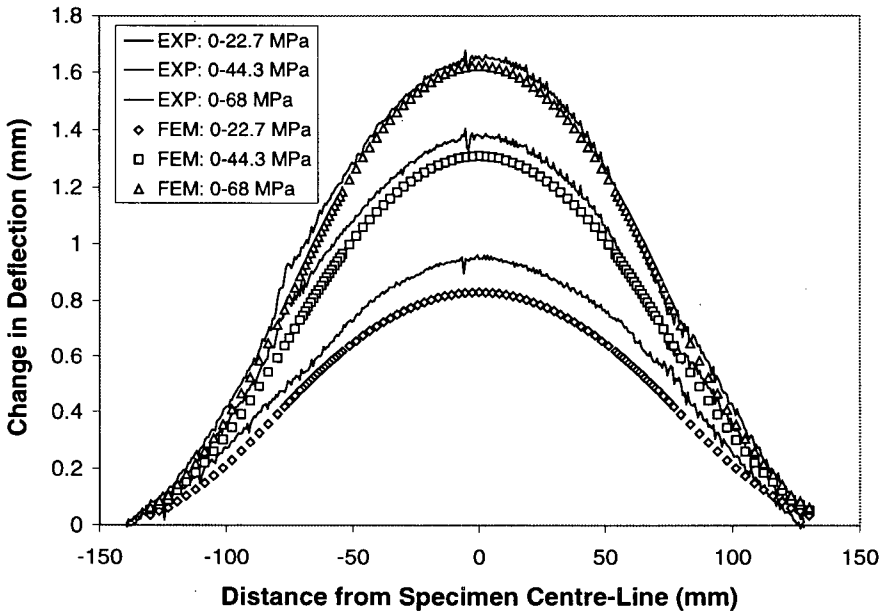

Figure 7-12: Uncracked SLJ lateral deflections

Finally, load-displacement curves were generated for each of the specimens. These are plotted in Figure 7-13, where it can be seen that the cracked specimens all exhibited more compliance than the corresponding uncracked specimen, and that both the DLJ and HS-DLJ specimens exhibit nearly linear behaviour. Overall, the difference in compliance between the DLJ and HS-DLJ specimens is relatively small, and is not very evident in the load-displacement curves. For the SLJ specimen, the deflection was obtained by using the average deflection for the displacement transducers applied to either side of the specimen. Similarly, the rotation of the specimen near the grips can be measured from the difference between the deflections measured by the probes.

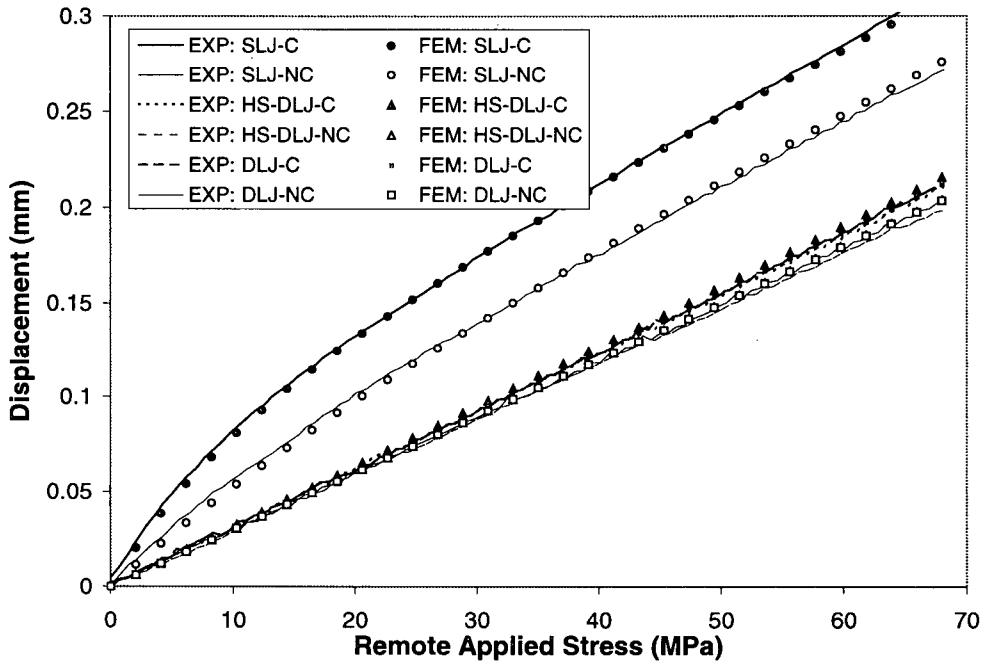

Figure 7-13: Load vs. displacement curves

In the next section, the Rose model for reinforced cracks will be introduced, the load-deflection data will be used to estimate the stress intensity under a repair, and the results will be compared to those from the two-dimensional bonded joint finite element model.

7.4 Stress intensity calculation: the Rose model

The stress intensity is an important life determining factor, and may be calculated using the Rose model. Rose observed that for very long cracks reinforced by springs, the crack opening displacement is restricted only by the springs bridging the crack faces and stresses and strains near the crack tip become independent of crack length. The process is illustrated in Figure 7-14. Here, the strain energy release rate, G_{∞}, reaches a limit [4,6,11] that can be calculated from the difference in the total potential energy for strips of the structure taken well away from the crack (Section B-B), and over the crack, but far from the crack tip (Section A-A).

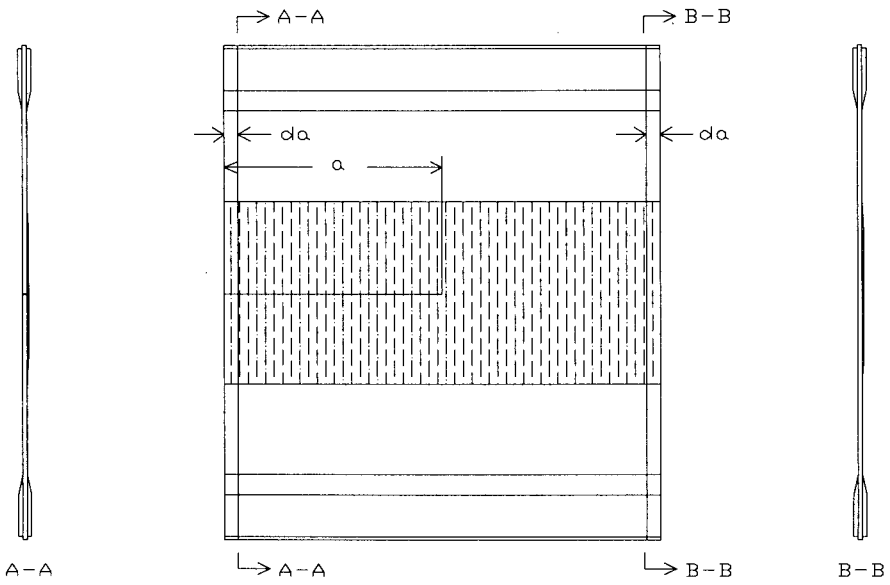

Figure 7-14: The energy method: A-A and B-B show cracked and uncracked joints

For a balanced repair there is very little bending, and the work done on and strain energy in the two strips is equal except in the energy balance for the springs bridging the crack. Here, the energy available for crack growth can be determined by calculating the energy required to open the crack faces far from the crack tip. For a plate of thickness $2h$ bridged by springs of stiffness k_s (in Pa/m), and subject to a stress σ_0 acting to open the crack, the energy release rate is defined as follows.

$$G_\infty = 4h\int_0^\infty \sigma dx = 4h\int_0^\infty k_s x dx = 2hu^2 = \frac{2h\sigma_0^2}{k_s} \qquad (1)$$

As the springs bridging the crack have little effect for short cracks, interpolation between this long-crack limit and a short-crack limit given by the nominal fracture solution for a crack without reinforcing springs allows an accurate assessment of the stress intensity for cracks of arbitrary length. Adhesive stresses and plate loads in the composite repair can be estimated in a similar manner [2]. The Rose model has been shown to be accurate for the extension of double-sided or symmetric repairs, and the authors have extended it to the case of linear coupled extension and bending by 1) applying plate bending geometry correction factors to account for transverse shear and pressurization of the crack tip, 2) correcting the long-crack limit solutions, and 3) developing a new method for interpolation for arbitrary crack lengths [18].

Current means for closed-form nonlinear analysis of one-sided repairs use geometrically nonlinear models to calculate the nominal stresses acting in the repaired plate in the region of the crack, which are then applied as crack-opening stresses in a linear crack-

bridging model [7]. This method ignores nonlinear effects due to additional compliance from the crack, which will result in additional lateral deflections of the cracked portion of the structure, increasing the nonlinearity caused by stress-stiffening. This existing approach has been shown to be conservative, and hence is useful for airworthiness evaluation. However, in the case of long cracks this existing approach is prohibitively conservative and does not allow a reasonable evaluation of structure life to be determined. Hence, the existing method is only applicable to short cracks or for lightly loaded parts. The limitations of the existing approach are due to the application of superposition when stresses determined by nonlinear analysis of a repair without a crack are used to calculate the stress intensity using a linear crack bridging model, a principal that cannot be applied in a general manner to nonlinear problems. To address this, the authors refer to the original basis of the Rose model and apply the full definition of the strain energy release rate, i.e. the difference between the potential of external loads (W) and the strain energy stored in the structure (U). Using this approach, a formulation may be developed which does not rely on superposition. Here, the subscript c refers to the cracked section A-A, and nc refers to the section without a crack, i.e. B-B.

$$G_{\infty} = \frac{d}{da}(W - U) = \frac{d}{da}(W_c - W_{nc} - U_c + U_{nc}) \tag{2}$$

As before, the strain energy release rate for a long reinforced crack may be calculated by considering a strip of material remote from the crack and a strip taken at the centre of the crack. The potential work done by the applied load is calculated from the difference in the deflection of the two strips at the current value of the applied load. For a plate experiencing an applied tensile load σ_0, the change in potential for external load is given by the following, where u_c, u_{nc} are the deflections of the cracked and uncracked strips, respectively.

$$W = \int_A \sigma_0 (u_c - u_{nc}) dA \tag{3}$$

The change in energy stored in the structure may be calculated directly from the stresses and strains in each of the strips. Here, the change in strain energy is given as follows, where V represents the volume of a strip.

$$U = \int_V \sigma_{ij} \varepsilon_{ij} dV \tag{4}$$

For the linear case, $W = 2U$, and the strain energy release rate may be determined if either quantity is known. Here, the contribution of externally applied loads may be isolated by examining the load-deflection history and calculating the work done on the cracked and uncracked strips. This is a useful method that can be applied in the

laboratory to determine the effectiveness of a repair by mechanical testing of equivalent lap joints. By this method, one can use either the experimental or the FEM load-displacement results to determine the energy available for cracking. Figure 7-15 shows these results.

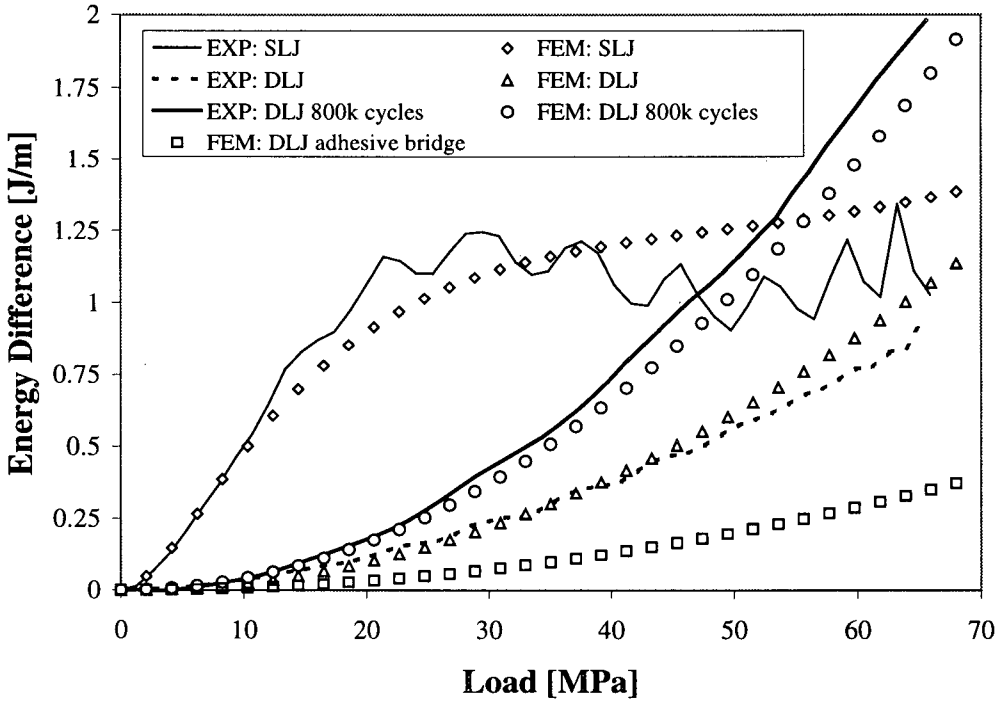

Figure 7-15: Change in strain energy

The experimental results for the energy available for crack growth have been calculated from strain and deflection data averaged over 100 cycles of loading applied at 2 Hz with a sinusoidal waveform. The oscillations in the experimental results for the SLJ specimen arise from repeatable fluctuations in the signal from the custom-made displacement probe, and are characteristics of the mechanical response of this particular probe under extension. The peak and plateau in the SLJ specimen results are due to geometrically non-linear bending. FEM results for higher applied stresses (in the order of 100 MPa - not shown as experimental results extend only to 68 MPa) show that once stress-stiffening dominates the behaviour of both the cracked and uncracked SLJ specimens, the available energy increases in a one-to-one fashion, in the characteristic manner of a linear system as observed for the DLJ and HS-DLJ specimens. Results from the finite element model for the DLJ specimen have been shown for the additional case where adhesive bridging of the crack faces provides additional restraint, reducing the energy available for cracking, and for the case where a significant disbond exists over the crack.

In a similar manner, the energy available due to thermal residual stresses can be derived from the FEM results. The authors calculated this energy by summing the elastic strain

energy stored in all of the elements in the model. Table 7-2 shows the results. The final column, titled 'Difference', is the energy available for crack growth.

Specimen ID	Uncracked	Cracked	Difference
SLJ (cracked)	77.46	76.45	1.01
HS-DLJ	87.31	84.63	2.68
DLJ	87.45	85.61	1.84

Table 7-2: Thermal residual elastic strain energy (J/m).

The strain energy may be converted into a stress intensity factor by observing the result of Kotousov and Wang [9,10] and Clark and Romilly [15] that, in terms of the plate-averaged membrane and bending stress intensity, the crack tip is always in a state of plane strain. ΔU is the difference in stored internal energy per unit width, while t and E are the thickness and modulus of the substrate.

$$K_{\infty} = \sqrt{\frac{E}{1-\nu^2} \cdot \frac{\Delta U}{t}} \tag{5}$$

Using the method outlined above, the long-crack limit stress intensity due to thermal residual strains in the honeycomb-separated joint is $K_{\infty} = 5.23\ MPa\sqrt{m}$. This compares well to the result of $K_{\infty} = 5.11\ MPa\sqrt{m}$ found with the classical Rose model [5].

7.5 Comparison to a 3D FE model and mode separation

The authors have developed a three-dimensional finite element model of the AMRL specimen [16], which has been validated against strain gauge data from mechanical testing. The model includes nonlinear effects such as stress stiffening and adhesive plasticity. The finite element results presented in this paper for the purpose of verifying the Generalized Rose (GR) model were generated from an idealized geometry, chosen to limit the effects of finite patch and plate size exhibited by the actual AMRL specimen. For this reason, the patch was made to extend uniformly across the entire width of the plate, and the plate width was increased such that it would be much longer than the repaired crack. This geometry is an approximation to the 'infinitely long' patch used to develop the Generalized Rose model. Figure 7-16 shows the geometry employed for the repaired crack, where (a) shows the front view of the entire model and (b) shows a close-up view of the crack-tip region. The left edge of the plate is restrained against rotation but allowed to translate freely. The lower edge and right edge of the plate are restrained to model symmetry, other than the crack face, which is free of restraint. The lower and right edges of the patch are constrained to model symmetry.

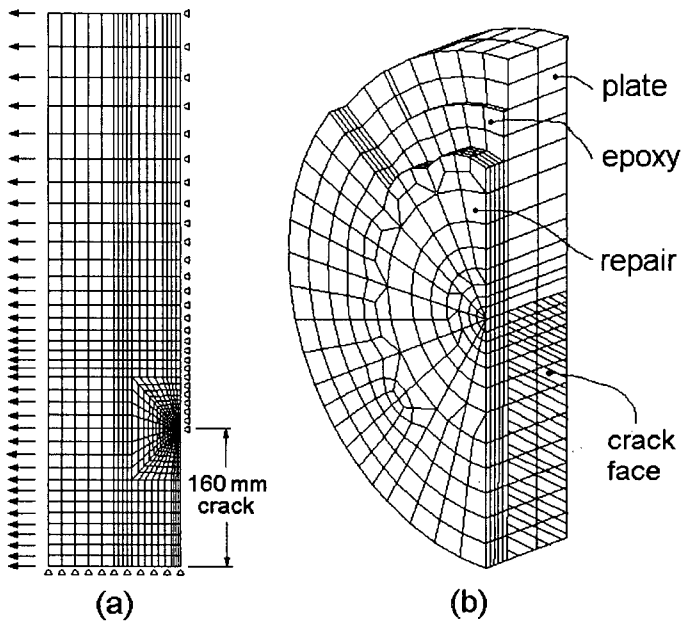

Figure 7-16: Finite element model (a) front view and (b) crack-tip region.

The plate was modeled using two layers of elements, which was found to be sufficient to assess the thickness effects on the membrane and bending stress intensity. The patch was modeled using four elements through the thickness, and the adhesive with one element. The stress intensity through the thickness of the plate was calculated from the stresses at the integration points in the wedge elements along the line of the crack, using quarter-point singular crack tip elements. The membrane and bending stress intensity factors were calculated using a least squares fit of a line to the integration point results. The bending stress intensity was calculated from the slope of the line and the membrane stress intensity was calculated using the intersection with the neutral axis of the plate. To test the Rose model, these two results were combined using equation (6), by which the root mean square stress intensity, K_{RMS}, is defined.

$$K_{RMS} = \sqrt{\frac{G_\infty E}{1-\nu^2}} = \sqrt{K_m^2 + \frac{1}{3}K_b^2} \tag{6}$$

Figure 7-17 shows the nonlinear variation in K_{RMS} under a remote applied stress. The three-dimensional finite element results are shown to approach the long-crack limit obtained from the Rose model. The result obtained through superposition and the application of a linear crack-bridging model is shown to greatly over-predict the stress intensity, particularly for long cracks. This demonstrates the effectiveness of the Rose model for evaluation of one-sided repairs. Note that the results include the effects of thermal residual strains, showing that the method is applicable to repairs experiencing nonlinear bending and the presence of initial stresses.

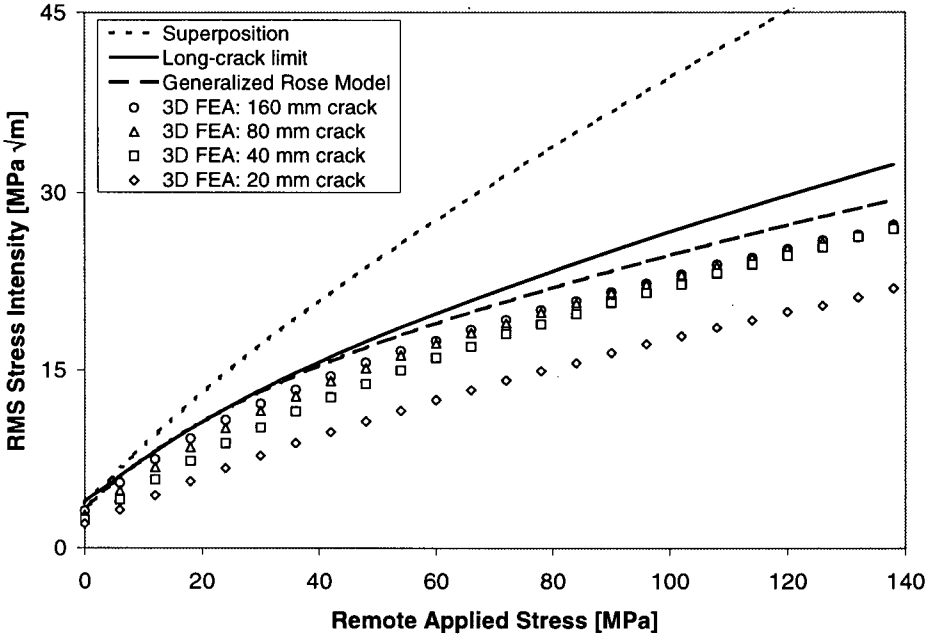

Figure 7-17: Nonlinear variation in RMS stress intensity

The two-dimensional finite element models used to calculate the external potential and stored energy for the cracked and uncracked strips contain no special elements and are easily extendable to multi-physics analysis including effects such as diffusion of water into the joint. They may also easily be extended to the analysis of a disbonding patch, and to the examination of repairs with different materials, repair thickness, and overlap lengths. For this reason the GR model is seen as a very useful tool for damage tolerance analysis and design of repairs, however the method faces significant challenges. A method is required to separate the membrane and bending stress intensity components to allow prediction of fatigue and fracture, a suitable interpolation is required for finite-length cracks, and means must be developed by which the stresses in the composite repair and the adhesive may be known.

7.5.1 Mode separation

In previous efforts, the authors attempted to perform mode separation by separating the energy stored in the structure into components related to bending and extension [18]. Unfortunately, energy-based methods yielded poor results, as it proves to be difficult to come up with a sound means for separating the strain energy in a composite structure into membrane and bending components, particularly for the edge regions where the plate and patch cannot be described by simple composite beam theory. It is also not readily discernable which part of the potential energy of the applied load is related to bending or extension, as the displacement at the point of application of the load results from a

combination of bending and tensile modes that cannot be decomposed under the influence of nonlinear effects. Instead, a nonlinear crack-bridging model was developed based upon the linear crack-bridging model [18], which allows the calculation of the membrane and bending stress intensity factors, and the membrane and bending crack face displacements for a crack bridged by springs. For the analysis of a crack with a finite length, the model assumes that the deflection of the crack faces is governed by a linear relationship, where the subscripts m and b stand for membrane and bending components of the stresses, stiffnesses, and displacements. As examples, k_{mm} is the membrane stiffness of the patch as it bridges the crack, and k_m^p is the membrane stiffness of the cracked plate.

$$\begin{pmatrix} \sigma_m^0 \\ \sigma_b^0 \end{pmatrix} = \begin{bmatrix} k_{mm} + k_m^p & k_{mb} \\ k_{bm} & k_{bb} + k_b^p \end{bmatrix} \begin{pmatrix} u_m \\ u_b \end{pmatrix} \tag{7}$$

To extend this model to the case of nonlinear coupled bending and extension, one must derive a stiffness term for the nonlinear stiffening effects acting upon the repair. Consider a very long composite beam (i.e. a boron-epoxy patch bonded to an aluminum substrate) with one end pinned at the neutral axis and with an applied force T acting at the far end as shown in Figure 7-18. The nonlinear response of the beam is characterized by the parameter $\lambda = sign(T)\sqrt{T / EI_{rp}}$, where EI_{rp} is the beam bending stiffness of the repaired plate.

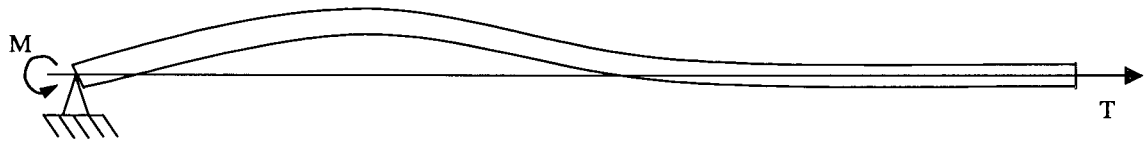

Figure 7-18: Stress-stiffening beam model

The rotation at the end of the beam is given as follows:

$$\theta = \frac{M}{EI_{rp}\lambda} \tag{8}$$

Expressing the rotation in terms of the bending displacement of the outer fibre of the aluminum substrate, u_b, and expressing the moment in terms of the bending stress in the outer fibre, σ_b, this may be rewritten as follows.

$$u_b = \frac{\sigma_b I_p}{EI_{rp}\lambda} \tag{9}$$

Here, I_p is the second moment of area of the aluminum substrate plate alone. A bending stiffness coefficient can now be defined as follows:

$$k_{nl} = \frac{EI_{rp}\lambda}{I_p} \tag{10}$$

With this new bending stiffness term in hand, it is now possible to carry out a nonlinear crack-bridging analysis. An overview of the method follows.

Step 1: Considering only thermal residual stresses, the nominal membrane and bending substrate stresses (σ_m^0 and σ_b^0) and the composite patch membrane stress (σ_{mc}^0) at the crack plane are determined by the nonlinear analysis of a single lap joint without a crack.

Step 2: A linear crack-bridging analysis is carried out considering only the thermal residual stresses in the crack plane. The deflection results from this analysis are used to calculate the tensile line-force, T_0, carried by the patch as it bridges the crack under thermal residual stresses alone.

$$T_0 = (k_{mm}u_m + k_{mb}u_b)t_p + \sigma_{mc}^0 t_r \tag{11}$$

Step 3: Considering both thermal residual stresses and an applied tensile load, the nominal membrane and bending stresses in the crack plane are recalculated.

Step 4: An initial guess for the total tensile line-force carried by the patch as it bridges the crack is made, as follows:

$$T = \sigma_a t_p \tag{12}$$

Step 5: Based on the derivation presented above, a nonlinear bending stress-stiffening term is calculated to account for nonlinear effects.

Step 6: The crack plane stresses from step 3 are applied as crack-opening stresses in the linear crack-bridging model. The stiffness matrix includes the nonlinear term k_{nl}.

$$\begin{pmatrix} \sigma_m^0 \\ \sigma_b^0 \end{pmatrix} = \begin{bmatrix} k_{mm} + k_m^p & k_{mb} \\ k_{bm} & k_{bb} + k_b^p + k_{nl} \end{bmatrix} \begin{pmatrix} u_m^r \\ u_b^r \end{pmatrix} \tag{13}$$

Step 7: The resulting membrane and bending crack opening deflections are used to calculate the actual line-force carried by the patch as it bridges the crack. A correction is made to account for T_0, which is not considered to contribute to stress stiffening.

$$T = (k_{mm}u_m + k_{mb}u_b)t_p + \sigma_{mc}t_r - T_0 \tag{14}$$

Step 8: Return to step 3 using a bisection method to arrive at a new estimate of the line-force and iterate towards the solution. The nonlinear bending stiffness term is updated for each iteration. Repeat until the line-force value converges. At this point, the line-spring

model provides the as-reinforced membrane and bending stress intensity factors and the crack opening displacements at the centre of the crack.

This method accounts for the fact that the remote applied load is generally shed from the reinforced region near the centre of the crack, reducing the nonlinear stiffening effects. To demonstrate the utility of this closed-form interpolation approach, the authors have applied it to a bonded composite repair for a range of finite width cracks. These results are shown in Figures 7-19 through 7-22 where they are compared to three-dimensional finite element results for the same repair geometry. Also shown are the long-crack limit results found by applying the stresses determined in step 3 to a linear crack-bridging analysis. These results are generally very conservative and are labelled as 'superposition' on the figures. The nonlinear long-crack limit results are found by excluding the plate stiffness terms (k_m^p and k_b^p) from the nonlinear crack-bridging analysis.

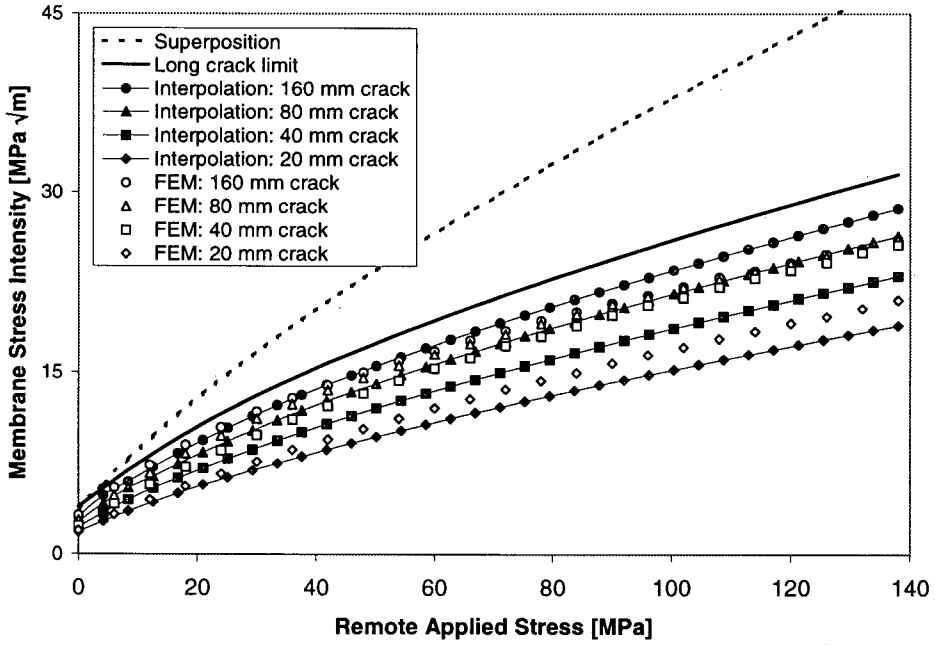

Figure 7-19: Membrane stress intensity.

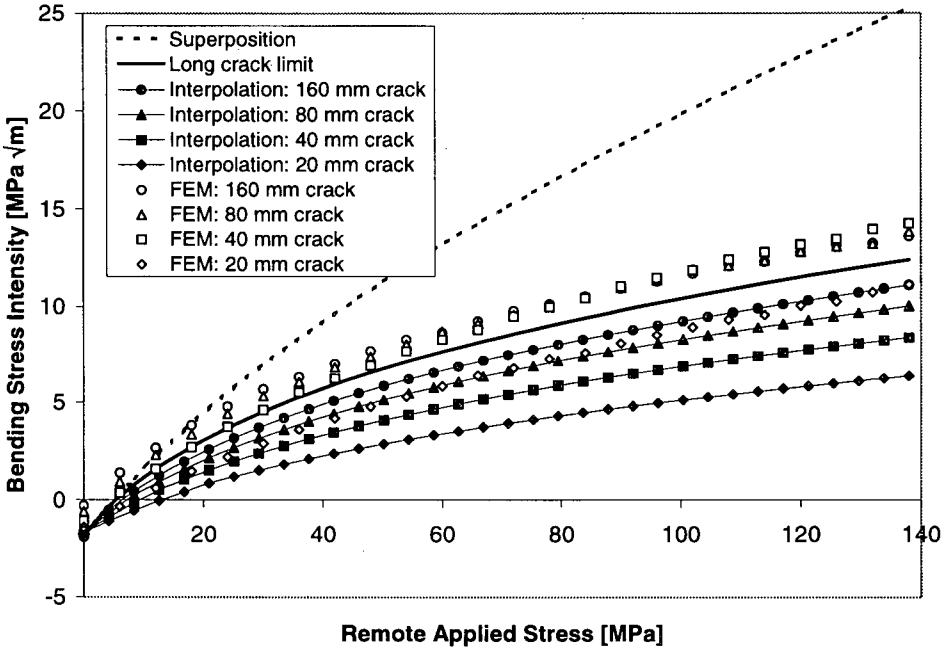

Figure 7-20: Bending stress intensity

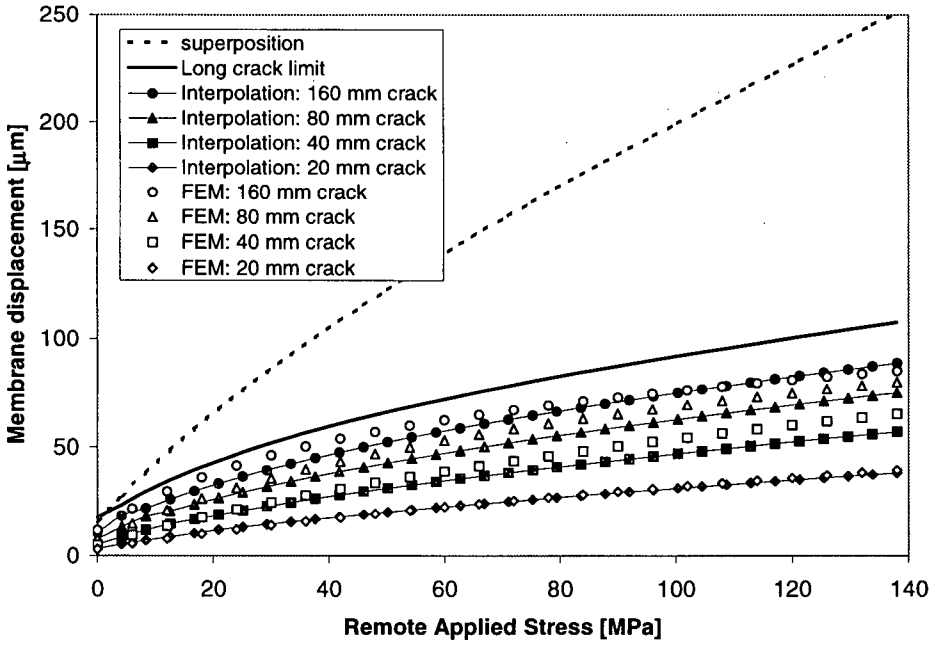

Figure 7-21: Membrane crack face displacement

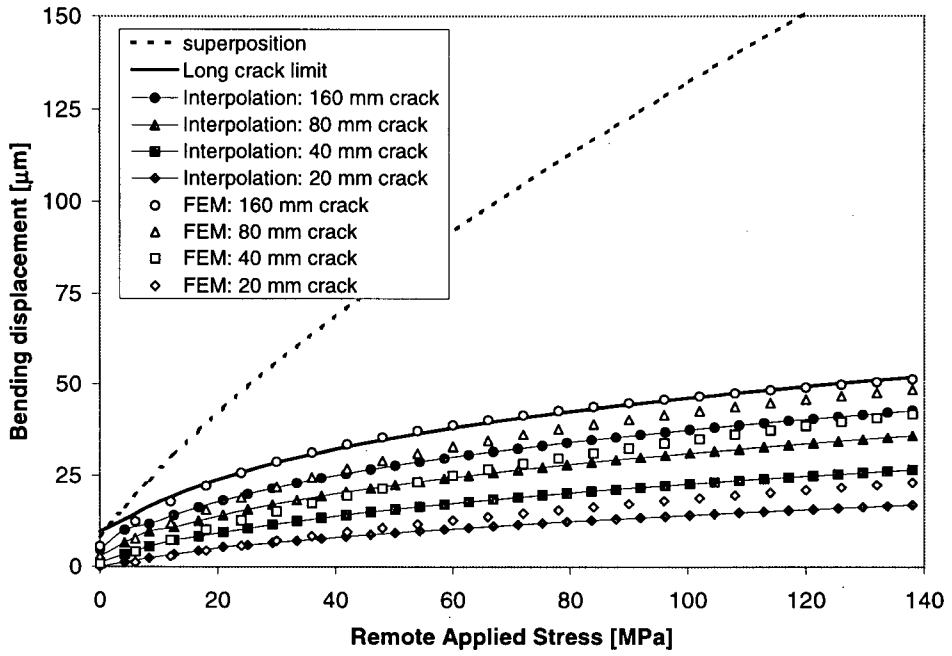

Figure 7-22: Bending crack face displacement

As illustrated in the figures, the results using this closed-form interpolation approach are much more accurate than would be achieved by superposition alone, and should provide much more realistic estimates of the strength and life of a repair, but are not sufficiently accurate to be used alone as a basis for airworthiness certification and cannot be shown to be conservative in a general manner. Accordingly, the authors see this approach as a valuable tool for design optimization and the determination of the effectiveness of a single-sided repair, however they are not yet a replacement for a comprehensive and detailed analysis. The approach involves highly idealized models, particularly in regard to the patch and plate geometry, which are considered to be of infinite planar extent throughout. A combined approach of design optimization and life assessment by this crack-bridging model along with verification at selected crack lengths by full three-dimensional finite element analysis is suggested as being appropriate. Comparisons should also be drawn to test data wherever possible, particularly as regards the evaluation of the strength and life of adhesive and composite.

7.5.2 Adhesive and Composite Failure

Given the experimental results described in Section 7.2, the peel stresses in the adhesive and the bending stresses in the composite plate have a central role in the failure of a one-sided repair. Reliable methods are required for the prediction of these stresses under the combined effects of thermal residual strains and nonlinear bending. Baseline stresses for the repair of a very long crack may easily be determined from the two-dimensional model of an equivalent cracked lap joint, such as the FE model that was validated in Section 7.3.

This provides long crack limit values, similar in nature to the long crack limit stress intensity determined by the Rose model. The adhesive and composite stresses for a reinforced crack of arbitrary length may be determined from the crack face displacements calculated in Section 7.5.1 if one considers the geometrically nonlinear bending to be a function of the greater geometry of the repaired plate, and the local adhesive and composite stresses to be locally linear. In this case, the adhesive stresses may be determined from either the FE results or the closed-form analysis presented by the authors in reference (19). Using the FE results for the tested specimen geometry, the crack opening stress required to develop the displacements calculated in Section 7.5.1 may be calculated as follows:

$$\begin{pmatrix} \sigma_m \\ \sigma_b \end{pmatrix} = \begin{bmatrix} 2.814 & -3.591 \\ -10.783 & 16.189 \end{bmatrix} \begin{pmatrix} u_m \\ u_b \end{pmatrix} \tag{15}$$

Here, the stresses are expressed in units of MPa and the displacements in μm. Again using the FE results, the adhesive stress may be found as follows:

$$\begin{pmatrix} \sigma_p \\ \tau_a \end{pmatrix} = \begin{bmatrix} -1.359 & -0.125 \\ 4.447 & 1.206 \end{bmatrix} \begin{pmatrix} \sigma_m \\ \sigma_b \end{pmatrix} \tag{16}$$

The results of this calculation are shown in Figures 7-23 and 7-24 where it can be seen that, when compared to three-dimensional FE analysis, the adhesive stresses follow the correct trend and should provide reasonable results for strength and life estimation.

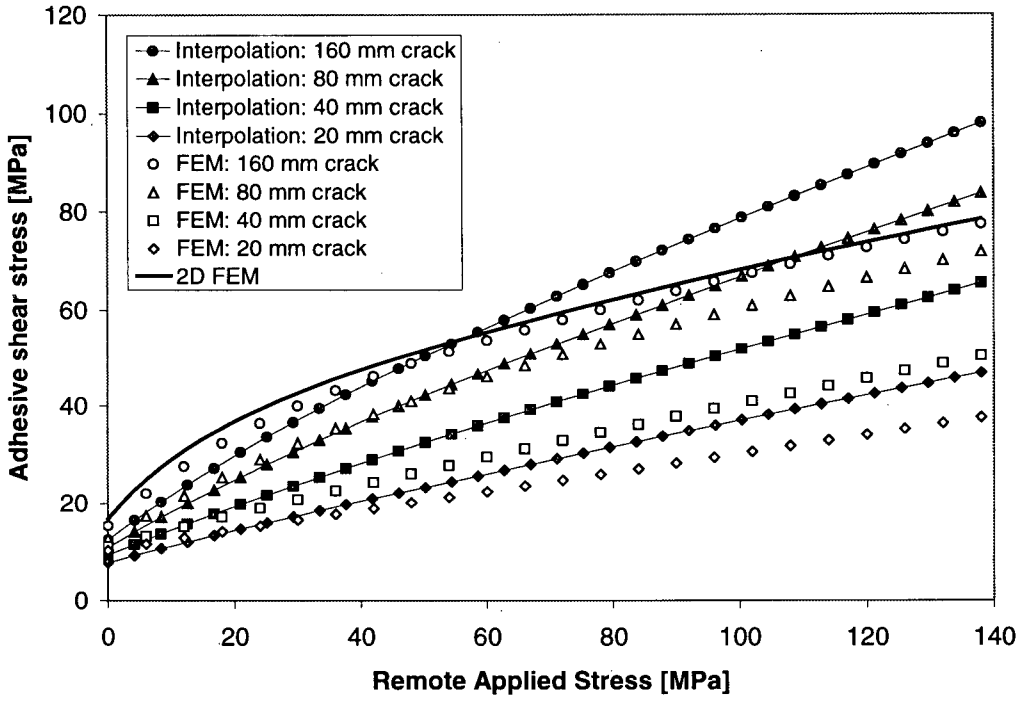

Figure 7-23: Adhesive shear stress

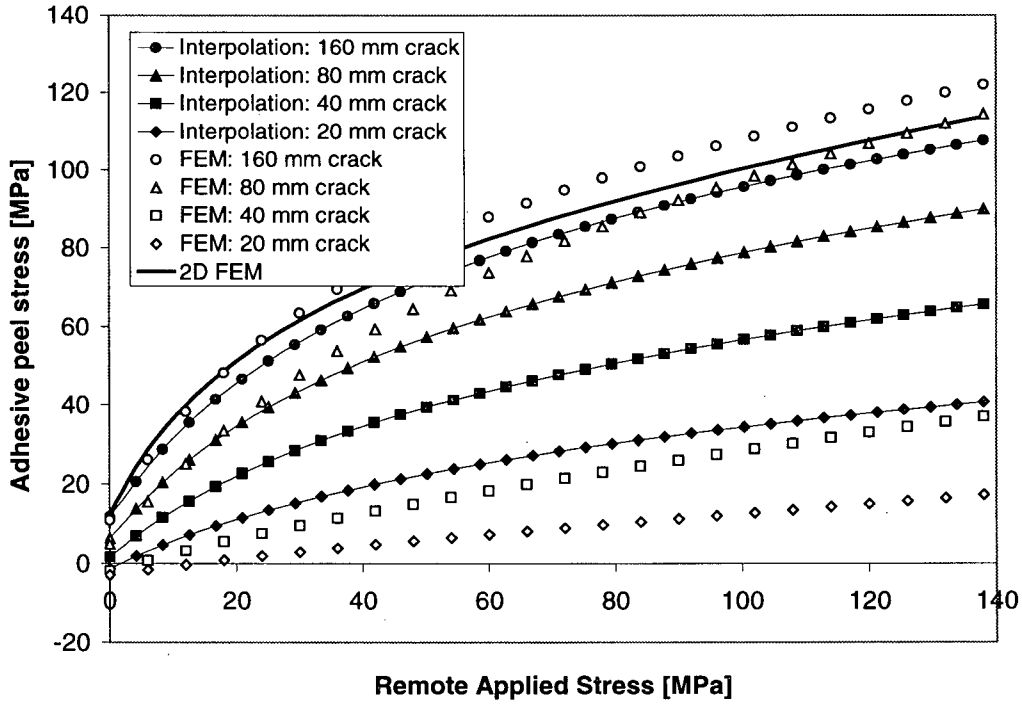

Figure 7-24: Adhesive peel stress

By a similar technique, it is possible to calculate the stresses in the composite patch. Here, it is possible to calculate the crack bridging component of the membrane and bending stresses in the patch directly from the resultant force and moment given by the

effective crack opening stresses in equation (15). The nominal stresses in the patch may be determined from the two-dimensional model presented in Section 7.3.

$$\begin{pmatrix} \sigma_m^c \\ \sigma_b^c \end{pmatrix} = \begin{bmatrix} \frac{t_p}{t_c} & 0 \\ \frac{3t_p(t_p+t_c)}{t_c^2} & \frac{t_p^2}{t_c^2} \end{bmatrix} \begin{pmatrix} \sigma_m \\ \sigma_b \end{pmatrix} + \begin{pmatrix} \sigma_{mc}^0 \\ \sigma_{bc}^0 \end{pmatrix} \tag{17}$$

Figures 7-25 and 7-26 show the results of this calculation. It is again observed that the results follow the correct trends. It must be noted that the patch bending stresses are very high for single-sided repairs, and therefore must be carefully considered during design of the resulting hybrid structural repair.

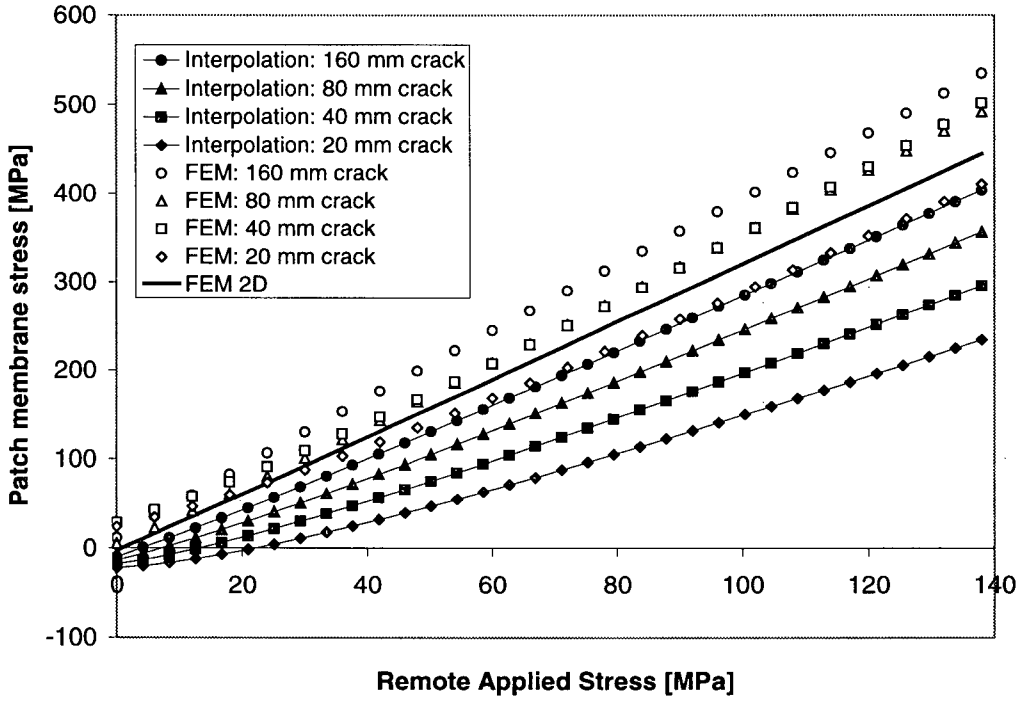

Figure 7-25: Patch membrane stress

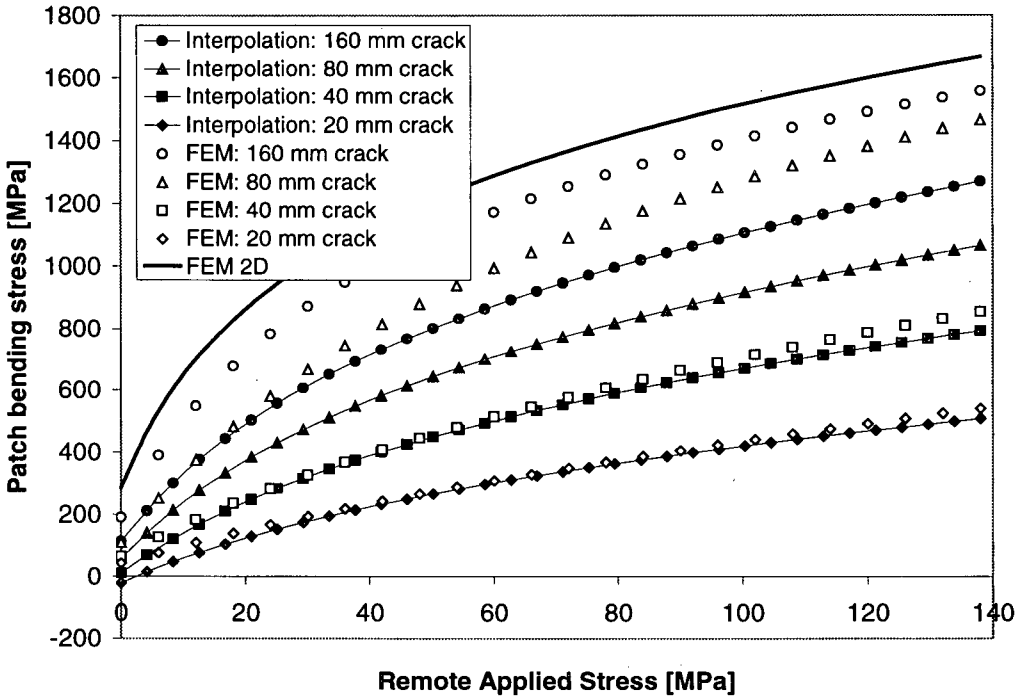

Figure 7-26: Patch bending stress

7.6 Discussion

A set of bonded joint specimens have been designed, built, and tested in order to determine the extent to which bending restraint affects the mechanical response of a repair. The developed approach allows for the direct experimental evaluation of the effects of nonlinear coupled bending and extension on the energy available to drive crack growth in the repair of a long crack. The method requires very precise measurements of the deflection and load carried by the specimen, and the use of two extensometers such that the deflection at the load-line can be calculated. By comparison to finite element results, the effects of bending restraint, disbonding, and the adhesive bridge over the crack faces are all measurable. The authors see this approach as a very direct means to assess the effect of various materials and patch geometries on repair performance. By testing materials that are in different conditions (e.g. hot/wet), data regarding the effectiveness of a particular repair strategy can be garnered while tests to determine disbonding rates and failure modes of bonded joint specimens are conducted.

The experimental results indicate a change in disbonding mechanism from cohesive failure of the adhesive for a symmetric or double-sided joint to failure at the interface of the patch and adhesive and within the first ply of the composite patch for a single-sided repair that is not restrained against bending. This change in damage mode accompanies a large increase in the rate of disbonding and culminates in the eventual failure of the composite patch due to bending and peel stresses. The detrimental effects of peel stresses

and bending on the performance of bonded composite repairs is well known, and is warned against both in the literature [e.g. 20] and in FAA circulars, which require the assessment of composite failure modes. The results in this paper verify the importance of geometrically nonlinear bending effects on the strength and life of a repair and provide new means by which they can be assessed in terms of the repaired plate, the adhesive bond, and the composite repair.

By comparison with measured strains, lateral deflections, and load/deflection curves, it has been demonstrated that two-dimensional FE models can easily model the complex behaviour of the single lap joint. Through the Rose model and by comparison with experimental results, it has been shown that developed two-dimensional FE model results provide an accurate assessment of the energy available for crack growth and the root-mean-square stress intensity for a long crack under a single-sided repair. It is also possible to evaluate the adhesive and composite stresses in a repair containing a long crack. Unfortunately, this approach does not provide data for short cracks or cracks of arbitrary length, and as such, while useful for the evaluation and ranking of different repair configurations, is not particularly useful for life assessment and damage tolerance analysis. As much of the life of a structure occurs during the initial growth of a crack, methods are required to analyse the stress intensity and adhesive/composite stresses for an arbitrary crack length. For this purpose, the authors introduce a nonlinear crack-bridging model, which, by comparison to three-dimensional FE models, provides a significant improvement in analytical capability over existing methods.

The nonlinear crack-bridging model provides reasonable results that should provide a sound evaluation of the life of the repaired plate. It has not, however, been established that the results are conservative and validation against test data or verification against finite element models is still required, particularly with respect to concerns related to the evaluation of the effects of the planar geometry of the patch and plate. It is proposed that initial analysis and design verification proceed by first designing the best possible bonded joint based on a two-dimensional finite element or analytical bonded joint model. Ideally, the joint should be capable of carrying the entire load in the plate and be designed such that adhesive stresses are below a threshold. Damage tolerance assessment of the repair itself would first be attempted by the conservative linear crack-bridging method. Acceptable results at this stage should preclude much additional verification/validation work as the models are inherently very conservative. In cases where such results are not acceptable, it would be necessary to move to the next level of analysis and use the nonlinear crack-bridging model described in this paper to obtain a more realistic assessment of the life of the repair. It is recognized however that, depending on the margins involved, significant validation work via finite element analysis and/or

comparison to test results may still be necessary to ensure the conservatism of the analysis and obtain airworthiness certification.

With a nonlinear crack-bridging model in hand, it is possible to perform a comprehensive damage tolerance assessment of a single-sided bonded repair. It remains to develop a nonlinear bonded joint model suitable for inclusion in a damage tolerance analysis software package, and to develop a process for arriving at allowable stress levels for the adhesive and the composite patch matrix. With these two further pieces in place, it should be possible to optimize and certify repair designs with relative ease, at least for 'easy' cases where stresses are low and/or the plate being repaired is relatively thin such that induced bending is not overly severe. It is likely that complex problems with high stresses or unusual geometries will always require additional experimental verification and in these cases, bonded composite repairs will likely only make sense on a fleet-wide basis or where scrapping of a part is prohibitively expensive or a structural component cannot be removed from the plane.

7.7 Concluding Remarks

The goal of damage tolerance analysis is to demonstrate that the structure will retain strength in the presence of detectable damage from known damage sources, and that sufficient inspection regimes have been prescribed to prevent catastrophic failure. By an experimental and finite element investigation of lap joints that are representative of a one-sided bonded composite repair, it has been confirmed that geometrically nonlinear coupled bending and extension along with adhesive and composite failure modes play a key role and must be evaluated in a comprehensive manner. However, while well recognized within the structural repair community, with the exception of performing a full numerical analysis of a particular repair scenario, few design tools exist that can fully assess nonlinear effects in such a manner that a realistic estimate of the life of the repair can be made. Currently there is very little design information present for the evaluation of the adhesive and composite strength under nonlinear bending.

To this end, the authors have evaluated the nonlinear Rose model and validated it against both experimental and finite element results. The long-crack limit root-mean-square stress intensity results were shown to be very good. This is sufficient to rank the effectiveness of various repair designs in slowing or stopping the growth of long cracks, but is unfortunately not sufficient for the calculation of the strength of the repair or the rate of crack growth. More capable means are required, as the largest part of the life of a repair will occur when the crack is small, and both the membrane and bending stress intensity factor are required in order to predict the strength and rate of crack growth. This method also does not provide sufficient information to fully evaluate the strength of the adhesive or the composite with short cracks.

Based upon a linear crack-bridging model previously developed by the authors, the authors have developed a new method for the nonlinear analysis of repaired cracks of arbitrary length. It is an improvement over existing approaches, allowing the determination of much improved estimates of the stress intensity in the repaired plate and the stresses in the adhesive and the composite repair. Accordingly, it should provide a better evaluation of the life and strength of a repair. More work is need to develop nonlinear bonded joint models suitable for incorporation into damage tolerance software and in developing stress allowables for the adhesive and composite matrix such that repairs can be easily designed and optimized for damage tolerance.

7.8 References

[1] Baker, A.A. Repair Efficiency in Fatigue Cracked Aluminum Components Reinforced with Boron/Epoxy Patches. Fatigue and Fracture of Engineering Materials and Structures, 16, 753, 1993.

[2] Clark, R.J. and Romilly, D.P., Fatigue Damage Prediction for Bonded Composite Repairs Applied to Metallic Aircraft Structures. SAE Transactions - Journal of Aerospace (2001).

[3] Clark, R.J. and Romilly, D.P., Experimental Study of a Bonded Composite Repair presented at the 2002 CSME Forum, Kingston, Ontario, May 21-24, 2002. 9 p.

[4] Rose, L.R.F., 1988. Theoretical Analysis of Crack Patching. In: Baker, A.A., Jones, R., (eds.), Bonded Repair of Aircraft Structures, Martinus Nijhoff, Dordrecht, pp. 77-106 (1988).

[5] Albat, A.M., Thermal Residual Stresses in Bonded Composite Repairs on Cracked Metal Structures, Faculty of Graduate Studies, Department of Mechanical Engineering, University of British Columbia, 1998.

[6] Rose, L.R.F., A Crack Repaired by Bonded Reinforcement, International Journal of Fracture, 18(2), 135-144 (1982)

[7] Wang, C.H., Rose, L.R.F., A Crack-Bridging Model for Bonded Plates Subjected to Tension and Bending, International Journal of Solids and Structures, 36, 1985-2014 (1999)

[8] Clark, R. J., Romilly, D. P., Non-linear Bending Study of Hybrid Aluminum and Boron-Epoxy Bonded Joints presented at CANCOM, Ottawa, Ontario, 10p, 2003.

[9] Kotousov, A., Wang, C. H., Fundamental Solutions for the Generalised Plane Strain Theory, International Journal of Engineering Science, 40, 1775-1790 (2002)

[10] Kotousov A. and Wang C.H. A generalized plane strain theory for transversally isotropic plates. Acta Mechanica 161 (2003) 53-64

[11] Rose, L.R.F., An Application of the Inclusion Analogy for Bonded Reinforcements, International Journal of Solids and Structures, 17, 827-838 (1980)

[12] Baker AA, Roberts JD, Rose LRF. Experimental study of overlap joint parameters relevant to k eduction due to crack patching. 28th National SAMPE Symposium, 1983, 627-639.

[13] Sun CT, Kug J, Arendt C. Analysis of cracked aluminum plates repaired by bonded composite patches. AIAA Journal, 34, 369-374, 1996.

[14] Naboulsi S, Mall S. Nonlinear analysis of bonded composite patch repair of cracked aluminum panels. Composite structures 41, 303-313, 1998.

[15] Clark RJ and Romilly DP. Transverse shear and pressurization effects in the bending of plates with reinforced cracks, accepted by Engineering Fracture Mechanics.

[16] Clark RJ. Damage tolerance of bonded composite aircraft repairs. Ph.D. thesis, University of British Columbia, 2006.

[17] Clark, R. J., Romilly, D. P. Coupled bending and extension of bonded composite repairs, presented at CANCOM, Vancouver, British Columbia, 12p, 2005.

[18] Clark, R.J., Romilly D.P. Linear coupled bending and extension of an unbalanced bonded repair, accepted by International Journal of Solids and Structures.

[19] Clark, R.J., Romilly D.P. Elastic analysis of hybrid bonded joints and bonded composite repairs. Submitted to Composite Structures, October 2, 2006.

[20] Jones, R., Chiu, W.K., Smith, R. Airworthiness of composite repairs: failure mechanisms. Engineering Failure Analysis Vol. 2, 1995, pp. 117-128.

Chapter 8: Results, contributions, and future work

R.J. Clark

University of British Columbia Department of Mechanical Engineering

8.1 Introduction

In this chapter, the author summarizes the results of the work presented in the proceeding chapters, illustrates the objectives that have been met and the contributions to the field, and provides guidance for those who would follow up on the work. The overall objective of the UBC BCRP program is to develop the design methodology, tools, and experimental data required to move the bonded composite repair technology from the military realm into widespread use in the civil aviation repair and overhaul industry. In the literature review in Chapter 1, the author identified damage tolerance analysis requirements and the resulting need for comprehensive fatigue testing of any repair scenario or geometry as a major barrier to the use of the technology in civilian aerospace. In particular, shortcomings in our ability to easily characterize bending and plate thickness effects on: a) the rate of failure of the repaired substrate, and b) the composite patch and adhesive damage mechanisms, were identified as critical impediments. Accordingly, the overall objective of this thesis was defined as follows:

"To develop and validate methods for damage tolerance substantiation of bonded composite repairs, with a focus on quantifying the effects of bending and plate thickness"

This objective has been met through a rigorous program of mechanical testing, finite element modelling, and closed-form analytical work that lead to the development of new innovations in the several areas of solid body mechanics, including: a) fundamental topics of linear elastic fracture mechanics, b) bonded joint mechanics, c) the analysis of reinforced cracks, d) the development of new engineering methodologies for bonded joint design and e) damage tolerance substantiation of repairs.

For the purposes of this final chapter, discussion of this research has been divided into four stages:

1) full-scale patch testing and three-dimensional finite element modelling,

2) development of generalized plane strain plate models for coupled extension and bending of reinforced plates,

3) analysis of orthotropic patches under combined extension and bending, and

4) analysis of bonded repairs experiencing geometrically nonlinear effects.

For each of these topics, the author will identify the work that has been done, describe how it fulfills the thesis and program objectives, and then demonstrate its uniqueness or novelty. Following this, the final sections of this chapter have been organized to properly place the contributions of this work in the context of the industrial application of bonded repairs. This discussion addresses the following topics: a) how this work contributes to the program goals and to the aircraft repair and overhaul industry as a whole (the reader is hereby directed to review Table 8.1 for a overview of the design and certification process for an aircraft repair and see how the current work contributes to this process), b) the future work that would be required to bring the bonded repair technology into widespread use, and c) the significance of the contributions of the work.

The chapter is then concluded with recommendations regarding the future development of the bonded repair technology.

8.2 Patch testing and finite element analysis

The first stage of this portion of the work involved full-scale testing of a heavily instrumented bonded repair specimen (tested with and without bending constraint) and the development of a matching three-dimensional finite element model of a repair. By observing the damage accrued during fatigue testing, it was found that composite damage mechanisms (i.e. disbonding, interply delamination, and fibre fracture) dominate the response of the repair when bending is not restrained, ultimately leading to rapid failure. The nonlinear nature of the deformations of the structure under combined bending and extension was confirmed by strain data recorded at the critical locations in the patched structure. This data was also used to verify the three-dimensional finite element model of the repaired structure, which confirmed the primacy of the composite failure mechanisms. The model results also indicated: a) that the adhesive and matrix stresses, along with bending stresses in the fibres of the composite patch, were all very high under nonlinear bending conditions, b) that under compressive loads crack closure has a large effect on the patch stresses, and c) that the cracked plate geometry plays a large role and leads to increased load transfer to the repair for an edge-cracked plate.

In the second half of this work, the test data and the finite element results were used as an example, providing a context in which to explore the failure criteria available for the various components of a repair, and to evaluate the effectiveness of the methods and data currently available in the open literature for damage tolerance substantiation. This enabled the authors to develop stress-based adhesive design allowables for fatigue and fracture that account for both adhesive failure and composite transverse failures. By applying probabilistic methods and the principle of compounded conservatism to the findings, the authors were able to develop a new repair classification methodology based

upon the residual strength of the underlying structure and the stresses in the composite/adhesive. This classification scheme allows the repair designer to assign requirements for testing of specimens (fatigue, static, or both) and for in-service inspections based upon the actual risk involved in the application of a repair. The fundamental principle involved in this classification scheme is that the repair (including the assigned inspection and testing program) should either: a) result in a level of risk that is significantly lower than that implied by the design of a new damage tolerant structure, or b) that the designer be forced to follow a certification program that corresponds to the full fatigue testing and certification requirements that are imposed during the design of a new composite structure.

The combined patch testing and FEM analysis work is important to the objectives of the thesis in many ways. It establishes the composite failure mechanisms as an important consideration for assessing damage tolerance and demonstrates that many different failure modes act concurrently during the failure of a single-sided repair. This conclusion agrees with the views of Jones et al [1] and the FAA [2] that both composite and adhesive failure mechanisms must be fully accounted for in composite repair design to ensure reliability of the repair. The strain data collected during the experimental testing during this research work has proven to be very useful in the validation of finite element models of repairs, and both the finite element and experimental strain data illustrate the importance of nonlinear bending effects, crack-closure, and cracked-plate geometry in the modelling of a repair. The developed and validated finite element model was employed extensively in subsequent chapters, where the closed-form methods for assessment of repairs are developed and tested. Another important contribution of this work was the development of stress-based criteria for adhesive fracture and fatigue, an approach that may bring together diverging views on how best to approach the damage tolerant design of adhesive joints. The developed stress-based criteria and the combined plot of fracture and stress results (Figure 2-19) allows one to bring together all of the following considerations into one set of criteria:

1) the detrimental effects of hot and wet environment on both the yield and fatigue strength of the adhesive,

2) the possibility of fracture under cold conditions,

3) detrimental pressurization and peel stress effects, and

4) a clear definition of safe life and damage tolerant allowables.

These effects are difficult to deal with in isolation, imposing a large burden on repair designers. The classification of repairs according to the severity of the adhesive/composite matrix stresses and the residual strength of the underlying structure, and the use of probabilistic loads assessment and compounded conservatism overcome

issues related to bond durability. Overcoming this durability issue through such a classification process should allow the rapid certification of a large variety of non-critical repairs to dents, scratches, over-sized holes, and minor corrosion grind-outs in primary structures without the need for physical testing.

This work has provided a very large contribution to the overall goal of the UBC bonded composite repair program by providing a new path by which the burden of damage tolerance substantiation may be relieved for the design of patches for the vast majority of day-to-day repair scenarios in lightly stressed and lightly damaged structure. There are many new and unique elements to this work, starting with the test program itself. In the knowledge of the author, there is only one other set of bonded repair fatigue tests that explicitly tests a repair geometry under varying degrees of bending restraint, i.e. Sabelkin et al, 2006 [13]. The testing carried out for this thesis and the validated finite element models allowed the authors to bring forward many new ideas. The stress-based adhesive criteria is not new, but the observation that it can be used to address most of the major concerns related to fatigue and fracture including mode mixity (the combination of peel and shear stresses) and environmental effects is new. The repair classification scheme and the use of probabilistic loads assessment to overcome adhesive durability concerns are both new and very significant developments for repair design. Probabilistic loads assessment is a new approach by which the emerging concept of 'get home ability' (the ability to safely land in the event that gross damage or failure occurs that will be noticed by the ground crew) can be quantified. This is an emerging supplement/alternative to classical damage tolerance approaches.

8.3 Plate models and linear coupled bending and extension

The principal analytical work of this thesis has been two-fold: a) the development of a set of consistent line-spring models for bending and extension of plates and b) the development of a new interpolation model for the case of combined extension and bending of finite-thickness plates. As described in Chapters 3 through 5, this work had three components:

1) extension of reinforced cracked plates in a generalized plane strain plate,

2) development of a new 'generalized plane strain' plate bending model and its application to the bending analysis of a reinforced cracked plate, and

3) combined bending and extension of a single-sided repair applied to a cracked plate.

The first part of the work was the development of a hyper-singular integral equation relating stresses along the plane of a crack with the crack face deflections. The hyper-singular equation was developed from the generalized plane strain model of Mindlin as refined by Wang and Kotousov [3,4]. By orthogonal expansion and the use of a

collocation method, this allowed the development of a new line-spring model for cracked generalized plane strain plates. This line-spring model was then used to develop geometry correction factors that account for plate thickness effects and to test their application to crack-bridging problems. The generalized plane strain model was chosen as it is the simplest model that considers the effects of transverse stresses acting about a crack tip, and allows the analyst to avoid the somewhat arbitrary decision as to whether the plate is in a state of plane stress or plane strain. The new line-spring model and geometry correction factors also allow for the proper consideration of thickness effects in cracked plates, and have been used to correct the Rose model for the analysis of reinforced cracks. This contributes to the research objectives by allowing repair designers to properly account for the transverse stresses that build up at the crack tip due to elastic plate thickness effects.

The second part of this work involved the development of a new plate bending model following the precepts of the generalized plane strain model for extension. The result was an eighth-order plate bending model which allowed the evaluation of 'pinching shear' forces in addition to the normal moment, twisting moment, and shear force boundary conditions of traditional plate bending models. This allowed the evaluation of through-thickness stresses in regions with large in-plane stress gradients, such as the one that exists near a crack tip. The author proceeded in the manner described above for the case of extension of plates, developing a hyper-singular integral and a line-spring model, by which geometry correction factors accounting for transverse shear forces and the accompanying deformations were developed, and the Rose model was extended to the case of bending. There are several significant contributions in this work. The eighth-order plate bending model is new and allows the accurate determination of thickness-effects. The development of the line-spring model, the accompanying geometry correction factors, and the extension of the Rose model to the analysis of cracked plates are new developments and can effectively eliminate errors in the evaluation of the bending stress intensity. It is noted these errors can be as high as 60% using classical plate models. An additional important result to the field of linear elastic fracture mechanics is the observation that, in terms of the plate bending stress intensity, the crack tip in bending may be considered to be in a state of plane strain. This resolves some inconsistencies observed by Joseph and Erdogan [5] for the use of linear elastic fracture mechanics methods in classical plate bending models, and allows the proper use of energy methods in the analysis of reinforced cracked plates. This is a new and significant result for the field of linear elastic fracture mechanics and for the damage tolerance analysis of cracked plates.

The final part of this analytical work is the assessment of combined bending and extension of reinforced plates, whereby the method of Wang and Rose [6,7] was

corrected to account for a variety of significant issues: 1) finite plate thickness effects in bending and extension of cracked plates (addressed using the geometry correction factors found above), 2) plane strain conditions that exist at the crack tip in bending of a cracked plate, and 3) the asymmetry of the spring compliance matrix and coupling of the membrane and bending stress intensity factors that is required to satisfy Maxwell's reciprocal theorem. This corrected method for determination of the limit stress intensity factors was verified by using the new plate models developed in the previous chapters, and was then used to create a coupled line-spring model in the manner of Wang and Rose [8]. From this work, a new interpolation method was developed that is applicable to any length of crack. The significance of this new method is that it has a clear physical meaning as it is based upon an evaluation of the stiffness of a finite thickness plate containing a finite length crack. The closed-form results using this new interpolation method were verified against results from two- and three-dimensional finite element models, whereby it was shown that errors would arise mainly from the methods used to determine the nominal stresses acting under the repair and the stiffness of the springs. The main contributions of this work are the correction of the energy methods for the analysis of coupled bending and extension of repaired cracks, and the development of a new interpolation method for the analysis of cracks of arbitrary length. These are new and fundamental results that allow the satisfaction of Maxwell's reciprocal theorem in the analysis of reinforced cracks experiencing combined bending and extension, and allow the analysis of reinforced cracks of arbitrary length using an interpolation technique that is based upon physical phenomena rather than approximations based upon curve fitting. The author expects that this new interpolation model will become the standard analytical technique for the analysis of reinforced cracks.

8.4 Hybrid bonded joints and orthotropic patches

The third part of the work involved the development of an advanced closed-form model for the mechanics of a hybrid bonded joint, and is described in Chapter 6. This model includes the coupling of the shear and peel response of the joint, transverse shear deformations, and composite deformation modes (such as the shear and peel compliance of the matrix), and was based on the work of Delale et al [9] and Bigwood and Crocombie [10]. The model was validated against two-dimensional finite element model results, and applied to the analysis of a bonded composite repair using the interpolation model developed in previous chapters. The interpolation model results were then compared to three-dimensional finite element models of a bonded repair, demonstrating excellent correlation and predictive capabilities. The developed methods constitute a significant improvement over conventional engineering models for bonded joints that have traditionally been applied to the analysis of composite repairs because they allow a repair designer to account for all of the relevant composite deformation mechanisms.

This work allows the accurate assessment of both the stiffness of a bonded repair as it acts to bridge the underlying crack, and the adhesive peel and shear stresses (and hence an estimate of the strain energy release rate and stress intensity) acting near the crack. Both of these results are critical to assessing the damage tolerance of a repair, and thus the model is an important contribution to the objectives of this thesis and the bonded composite repair program. This work is new in that it represents the first time that such a comprehensive bonded joint analysis has been applied to the assessment of the effectiveness of a repair, i.e. in that it validates the bonded repair analysis techniques developed in Chapters 3 through 5 for the case of an orthotropic patch.

8.5 Geometrically nonlinear bending

Finally, in Chapter 7, mechanical testing of hybrid bonded joint specimens subjected to varying degrees of bending restraint was used to validate a series of two-dimensional finite element models that are representative of repairs. These models, and the three-dimensional finite element model applied throughout the thesis, were used to test strategies for the separation of the bending and membrane stress intensity components when nonlinear bending effects dominate the response of a repair. It was found that the generalized Rose model [11] provides an excellent assessment of the total energy available for cracking in the substrate, but no convenient means was found whereby this energy could be separated into membrane and bending components. Instead, the author developed a nonlinear version of the interpolation model to account for stress-stiffening under applied tensile loads. The nonlinear interpolation model yields results that are significantly more accurate than those determined by existing approaches, but unfortunately does not always provide conservative results, a topic that remains to be addressed by subsequent researchers.

This work fulfils the objectives of the thesis in several ways. The test data should prove invaluable in the validation of closed-form models for the analysis of combined bending and extension of hybrid joints. Nonlinear effects have been shown by several researchers to be a significant factor in the fracture analysis of joints experiencing combined tension and bending [e.g. 14,15]. Closed form models for bonded joint mechanics will ultimately prove to be very useful in the development of fatigue life assessment computer programs for damage tolerance assessment and optimization of bonded repairs. The fatigue data and finite element models also validate the generalized Rose model for the nonlinear bending of a single-sided repair, allowing it to be used for the evaluation of the limit root-mean-square stress intensity in the cracked plate, an important design parameter. The extension of the new interpolation model for coupled bending and extension of reinforced cracks to include nonlinear effects is pioneering work, and opens up a new avenue for the

analysis of single-sided repairs. This is an important development as a linear approach will be overly conservative and unworkable for many repair scenarios.

8.6 Contributions and recommendations for future work

This work has moved the bonded composite repair technology toward certification and widespread use in several important ways:

1) By fully incorporating the effects of bending, it demonstrates to regulatory authorities that the mechanics of a patch are well understood, and that the models include all of the relevant physical phenomena that affect the membrane and bending stress intensity and adhesive shear and peel stresses.

2) The closed-form crack-bridging models provide a simple check against finite element model results for real-world, complex repair geometries, easing the requirements for verification of such models.

3) The closed-form crack-bridging models, when combined with the stress-based safe life and damage-tolerant adhesive stress allowables, allow the development of a computer code to predict the fatigue life of a repair and provide a rational method for assigning inspection intervals.

4) The development of stress-based criteria for the adhesive allows the designer to include complicated environmental effects and assess damage tolerance without a sophisticated elastic-plastic fracture mechanics analysis or extensive testing. This approach conforms to 'best practice' as advocated by Hart-Smith [16], whereby a bonded joint should be designed to not fail by controlling the stresses, using an adequate overlap length to provide a large elastic well and avoid plastic racheting, and ensuring that the joint itself is never the weak link. The bonded joint is just one example of many types of aircraft structures where damage tolerance does not replace other design principles (e.g. good fatigue design) but is instead a supplemental requirement.

5) The repair classification methodology provides a simple risk-based approach to assign damage tolerance substantiation and in-service inspection requirements, which could greatly ease the substantiation requirements for repair of lightly loaded or lightly damaged structures, accounting for a large fraction of repair work.

To illustrate how this work fits into the repair design process, Figure 8-1 shows the major steps required to certify a repair from the documentation of a design process to the final certification of an installed repair on an aircraft. A typical timeline for a repair would be the production of a design and engineering drawing within a week or two (possibly produced in parallel with the work done on the aircraft), approval of the static assessment before first flight allowing operation for one year, and final approval of the DTA substantiation report and inspection requirements within that year. To illustrate how

the work in this thesis would be applied, a brief description of the contributions provided by this research work is included for each step where applicable, including the location of the relevant information. From this figure, it is apparent that there are two main types of contributions, those related to the methodology used to approach a repair (primarily addressed in Chapter 2), and those related to modelling of a repair (Chapters 3-7). The modelling work primarily addresses the problem of crack bridging in the different types of situations that might arise for a fuselage or wing-skin repair, where the structure might experience plane extension in areas with a large degree of bending restraint, unrestrained bending, coupled bending and extension, and geometrically nonlinear bending and extension. This allows the calculation of the stress intensity factor in the plate and the stresses in the adhesive and composite, which for the limit load case must all be kept below the design allowables developed as per the methodology document. Damage growth would be modelled by applying linear elastic fracture mechanics to the crack alone for repairs that have low adhesive and composite stresses (below allowable limits defined in Chapter 2), and the methods developed in this thesis could lead to very rapid design and certification of a repair. For other repairs (i.e. the 'Quadrant D' repairs defined in Chapter 2) rigorous physical testing and finite element analysis would likely be required and the repair approval process would not follow this simple schematic or benefit greatly from the methods developed in this thesis.

Step/requirement for repair design	Research contribution and location
(1) Build a methodology document for approval by regulator. This document defines the repair approval process, acceptable information sources, terminology, load and spectrum definitions, material property sources and test methods, prescribed inspection procedures, assumed flaw sizes, etc.	- Developed repair classifications based on new proposed DTA substantiation requirements (Ch 2.6). - Defined safe life and damage tolerant adhesive allowables (Ch 2.5.2). - Proposed probabilistic loads assessment (Ch 2.6) for certification of repairs to damaged structure.
(2) Develop materials allowables.	- Proposed/recommended allowables for FM73M (Ch 2, Equation 1) and Textron 5521 Boron-epoxy (Ch 2.5.3)
(3) Design repair and produce drawings. Use allowables, proper overlap lengths, and simple models to design the repair.	- Corrected linear crack bridging models and developed a new interpolation model to allow analysis of repairs under linear bending and extension (Ch. 3-5). - Enhanced bonded joint model to evaluate adhesive stresses and patch stiffness for crack bridging models (Ch. 6) - Developed new crack bridging model allowing analysis of geometrically nonlinear bending effects (Ch. 7).
(4) Static evaluation for preliminary approval. May need static test if existing structure has low residual strength.	
(5) Damage tolerance assessment for final approval. May require fatigue test for 'Quadrant D' repairs.	
(6) Assign inspection requirements.	

Table 8-3: Steps for repair design, application, and certification

The focus of this thesis has been the development of closed-form models and methods for damage tolerance substantiation that do not require sophisticated or detailed analysis. The alternative is to perform damage tolerance analysis using finite element models, which is very time consuming as that the model must be run with several different damage states to assess the rate of degradation of the repair. This task becomes even more formidable if the structure experiences effects such as geometrically nonlinear bending, plasticity, or rheological behaviour of the composite or adhesive. It is also time-consuming if the structure requires assessment for several different load states or environments – e.g. at cold or hot temperatures, or under different operating conditions

(e.g. during landing, during stable flight, fatigue under a specified load spectrum, or under design limit load). In this regard, the elastic adhesive stress criterion should prove very helpful in minimizing the engineering effort required for certification. Risk assessment and categorization of repairs has proven to be an effective manner of dealing with the issue of bond durability without invoking the requirement for detailed analysis of environmental effects or incurring new process controls or inspection criteria.

This work has met its objectives (i.e. to develop and validate methods for damage tolerance substantiation of bonded composite repairs) and advanced the state-of-the-art in many ways, however the greater topic of widespread use of bonded repairs is sweeping and involves the development of easy-to-apply analysis tools and the development of design data for application of repairs in many different scenarios (i.e. involving different materials, geometries, and loading or environmental conditions). Work in the area of aircraft structures also requires a very high standard of verification, and significant work is required to develop new methodologies to the point of widespread acceptance, representing a scope of work that is well beyond what is possible for a single individual to undertake. Accordingly, some of the elements required for the complete damage tolerance substantiation of a repair are still missing. Significant additional work is required in at least four areas:

1) more test data is required to characterize the effect of the environment on the fracture toughness and fatigue threshold for boron-epoxy/FM73M/aluminum hybrid bonded joints under mixed shear and peel loading and with different adhesive thicknesses to fully develop the stress-based adhesive failure criteria,

2) the new design classification technique and the adhesive stress criteria need to be evaluated against a set of in-service repairs to ensure that they provide conservative results when compared to current practice,

3) significant work is required to improve the nonlinear crack-bridging model and validate it against a wider range of repair geometries,

4) the new crack-bridging models need to be extended to the case of a partially-disbonded repair and placed into a computer code that employs the new design equations to estimate of fatigue life of the repair and assign inspection criteria, and

5) a compilation of engineering fracture mechanics correction factors for the crack face displacement is required in order to apply the new crack-bridging models to plates with finite geometries (e.g. for a repair applied to an edge-cracked plate).

The stress-based design criteria developed in Chapter 2 is particularly promising and probably offers the most immediate rewards in terms of advancing the bonded composite repair technology if carried further. The development of more test data for the effect of

the environment on the fracture toughness and fatigue threshold for boron-epoxy/FM73M/aluminum hybrid bonded joints, including a thorough assessment of the effects of mixed shear and peel loading and with different adhesive thicknesses, would allow for the development of a definitive stress-based design criteria for repairs. The development of such a design criteria could overcome the most onerous requirements for the acceptance of a major repair (i.e. physical testing for static strength, fatigue, and impact damage). Ideally, the process would be documented and standardized to promote the development of design data for other repair systems. This would ultimately allow the repair designer to select the ideal repair system for an application from a number of candidates, including epoxy or acrylic adhesives with boron-, carbon-, glass-fibre or GLARE patches. When combined with the probabilistic loads assessment technique and a system for the categorization of repairs, it should ultimately be possible to certify a typical bonded repair with no more engineering effort than is currently required for a mechanically fastened repair.

The repair classification scheme and the probabilistic approach used to handle the adhesive durability issue need to be tested against the current comprehensive damage tolerance substantiation requirements for a repair to ensure that the resulting designs are conservative when compared to existing practice. It would also be extremely helpful to develop a set of reference spectra for various types of aircraft structure that will generally be deemed to be conservative when compared to the actual in-service spectra for a passenger/transport aircraft. A once-per-flight limit load spectra will generally be very conservative, but may be too onerous and lead to unreasonably stringent inspection criteria. It may be adequate to assign some fraction of the limit load based upon a survey of existing aircraft. The probabilistic design criteria specified in Chapter 2 is a very effective way to provide an analytical meaning to the ability to 'get home' after the failure of a repair, and accordingly it is a topic with much promise and demands further investigation.

Finally, while significant progress has been made in fundamental topics regarding the mechanics of unbalanced repairs and reinforced cracks, additional work is required to finish the task and provide a complete tool kit to repair designers. Specifically, the development of the new nonlinear crack-bridging model is really in its very early stages, and needs to be extended to specific geometries (e.g. finite-sized repairs), validated against a wider range of repair geometries, and extended to the case of partial disbonding about the repaired crack. The linear crack-bridging model can be considered to be much more mature, but also requires extension to the case of a partially-disbonded repair. This could be done by using a boundary element model to test a wide range of practical patch geometries as has been previously done by the author for extension of bonded repairs [12]. Finally, the new design equations should be incorporated into a computer code to

allow rapid estimates of the fatigue life of a repair and to perform risk analysis and assign inspection criteria, and be extended to other cracked plate geometries by cataloguing crack face displacement geometry correction factors.

In this thesis, several fundamental barriers preventing widespread use of bonded repairs have been removed, and the author is certain that the future recommended research topics described in this section would quickly move the larger project toward completion and enable the widespread use of bonded composite repairs. Particularly rapid gains would be achieved through further development of the adhesive failure criteria and the repair classification process, allowing the rapid deployment of bonded repairs in a large number of day-to-day repair scenarios for lightly damaged or moderately loaded structures.

8.7 Concluding Remarks

This thesis has addressed many fundamental issues in bonding and linear elastic fracture mechanics, and in the engineering problem of certification of bonded repairs of aircraft structures. Significant contributions have been made in:

1) the development of a repair classification process,
2) the introduction of a simplified stress-based fracture and fatigue assessment methodology for adhesive joints that encapsulates environmental effects,
3) the use of probabilistic loads assessment to treat the issue of adhesive bond durability,
4) the collection of new test data for balanced and unbalanced repairs and hybrid joints,
5) the development of a new plate bending model for cracked plates,
6) the development of simple engineering geometry correction factors to account for plate thickness effects in fracture and fatigue,
7) the correction of the energy method for determining the long-crack limit stress intensity for reinforced cracks experiencing coupled extension and bending,
8) the development of a new interpolation technique for reinforced cracks that has a sound physical basis (i.e. not just a curve fit),
9) the development of a new elastic model for hybrid bonded joints that includes all of the relevant composite deformation modes,
10) experimental and finite element verification of the nonlinear Rose model, and
11) the introduction of a nonlinear crack bridging model for unbalanced repairs

This work represents a significant advancement in the understanding of the mechanics of bonded repairs and reinforced cracks in general, and the methodology, models, and test data should ultimately enable the widespread use of bonded composite repairs in civilian aircraft. Some recommendations have been made for future work in this field, with the most practical and immediately useful work being the further development of the stress-based adhesive fatigue and fracture methodology (possibly including the development of a standard to encourage the development of design data for other bonded joint systems), the actual application of phenomenological probabilistic methods to the classification of in-service repairs, and the incorporation of the new design equations into a computer code for design and life assessment of bending repairs.

8.8 References

[1] R. Jones. Assessing and maintaining continued airworthiness in the presence of widespread fatigue damage: an Australian perspective. Engineering Fracture Mechanics 60, 1998, 109-130.

[2] F.A.A. Advisory Circular 25.1529-1. Instructions for continued airworthiness of structural repairs on transport airplanes. U.S. Department of Transportation, Federal Aviation Administration, 1991.

[3] A Kotousov, CH Wang. A generalized plane strain theory for transversally isotropic plates. Acta Mechanica, 161, 2003, 53-64.

[4] A Kotousov, CH Wang. Fundamental solutions for the generalised plane strain theory. International Journal of Engineering Science, 40, 2002, 1775-1790.

[5] PF Joseph and F Erdogan. Surface crack problems in plates. International Journal of Fracture 41, 1989, 105-131.

[6] CH Wang, LRF Rose. On the design of bonded patches for one-sided repair. Proceedings of the 11th International Conference on Composite materials, Gold Coast, Australia, 5, 1997, 347-356.

[7] CH Wang, RJ Callinan, LRF Rose. Analysis of out-of-plane bending of a one-sided repair. International Journal of Solids and Structures 35/14, 1998, 1653-1675.

[8] CH Wang, LRF Rose. A crack bridging model for bonded plates subjected to tension and bending. International Journal of Solids and Structures 36, 1991, 1985-2014.

[9] Delale F, Erdogan F, Aydinoglu MN. Stresses in adhesively bonded joints: a closed-form solution. Journal of Composite Materials, 1981;15:249-271.

[10] Bigwood DA and Crocombe AD. Elastic analysis and engineering design formulae for bonded joints. International Journal of Adhesion and Adhesives 1989;9(4):229-242.

[11] LRF Rose. Theoretical aspects of crack-patching. In: AA Baker, R. Jones. Bonded repair of aircraft structures. Martinus Nijhoff, Dordrecht, The Netherlands, 1988.

[12] RJ Clark, DP Romilly. Fatigue damage prediction for bonded composite repairs applied to metal aircraft structures. 2001 SAE Transactions - Journal of Aerospace, 10 p.

[13] V Sabelkin, S Mall, JB Avram, "Fatigue crack growth analysis of stiffened cracked panel repaired with bonded composite patch", Engineering Fracture Mechanics, 73, 2006, 1553-1567.

[14] WS Johnson, "Stress Analysis of the cracked-lap shear specimen: an ASTM round-robin", Journal of Testing and Evaluation, Vol. 6., 1987, pp. 303-324.

[15] G Fernlund, M Papini, D McCammond, JK Spelt, "Fracture load predictions for adhesive joints", Composites Science and Technology, 51, 1994, 587-600.

[16] LJ Hart-Smith, "Design and analysis of bonded repairs for metal aircraft structures". In: "Bonded repair of aircraft structures", Baker AA and Jones R, eds. Martinus Nijhoff Publishers, 1988, pp.31-47.

Appendix A: Bonded joint specimen construction

This appendix describes the geometry, parts, materials, and manufacture of the lap, double-lap, and cracked lap-shear bonded joint specimens.

A.1 Description of specimen types

For the purposes of this thesis, four different types of bonded joint specimens were designed, manufactured, and prepared for testing. These have been referred to as the single lap joint specimen (SLJ), the double-lap joint specimen (DLJ), the honeycomb-separated double lap joint specimen (HS-DLJ), and the cracked lap-shear specimen (CLS). The SLJ, DLJ, and HS-DLJ specimens are of a geometry similar to that of the AMRL specimen, modelling a strip of patch removed perpendicular to the crack. The SLJ specimen models a single-sided repair that is free to bend, experiencing mixed-mode loading. The DLJ specimen is expected to experience only shear loading, and the HS-DLJ specimen includes a honeycomb spacer and is built to model the effects of a repair over underlying structure, allowing limited bending and mixed-mode loading. The CLS specimen is commonly used geometry that is used to test mixed mode loading with a moderate opening mode contribution and is popular with researchers investigating fatigue and fracture of adhesive joints. Figures A-1 through A-4 show the geometry of these specimens.

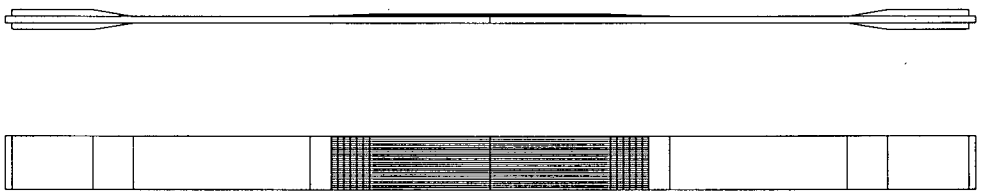

Figure A-1: Single lap joint specimen

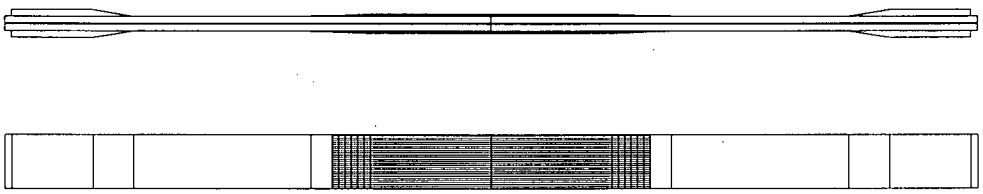

Figure A-2: Double lap joint specimen

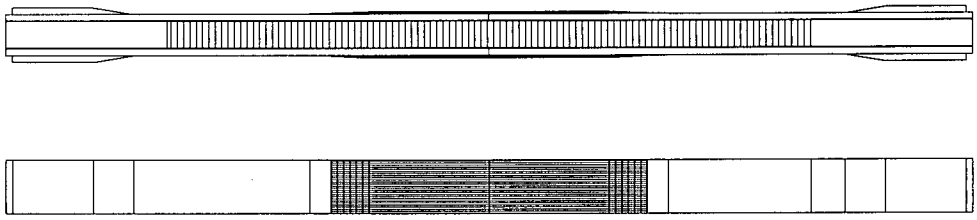

Figure A-3: Honeycomb separated double lap joint specimen

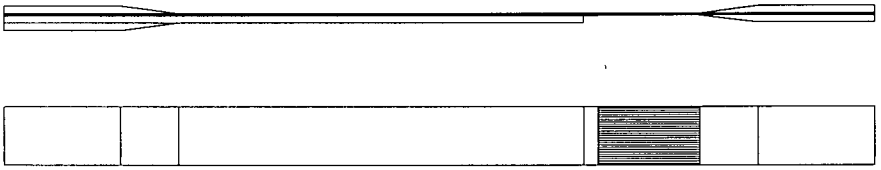

Figure A-4: Cracked lap-shear specimen

The specimens are 1 inch in width, corresponding to ASTM standards for adhesive testing of metal-metal bonded joints. This exceeds the ¾ inch minimum width specified for testing of composites. Tape inserted at the lap edge in the CLS specimen will force disbond initiation in the adhesive layer. The materials and manufacturing techniques for the bonded joint specimens largely match those of the AMRL specimen. The next section specifies the parts and materials required for their manufacture, and subsequent sections go on to explain the methods employed.

A.2 Parts and materials

Manufacture of the specimens was accomplished without a jig. The aluminum panels and spacer blocks were held in position using guide holes in the edges of the panels. This outer part of the panel was not used for fatigue testing, in conformance with the ASTM specifications for bonded joint coupons. Plugs inserted in the guide holes aligned and supported the parts. The panels rested on the heads of the aluminum plugs during curing. The composite 'patches' were supported by high temperature tape, which will also prevented the adhesive from running. Table A-1 lists the parts required for construction of the panels. Figures A-5 through A-8 are assembly drawings showing the panels from which the bonded joint specimens were machined. Figures A-9 through A-11 show the aluminum face sheets and figures A-12 through A-15 show other components necessary for the construction of the panels.

Panel type	Qty.	Material	Dimensions
CLS	1	Boron 5521/4 tape	105"x6"
	1	2024-T3 Aluminum sheet	10"x6"x0.125"
	1	FM73M Adhesive	20"x0.06 psf
SLJ	1	Boron 5521/4 tape	38"x6"
	1	2024-T3 Aluminum sheets	18"x6"x0.125"
	1	FM73M Adhesive	50"x6"x0.06 psf
DLJ	1	Boron 5521/4 tape	76"x6"
	2	2024-T3 Aluminum sheets	18"x6"x0.125"
	1	FM73M Adhesive	64"x6"x0.06 psf
	4	Plugs	
HS-DLJ	1	Boron 5521/4 tape	76"x6"
	2	2024-T3 Aluminum sheets	18"x6"x0.125"
	1	FM73M Adhesive	100"x6"x0.06 psf
	1	Aluminum honeycomb	
	2	6061-T651 Aluminum spacer blocks	12"x6"x0.5"
	4	Plugs	3"x6"x0.5"

Table A-4 : Coupon specimen materials

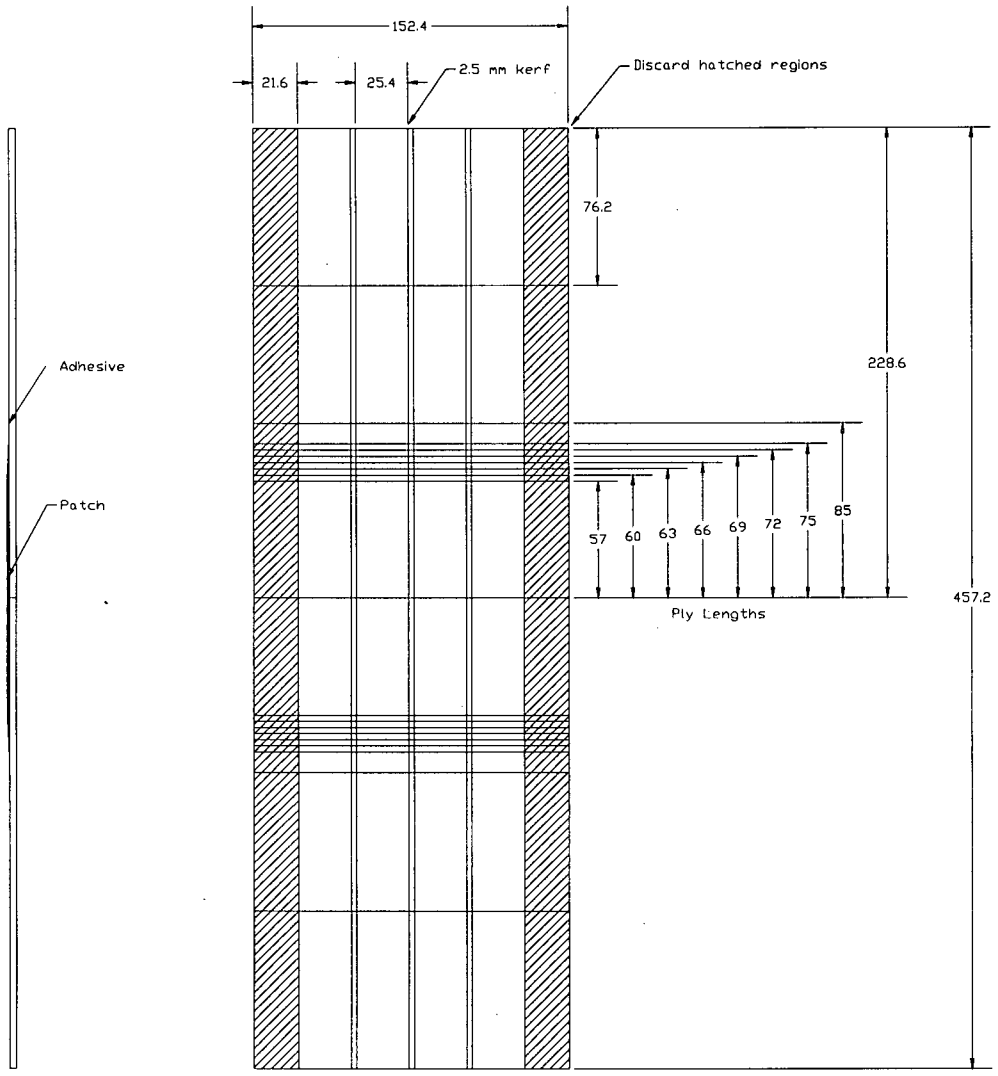

Notes: 1. Specimens to be machined from composite panel.
2. End tabs bonded to specimens after machining.

Project		
LJ Specimen (Assembly)		
Material	Scale	Copies
N/A	Not to Scale	1
DWG#	Units	Drawn
1	Millimeter	R. J. Clark

Figure A-5: LJ specimen composite panel assembly drawing

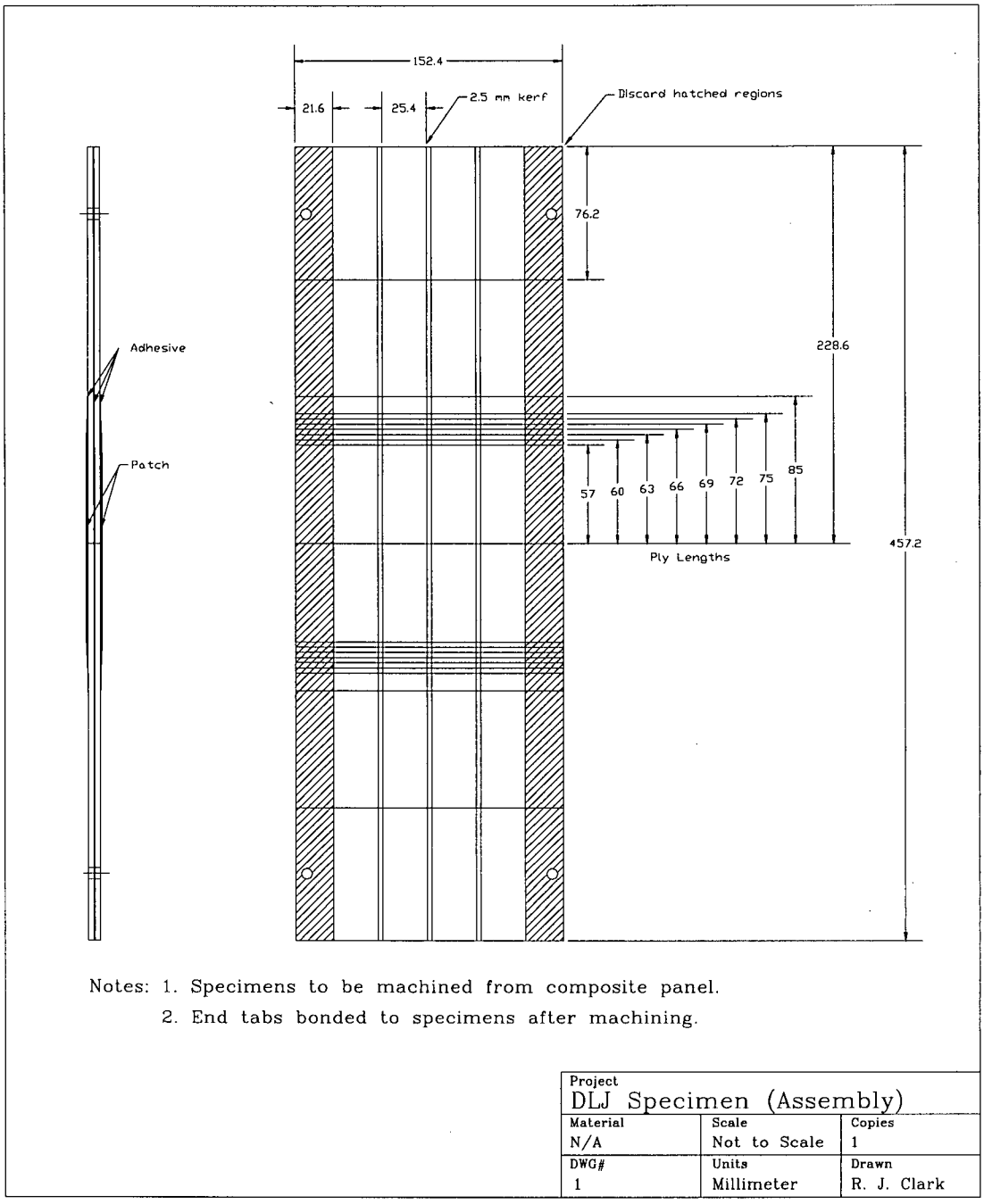

Notes: 1. Specimens to be machined from composite panel.
2. End tabs bonded to specimens after machining.

Project DLJ Specimen (Assembly)		
Material N/A	Scale Not to Scale	Copies 1
DWG# 1	Units Millimeter	Drawn R. J. Clark

Figure A-6: DLJ specimen composite panel assembly drawing

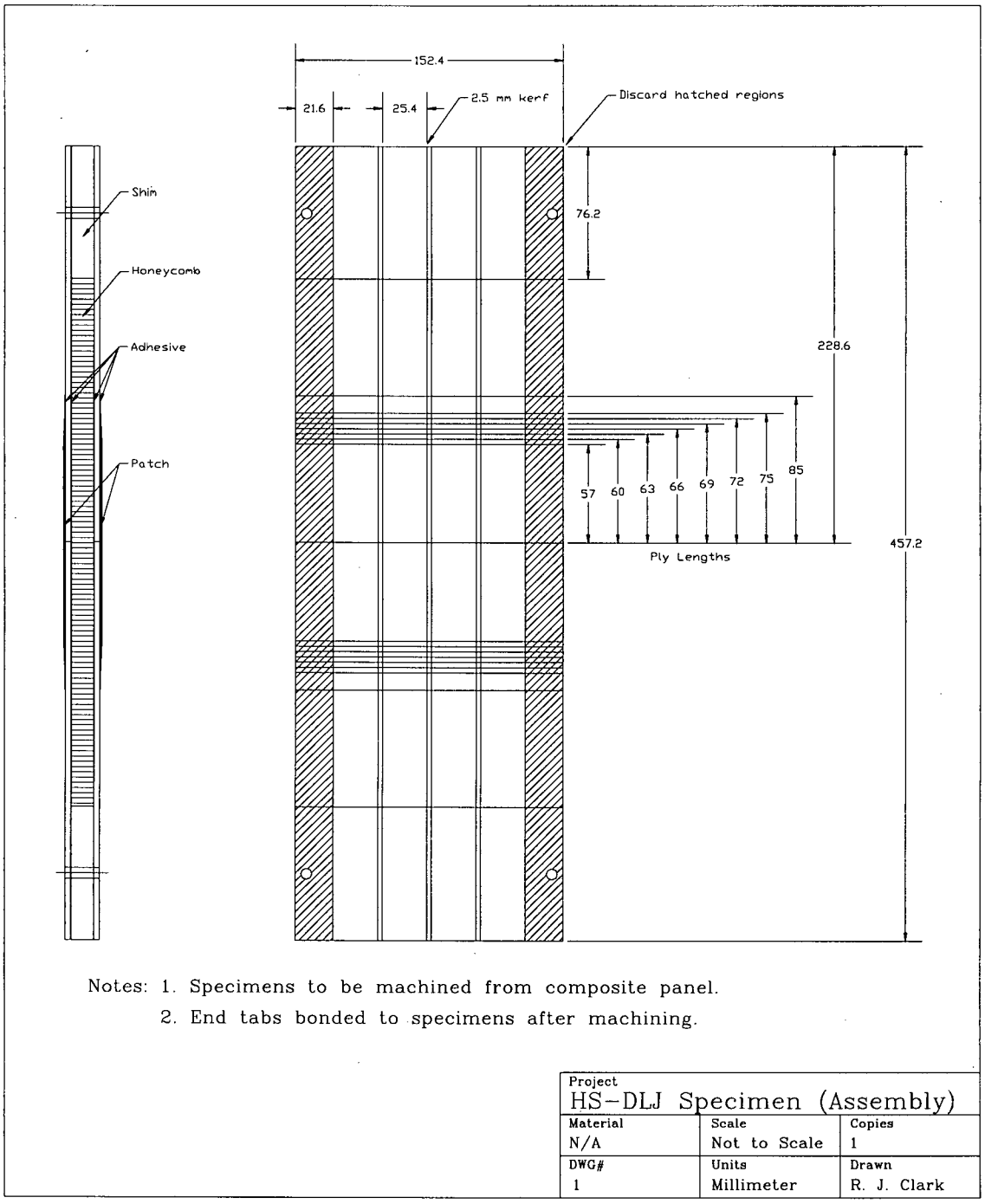

Notes: 1. Specimens to be machined from composite panel.
2. End tabs bonded to specimens after machining.

Project		
HS-DLJ Specimen (Assembly)		
Material	Scale	Copies
N/A	Not to Scale	1
DWG#	Units	Drawn
1	Millimeter	R. J. Clark

Figure A-7: HS-DLJ specimen composite panel assembly drawing

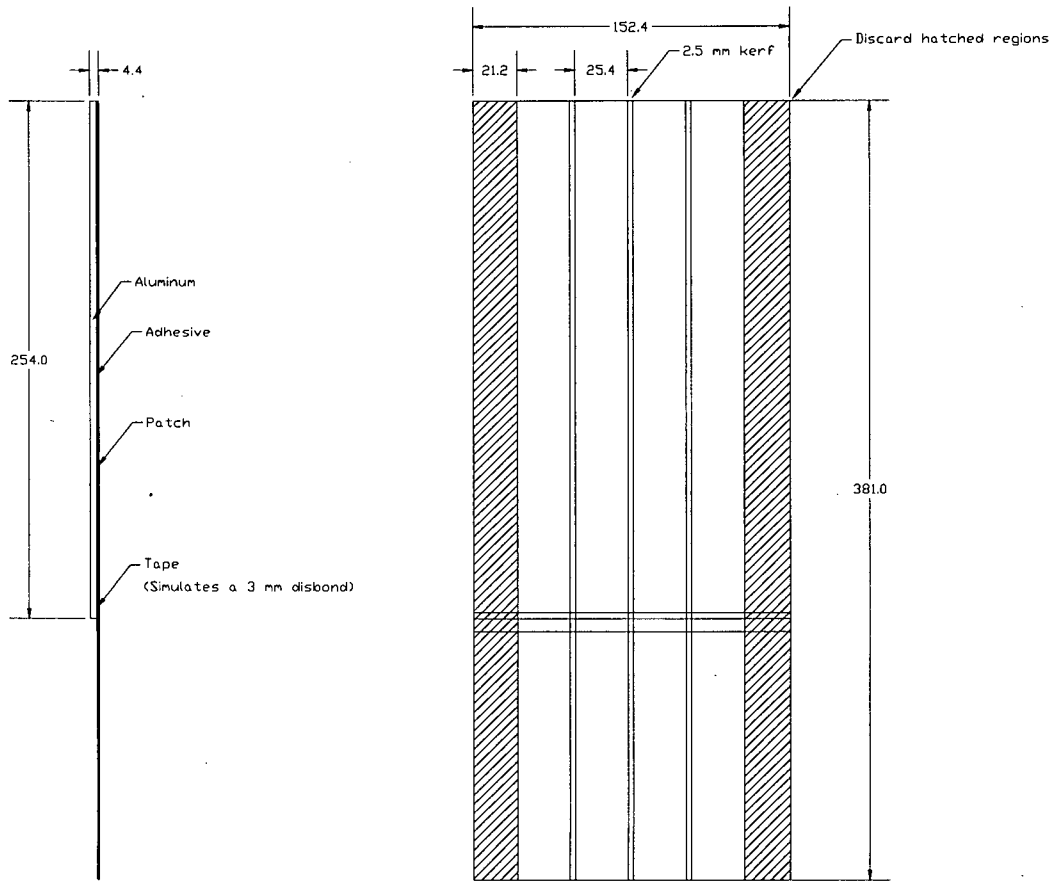

Notes: 1. Specimens to be machined from composite panel.
2. End tabs bonded to specimens after machining.

Project		
CLS Specimen (Assembly)		
Material	Scale	Copies
N/A	Not to Scale	1
DWG#	Units	Drawn
1	Millimeter	R. J. Clark

Figure A-8: CLS specimen composite panel assembly drawing

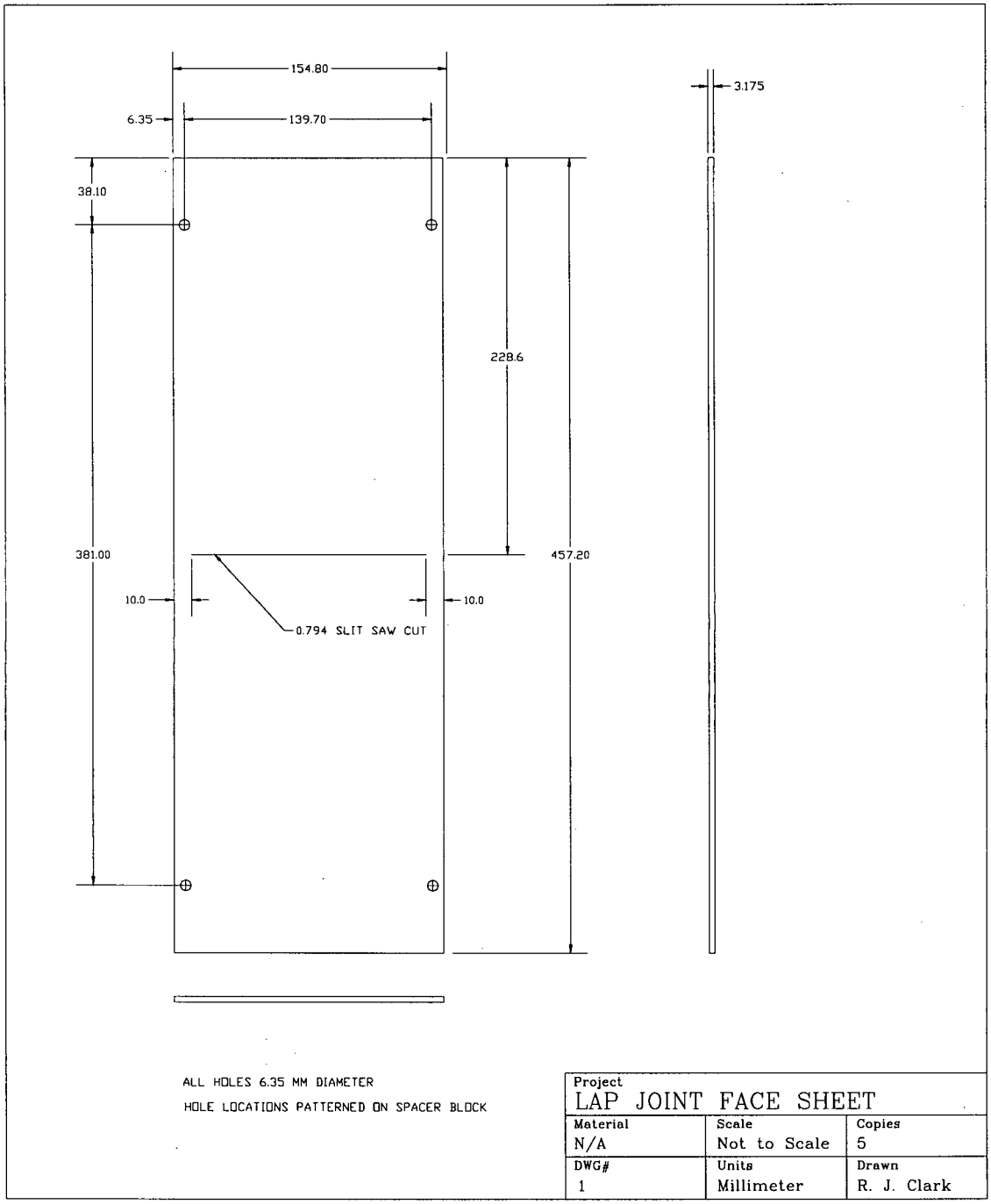

Figure A-9: LJ specimen face sheet drawing

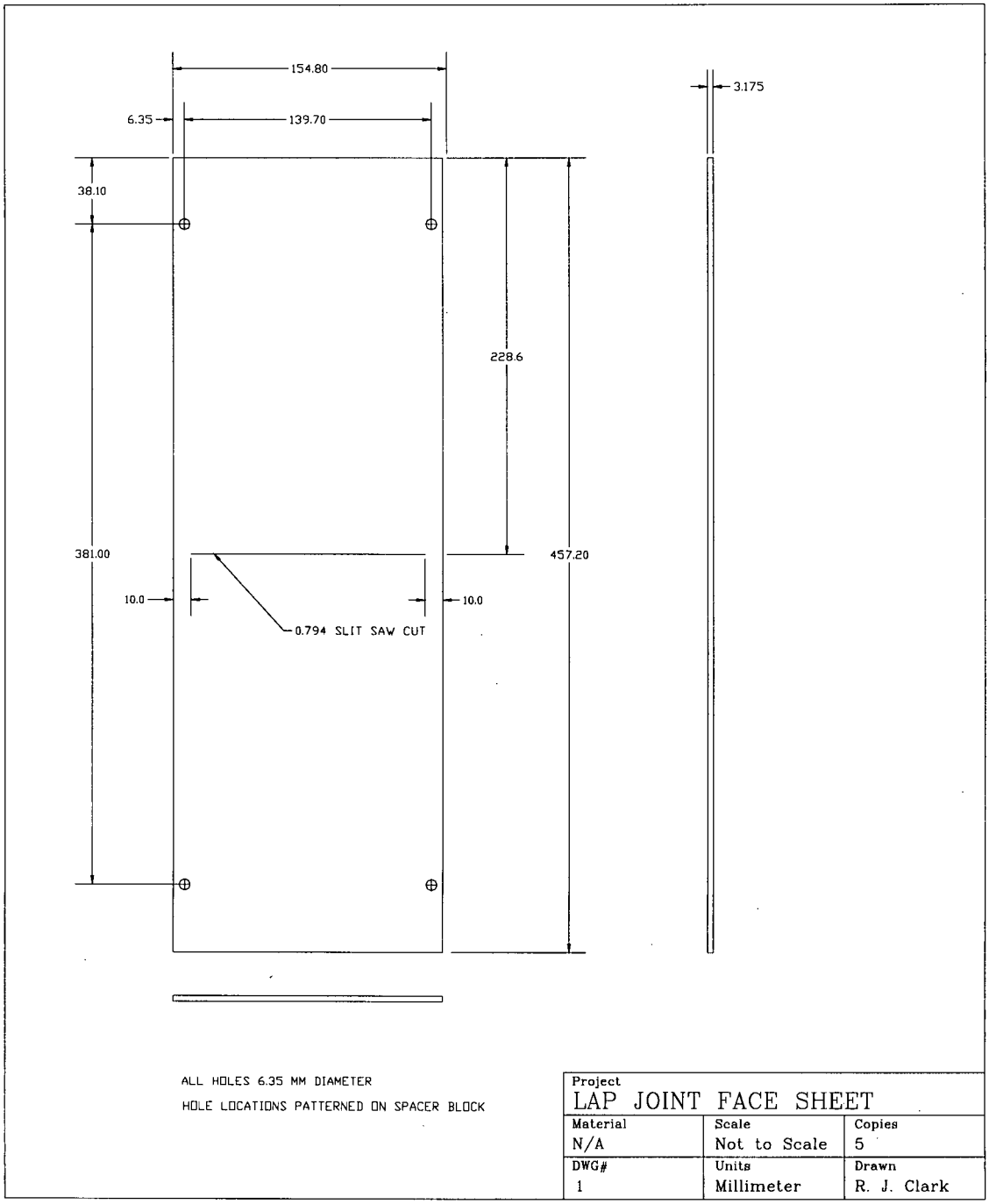

Figure A-10: DLJ and HS-DLJ specimen face sheet drawing

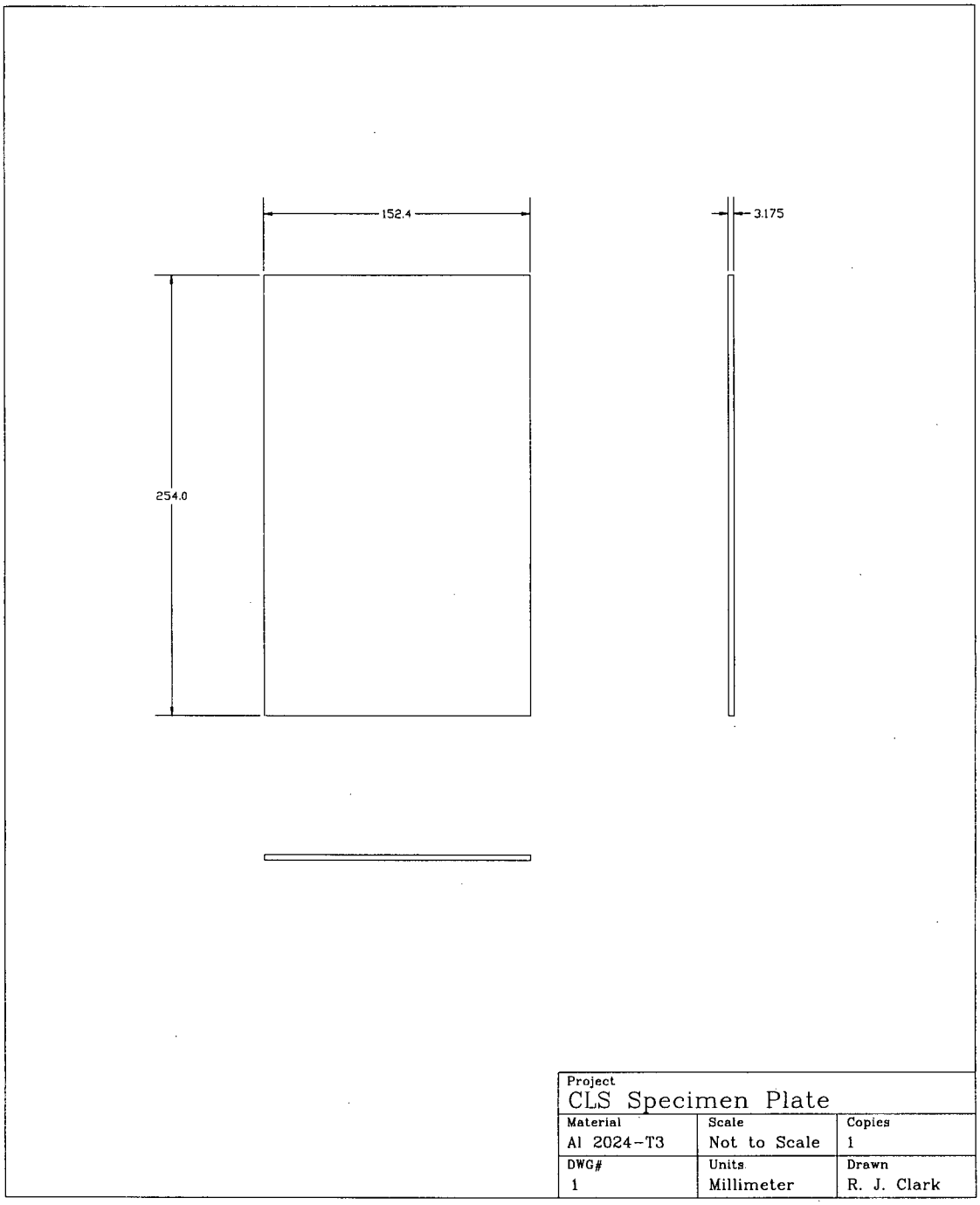

Figure A-11: CLS specimen face sheet drawing

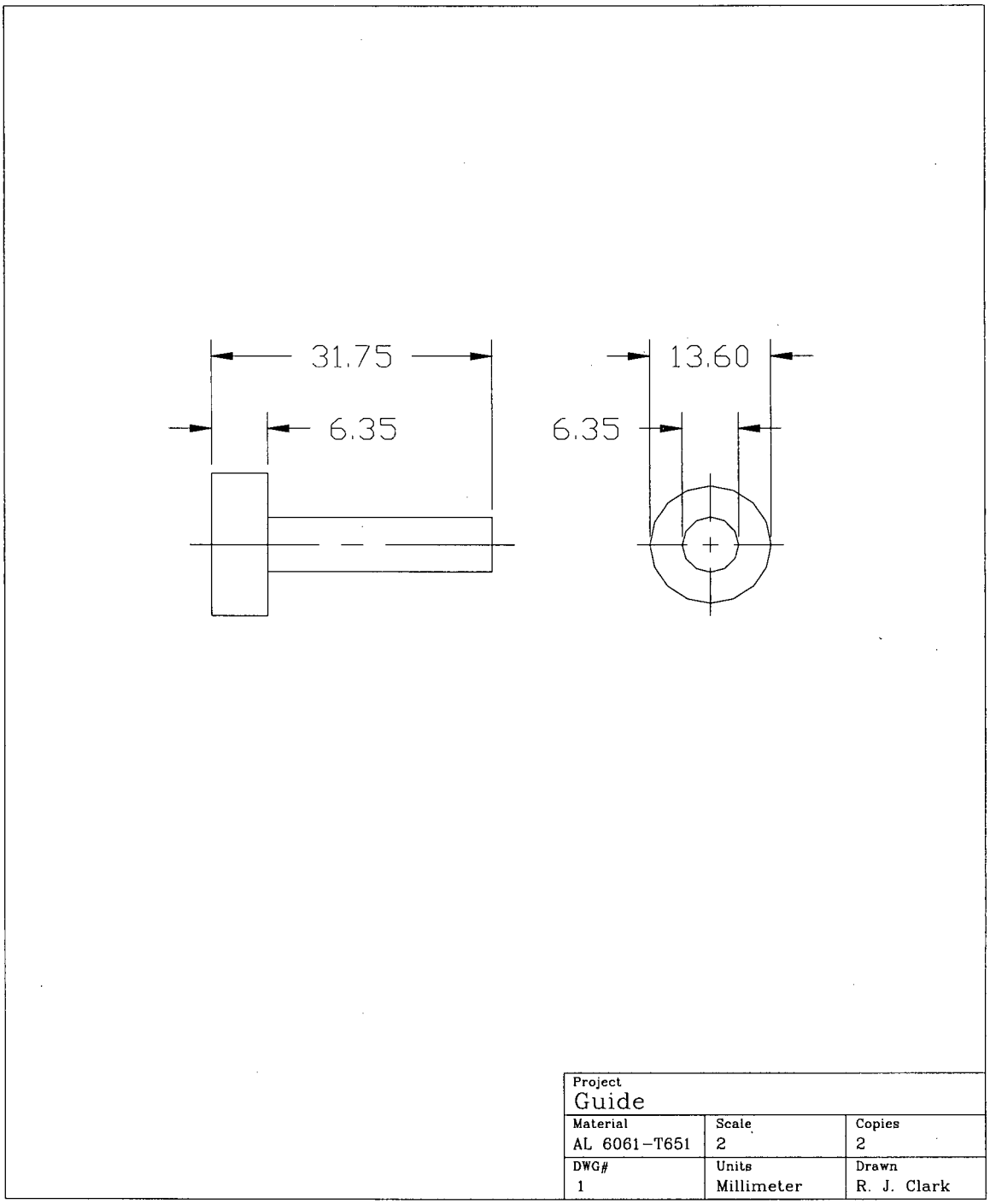

Figure A-12: Guide plug drawing

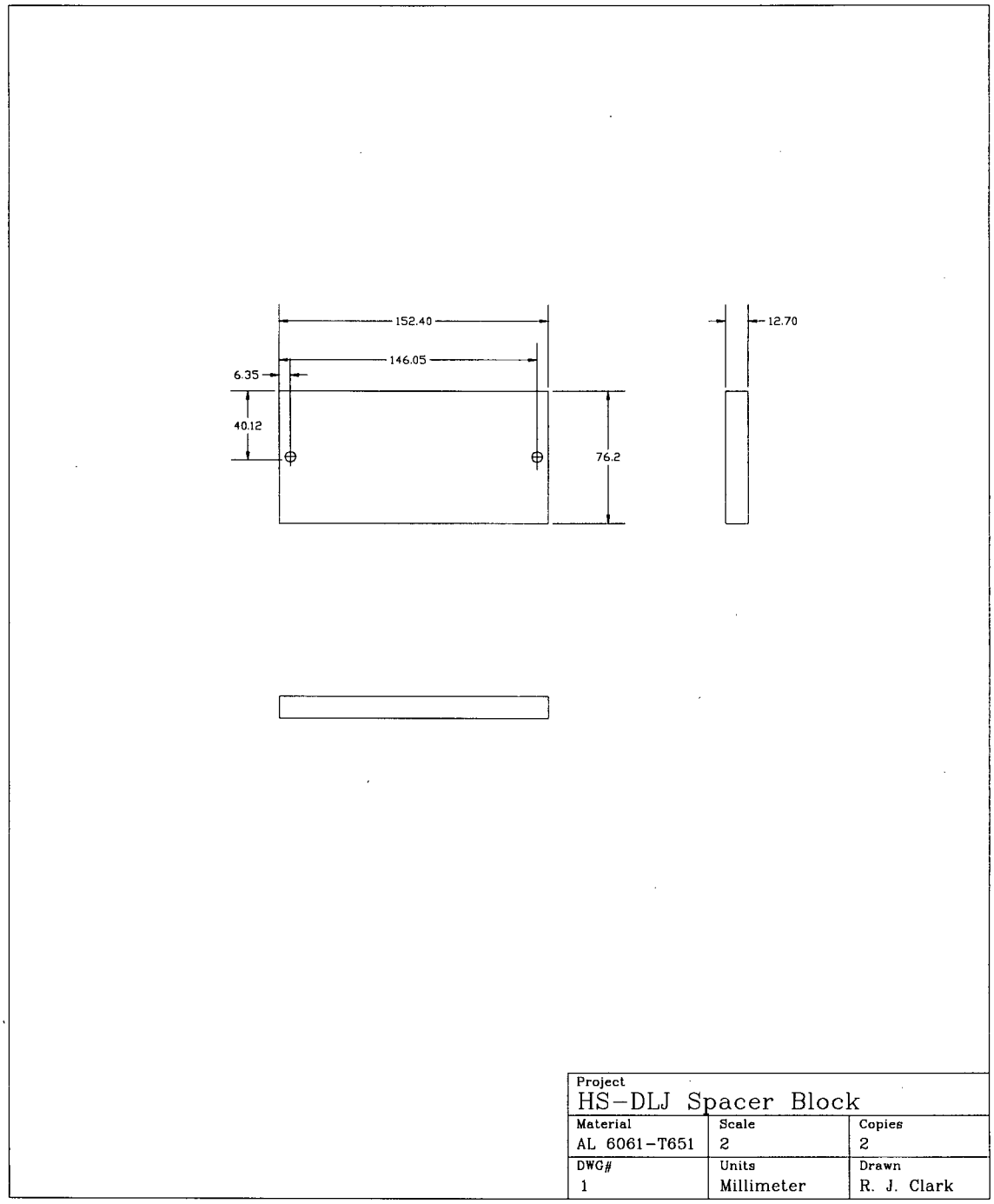

Figure A-13: HS-DLJ spacer block drawing

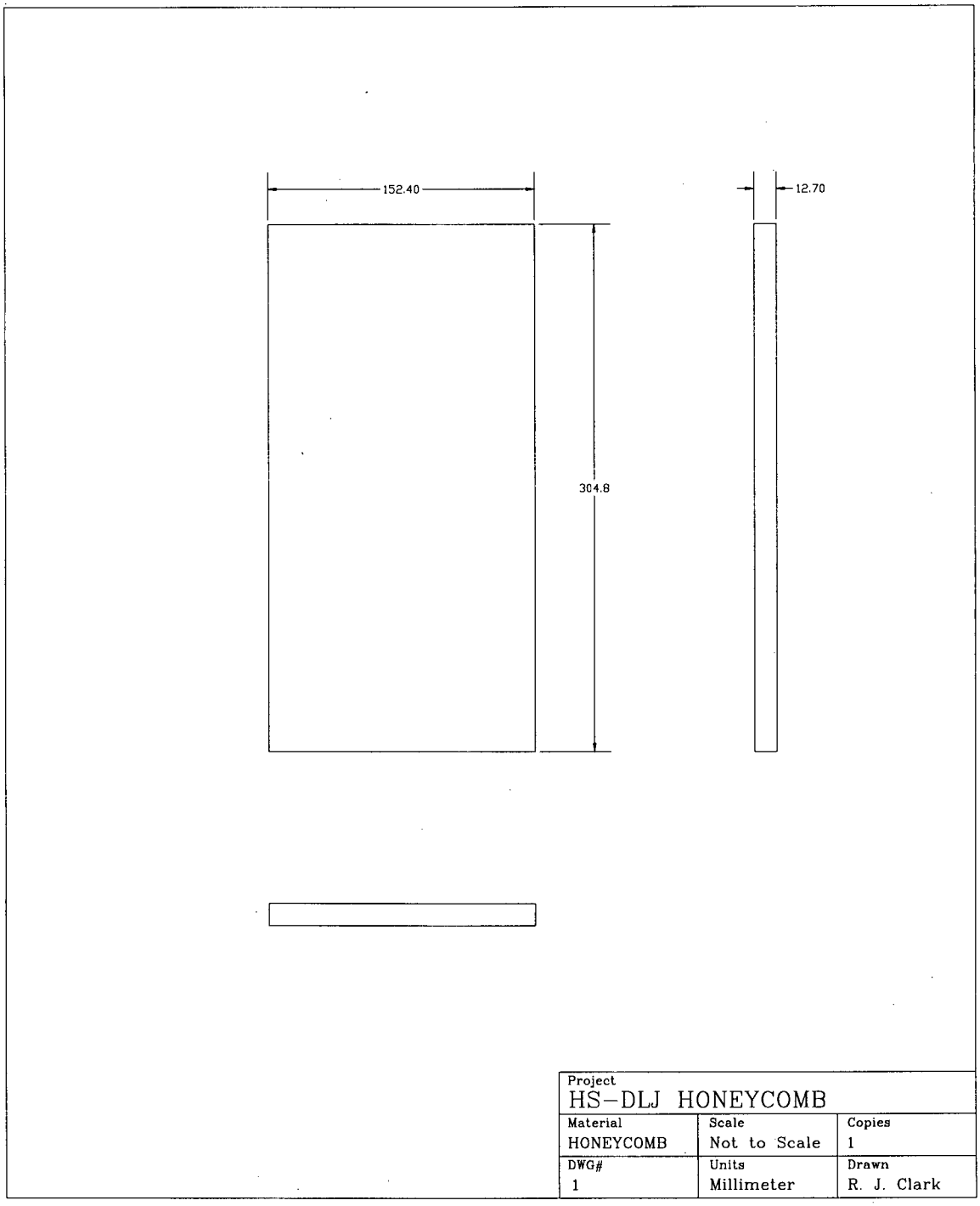

Figure A-14: HS-DLJ honeycomb drawing

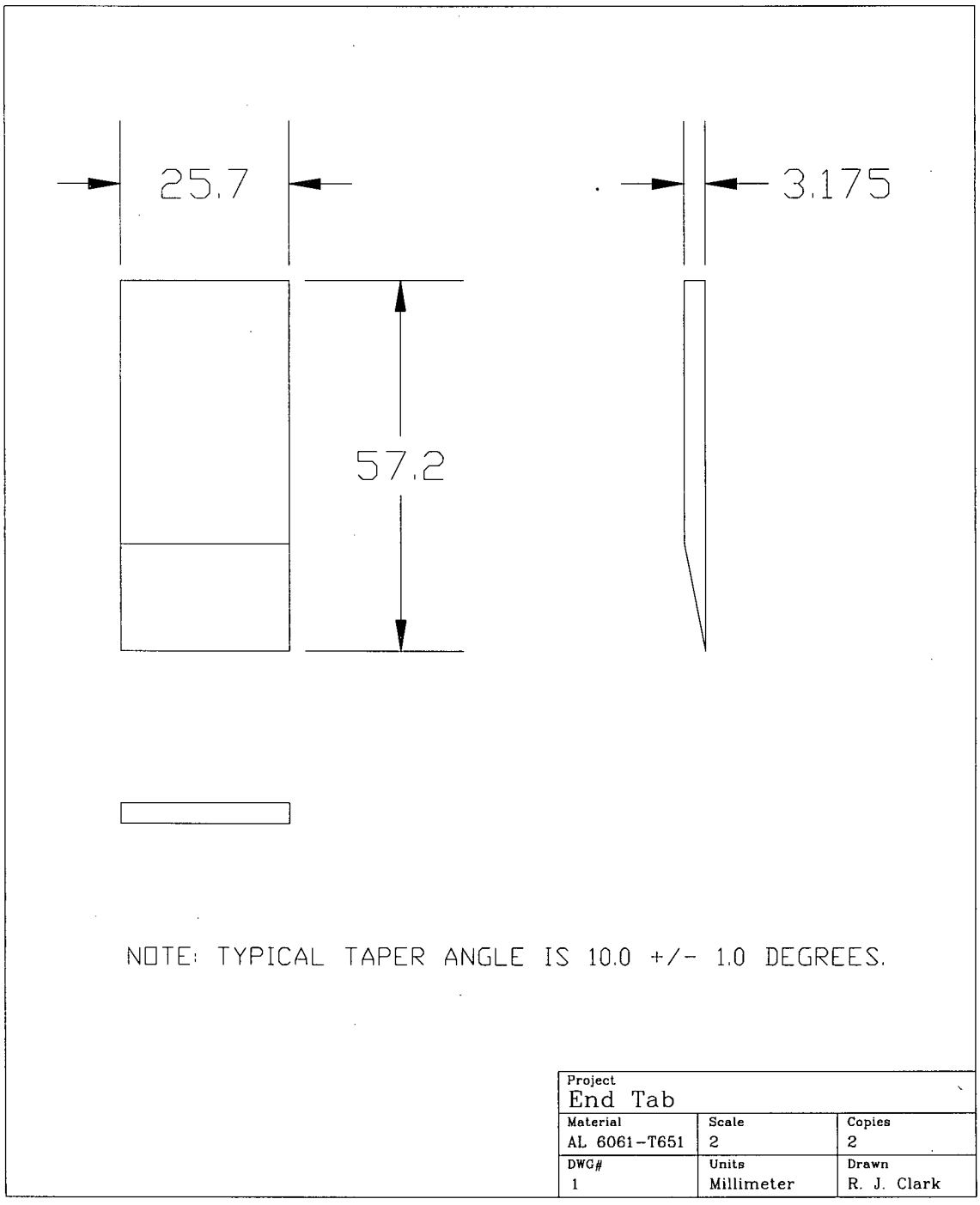

Figure A-15: End tab drawing

A.3 Panel construction

This section describes the construction for the panels shown in figures A-5 through A-8, which was carried out at the Canadian National Research Council Institute for Aerospace Research.

A.3.1 Composite manufacture

Before the panels could be built, the composite patches and the CLS panel had to be made from the boron/epoxy prepreg. Figure A-16 shows the workspace for lay-up of the patches. The prepreg was cut to the proper lengths and laid-up in a reversed stacking sequence, starting with the shortest piece and ending with the longest. The patch was co-cured with one layer of FM73M adhesive film to improve the strength of the composite matrix and provide a compatible bond line.

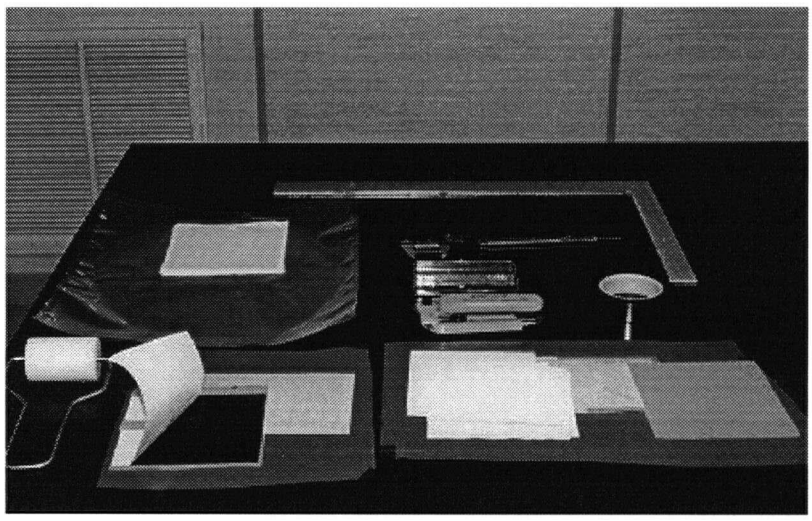

Figure A-16: Workspace for patch lay-up

The patch was covered on both sides with peel ply, to allow bleeding of any excessive resin or adhesive, and to provide a clean surface for bonding. Figure A-17 shows the peel ply being applied. Note the solder tabs for the embedded strain gauge.

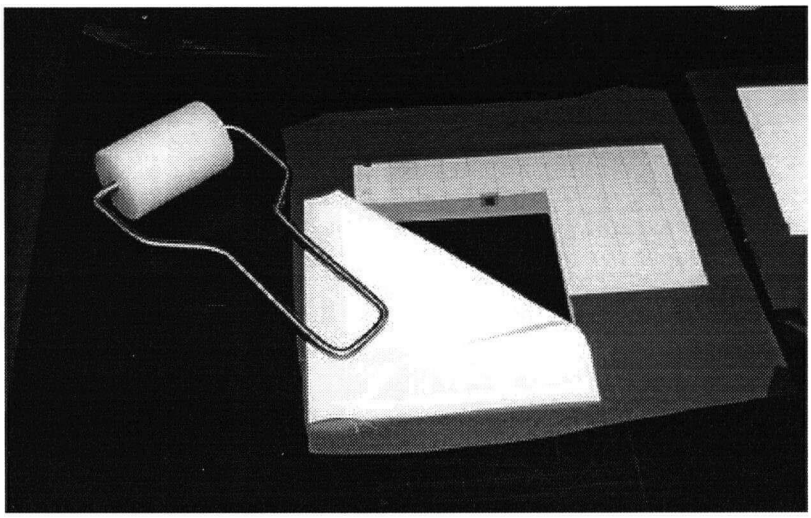

Figure A-17: Application of peel ply

The composite panel for the CLS specimen was formed in the same manner. The prepreg was cut to the proper lengths, laid up one sheet at a time, and rolled to remove any trapped air. A sheet of FM73M adhesive was rolled onto to bottom of the panel and peel ply was applied to both sides. Figure A-18 shows the workspace and lay-up of these panels, with the placement of an embedded strain gauge shown in figure A-19.

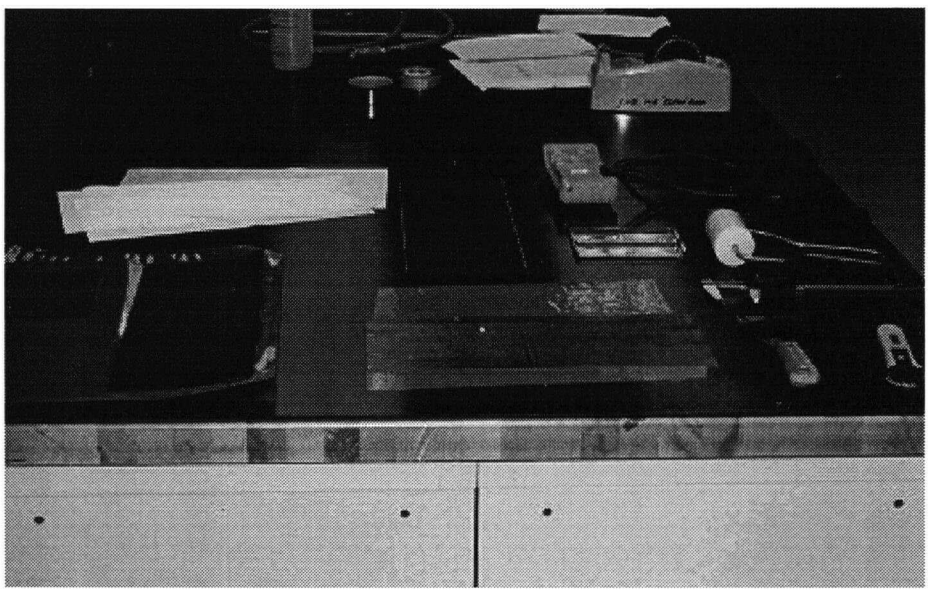

Figure A-18: Workspace for CLS panel lay-up

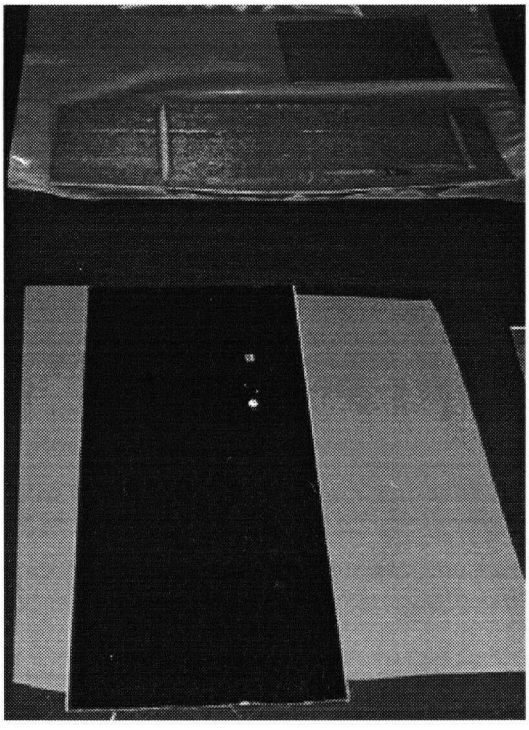

Figure A-19: Strain gauge placement (finished panel in background)

Five patches were cured in one batch, with the adhesive face down on the tooling plate to provide a flat finish. The CLS panels were cured in a separate batch. The layout of the patches is shown in figure A-20, and the vacuum bagging and debulking shown in figure A-21.

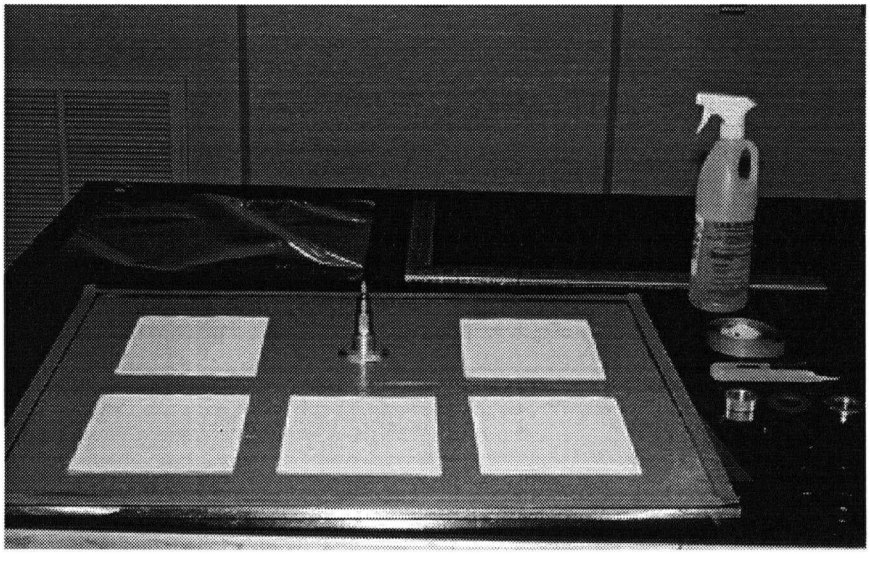

Figure A-20: Layout on the tool plate

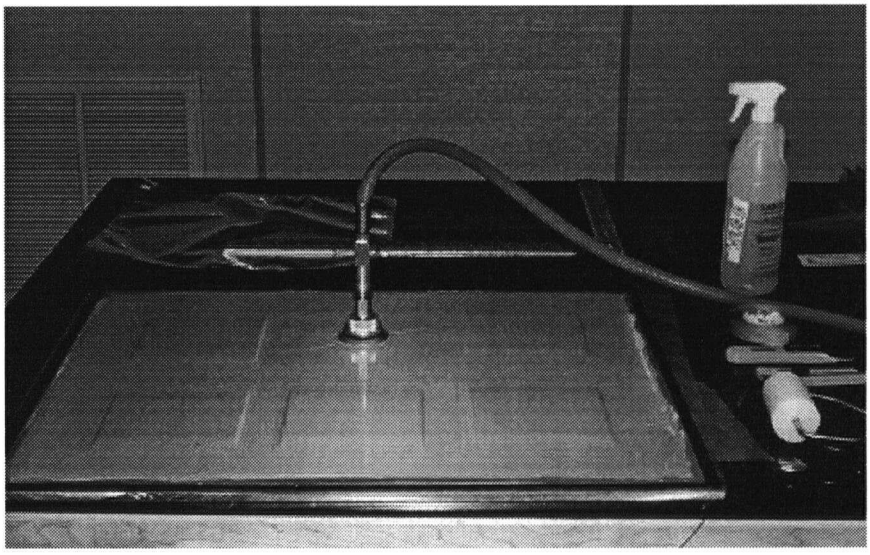

Figure A-21: Vacuum bagging and debulking

The composite parts were cured at 121 C for 1 hour. After curing, the final step was grit blasting to remove excess adhesive and to clean any possible contamination from peel ply release agents, and ensuring a clean and compatible bond-line.

A.3.2 Aluminum surface preparation

This section details the aluminum surface preparation procedure, a process that determines the durability of the adhesive bond. A reactive epoxy silane process was chosen, matching the method previously used for construction of seven AMRL specimens. There are seven steps: clad removal, degrease, grit blast, silane application, priming, drying/curing, and wedge test.

The first step, cladding removal, was carried out at UBC. An aluminum sanding block and wet 220 grit sand paper were used to remove the 0.079 mm pure aluminum coating on the surface of the 2024-T3 aluminum panels. A second round of grinding with 320 grit paper smoothed the surface in preparation for grit blasting. The sheets were than thoroughly cleaned with running water and clean white paper towels, wiping in one direction only, until little trace of contamination was evident. The parts were then dried and wrapped in Kraft paper for shipment to Ottawa.

Degreasing involved a thorough wiping, in one direction only, with clean 'KimTuff wipers' and Methyl Ethyl Ketone (MEK). This procedure was carried out until no trace of contamination was detectable on the wipers. The parts were then wrapped in Kraft paper to protect them from contamination. From this point on, it was attempted not to touch the bonding surfaces. The next step, grit blasting, was carried out immediately prior to application of the silane and primer. The grit blaster was cleaned and filled with new 220 grit aluminum oxide. All of the remaining steps were carried out during the same day.

Nitrogen, at a pressure of 80 psi, was used for the grit blasting. Figure A-22 shows the grit blaster. Blasting was carried out using longitudinal and perpendicular passes until a uniform 'frosted' appearance was evident. Care was taken to grit blast the edges of the plates to ensure good bonding of excess adhesive about the edges of the joint. The face sheets were then cleaned by nitgrogen blasting and again wrapped in Kraft paper.

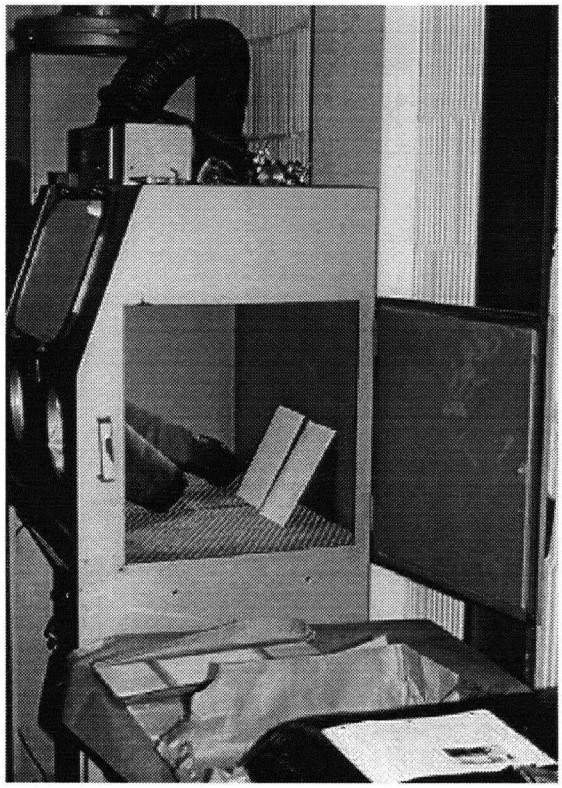

Figure A-22: Grit blasting

A 1% silane solution was mixed before starting the grit blasting process. Graduated cylinders were used to measure 372 ml of distilled de-ionized water and 3.75 ml of silane to form the solution. An agitator mixed the solution during the 3 hours required for the grit blasting. All containers were rinsed with distilled de-ionized water prior to use. The aluminum parts were placed at a steep angle on a honeycomb block, allowing the silane to run down into a collecting bowl. Silane was applied by a spray dispenser and was wiped down the part with a clean brush. This drives contaminants into the collection bowl. The parts were treated consecutively, maintaining a wetted and water-break free surface for 15 minutes. The parts were treated in groups of four, and were placed on clean Kraft paper once treated.

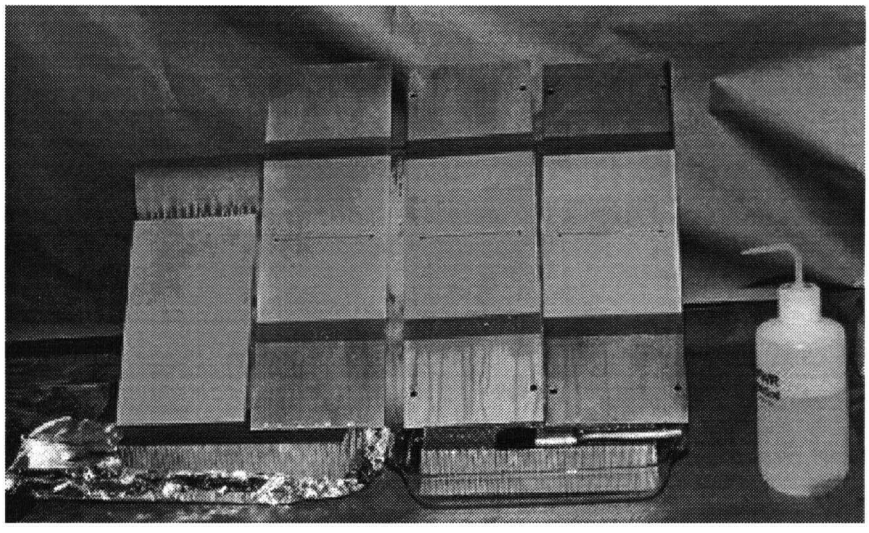

Figure A-23: Silane application

Once all of the parts were treated with silane, and had air-dried until no wetness was visible, they were placed in a temperature-controlled oven at 80 C for 30 minutes. After allowing 30 minutes to cool, the BR127 corrosion-inhibiting primer was applied in very light strokes transverse to the rolling direction of the plates. The primer had been warmed to room temperature before application, and it was ensured that sufficient MEK was available to clean the spray gun due to the very fast drying time of the primer. The primer was applied in a very thin coating, thinner than recommended by the manufacturer. This thin treatment has been shown by the NRC-IAR to result in the most durable joints. Excess primer has been shown to decrease durability. After application of the primer, the primer was allowed to air-dry for 30 minutes, and then was cured at 121 C for 60 minutes. The parts were then wrapped in Kraft paper and stored until needed for construction of the bonded joint specimens.

A.3.3 Laminated panel construction

This section illustrates the method used to construct the HS-DLJ laminated panel. The other panels were constructed in an analogous manner. Figure A-24 shows the workspace prior with the components required for the assembly of the panel. The components are placed approximately in the sequence of construction. The first step is to roll the adhesive onto the surface-treated back of the aluminum face sheets, as shown in figure A-25, following with, the guide plugs were inserted and the honeycomb and spacers were pressed onto the adhesive, as shown in figure A-26. Figures A-27 through A-29 show the application of the adhesive and then the patch to the aluminum plate. The adhesive edges were sealed with tape to prevent excessive run-out and to provide a smooth shape to the adhesive fillet. Figures A-30 through A-32 show the vacuum bagging of the laminated panels and the cured panels after removal from the autoclave.

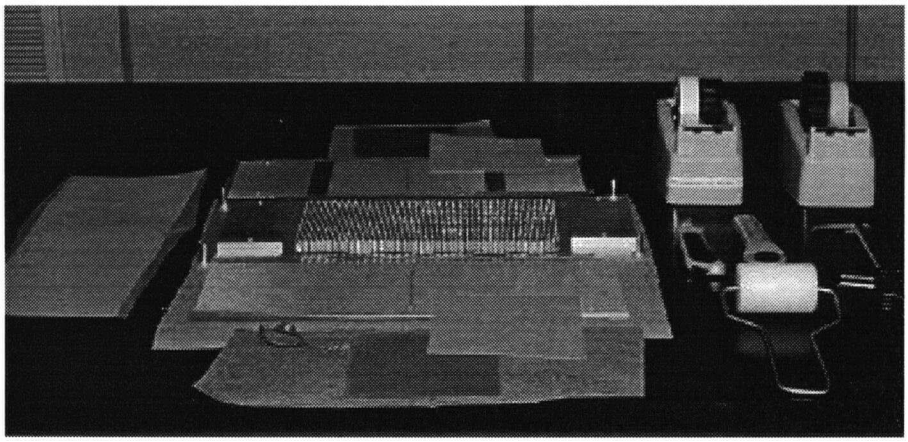

Figure A-24: Workspace for construction of the HS-DLJ panel

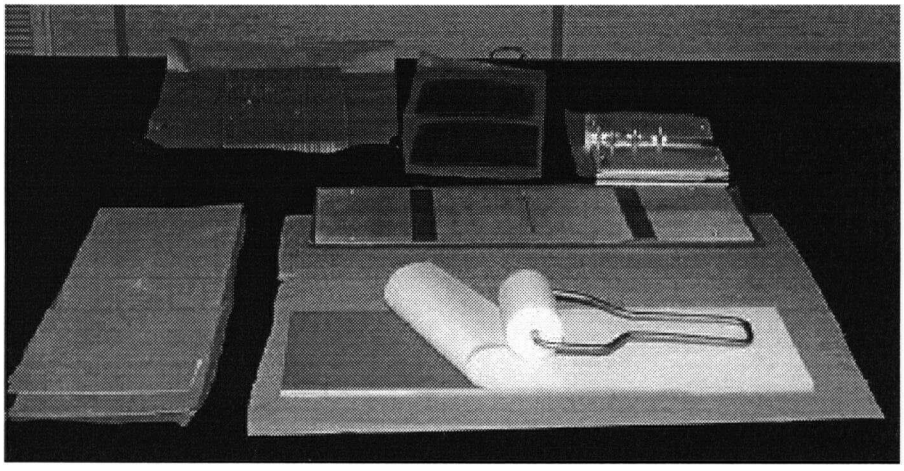

Figure A-25: Rolling the adhesive on to the back of the face plate

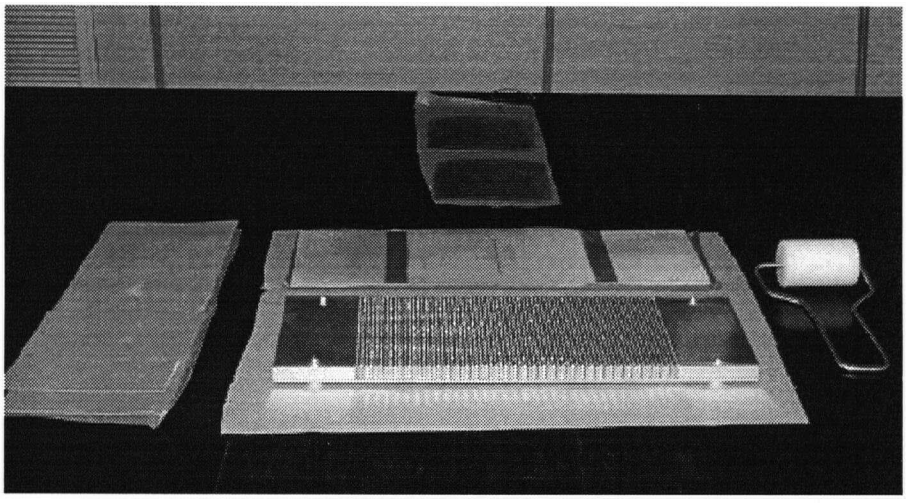

Figure A-26: Positioning the spacer blocks and honeycomb

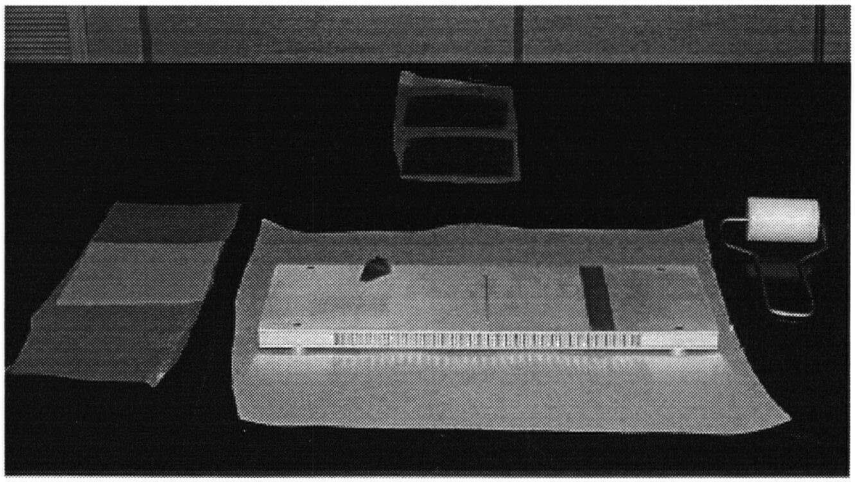

Figure A-27: Ready to apply the composite patches

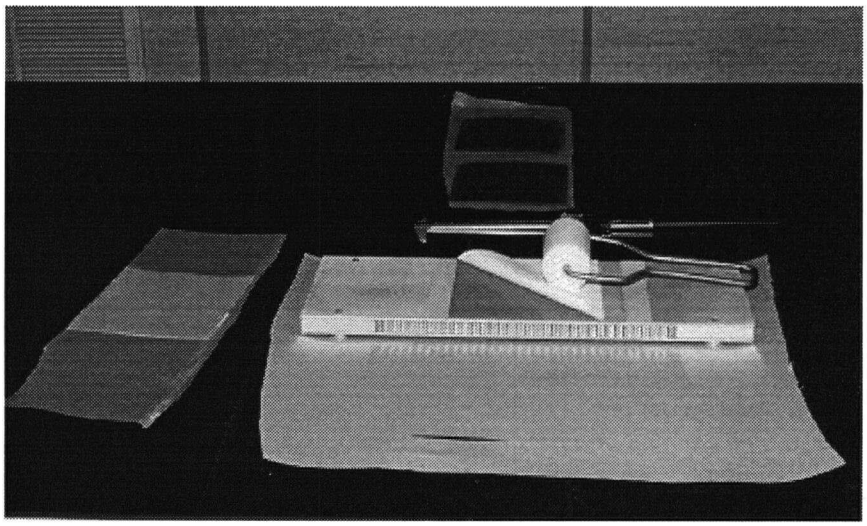

Figure A-28: Applying the adhesive

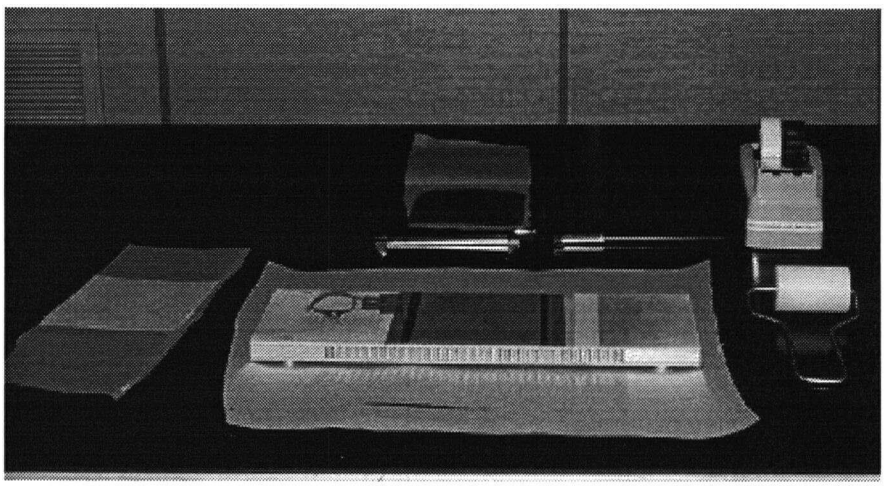

Figure A-29: Applying an instrumented patch

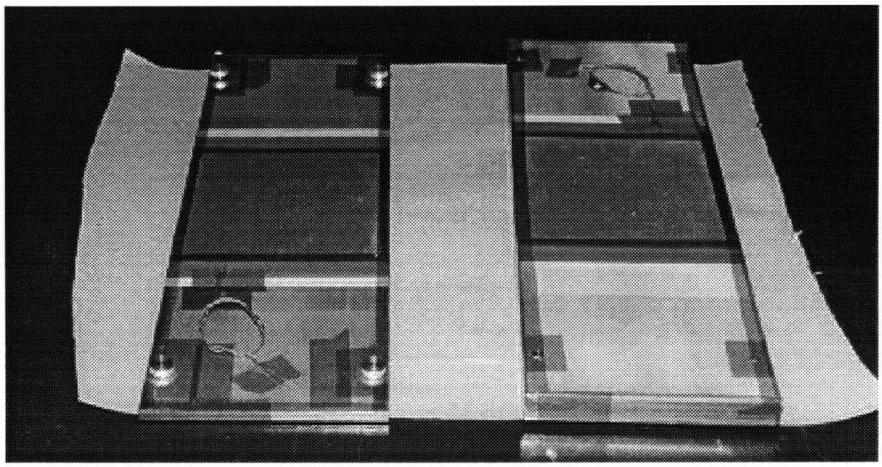

Figure A-30: Double lap joint specimens, ready for vacuum bagging

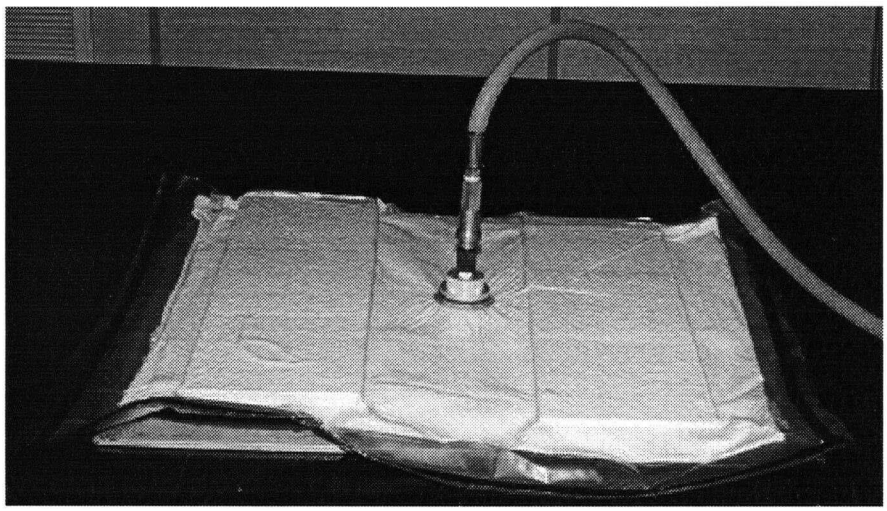

Figure A-30: Vacuum bagging and debulking of double lap joint specimens

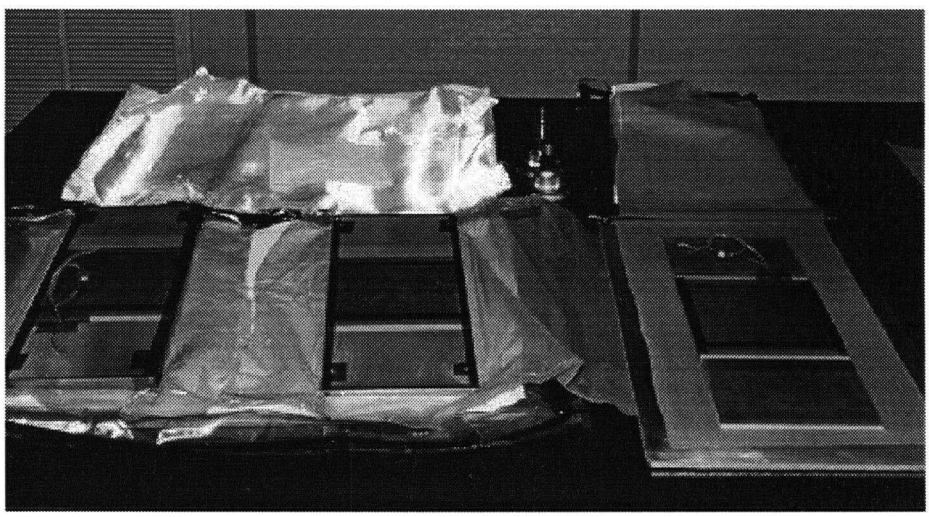

Figure A-32: The cured specimens

Step	Procedure	Materials
Clad removal	Sand with wet 220 grit paper. Wipe in one direction. Sand with 320 grit paper. Wipe in one direction.	220 grit sand paper Kimtuff Wipers 320 grit sand paper flat aluminum sanding block
Clean	Water-clean with tap water. Break-free surface. Air dry overnight. MEK wipe.	Kimtuff Wipers MEK
Package	Package in Kraft paper	Gloves Kraft Paper & Masking tape
Grit blasting	Clean the grit-blasting unit. Use new aluminum oxide. 690 kPa pressure. Alternate horizontal and vertical passes. Stop when even surface texture	Grit blaster Aluminum oxide 220 grit, 75 micron diameter Nitrogen gas
Silane treatment	Warm silane to room temperature ~1 hr. Mix silane and water. Agitate ~1 hr. Stand specimens on the honeycomb blocks. Apply silane, 10 minutes per side. Heat @ 80 °C for 30 minutes	2.5 ml Silane / sheet 250 ml de-ionised distilled water / sheet polyethylene container w/ dispenser graduated cylinder pipette mixing agitator, sealed magnet honeycomb blocks shallow silane collection bowls fine-haired 1 inch wide paint brush gloves temperature-controlled oven
Primer	Warm primer to room temperature. Mix primer. Support specimens on aluminum bars. Agitate while applying. One pass is adequate. Heat @ 120 °C for 1 hr.	BR127 Primer Nitrogen gas (@ 345 kPa pressure) Rags Spray gun Aluminum bars to support the specimens Temperature-controlled oven Kraft paper & masking tape Gloves

Table A-5: Aluminum surface preparation

Step	Procedure	Materials
Surface Preparation	Aluminum sheets will act as travellers during surface treatment	
Curing	Roll adhesive onto aluminum plates. Use Teflon foil for 0.75" starter notch. Seal edges with tape. Cure @ 80 Degrees C for 8 hours. Cut into 5 1" strips.	Release film Teflon roller Teflon foil High temperature tape Autoclave Band saw Milling machine
Testing	Insert wedges. Measure crack length Wait 1 hr. Measure again. Expose @ 65 °C, 96% humidity, 1 hr. Measure again. Expose @ 65 °C, 96% humidity, 8 hr. Measure again. Split specimens to check for cohesive failure.	Microscope Temperature/humidity chamber Steel wedges

Table A-6: Wedge test procedure

Step	Procedure	Materials
Cut prepreg	Thaw prepreg and adhesive for 1 hour Unroll prepreg with backing down Place perforated release film on top Clamp aluminum template onto prepreg Cut prepreg Place in polyethylene bag Repeat for adhesive	Perforated release film Aluminum templates C-Clamps Roller cutter Polyethylene storage bags Gloves
Lay-up	Place release film over template Remove release film from prepreg Sequentially roll plies onto template Roll on a layer of peel ply Flip over Apply adhesive Apply another layer of peel ply Place in polyethylene bag	Perforated release film Template Teflon roller Knife Peel ply Gloves
Cure	Put non-perforated release film on plate Place specimen on plate, adhesive down Place 1 layer of perforated release film Place 3 layers of bleeder cloth Place 2 layers of breather cloth Vacuum bag the specimen Autoclave @ 50 psi, 121.1 °C, 1 hr 2.78 °C/min, 35 minute transient Grind/cut specimens to the proper size.	Aluminum plates (0.25 in thick) Non-perforated release film Perforated release film Fiberglass bleeder cloth Breather cloth Vacuum bag /Vacuum fitting Sealant tape Autoclave Grinder Diamond-coated blade / table saw
NDE	Ultrasonic C-scan	ARIUS, 15 MHz focussed transducer

Table A-7: Composite parts fabrication

Step	Procedure	Materials
Prepare Honeycomb	MEK rinse the honeycomb Heat @ 50 °C for 30 minutes Wrap in Kraft paper	MEK Oven Kraft paper
Prepare the aluminum	Roll adhesive onto face-sheets Use the heat gun if necessary	Teflon roller Heat gun High-temperature tape
Assemble	Press a shim onto a face sheet Roll honeycomb onto face sheet Press second shim onto face sheet Press on second face sheet	Teflon roller
'Pin' Specimen	Place bolts into guide holes Thread on the nuts, finger tight Bolts will act as locator/ support	Bolt and nuts
Place 'Patch'	Roll adhesive onto specimen Place patch High temperature tape seals the adhesive Roll over and repeat	High temperature tape
Cure	Put release film on table Put 2 layers of breather cloth on table Place specimen on cloth Loosen nuts Wrap in breather cloth / release film Allow room for the vacuum fitting Vacuum bag the specimen Autoclave @ 50 psi, 121 °C, 1 hr 2.78 °C/min, 35 minute transient	Perforated release film Bleeder cloth Breather cloth Vacuum bag Vacuum fitting Sealant tape Autoclave
Cut Specimens	Remove panel from vacuum bag. Sand edges to remove excess adhesive. Cut specimens to appropriate size. Discard edges	220 grit sand paper Diamond saw

Table A-8: HS-DLJ specimen assembly

Step	Procedure	Materials
Prepare the aluminum	Roll the adhesive onto the al sheet Use the heat gun if necessary	Teflon roller Heat gun High-temperature tape
Assemble	Press aluminum onto the b/ep panel	
Cure	Wrap in release film and breather cloth Wrap again in breather cloth Allow room for the vacuum fitting Vacuum bag the specimen Autoclave @ 50 psi, 121 °C, 1 hr 2.78 °C/min, 35 minute transient	Perforated release film Bleeder cloth Breather cloth Vacuum bag Vacuum fitting Sealant tape Autoclave
Make tabs	Prepare the tabs	E-glass prepreg Non-perforated release film Perforated release film Breather cloth Bleeder cloth Vacuum bag and fitting
Shape tabs	Cut tabs to shape	Grinder 220 grit Sand paper Diamond-coated blade / table saw
Glue to specimen	Adhere tabs to specimens	Non-perforated release film Scrim cloth Hysol EA 9396 QT adhesive Mixing container
Cut specimens	Remove panel from vacuum bag Sand edges to remove extra adhesive Cut specimens to appropriate size	220 grit sand paper Diamond saw

Table A-9: CLS specimen assembly

Appendix B: Instrumented repair specimen

This appendix provides a description of the AMRL specimen and the locations of the strain gauges on the instrumented AMRL specimen.

B.1 AMRL specimen geometry

Figure B-1 shows the geometry of the AMRL specimen.

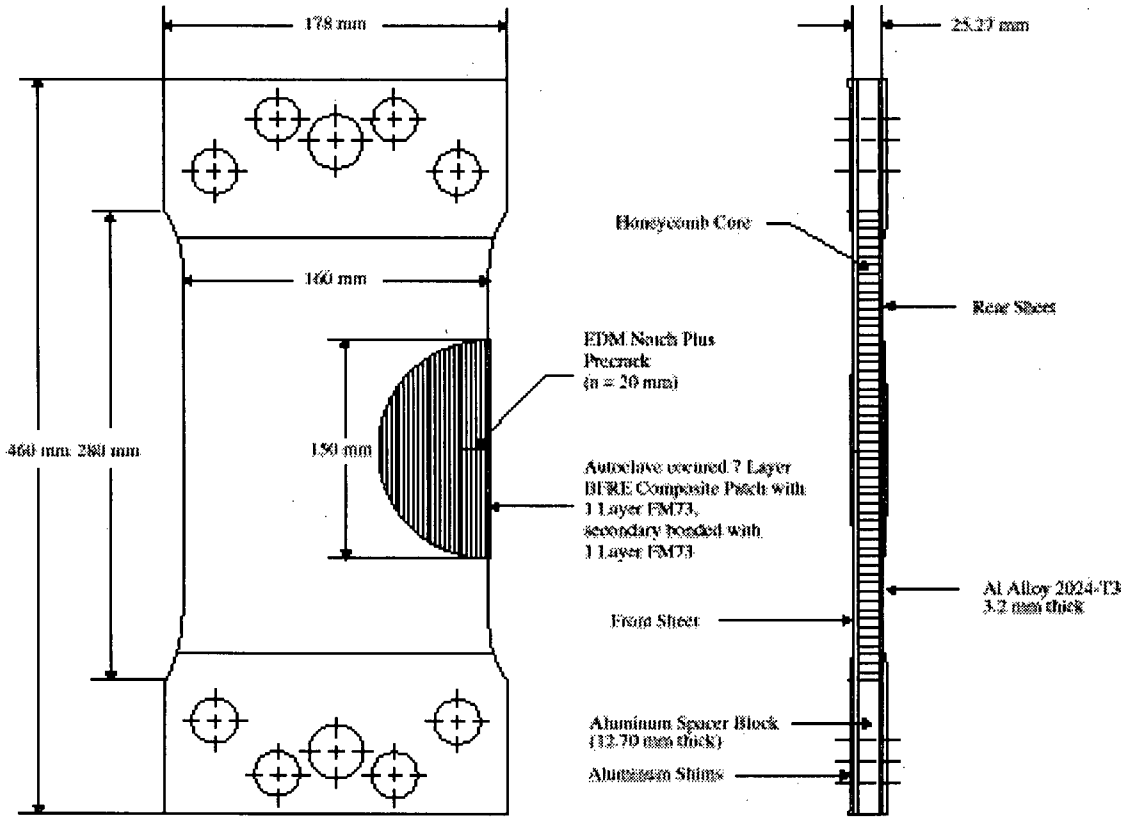

Figure B-1: AMRL specimen dimensions

B.2 Instrumented specimen

Figures B-2 through B-4, below, show the locations of the strain gauges on the instrumented specimen. The gauges in location A, in the crack plane, measure the longitudinal strains in the patch. Over the crack, these strain measurements will directly verify the boundary element model. On the aluminum adjacent to the patch, the gauges at location B allow an estimate of the stresses in the crack plane at the edge of the patch. This stress distribution is critical to an assessment of the residual strength of a repair with a large crack. It is applied within the analysis as a crack-opening pressure. Ideally, these

stresses would closely match those determined by the inclusion model employed by Rose in the two-step analysis process for a repair. At location C, a strip gauge allows the assessment of the validity of the classical theory of bonded joints in the analysis of a repair. As the disbond grows under this gauge, a history of the stresses in the patch will be generated. The gauges are placed far enough from the edge of the patch to be relatively unaffected by the free edge. The strain gauge at location D allows an assessment of the appropriateness of the use of unidirectional springs to model the patch, and will assist in the evaluation of edge effects. Unidirectional springs bridging the crack are the basis of both the boundary element and interpolation models. It is unlikely that this load transfer is significant, due to the extreme anisotropy and low shear modulus of the boron-epoxy patch, but strain data would be useful in the event that models are required to account for shear load transfer within the patch. The free edge will cause adhesive stresses due to the mismatch in Poisson's ratios between the aluminum and boron-epoxy adherends. The strain gauge strips at location E allow an estimate of the stress concentration in the critical area at the tips of the patch. The strain gauges at location F allow an estimate of in-plane bending and its effect on the stress distribution in the crack plane. Finally, the strain gauges at location G allow an assessment of the uniformity of loading of the AMRL specimen. It will allow an assessment of the amount of in-plane bending in the specimen, and on how evenly stresses are distributed across the specimen by the loading grips.

Table B-1 shows the strain gauge specifications. They have been matched to the thermal expansion coefficient of 2024 aluminum.

Locations	Type	Manufacturer	Catalogue Number
A, B, D	10 gauge strip, transverse grid, 2.03 mm spacing	Micro-Measurements	EA-13-031ME-120
C	10 gauge strip, parallel grid, 2.03 mm spacing	Micro-Measurements	EA-13-031MF-120
E	10 gauge strip, parallel grid, 2.03 mm spacing	Micro-Measurements	EA-13-031MF-120
F, G	General purpose	Micro-Measurements	EA-13-062AK-120

Table B-1: Strain gauge types

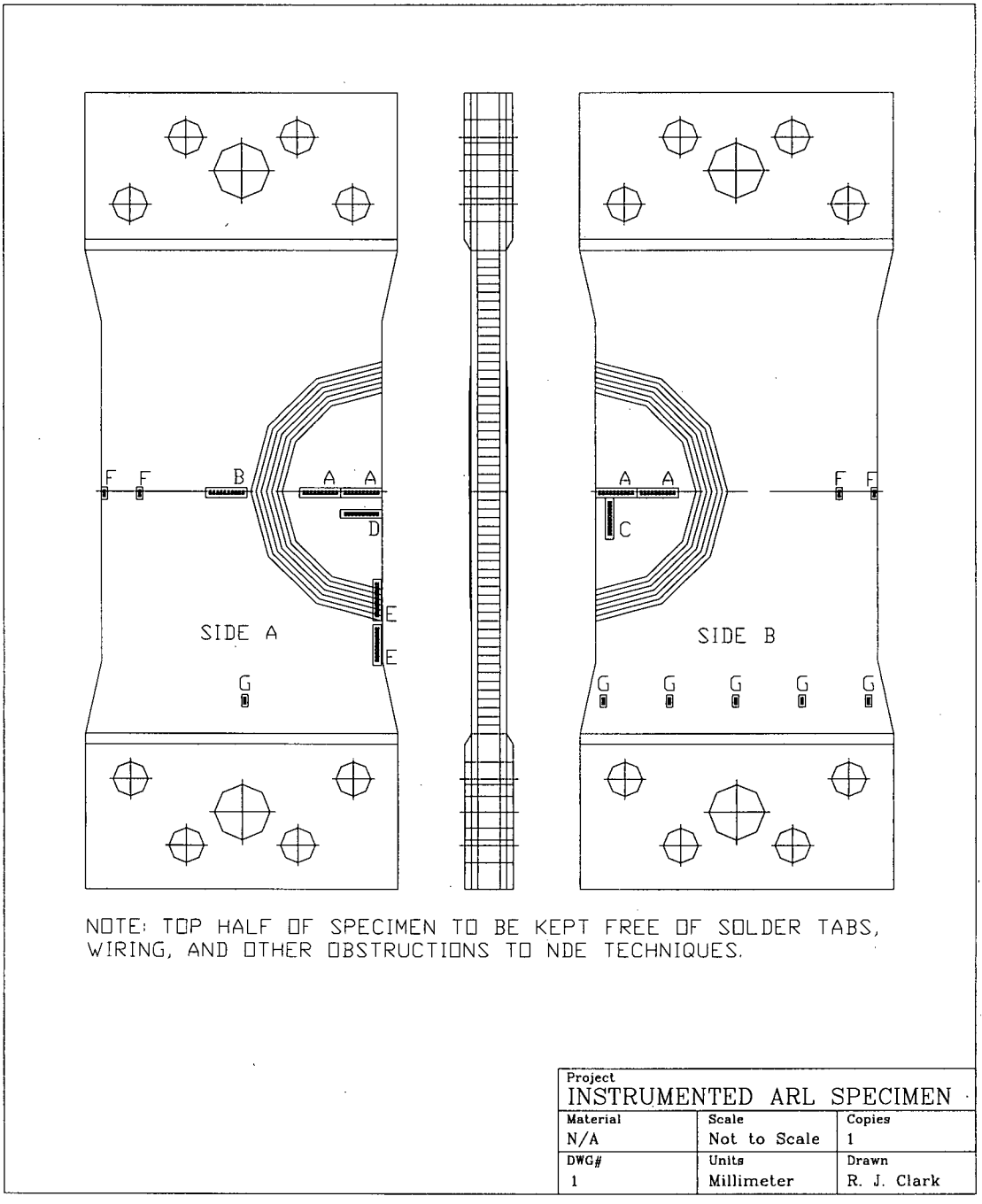

Figure B-2: Instrumented AMRL specimen drawing

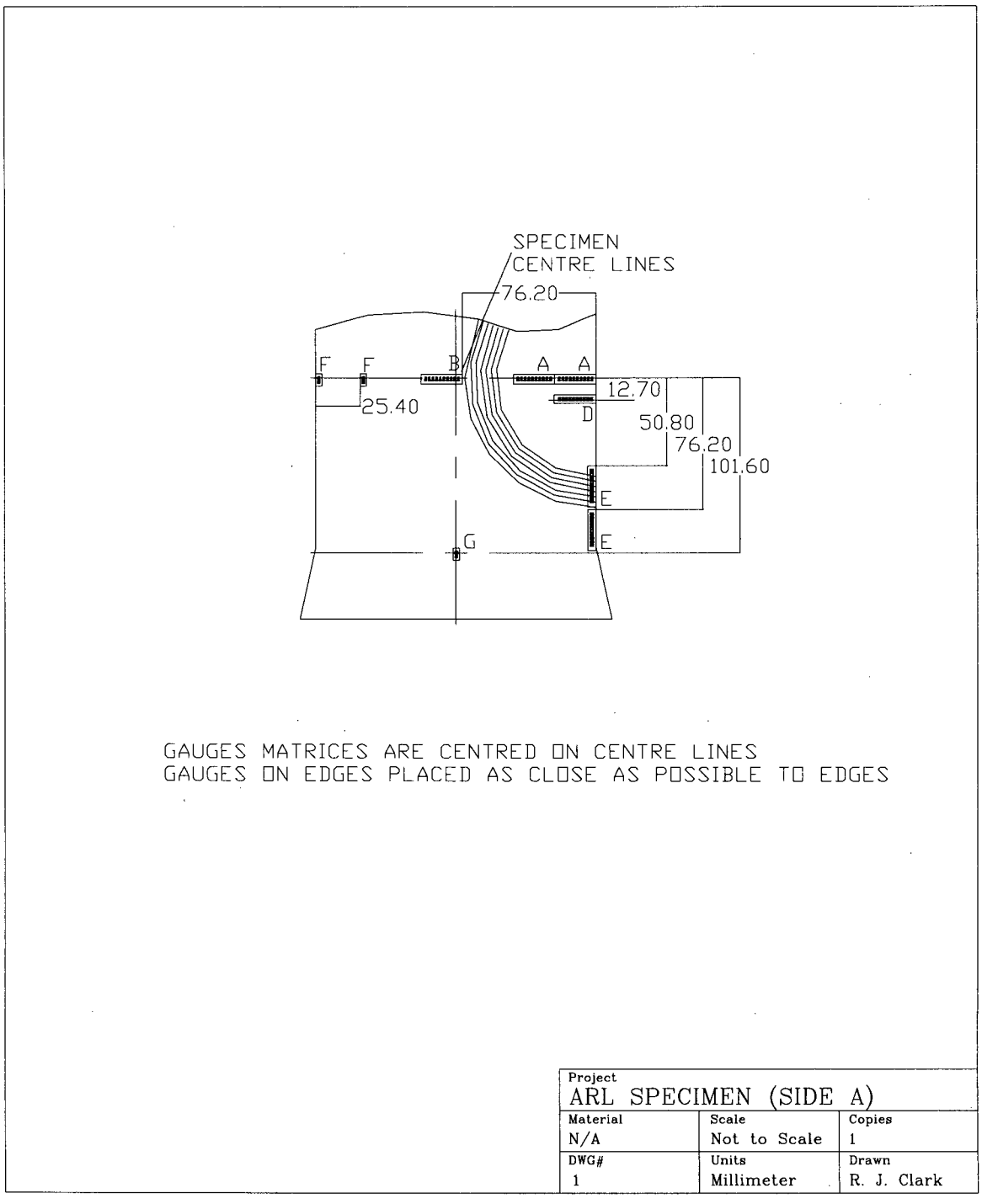

Figure B-3: Instrumented ARL specimen drawing, side A

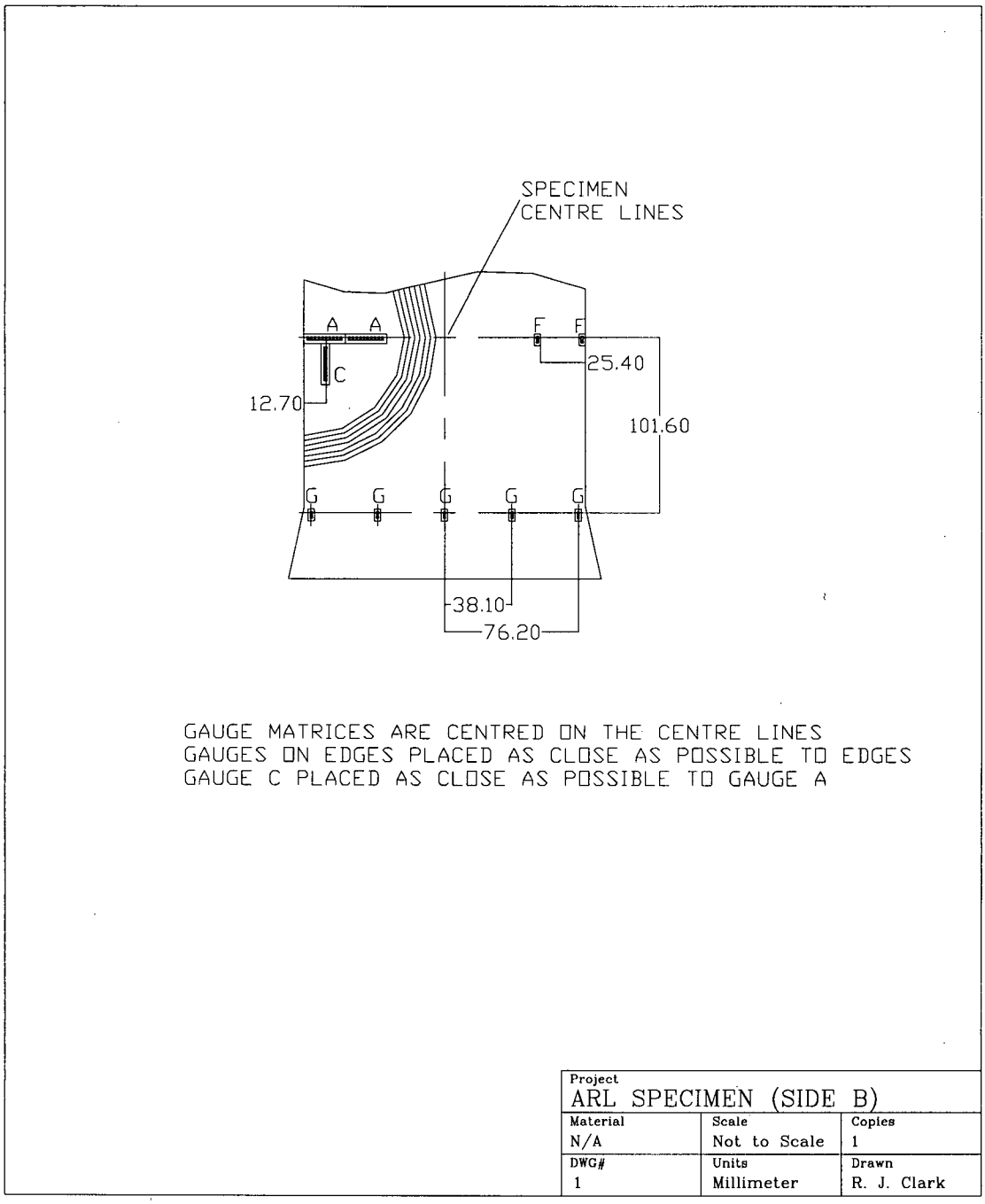

Figure B-4: Instrumented AMRL specimen drawing, side B

Appendix C: Test data

This appendix contains additional information not presented in the body of the thesis. Specifically, it contains strain gauge data from testing of the patch specimens. This data is presented for other researchers to use for the validation of bonded repair and hybrid joint models. The testing of the repair proceeded in stages, the first stage being the static testing of the instrumented AMRL specimen with an initial crack length of 20 mm. The strain data presented is organized according to the drawings in Appendix B.

Applied stress	Strains for Connector A1 (microstrain)									
(MPa)	A1-1	A1-2	A1-3	A1-4	A1-5	A1-6	A1-7	A1-8	A1-9	A1-10
137.7	1204	1218	1192	1208	1190	0	1288	1329	1219	1148
128.6	1124	1133	1107	1128	1104	0	1200	1235	1133	1071
119.4	1042	1050	1026	1045	1022	0	1111	1141	1048	993
110.2	959	971	947	962	943	0	1023	1054	966	914
101.1	877	887	871	881	860	0	935	964	886	836
92.0	798	808	791	801	783	0	850	878	804	760
82.6	718	726	707	721	704	0	766	786	721	685
73.4	639	642	628	642	622	0	679	697	643	608
64.1	558	560	552	560	543	0	593	610	563	531
55.1	478	481	475	481	466	0	510	524	485	455
45.9	396	400	394	399	387	0	421	435	400	378
36.6	316	321	311	316	309	0	335	346	316	300
27.5	238	236	231	238	228	0	250	255	237	225
18.4	156	157	155	156	152	0	164	170	157	147
9.2	78	77	77	78	74	0	81	84	78	73
0.0	0	0	0	0	0	0	0	0	0	0
-9.3	-79	-78	-80	-79	-76	0	-84	-86	-82	-75
-18.6	-156	-155	-158	-157	-151	0	-166	-171	-160	-149
-27.7	-229	-234	-233	-230	-226	0	-245	-254	-234	-218
-36.9	-306	-312	-308	-307	-303	0	-326	-337	-308	-290
-46.2	-385	-386	-381	-386	-374	0	-407	-415	-385	-362
-55.2	-464	-472	-467	-468	-458	0	-496	-514	-474	-444

Table C-1 : Strains for connector A1

Applied stress	Strains for Connector A2 (microstrain)									
(MPa)	A2-1	A2-2	A2-3	A2-4	A2-5	A2-6	A2-7	A2-8	A2-9	A2-10
137.7	959	840	746	647	629	585	548	689	788	982
128.5	893	780	691	605	586	541	515	645	735	922
119.4	824	720	639	557	544	503	476	601	681	854
110.2	760	660	591	513	496	463	437	551	628	788
101.1	696	600	537	469	456	420	402	504	572	722
91.8	629	540	489	423	412	383	362	459	518	655
82.6	568	490	438	383	370	342	328	411	464	592
73.5	501	440	392	337	329	305	290	365	414	525
64.2	440	380	343	296	286	267	254	319	361	460
55.1	375	330	291	253	248	226	216	275	305	394
45.9	314	270	242	211	202	189	181	225	253	329
36.9	246	220	193	165	164	150	142	181	200	259
27.5	181	160	144	120	119	114	102	129	146	188
18.4	120	120	94	80	82	73	69	88	95	126
9.1	62	50	48	42	40	38	38	43	49	65
0.0	0	0	0	0	0	0	0	0	0	0
-9.3	-63	-50	-44	-44	-40	-33	-35	-41	-46	-62
-18.4	-123	-100	-93	-82	-78	-73	-68	-84	-95	-121
-27.8	-181	-150	-139	-124	-121	-110	-105	-131	-145	-186
-36.9	-240	-200	-183	-165	-158	-147	-142	-174	-197	-249
-46.1	-299	-250	-223	-205	-198	-182	-179	-220	-244	-312
-55.1	-371	-310	-277	-252	-243	-226	-222	-273	-308	-392

Table C-2: Strains for connector A2

Applied stress	Strains for Connector A3 (microstrain)									
(MPa)	A3-1	A3-2	A3-3	A3-4	A3-5	A3-6	A3-7	A3-8	A3-9	A3-10
137.8	1076	1037	1023	1037	1077	1118	1141	1132	1143	1152
128.6	1007	971	955	963	1002	1013	1054	1062	1068	1072
119.4	938	898	882	895	927	936	979	983	990	998
110.0	864	826	813	819	850	864	900	905	913	916
101.1	792	759	742	748	780	790	825	832	838	841
92.0	724	690	671	679	709	713	751	757	759	766
82.7	653	618	606	610	633	644	674	679	686	688
73.5	582	554	535	541	566	567	600	605	607	614
64.3	515	481	468	476	491	494	528	528	533	540
55.0	439	415	397	404	422	417	449	453	454	459
45.9	366	345	332	334	350	347	373	377	379	382
36.8	290	272	264	264	275	275	296	297	301	302
27.5	219	198	191	198	201	196	220	219	221	226
18.3	144	132	123	130	134	122	146	144	144	148
9.1	71	64	62	64	64	57	71	70	72	74
0.0	0	0	0	0	0	0	0	0	0	0
-9.3	-72	-68	-66	-66	-68	-69	-73	-73	-75	-75
-18.6	-141	-134	-135	-128	-137	-143	-143	-148	-152	-147
-27.8	-216	-201	-201	-196	-205	-214	-218	-221	-227	-223
-36.9	-291	-269	-268	-265	-274	-280	-294	-295	-302	-299
-46.1	-369	-343	-337	-336	-348	-353	-372	-373	-381	-377
-55.2	-462	-430	-424	-420	-436	-442	-464	-465	-472	-468

Table C-3: Strains for connector A3

Applied stress	Strains for Connector A4 (microstrain)									
(MPa)	A4-1	A4-2	A4-3	A4-4	A4-5	A4-6	A4-7	A4-8	A4-9	A4-10
137.7	1234	1244	1255	1277	1284	1243	1254	1236	1210	1245
128.5	1152	1159	1168	1193	1197	1159	1169	1151	1126	1161
119.4	1069	1076	1084	1107	1111	1085	1084	1068	1044	1076
110.2	985	994	998	1020	1025	1002	998	985	962	992
101.1	902	914	917	933	943	920	913	905	884	908
91.8	823	828	832	852	855	833	832	820	802	827
82.7	739	750	749	765	773	749	747	741	722	742
73.3	653	666	666	678	685	667	663	657	641	658
64.4	576	583	586	597	600	586	583	575	564	578
55.1	494	501	498	510	515	498	498	494	479	495
46.0	409	416	418	424	428	418	414	411	402	411
36.6	326	329	326	338	339	326	330	325	316	327
27.5	241	245	246	249	252	246	244	241	238	243
18.3	157	164	159	163	167	158	160	160	155	158
9.1	79	84	76	81	85	77	80	81	75	79
-0.1	0	0	0	0	0	0	0	0	0	0
-9.2	-80	-76	-85	-84	-80	-85	-81	-78	-80	-81
-18.4	-158	-161	-164	-164	-168	-164	-160	-160	-158	-161
-27.7	-241	-239	-246	-251	-249	-247	-244	-240	-239	-244
-36.9	-318	-323	-332	-331	-334	-332	-323	-322	-318	-324
-46.0	-403	-409	-417	-417	-423	-418	-408	-408	-401	-408
-55.2	-496	-501	-507	-511	-516	-508	-498	-497	-486	-496

Table C-4: Strains for connector A4

Applied stress	Strains for Connector B1 (microstrain)									
(MPa)	B1-1	B1-2	B1-3	B1-4	B1-5	B1-6	B1-7	B1-8	B1-9	B1-10
137.7	1797	1769	1775	1773	1744	1748	1684	1657	1630	1609
128.6	1657	1644	1652	1647	1621	1624	1562	1540	1518	1496
119.4	1523	1523	1532	1525	1499	1504	1445	1425	1407	1386
110.2	1399	1401	1409	1401	1379	1385	1329	1309	1295	1274
100.9	1277	1281	1288	1280	1260	1265	1212	1192	1185	1164
91.7	1158	1163	1165	1159	1144	1144	1100	1086	1073	1056
82.6	1035	1044	1044	1041	1026	1024	986	978	962	949
73.5	916	924	927	925	909	907	875	865	854	842
64.2	793	803	806	805	790	787	761	750	743	734
55.1	672	684	691	687	673	676	649	638	636	627
45.9	560	568	573	571	557	559	539	528	527	521
36.8	444	452	459	454	444	448	428	420	421	415
27.4	329	338	342	336	331	334	316	312	314	308
18.3	219	227	228	225	223	223	212	207	209	206
9.1	109	111	117	114	109	114	107	103	107	104
-0.1	0	0	0	0	0	0	0	0	0	0
-9.2	-106	-116	-112	-109	-112	-109	-103	-106	-104	-100
-18.4	-221	-229	-223	-226	-221	-217	-211	-209	-204	-204
-27.7	-330	-340	-337	-336	-330	-326	-317	-311	-309	-306
-36.8	-443	-449	-448	-445	-436	-433	-413	-414	-408	-406
-46.1	-555	-560	-557	-555	-545	-539	-516	-517	-510	-505
-55.3	-662	-668	-662	-660	-651	-642	-615	-619	-608	-604

Table C-5: Strains for connector B1

Applied stress	Strains for Connector C1 (microstrain)									
(MPa)	C1-1	C1-2	C1-3	C1-4	C1-5	C1-6	C1-7	C1-8	C1-9	C1-10
137.7	862	913	898	1000	1015	975	1201	1217	1172	1543
128.6	807	855	836	935	953	908	1124	1139	1091	1444
119.3	751	795	776	870	886	841	1044	1058	1011	1342
110.3	696	732	718	808	816	781	967	977	933	1242
100.9	636	674	662	737	750	719	885	899	856	1138
91.8	580	613	604	672	685	658	807	820	779	1035
82.6	524	554	546	606	619	594	727	740	701	935
73.5	467	496	487	542	553	528	649	662	623	835
64.4	412	439	426	478	489	463	572	584	545	735
55.1	356	375	365	412	420	396	493	500	468	633
46.1	300	313	308	347	350	333	414	419	392	531
36.8	237	249	244	275	278	262	328	332	310	422
27.5	174	183	182	200	205	198	239	245	230	308
18.3	115	123	121	132	137	133	158	163	154	205
9.2	54	62	60	62	70	66	76	83	76	100
0.0	0	0	0	0	0	0	0	0	0	0
-9.2	-61	-62	-57	-71	-67	-63	-85	-82	-74	-106
-18.4	-120	-120	-120	-139	-132	-129	-165	-161	-152	-210
-27.8	-178	-187	-183	-207	-206	-197	-248	-249	-230	-315
-36.8	-235	-248	-239	-273	-274	-258	-326	-328	-302	-416
-46.1	-295	-308	-296	-342	-340	-318	-409	-408	-376	-520
-55.1	-364	-378	-371	-423	-419	-396	-504	-502	-466	-642

Table C-6: Strains for connector C1

Applied stress	Strains for Connector C2 (microstrain)									
(MPa)	C2-1	C2-2	C2-3	C2-4	C2-5	C2-6	C2-7	C2-8	C2-9	C2-10
137.6	1023	1089	0	1142	1189	0	1294	1364	1426	1445
128.5	960	1018	0	1074	1113	0	1213	1283	1334	1356
119.3	889	947	0	999	1034	0	1132	1192	1245	1265
110.2	825	881	0	924	959	0	1048	1106	1156	1171
101.2	762	808	0	852	887	0	964	1020	1064	1078
91.8	692	738	0	776	807	0	878	930	972	983
82.6	623	666	0	702	727	0	798	841	879	892
73.4	560	596	0	626	654	0	711	753	787	795
64.4	492	527	0	552	575	0	628	663	696	702
55.1	422	449	0	475	492	0	540	569	595	604
46.0	355	380	0	395	415	0	450	478	501	504
36.8	283	300	0	319	328	0	363	382	399	405
27.7	208	226	0	236	245	0	271	285	300	304
18.3	139	147	0	157	162	0	178	189	196	199
9.1	64	74	0	72	77	0	85	89	97	96
0.0	0	0	0	0	0	0	0	0	0	0
-9.2	-74	-72	0	-82	-82	0	-89	-97	-97	-101
-18.4	-140	-146	0	-154	-161	0	-175	-186	-193	-196
-27.5	-212	-217	0	-238	-243	0	-267	-282	-290	-298
-36.8	-282	-297	0	-312	-325	0	-354	-373	-390	-396
-46.0	-357	-368	0	-398	-407	0	-446	-471	-487	-499
-55.3	-441	-463	0	-491	-506	0	-552	-581	-605	-615

Table C-7: Strains for connector C2

Applied stress	Strains for Connector D1 (microstrain)									
(MPa)	D1-1	D1-2	D1-3	D1-4	D1-5	D1-6	D1-7	D1-8	D1-9	D1-10
137.8	0	0	1299	1323	1319	1366	1342	1415	1493	0
128.6	0	0	1213	1203	1206	1272	1262	1333	1381	0
119.5	0	0	1127	1119	1121	1178	1177	1242	1285	0
110.2	0	0	1043	1030	1037	1089	1085	1149	1189	0
101.1	0	0	955	947	957	1000	1001	1060	1092	0
91.7	0	0	870	865	870	910	914	965	996	0
82.5	0	0	788	781	783	824	826	870	902	0
73.4	0	0	703	692	701	738	736	778	805	0
64.2	0	0	614	610	619	647	648	686	707	0
55.1	0	0	532	525	530	559	558	588	611	0
45.9	0	0	440	438	441	462	464	490	506	0
36.8	0	0	354	345	351	371	367	390	405	0
27.5	0	0	262	260	263	274	277	292	301	0
18.3	0	0	177	169	173	185	179	192	200	0
8.6	0	0	78	78	80	82	81	87	89	0
0.0	0	0	0	0	0	0	0	0	0	0
-9.2	0	0	-88	-87	-89	-90	-92	-99	-101	0
-18.3	0	0	-174	-174	-178	-182	-186	-196	-200	0
-27.7	0	0	-267	-260	-265	-275	-276	-292	-302	0
-36.9	0	0	-355	-345	-349	-360	-366	-385	-396	0
-45.9	0	0	-444	-427	-431	-447	-453	-476	-490	0
-55.2	0	0	-558	-535	-541	-560	-569	-598	-618	0

Table C-8: Strains for connector D1

Applied stress	Strains for Connector E1 (microstrain)									
(MPa)	E1-1	E1-2	E1-3	E1-4	E1-5	E1-6	E1-7	E1-8	E1-9	E1-10
137.7	2227	2110	2030	1953	1952	1983	2028	2119	2162	2192
128.6	2082	1976	1898	1820	1824	1849	1895	1983	2020	2050
119.4	1933	1839	1766	1687	1695	1721	1759	1844	1879	1904
110.2	1789	1699	1634	1558	1563	1589	1624	1704	1737	1757
101.1	1644	1560	1500	1431	1433	1457	1488	1561	1592	1610
91.8	1498	1425	1363	1300	1305	1325	1352	1423	1446	1463
82.6	1351	1284	1225	1172	1176	1189	1216	1280	1298	1314
73.5	1208	1143	1093	1047	1046	1058	1083	1137	1154	1170
64.2	1058	1004	956	915	916	925	946	995	1009	1020
55.1	909	865	824	785	787	798	811	854	868	874
46.0	758	721	690	655	653	667	676	709	725	726
36.6	604	571	545	522	518	525	537	562	571	578
27.4	445	425	401	383	386	387	395	417	422	427
18.4	296	282	268	256	256	257	263	277	281	282
9.2	149	141	134	129	127	130	132	138	141	141
0.0	0	0	0	0	0	0	0	0	0	0
-9.2	-149	-141	-131	-127	-130	-125	-133	-137	-137	-141
-18.4	-300	-285	-269	-256	-258	-257	-265	-275	-279	-282
-27.5	-453	-429	-405	-386	-385	-385	-395	-410	-416	-421
-36.9	-600	-563	-534	-515	-508	-511	-528	-544	-553	-562
-46.0	-742	-703	-662	-635	-634	-633	-652	-678	-685	-694
-55.2	-922	-869	-826	-790	-783	-789	-810	-839	-853	-863

Table C-9: Strains for connector E1

Applied stress	Strains for Connector F (microstrain)									
(MPa)	F1	F2	F3	F4	G1	G2	G3	G4	G5	G6
137.7	1772	1947	2149	1920	1735	0	1972	1792	1923	2011
128.7	1652	1811	2014	1800	1624	0	1833	1678	1787	1869
119.3	1529	1670	1873	1673	1508	0	1692	1559	1651	1724
110.2	1412	1535	1734	1552	1395	0	1559	1442	1523	1588
100.9	1292	1397	1592	1430	1283	0	1425	1325	1390	1451
92.0	1177	1264	1450	1310	1175	0	1294	1212	1259	1318
82.6	1056	1124	1306	1184	1060	0	1159	1095	1128	1180
73.5	938	986	1165	1061	948	0	1026	979	996	1043
64.2	817	848	1019	934	835	0	892	861	865	906
55.1	700	711	877	808	721	0	760	745	737	773
46.1	582	580	735	677	605	0	630	626	613	642
36.6	461	456	586	539	485	0	497	500	487	507
27.5	346	340	434	404	367	0	373	377	363	379
18.4	233	230	286	270	248	0	251	254	241	255
9.1	115	114	142	134	125	0	124	129	118	125
0.0	0	0	0	0	0	0	0	0	0	0
-9.2	-115	-119	-139	-125	-118	0	-126	-120	-128	-129
-18.4	-239	-225	-267	-261	-245	0	-252	-250	-248	-257
-27.7	-357	-346	-399	-388	-368	0	-380	-377	-372	-388
-36.8	-477	-454	-533	-523	-495	0	-505	-505	-489	-511
-46.0	-599	-566	-667	-662	-625	0	-634	-633	-608	-637
-55.2	-712	-666	-826	-808	-752	0	-746	-760	-726	-758

Table C-10: Strains for connector F

After 175,000 fatigue cycles, the crack had grown to a length of 40 mm and a small disbond had grown under the patch. Tables 11-20 show the strains recorded at this point.

Applied stress	Strains for Connector A1 (microstrain)									
(MPa)	A1-1	A1-2	A1-3	A1-4	A1-5	A1-6	A1-7	A1-8	A1-9	A1-10
137.8	862	862	694	680	573	0	619	636	492	483
128.6	809	813	655	638	535	0	578	600	465	453
119.4	759	761	609	597	496	0	540	558	432	423
110.3	708	703	565	557	452	0	500	514	400	393
101.1	647	645	521	507	409	0	453	471	368	356
91.7	591	592	473	461	372	0	413	429	332	324
82.6	534	535	428	416	332	0	370	386	298	292
73.5	477	475	378	370	290	0	329	339	263	258
64.3	417	413	331	323	246	0	285	292	231	224
55.1	358	352	282	276	210	0	241	248	195	190
46.0	299	295	237	229	173	0	199	206	165	157
36.8	240	238	194	184	136	0	159	166	135	127
27.5	177	177	143	136	97	0	116	122	100	93
18.3	116	121	92	87	64	0	77	83	65	61
9.1	58	61	45	42	30	0	38	40	32	31
0.0	0	0	0	0	0	0	0	0	0	0
-9.2	-47	-45	-32	-31	-20	0	-27	-28	-19	-18
-18.4	-89	-83	-59	-62	-38	0	-54	-53	-40	-37
-27.5	-116	-112	-85	-81	-51	0	-70	-73	-55	-49
-36.6	-136	-143	-104	-100	-71	0	-86	-98	-70	-60
-46.0	-164	-172	-128	-130	-81	0	-112	-123	-94	-86
-55.2	-196	-213	-161	-161	-112	0	-141	-151	-114	-99

Table C-11: Strains for connector A1

Applied stress	Strains for Connector A2 (microstrain)									
(MPa)	A2-1	A2-2	A2-3	A2-4	A2-5	A2-6	A2-7	A2-8	A2-9	A2-10
137.7	301	360	448	525	596	632	715	885	1206	1548
128.5	286	340	426	494	564	600	675	837	1137	1447
119.5	264	320	396	457	529	560	630	786	1057	1339
110.3	245	300	363	424	489	516	586	730	971	1228
101.1	224	260	329	389	444	472	539	668	886	1118
91.8	203	240	301	350	403	432	491	607	802	1004
82.7	183	210	273	315	363	391	443	549	718	894
73.5	162	190	241	278	322	348	395	489	632	782
64.2	138	160	207	240	280	302	344	425	543	669
55.2	116	140	173	202	239	256	293	363	454	562
45.9	96	110	142	167	197	211	244	301	367	454
36.6	73	80	106	131	151	160	192	232	278	351
27.7	54	60	76	96	107	118	142	168	200	253
18.3	37	40	52	62	71	80	93	111	129	160
9.2	19	20	26	31	33	39	46	53	63	77
0.0	0	0	0	0	0	0	0	0	0	0
-9.3	-14	-20	-18	-23	-31	-33	-39	-50	-57	-73
-18.4	-20	-30	-27	-35	-52	-60	-74	-95	-111	-146
-27.8	-27	-30	-30	-45	-70	-83	-108	-140	-168	-223
-36.9	-26	-30	-26	-41	-75	-95	-127	-168	-206	-282
-46.0	-21	-40	-20	-31	-76	-106	-140	-201	-256	-347
-55.1	-26	-40	-8	-25	-70	-97	-144	-218	-288	-401

Table C-12: Strains for connector A2

Applied stress	Strains for Connector A3 (microstrain)									
(MPa)	A3-1	A3-2	A3-3	A3-4	A3-5	A3-6	A3-7	A3-8	A3-9	A3-10
137.7	1658	1481	1358	1286	1246	1182	1068	960	880	794
128.6	1555	1388	1273	1208	1168	1109	1005	901	824	746
119.4	1445	1297	1191	1123	1091	1036	933	839	768	689
110.2	1335	1204	1102	1041	1012	956	863	776	706	635
101.1	1225	1107	1014	960	931	877	793	711	646	582
91.8	1113	1006	926	877	846	800	722	644	588	528
82.6	995	907	839	789	762	722	647	578	528	471
73.5	881	810	745	702	681	639	575	516	466	417
64.2	769	705	653	617	593	559	506	448	406	364
55.2	656	603	563	531	506	481	432	382	348	311
46.0	539	503	473	443	423	403	360	319	290	256
36.8	428	403	375	354	341	319	287	255	229	203
27.5	317	299	287	266	251	242	215	188	174	149
18.3	212	202	191	180	170	159	145	126	113	100
9.1	105	100	102	91	83	85	73	62	60	49
-0.1	0	0	0	0	0	0	0	0	0	0
-9.2	-98	-95	-90	-84	-82	-73	-67	-59	-52	-47
-18.4	-179	-175	-165	-153	-148	-134	-121	-107	-92	-79
-27.7	-268	-262	-249	-229	-222	-199	-181	-160	-138	-119
-36.8	-360	-350	-333	-307	-294	-264	-238	-210	-181	-154
-46.0	-440	-428	-409	-374	-359	-321	-291	-258	-222	-191
-55.2	-519	-512	-488	-443	-427	-380	-341	-310	-266	-230

Table C-13: Strains for connector A3

Applied stress	Strains for Connector A4 (microstrain)									
(MPa)	A4-1	A4-2	A4-3	A4-4	A4-5	A4-6	A4-7	A4-8	A4-9	A4-10
137.8	625	726	910	965	955	949	901	817	766	704
128.5	584	677	851	903	891	886	840	760	710	646
119.3	540	630	790	837	827	822	777	703	655	591
110.2	497	580	728	771	762	757	715	646	599	540
101.1	455	532	666	706	699	692	654	590	546	489
92.0	419	478	601	642	630	624	593	532	490	442
82.7	375	426	542	577	563	561	531	473	439	392
73.6	328	378	482	507	499	500	467	419	389	341
64.2	284	329	414	439	433	430	405	364	334	295
55.1	243	280	354	376	369	366	345	308	282	249
46.0	202	230	294	315	302	304	287	253	233	206
36.8	160	183	236	250	240	244	229	200	187	162
27.5	113	132	174	181	174	181	165	145	137	118
18.4	73	87	115	119	114	120	107	96	90	77
9.2	36	43	56	59	57	59	53	48	44	39
0.0	0	0	0	0	0	0	0	0	0	0
-9.2	-39	-46	-56	-58	-58	-54	-51	-45	-41	-34
-18.4	-69	-85	-104	-109	-103	-99	-90	-82	-78	-70
-27.8	-101	-127	-150	-152	-148	-137	-123	-117	-110	-103
-36.8	-129	-159	-189	-189	-180	-168	-149	-146	-142	-141
-46.0	-158	-192	-224	-220	-207	-193	-174	-174	-175	-182
-55.1	-184	-222	-252	-247	-230	-216	-201	-211	-215	-234

Table C-14: Strains for connector A4

Applied stress	Strains for Connector B1 (microstrain)									
(MPa)	B1-1	B1-2	B1-3	B1-4	B1-5	B1-6	B1-7	B1-8	B1-9	B1-10
137.7	78220	1831	1835	1842	1861	1803	1791	1718	1709	1689
128.5	48320	1709	1711	1710	1747	1680	1659	1605	1592	1569
119.4	12320	1585	1587	1586	1615	1557	1535	1490	1476	1455
110.2	55220	1460	1461	1460	1478	1431	1410	1372	1359	1340
101.1	42420	1336	1337	1341	1345	1308	1292	1256	1243	1229
92.1	183920	1213	1219	1216	1218	1191	1172	1139	1132	1116
82.6	47120	1087	1090	1087	1090	1067	1047	1021	1014	998
73.4	69920	966	967	965	971	944	928	906	899	887
64.3	-3830	843	845	847	848	824	815	790	785	777
55.0	-46670	722	721	719	728	705	692	675	671	661
46.0	10080	604	602	599	607	586	577	562	559	551
36.6	-69741	480	476	477	486	463	458	447	443	438
27.5	330	356	355	359	362	346	346	332	330	329
18.3	26320	236	237	237	244	230	227	222	219	218
9.1	-75585	115	120	120	119	117	114	107	112	109
0.0	0	0	0	0	0	0	0	0	0	0
-9.2	-62453	-119	-117	-118	-121	-114	-114	-112	-107	-108
-18.4	-65415	-238	-236	-232	-239	-231	-222	-223	-218	-213
-27.8	-67011	-348	-350	-346	-349	-340	-330	-327	-322	-317
-36.9	-68111	-467	-468	-462	-465	-456	-443	-437	-432	-424
-46.0	-68970	-578	-577	-570	-573	-563	-548	-540	-532	-525
-55.2	-69888	-696	-695	-688	-687	-677	-659	-651	-641	-632

Table C-15: Strains for connector B1

Applied stress	Strains for Connector C1 (microstrain)									
(MPa)	C1-1	C1-2	C1-3	C1-4	C1-5	C1-6	C1-7	C1-8	C1-9	C1-10
137.8	843	884	871	977	974	958	1183	1186	1122	1499
128.5	785	824	810	909	907	889	1101	1104	1040	1397
119.4	729	764	751	844	841	825	1024	1023	962	1297
110.2	673	705	691	779	774	760	944	943	884	1198
101.1	617	644	633	714	708	695	865	866	807	1098
91.8	562	585	574	650	642	629	789	787	728	1000
82.6	504	529	514	583	581	563	708	710	651	898
73.4	446	470	457	516	517	502	627	632	576	796
64.2	389	409	400	452	449	441	548	549	501	695
55.2	335	349	345	389	381	377	472	471	429	598
46.0	279	289	285	324	315	312	393	390	354	497
36.8	224	230	226	261	256	245	314	310	280	398
27.4	165	173	166	191	192	182	232	233	206	294
18.3	109	116	112	128	130	122	155	156	138	197
9.1	54	57	56	63	64	61	77	79	69	98
0.0	0	0	0	0	0	0	0	0	0	0
-9.2	-56	-58	-56	-66	-64	-63	-76	-79	-70	-99
-18.4	-114	-120	-117	-133	-132	-128	-159	-161	-145	-202
-27.7	-169	-180	-173	-197	-197	-189	-237	-242	-213	-302
-36.9	-224	-239	-229	-261	-262	-253	-313	-320	-284	-399
-46.1	-281	-300	-291	-326	-328	-320	-392	-400	-358	-499
-55.2	-334	-350	-342	-389	-385	-375	-468	-469	-421	-594

Table C-16: Strains for connector C1

Applied stress	Strains for Connector C2 (microstrain)									
(MPa)	C2-1	C2-2	C2-3	C2-4	C2-5	C2-6	C2-7	C2-8	C2-9	C2-10
137.7	1260	1400	0	1621	1735	0	1977	2002	1890	4030
128.6	1179	1305	0	1518	1619	0	1847	1866	1764	5290
119.3	1095	1216	0	1410	1508	0	1715	1735	1635	3642
110.2	1010	1123	0	1302	1393	0	1583	1599	1510	2399
101.1	929	1028	0	1198	1277	0	1452	1464	1385	1421
92.0	846	936	0	1090	1165	0	1321	1332	1260	1326
82.6	764	843	0	982	1047	0	1191	1197	1130	1858
73.4	678	749	0	874	933	0	1058	1064	1004	1429
64.2	592	657	0	763	818	0	924	932	876	1248
55.1	507	563	0	654	702	0	792	799	752	1206
46.1	423	469	0	545	585	0	659	666	629	1365
36.6	337	371	0	435	463	0	526	528	502	1980
27.5	254	277	0	328	346	0	397	395	376	2489
18.3	169	185	0	217	232	0	263	263	249	3734
9.2	87	97	0	112	119	0	134	136	128	1447
0.0	0	0	0	0	0	0	0	0	0	0
-9.2	-87	-95	0	-111	-118	0	-134	-134	-127	214
-18.4	-168	-184	0	-214	-228	0	-259	-260	-245	-172
-27.7	-260	-287	0	-330	-357	0	-399	-404	-380	-424
-36.8	-347	-388	0	-442	-481	0	-534	-547	-519	-649
-46.2	-435	-483	0	-554	-597	0	-668	-681	-653	-832
-55.2	-517	-570	0	-657	-705	0	-793	-805	-776	-974

Table C-17: Strains for connector C2

Applied stress	Strains for Connector D1 (microstrain)									
(MPa)	D1-1	D1-2	D1-3	D1-4	D1-5	D1-6	D1-7	D1-8	D1-9	D1-10
137.8	0	0	1795	1842	1822	1903	1956	2015	2097	0
128.6	0	0	1674	1717	1697	1777	1824	1884	1959	0
119.3	0	0	1553	1592	1572	1650	1693	1745	1819	0
110.2	0	0	1432	1473	1451	1520	1566	1612	1677	0
101.1	0	0	1316	1349	1332	1398	1433	1477	1541	0
91.7	0	0	1190	1227	1209	1263	1302	1340	1394	0
82.6	0	0	1071	1103	1091	1136	1170	1208	1255	0
73.5	0	0	955	977	966	1013	1037	1071	1118	0
64.3	0	0	834	859	844	884	910	937	977	0
55.1	0	0	712	733	727	755	775	802	836	0
45.9	0	0	592	611	599	628	645	664	695	0
36.8	0	0	472	486	482	499	513	532	553	0
27.4	0	0	355	362	355	373	382	393	413	0
18.3	0	0	234	240	237	247	253	261	274	0
9.1	0	0	113	120	119	117	124	129	133	0
0.0	0	0	0	0	0	0	0	0	0	0
-9.2	0	0	-124	-124	-125	-131	-134	-140	-143	0
-18.4	0	0	-244	-238	-241	-256	-255	-269	-280	0
-27.7	0	0	-370	-367	-360	-387	-393	-406	-425	0
-36.8	0	0	-489	-484	-481	-508	-516	-538	-559	0
-46.1	0	0	-618	-607	-597	-637	-649	-670	-701	0
-55.2	0	0	-728	-710	-706	-749	-759	-788	-822	0

Table C-18: Strains for connector D1

Applied stress	Strains for Connector E1 (microstrain)									
(MPa)	E1-1	E1-2	E1-3	E1-4	E1-5	E1-6	E1-7	E1-8	E1-9	E1-10
137.8	2124	2063	1989	1880	1900	1921	1997	2074	2112	2144
128.6	1983	1924	1859	1754	1770	1793	1866	1934	1975	2004
119.3	1841	1789	1727	1623	1644	1662	1730	1798	1834	1859
110.2	1707	1653	1594	1503	1518	1533	1602	1662	1694	1721
101.1	1567	1515	1464	1375	1392	1409	1469	1525	1555	1579
91.7	1423	1379	1326	1248	1267	1276	1334	1387	1411	1433
82.6	1285	1242	1199	1127	1137	1152	1202	1248	1275	1293
73.4	1142	1108	1062	999	1014	1023	1068	1112	1132	1148
64.2	999	969	933	873	885	899	934	972	994	1005
55.1	857	829	803	751	757	770	802	832	852	863
46.1	717	695	667	627	633	640	673	696	711	723
36.6	569	557	533	498	507	512	534	557	566	574
27.7	427	421	402	372	382	386	401	419	427	432
18.4	288	279	267	251	254	256	269	278	285	290
9.1	142	144	138	124	130	133	133	141	148	145
-0.1	0	0	0	0	0	0	0	0	0	0
-9.2	-146	-141	-132	-128	-129	-126	-135	-142	-141	-145
-18.4	-282	-269	-262	-246	-244	-248	-262	-269	-276	-282
-27.7	-432	-413	-396	-375	-373	-376	-396	-408	-414	-424
-36.8	-565	-547	-521	-492	-496	-495	-520	-541	-547	-559
-46.0	-702	-675	-647	-610	-608	-613	-642	-662	-674	-687
-55.2	-839	-806	-772	-728	-728	-732	-768	-792	-806	-822

Table C-19: Strains for connector E1

Applied stress	Strains for Connector F (microstrain)									
(MPa)	F1	F2	F3	F4	G1	G2	G3	G4	G5	G6
137.7	1743	2009	2146	1899	1667	0	1971	1780	1973	2035
128.6	1634	1875	2005	1781	1572	0	1839	1658	1836	1898
119.3	1514	1744	1859	1648	1462	0	1699	1539	1701	1754
110.2	1401	1609	1719	1525	1345	0	1571	1418	1571	1621
100.9	1285	1479	1574	1398	1232	0	1438	1298	1436	1483
91.8	1168	1351	1432	1272	1120	0	1306	1182	1307	1347
82.7	1051	1219	1290	1144	1006	0	1173	1062	1177	1212
73.4	933	1081	1147	1017	889	0	1041	940	1046	1075
64.2	819	950	999	892	775	0	913	819	909	941
55.1	699	819	856	761	665	0	778	704	779	804
45.9	581	683	713	633	551	0	645	584	650	667
36.6	467	547	567	509	441	0	516	464	516	534
27.5	352	415	425	383	329	0	386	348	385	400
18.3	232	281	281	254	224	0	255	234	254	264
9.1	119	149	141	128	112	0	126	116	126	130
0.0	0	0	0	0	0	0	0	0	0	0
-9.3	-111	-132	-143	-122	-109	0	-126	-118	-132	-132
-18.4	-230	-267	-291	-263	-229	0	-256	-236	-253	-259
-27.8	-346	-395	-422	-388	-340	0	-386	-356	-381	-393
-36.8	-455	-503	-573	-532	-472	0	-505	-487	-498	-514
-46.1	-568	-634	-708	-655	-580	0	-635	-604	-631	-648
-55.2	-685	-739	-847	-795	-705	0	-761	-733	-752	-775

Table C-20: Strains for connector F

At this point, the honeycomb bending restraint was removed.

Applied stress	Strains for Connector A1 (microstrain)									
(MPa)	A1-1	A1-2	A1-3	A1-4	A1-5	A1-6	A1-7	A1-8	A1-9	A1-10
137.8	-3496	-3512	-3684	-3648	-3645	0	-4034	-4012	-3838	-3826
128.5	-3406	-3430	-3596	-3556	-3557	0	-3937	-3922	-3751	-3739
119.3	-3319	-3337	-3501	-3465	-3457	0	-3836	-3821	-3659	-3649
110.2	-3221	-3243	-3395	-3365	-3356	0	-3727	-3717	-3554	-3550
100.9	-3114	-3136	-3282	-3253	-3242	0	-3606	-3599	-3440	-3438
91.8	-2993	-3017	-3156	-3128	-3116	0	-3468	-3467	-3313	-3311
82.7	-2860	-2889	-3017	-2989	-2982	0	-3317	-3325	-3174	-3172
73.5	-2700	-2727	-2842	-2820	-2810	0	-3131	-3140	-2991	-2997
64.3	-2527	-2550	-2657	-2641	-2624	0	-2930	-2940	-2803	-2809
55.1	-2338	-2360	-2462	-2446	-2430	0	-2714	-2727	-2601	-2608
46.0	-2107	-2129	-2213	-2204	-2190	0	-2445	-2463	-2342	-2354
36.8	-1817	-1835	-1903	-1900	-1882	0	-2103	-2121	-2018	-2029
27.4	-1480	-1494	-1550	-1546	-1527	0	-1705	-1722	-1639	-1654
18.3	-1109	-1123	-1164	-1162	-1151	0	-1281	-1299	-1240	-1248
9.1	-668	-676	-707	-705	-702	0	-780	-794	-762	-764
0.0	0	0	0	0	0	0	0	0	0	0
-9.2	846	861	890	890	884	0	992	1018	955	960
-18.6	1160	1184	1233	1240	1221	0	1398	1448	1399	1437
-23.0	1168	1219	1269	1277	1281	0	1411	1484	1445	1495

Table C-21: Strains for connector A1

Applied stress	Strains for Connector A2 (microstrain)									
(MPa)	A2-1	A2-2	A2-3	A2-4	A2-5	A2-6	A2-7	A2-8	A2-9	A2-10
137.7	-4112	-3750	-3818	-3646	-3722	-3644	-3187	-2620	-1288	-401
128.5	-3984	-3640	-3714	-3550	-3625	-3553	-3112	-2567	-1299	-456
119.4	-3875	-3540	-3624	-3467	-3543	-3473	-3049	-2526	-1319	-519
110.2	-3758	-3440	-3530	-3377	-3455	-3389	-2979	-2482	-1336	-580
101.1	-3633	-3320	-3424	-3281	-3358	-3292	-2902	-2428	-1348	-637
91.8	-3488	-3210	-3300	-3164	-3242	-3178	-2809	-2361	-1350	-687
82.6	-3329	-3070	-3158	-3032	-3108	-3046	-2699	-2280	-1343	-728
73.5	-3160	-2920	-3008	-2889	-2967	-2907	-2581	-2200	-1332	-764
64.3	-2944	-2730	-2813	-2703	-2778	-2720	-2418	-2071	-1288	-776
55.1	-2709	-2520	-2594	-2499	-2569	-2511	-2243	-1934	-1234	-781
45.9	-2432	-2260	-2329	-2250	-2310	-2258	-2026	-1755	-1148	-759
36.8	-2146	-1990	-2063	-1987	-2044	-2009	-1808	-1586	-1069	-726
27.7	-1760	-1640	-1696	-1639	-1686	-1651	-1491	-1311	-898	-634
18.3	-1278	-1190	-1234	-1193	-1223	-1203	-1090	-957	-676	-491
9.1	-740	-690	-717	-689	-705	-699	-636	-562	-407	-299
0.0	0	0	0	0	0	0	0	0	0	0
-9.2	921	850	889	868	903	887	835	756	562	457
-18.4	1569	1470	1609	1604	1684	1690	1623	1491	1176	954
-23.0	1586	1520	1682	1696	1807	1820	1757	1635	1346	1093

Table C-22: Strains for connector A2

Applied stress	Strains for Connector A3 (microstrain)									
(MPa)	A3-1	A3-2	A3-3	A3-4	A3-5	A3-6	A3-7	A3-8	A3-9	A3-10
137.8	-360	-1697	-2355	-2552	-2676	-2657	-2914	-2935	-3049	-3198
128.5	-412	-1693	-2331	-2527	-2648	-2648	-2864	-2887	-2990	-3133
119.3	-474	-1699	-2317	-2511	-2626	-2617	-2826	-2844	-2939	-3078
110.2	-531	-1700	-2297	-2484	-2595	-2591	-2780	-2793	-2885	-3013
101.1	-584	-1694	-2268	-2445	-2555	-2556	-2722	-2733	-2817	-2936
92.0	-629	-1676	-2221	-2394	-2500	-2499	-2652	-2657	-2734	-2846
82.6	-669	-1646	-2161	-2325	-2427	-2426	-2561	-2562	-2633	-2734
73.4	-700	-1605	-2083	-2238	-2336	-2332	-2455	-2452	-2515	-2608
64.4	-720	-1549	-1983	-2128	-2220	-2214	-2324	-2318	-2373	-2457
55.1	-709	-1456	-1848	-1983	-2073	-2059	-2154	-2150	-2193	-2266
45.9	-694	-1348	-1687	-1808	-1890	-1873	-1955	-1948	-1983	-2047
36.8	-649	-1199	-1484	-1593	-1660	-1643	-1712	-1702	-1727	-1783
27.5	-567	-1006	-1230	-1320	-1376	-1358	-1410	-1402	-1419	-1463
18.3	-454	-771	-927	-989	-1026	-1014	-1054	-1043	-1058	-1088
9.1	-282	-456	-536	-565	-584	-577	-601	-593	-601	-617
0.0	0	0	0	0	0	0	0	0	0	0
-9.3	426	627	732	770	790	785	797	780	781	796
-18.4	1023	1376	1556	1627	1656	1628	1619	1546	1512	1478
-23.0	1189	1547	1738	1820	1850	1810	1785	1684	1628	1561

Table C-23: Strains for connector A3

Applied stress	Strains for Connector A4 (microstrain)									
(MPa)	A4-1	A4-2	A4-3	A4-4	A4-5	A4-6	A4-7	A4-8	A4-9	A4-10
137.9	-3511	-3023	-2532	-2480	-2520	-2414	-2365	-2500	-2460	-2684
128.6	-3079	-2648	-2203	-2170	-2197	-2110	-2093	-2227	-2216	-2484
119.3	-3022	-2606	-2184	-2154	-2176	-2091	-2075	-2197	-2187	-2443
110.0	-2961	-2562	-2161	-2134	-2152	-2069	-2052	-2164	-2151	-2394
100.9	-2883	-2505	-2126	-2099	-2117	-2036	-2016	-2119	-2106	-2333
92.0	-2790	-2433	-2079	-2049	-2067	-1991	-1965	-2063	-2049	-2261
82.7	-2680	-2345	-2018	-1987	-2000	-1930	-1903	-1989	-1977	-2171
73.8	-2553	-2238	-1938	-1911	-1918	-1855	-1826	-1903	-1891	-2071
64.2	-2395	-2105	-1835	-1809	-1813	-1755	-1727	-1792	-1780	-1942
55.1	-2211	-1948	-1710	-1686	-1686	-1634	-1606	-1663	-1650	-1794
45.9	-1991	-1759	-1552	-1530	-1528	-1484	-1458	-1504	-1494	-1616
36.6	-1729	-1533	-1359	-1339	-1337	-1301	-1275	-1312	-1302	-1403
27.4	-1421	-1265	-1127	-1109	-1106	-1077	-1055	-1083	-1074	-1150
18.3	-1042	-929	-832	-820	-816	-797	-779	-799	-794	-848
9.2	-587	-526	-473	-466	-466	-455	-442	-450	-444	-467
-0.1	0	0	0	0	0	0	0	0	0	0
-9.3	844	758	685	671	667	649	645	653	626	661
-18.4	1507	1333	1206	1163	1138	1089	1054	1044	972	1003
-23.2	1555	1375	1256	1211	1183	1138	1107	1101	1036	1073

Table C-24: Strains for connector A4

Applied stress	Strains for Connector B1 (microstrain)									
(MPa)	B1-1	B1-2	B1-3	B1-4	B1-5	B1-6	B1-7	B1-8	B1-9	B1-10
137.7	0	1526	1503	1483	1443	1395	1348	1273	1210	1142
128.3	0	1400	1380	1363	1322	1276	1232	1160	1103	1039
119.4	0	1283	1262	1239	1207	1164	1115	1054	1001	937
110.2	0	1161	1143	1124	1088	1049	1008	948	899	842
101.1	0	1045	1024	1009	974	935	899	844	797	746
91.7	0	929	907	889	862	825	788	743	699	648
82.7	0	814	797	776	750	720	684	642	605	556
73.5	0	701	686	667	641	617	583	545	514	468
64.2	0	590	572	560	536	509	486	452	419	383
55.2	0	485	467	455	442	412	392	364	334	302
46.0	0	382	366	355	343	320	300	279	254	224
36.8	0	279	272	260	245	235	217	197	180	155
27.7	0	190	180	175	165	151	144	127	110	95
18.3	0	108	101	99	91	83	79	65	56	45
9.2	0	39	36	37	34	29	28	22	15	12
0.0	0	0	0	0	0	0	0	0	0	0
-9.3	0	12	9	13	24	18	17	29	29	36
-18.6	0	56	60	57	84	61	59	67	68	76
-23.0	0	148	148	138	163	140	126	134	131	131

Table C-25: Strains for connector B1

Applied stress	Strains for Connector C1 (microstrain)									
(MPa)	C1-1	C1-2	C1-3	C1-4	C1-5	C1-6	C1-7	C1-8	C1-9	C1-10
137.8	598	646	644	765	808	875	1155	1242	1315	1806
128.6	556	601	600	714	755	817	1080	1162	1230	1694
119.4	514	557	555	662	700	759	1005	1083	1145	1582
110.3	473	513	511	611	645	702	930	1004	1062	1469
101.1	431	470	464	560	594	641	854	923	975	1355
91.7	389	424	419	505	537	583	775	840	887	1237
82.6	346	379	375	453	481	524	698	757	800	1118
73.5	306	332	338	399	425	469	620	673	714	998
64.3	265	285	293	348	368	408	541	588	623	876
55.0	225	240	245	296	312	345	463	503	530	752
45.9	184	195	200	243	255	284	383	418	439	627
36.8	143	151	157	191	198	224	304	331	348	500
27.5	102	108	113	139	141	165	224	245	258	372
18.4	60	68	75	87	86	111	144	160	172	243
9.1	25	29	36	38	33	53	68	74	83	116
0.0	0	0	0	0	0	0	0	0	0	0
-9.2	-17	-25	-21	-30	-36	-43	-57	-70	-75	-107
-18.6	7	-8	-4	-18	-32	-41	-67	-90	-101	-156
-23.2	38	22	26	9	-8	-19	-48	-76	-90	-151

Table C-26: Strains for connector C1

Applied stress	Strains for Connector C2 (microstrain)									
(MPa)	C2-1	C2-2	C2-3	C2-4	C2-5	C2-6	C2-7	C2-8	C2-9	C2-10
137.8	1289	1401	0	1527	1543	0	1673	1588	1121	0
128.5	1197	1298	0	1417	1427	0	1545	1459	1007	0
119.4	1106	1200	0	1307	1313	0	1424	1337	901	0
110.0	1013	1098	0	1195	1213	0	1296	1212	793	0
101.1	921	1000	0	1086	1106	0	1177	1093	692	0
92.0	830	899	0	977	993	0	1055	975	593	0
82.6	738	800	0	866	897	0	933	856	492	0
73.5	647	702	0	760	786	0	814	740	399	0
64.4	559	604	0	653	676	0	698	628	314	0
55.0	470	501	0	549	562	0	581	513	230	0
46.0	380	407	0	444	454	0	468	407	160	0
36.8	292	317	0	342	352	0	358	307	94	0
27.5	216	227	0	251	254	0	261	213	41	0
18.3	135	141	0	158	157	0	162	127	7	0
9.1	65	70	0	74	76	0	75	57	-14	0
0.0	0	0	0	0	0	0	0	0	0	0
-9.3	-43	-56	0	-53	-63	0	-53	-40	31	0
-18.6	-45	-57	0	-63	-68	0	-66	-36	77	0
-23.0	-3	-17	0	-20	-28	0	-25	2	118	0

Table C-27: Strains for connector C2

Applied stress	Strains for Connector D1 (microstrain)									
(MPa)	D1-1	D1-2	D1-3	D1-4	D1-5	D1-6	D1-7	D1-8	D1-9	D1-10
137.7	0	0	1556	1624	1621	1722	1791	1875	1986	0
128.7	0	0	1438	1505	1507	1595	1663	1746	1846	0
119.4	0	0	1326	1382	1383	1472	1532	1609	1708	0
110.2	0	0	1205	1263	1266	1342	1404	1477	1565	0
101.1	0	0	1092	1148	1146	1219	1277	1341	1429	0
91.8	0	0	981	1028	1029	1098	1146	1210	1293	0
82.6	0	0	865	910	917	972	1021	1080	1152	0
73.3	0	0	753	795	795	848	894	943	1014	0
64.1	0	0	645	677	680	730	765	814	878	0
55.1	0	0	536	565	574	611	644	689	743	0
45.9	0	0	431	461	463	494	526	561	609	0
36.6	0	0	333	351	355	383	405	437	479	0
27.7	0	0	236	250	259	276	294	321	352	0
18.3	0	0	142	155	163	171	186	205	224	0
9.2	0	0	67	77	77	83	94	103	115	0
0.0	0	0	0	0	0	0	0	0	0	0
-9.5	0	0	-39	-38	-41	-54	-56	-63	-81	0
-18.6	0	0	-15	-23	-24	-44	-55	-69	-98	0
-23.0	0	0	47	36	32	16	-2	-16	-47	0

Table C-28: Strains for connector D1

Applied stress	Strains for Connector E1 (microstrain)									
(MPa)	E1-1	E1-2	E1-3	E1-4	E1-5	E1-6	E1-7	E1-8	E1-9	E1-10
137.8	3313	3251	3141	2927	2882	2808	2806	2807	2767	2744
128.6	3127	3063	2966	2757	2718	2650	2647	2644	2613	2587
119.4	2935	2876	2786	2592	2553	2488	2489	2484	2455	2433
110.0	2736	2682	2599	2422	2385	2323	2327	2321	2293	2275
101.1	2536	2492	2412	2250	2220	2157	2163	2162	2131	2114
91.8	2327	2295	2221	2070	2047	1991	1993	1995	1968	1949
82.6	2113	2088	2026	1888	1866	1820	1820	1822	1800	1781
73.5	1900	1879	1826	1705	1684	1646	1646	1648	1629	1614
64.4	1681	1667	1623	1518	1499	1467	1469	1470	1454	1440
55.1	1454	1444	1407	1321	1304	1276	1282	1283	1268	1261
46.1	1223	1225	1192	1120	1113	1086	1092	1099	1082	1077
36.6	980	991	964	905	905	884	888	897	886	881
27.4	737	749	731	687	689	676	675	687	681	676
18.3	496	503	496	465	468	465	465	473	471	466
9.1	256	256	255	241	242	242	245	247	247	248
0.0	0	0	0	0	0	0	0	0	0	0
-9.3	-237	-242	-241	-233	-240	-237	-246	-252	-254	-259
-18.4	-438	-458	-467	-459	-474	-485	-506	-526	-537	-552
-23.0	-498	-524	-548	-546	-568	-591	-625	-652	-675	-699

Table C-29: Strains for connector E1

Applied stress	Strains for Connector F (microstrain)									
(MPa)	F1	F2	F3	F4	G1	G2	G3	G4	G5	G6
137.8	1903	2120	2584	2169	1876	0	1813	2033	1824	1842
128.5	1778	1984	2432	2037	1762	0	1675	1908	1684	1697
119.4	1655	1849	2282	1904	1649	0	1541	1785	1549	1558
110.2	1533	1713	2130	1770	1532	0	1406	1659	1416	1418
101.1	1416	1578	1981	1642	1414	0	1276	1534	1287	1284
91.7	1297	1441	1819	1509	1298	0	1144	1410	1149	1147
82.6	1175	1310	1666	1374	1185	0	1011	1287	1020	1011
73.5	1053	1170	1507	1238	1062	0	878	1157	888	875
64.3	938	1034	1341	1104	943	0	751	1030	754	746
55.1	810	900	1171	961	826	0	621	903	623	610
46.0	688	764	1002	821	705	0	497	772	498	483
36.8	559	621	826	671	576	0	371	633	377	355
27.5	427	475	639	518	448	0	252	492	258	237
18.3	294	331	442	360	313	0	146	342	149	128
9.0	150	162	241	189	159	0	48	181	60	43
0.0	0	0	0	0	0	0	0	0	0	0
-9.3	-203	-227	-272	-230	-200	0	-6	-225	6	32
-18.6	-449	-521	-555	-485	-454	0	101	-505	101	174
-23.2	-604	-718	-712	-624	-594	0	210	-667	206	318

Table C-30: Strains for connector F

Appendix D: Engineering plate models

In this appendix, the standard engineering plate models are presented and reduced to the form of a line spring model, demonstrating the methods used to develop the more advanced models in chapters three and four. The six models analyzed are:

- **Plane stress extension**: a standard plate extension model, developed by assuming vanishing through-thickness stresses.
- **Plane strain extension**: a standard plate extension model, developed by assuming vanishing through-thickness strains.
- **Plane stress bending**: the Kirchoff-Poisson plate bending model, developed by assuming vanishing through-thickness stresses.
- **Plane strain bending**: a new plate bending model, developed by assuming vanishing through-thickness strains.
- **Shear deformable plane stress bending**: very similar to the Reissner plate bending model [1], developed by including shear deformations and assuming vanishing through-thickness stresses.
- **Shear deformable plane strain bending**: the Mindlin plate bending model [2], developed by including shear deformations and assuming vanishing through-thickness trains.

These plate models will be expressed in the form of harmonic partial differential equations. Applying Fourier transforms, they will be used to form hyper-singular integrals for cracked plates that relate the crack face loading to the deflections of the crack faces. Joseph and Erdogan [3,4] have used this technique to analyse cracked plates assuming plane stress plate extension and Reissner plate bending. The more common approach to cracked plate problems is to use Muskhelishvilli's complex variable method [5] in the simplified form presented by Westergaard [6], an approach that cannot easily be extended to the analysis of higher-order plate models. The Fourier transform of a function and the inverse transform may be defined as follows.

$$\overline{f} = \overline{f}(x,\alpha) = \int_{-\infty}^{\infty} f(x,y) e^{i\alpha y} dy\,, \qquad f = f(x,y) = \frac{1}{2\pi} \int_{-\infty}^{\infty} \overline{f}(x,\alpha) e^{-i\alpha y} d\alpha \tag{1a,b}$$

Applying Fourier transforms to a function f, the following relationships arise, and may be used to reduce the plate models from partial to ordinary differential equations.

$$\int_{-\infty}^{\infty} \nabla^2(f)\, e^{i\alpha y} dy = \overline{f}_{,xx} - \alpha^2 \overline{f} \tag{2a}$$

$$\int_{-\infty}^{\infty} \nabla^4(f)\, e^{i\alpha y} dy = \overline{f}_{,xxxx} - 2\alpha^2 \overline{f}_{,xx} + \alpha^4 \overline{f} \tag{2b}$$

$$\int_{-\infty}^{\infty} \nabla^6(f)\, e^{i\alpha y} dy = \overline{f}_{,xxxxxx} - 3\alpha^2 \overline{f}_{,xxxx} + 3\alpha^4 \overline{f}_{,xx} - \alpha^6 \overline{f} \tag{2c}$$

The general solutions for the arising ordinary differential equations are generally not difficult to find. The next step is to use the symmetry conditions along the line of the crack to find expressions for the force boundary condition and the crack face deflection. By inverting the expression for the deflection, an integral equation relating the forces acting on the crack plane to the deflection of the crack faces may be found. These integrals contain terms involving the wavelength, α, and lead to singular and hyper-singular expressions. The following integral relationships are required, and arise from the Hadamard finite part of the expression:

$$\int_0^{\infty} \alpha e^{i\alpha(t-y)} d\alpha = \frac{-1}{(t-y)^2} \tag{3a}$$

$$\int_0^{\infty} \alpha^3 e^{i\alpha(t-y)} d\alpha = \frac{6}{(t-y)^4} \tag{3b}$$

$$\frac{1}{k^4} \int_0^{\infty} R\alpha^2 e^{i\alpha(t-y)} d\alpha = \frac{1}{2}\left(K_2\left(k|t-y|\right) - K_0\left(k|t-y|\right)\right) + \frac{3}{z^2} K_2(z) \tag{3c}$$

The resulting hyper-singular integral equations can be solved by expanding the crack face deflections and the crack face loading using Chebychev polynomials of the second kind.

$$U_n(t) = \frac{\sin\left((n+1)\arccos(t)\right)}{\sqrt{1-t^2}} \tag{4}$$

These polynomials obey the following integral identity.

$$\frac{1}{\pi} \int_{-1}^{1} \frac{\sqrt{1-t^2}\, U_n(t)}{(x-t)^2} dt = \begin{cases} -(n+1)U_n(x) & |x| < 1 \\ (n+1)\dfrac{\left(x-\sqrt{x^2-1}\right)^{n+1}}{\sqrt{x^2-1}} & |x| > 1 \end{cases} \tag{5}$$

Joseph and Erdogan [3,4] and Wang and Rose [7] have used this method to form crack-bridging models. In subsequent sections, the method is applied to the six plate models

described above, showing the evolution toward the advanced models resented in chapters three and four.

D.1 Plane stress extension

The plane stress solution follows by assuming vanishing transverse stresses through the thickness of the plate, and is considered valid for thin plates or thick plates with small stress gradients. The governing equations can be derived from an assumed set of displacements with identical results, but here the displacement method has been used to introduce concepts that will be applied to more advanced models. For a plate of thickness 2h, the displacement field is approximated as shown.

$$u_x = u_x(x,y), \quad u_y = u_y(x,y), \quad u_z = \frac{z}{h} w(x,y) \tag{6a,b,c}$$

Integrating through the thickness, and observing the traction-free surfaces of the plate, equilibrium reduces to the following three conditions. For models in which the stresses vary through the thickness, the integrated stresses and equilibrium equations will be expressed in terms of stress resultants, or line forces.

$$\sigma_{xx,x} + \sigma_{xy,y} = 0, \qquad \sigma_{yy,y} + \sigma_{xy,x} = 0, \qquad \sigma_{zz} = 0 \tag{7a,b}$$

The compatibility equations reduce to a single condition, automatically satisfied by the assumed displacements. This is a general characteristic of displacement-based solutions.

$$u_{x,xyy} + u_{y,xxy} = \gamma_{xy,xy} \tag{8}$$

Given the constant $\eta = \nu_z \sqrt{E/E_z}$, the inverted form of the constitutive equations for a transversally isotropic material in plane stress may be expressed in the following form.

$$\sigma_{xx} = \frac{2G}{1-\nu}\left[u_{x,x} + \nu u_{y,y}\right], \quad \sigma_{yy} = \frac{2G}{1-\nu}\left[u_{y,y} + \nu u_{x,x}\right], \quad \tau_{xy} = G\left(u_{x,y} + u_{y,x}\right) \tag{9a,b,c}$$

The transverse displacement is given by the following.

$$w = -\frac{\eta^2}{\nu_z(1-\nu)}\left(u_{x,x} + u_{y,y}\right) \tag{10}$$

Substituting the constitutive equations into the equilibrium equations yields a differential system expressed in terms of the displacements. It is convenient to define two functions.

$$\phi = u_{x,x} + u_{y,y}, \qquad \psi = u_{x,y} - u_{y,x} \tag{11a,b}$$

Adding and subtracting the derivatives of equilibrium equations, we find two harmonic equations.

$$\nabla^2\phi = 0, \qquad \nabla^2\psi = 0 \tag{12a,b}$$

These form a 4th order system if required by the boundary conditions, which are the normal and shear stresses acting on a cut. Denoting boundary data as barred quantities, and defining co-ordinates with directions ξ along the boundary and ς along the outward normal, the boundary conditions follow.

$$\sigma_{\varsigma\varsigma} = \bar{\sigma}_{\varsigma\varsigma}, \qquad \tau_{\xi\varsigma} = \bar{\tau}_{\xi\varsigma} \tag{13a,b}$$

The functions ϕ, ψ describe the normal and shear deflections of the plate. The traditional manner of solving plate extension problems is to note that the equilibrium requires the existence of a stress function, Φ, which is related to the stresses as follows.

$$\sigma_{xx} = \Phi_{,yy}, \qquad \sigma_{xy} = -\Phi_{,xy}, \qquad \sigma_{yy} = \Phi_{,xx} \tag{14a,b,c}$$

The stress function may now be expressed in terms of the introduced functions ϕ, ψ.

$$\nabla^2\Phi = \sigma_{xx} + \sigma_{yy} = \frac{E}{1-\nu}\phi \tag{15}$$

Substitution into (12a) leads to the biharmonic equation, and ψ becomes redundant. For shear deformable plate bending, this simplification is not possible.

$$\nabla^4\Phi = 0 \tag{16}$$

For shear deformable plate bending ϕ and ψ are required throughout the solution as the equilibrium equations are not so easily satisfied.

D.1.1 A cracked plate in plane stress

Using Fourier transforms, we may find the general solution to equation (16). Keeping only the roots that vanish as $x, y \to \infty$.

$$\Phi = \frac{1}{2\pi}\int_{-\infty}^{\infty}\left(A_1 e^{-|\alpha|x} + xA_2 e^{-|\alpha|x}\right) e^{-i\alpha y} d\alpha \tag{17}$$

The frequency, α, is assumed to be the absolute value in the remainder of the development. Symmetry dictates that shear stresses vanish along the line of the crack.

$$\sigma_{xy}(0, y) = -\Phi_{,xy}(0, y) = 0 \tag{18}$$

The stress function reduces to the following.

$$\Phi = \frac{1}{2\pi}\int_{-\infty}^{\infty}\left(e^{-\alpha x} + \alpha x e^{-\alpha x}\right) A_1 \; e^{-i\alpha y} d\alpha \tag{19}$$

From equilibrium (7a), we note that $\sigma_{xx,x}(0, y) = 0$ and by constitutive equation (9a):

$$u_{y,xy} = \frac{1}{1-\nu}\phi_{,x} \tag{20}$$

From constitutive equation (9c), $u_{x,yy} = -u_{y,xy}$ and we find the following:

$$u_{x,yy} = -\left(\frac{1}{1-\nu}\right)\phi_{,x} = -\frac{1}{E}\nabla^2\Phi_{,x} \tag{21}$$

The crack opening displacement, $u(y) = u_x(0, y)$ may now be expressed as follows.

$$u_{,yy}(y) = \frac{1}{2\pi}\int_{-\infty}^{\infty}\frac{-2}{E}\alpha^3 A_1 e^{-i\alpha y}d\alpha \tag{21}$$

Constant A_1 arises from the boundary condition $\sigma_{xx}(0, y) = -\overline{\sigma}(y)$. From (14a) we find an integral expression for the stresses along the crack.

$$\overline{\sigma}(y) = \frac{1}{2\pi}\int_{-\infty}^{\infty}\alpha^2 A_1 e^{-i\alpha y}d\alpha \tag{23}$$

We may now form an integral equation for the crack face rotation. Inverting Fourier transform (22), we find an expression for integration constant A_1.

$$\frac{-2}{E}\alpha^3 A_2 = \int_{-\infty}^{\infty}u_{,tt}(t)\ e^{i\alpha t}d\alpha \tag{24}$$

Integrating by parts twice and noting that displacements must vanish for $|y| \to \infty$:

$$\frac{2}{E}\alpha A_2 = \int_{-\infty}^{\infty}u(t)\ e^{i\alpha t}d\alpha \tag{25}$$

By substitution, we find an integral relating $u(t)$ to the applied stress.

$$\overline{\sigma}(y) = \frac{E}{4\pi}\int_L u(t)\int_{-\infty}^{\infty}\alpha e^{i\alpha(t-y)}d\alpha\ dt \tag{26}$$

By (3a), this may be rewritten as a hyper-singular integral.

$$\overline{\sigma}(y) = \frac{-E}{2\pi}\int_L\frac{u(t)}{(t-y)^2}dt \tag{27}$$

A solution may be found by Chebyshev polynomials expansion. For a crack of length $2a$, non-dimensional parameters $r = t/a$ and $s = y/a$ may be defined and we find:

$$\bar{\sigma}(s)=\frac{-E}{2\pi}\frac{h}{a}\int_{-1}^{1}\frac{u(r)}{(r-s)^2}dr \tag{28}$$

For $\bar{\sigma}(s)$ constant, given $u(r)=\sum_i \sqrt{1-r^2}U_i(r)h_i$, the solution follows from (26).

$$\bar{\sigma}=\frac{-E}{2a}\frac{h_0}{\pi}\int_{-1}^{1}\frac{\sqrt{1-r^2}U_0(r)}{(r-s)^2}dr=\frac{E}{2a}h_0 \tag{29}$$

$$h_0=\frac{2a\bar{\sigma}}{E} \tag{30}$$

The crack face deflection and stresses may now found as follows.

$$u(y)=\frac{2\bar{\sigma}}{E}\sqrt{a^2-y^2}\ ,\quad |y|<a \tag{31a}$$

$$\sigma(y)=\bar{\sigma}\frac{y-\sqrt{y^2-a^2}}{\sqrt{y^2-a^2}},\quad |y|>a \tag{31b}$$

From classical fracture mechanics, the stress intensity in a plane stress plate may be calculated from the tensile stresses or crack-face deflection.

$$k_1=\lim_{y\to a^+}\sqrt{2\pi(y-a)}\sigma_x(0,y) \tag{32a}$$

$$k_1=\lim_{y\to a^-}\frac{E\sqrt{\pi}}{2}\frac{u_x(0,y)}{\sqrt{2(y-a)}} \tag{32b}$$

The stress intensity obeys the classical result.

$$k_1=\bar{\sigma}\sqrt{\pi a} \tag{33}$$

By Irwin [8] the strain energy release rate may be defined as follows, where r is the distance from the crack tip.

$$g_1=\lim_{\delta\to 0}\frac{1}{\delta}\int_0^{\delta}\sigma_x(r)u_x(r)dr \tag{34}$$

Noting that $y=r+a-\delta$, and substituting from (31), we find the classical definition for the strain energy release rate under plane stress conditions.

$$g_1=\frac{\pi a\bar{\sigma}_b^{\,2}}{E}=\frac{k_1^2}{E} \tag{35}$$

D.2 Plane strain extension

The plane strain model follows from the assumption of vanishing transverse strain and is considered to be valid for plates where transverse deformations are restricted by surrounding materials and in regions with very high stress gradients, for example near a crack in a thick plate. Similar to the plane stress solution, the governing equations for plane strain follow from an assumed set of displacements. The transverse strain is assumed to vanish, and the displacement field may be approximated as shown.

$$u_x = u_x(x,y), \quad u_y = u_y(x,y), \quad u_z = 0 \tag{36a,b,c}$$

With the assumption of constant displacements (and stresses) through the thickness, the three-dimensional equilibrium equations reduce to the following. Here, P is the pressure applied to the surfaces of the plate in order to prevent transverse deformation.

$$\sigma_{xx,x} + \sigma_{xy,y} = 0, \qquad \sigma_{yy,y} + \sigma_{xy,x} = 0, \qquad \sigma_{zz} = P \tag{37a,b}$$

The compatibility equations are automatically satisfied, and the inverted form of the constitutive equations may be expressed in the following form.

$$\sigma_{xx} = \frac{2G(1-\eta^2)}{1-\nu-2\eta^2}\left[u_{x,x} + \frac{\nu+\eta^2}{1-\eta^2}u_{y,y}\right] \tag{38a}$$

$$\sigma_{yy} = \frac{2G(1-\eta^2)}{1-\nu-2\eta^2}\left[u_{y,y} + \frac{\nu+\eta^2}{1-\eta^2}u_{x,x}\right] \tag{38b}$$

$$\sigma_{zz} = \frac{2G(1-\eta^2)}{1-\nu-2\eta^2}\left[\frac{\nu_z(1+\nu)}{1-\eta^2}\left(u_{x,x} + u_{y,y}\right)\right] \tag{38c}$$

$$\tau_{xy} = G\left(u_{x,y} + u_{y,x}\right) \tag{38d}$$

Substituting the constitutive equations into the equilibrium equations again yields a fourth order system expressed in terms ϕ, ψ and equilibrium equations require the existence of a stress function, Φ, expressed as follows.

$$\nabla^2\Phi = \sigma_{xx} + \sigma_{yy} = \frac{E}{1-\nu-2\eta^2}\phi \tag{39}$$

As ϕ must obey the harmonic equation, the stress function is biharmonic.

$$\nabla^4\Phi = 0 \tag{40}$$

D.2.1 A cracked plate in plane strain

As for plane stress, the biharmonic equation has the solution given by (14), The solution process is identical, and we may find expressions for the crack face displacement and stresses along the line of the crack.

$$u_{,yy}(y) = \frac{1}{2\pi} \int_{-\infty}^{\infty} -2\frac{1-\eta^2}{E} \alpha^3 A_1 e^{-i\alpha y} d\alpha \tag{41}$$

$$\bar{\sigma}(y) = \frac{1}{2\pi} \int_{-\infty}^{\infty} \alpha^2 A_1 e^{-i\alpha y} d\alpha \tag{42}$$

It is straightforward to find an integral relating the crack face displacement to the applied stress. The form differs from (25) for plane stress by a multiplicative constant.

$$\bar{\sigma}(y) = \frac{-1}{2\pi}\left(\frac{E}{1-\eta^2}\right) \int_L \frac{u(t)}{(t-y)^2} dt \tag{43}$$

Using the non-dimensional parameters r and s again, (43) becomes:

$$\bar{\sigma}(s) = \frac{-1}{2\pi}\left(\frac{E}{1-\eta^2}\right)\frac{h}{a} \int_{-1}^{1} \frac{u(r)}{(r-s)^2} dr \tag{44}$$

Using Chebychev polynomials, the crack face deflection and stresses follow.

$$u(y) = \frac{2\bar{\sigma}(1-\eta^2)}{E}\sqrt{a^2 - y^2}, \quad |y| < a \tag{45}$$

$$\sigma(y) = \bar{\sigma}\frac{y - \sqrt{y^2 - a^2}}{\sqrt{y^2 - a^2}}, \quad |y| > a \tag{46}$$

By classical fracture mechanics, the stress intensity may again be determined from either the tensile stresses or the crack face deflections.

$$k_1 = \lim_{y \to a^+} \sqrt{2\pi(y-a)}\sigma_x(0, y) \tag{47a}$$

$$k_1 = \lim_{y \to a^-} \frac{E\sqrt{\pi}}{2(1-\eta^2)} \frac{u_x(0, y)}{\sqrt{2(y-a)}} \tag{47b}$$

The stress intensity for the plane strain plate extension problem follows.

$$k_1 = \bar{\sigma}\sqrt{\pi a} \tag{48}$$

The strain energy release rate may be determined from equation (34), and we find the classical definition for the strain energy release rate in a plane strain plate.

$$g_1 = \frac{\pi a \overline{\sigma_b}^2 (1-\eta^2)}{E} = \frac{k_1^2 (1-\eta^2)}{E} \tag{49}$$

Equations (35) and (49) are the expressions used to determine the stress intensity in a cracked plate given a strain energy release rate. With no means to distinguish between states of plane stress and plane strain, the arbitrary adoption of one equation or the other can lead to significant errors in the calculation of the stress intensity in a cracked plate.

D.3 Plane stress bending

The plane stress bending model is developed by neglecting transverse stresses and shear deflections. The result is a fourth order system with two boundary conditions, the normal moment and the effective shear stress (Kirchoff) boundary condition, which uses the equilibrium equations to combine the twisting moment and shear force acting on a cut. The development follows from an assumed form for the displacements in the bending plate. For a plate of thickness 2h, the displacement field is approximated as follows:

$$u_x = -z w_{,x}(x,y), \quad u_y = -z w_{,y}(x,y), \quad u_z = w(x,y) + \frac{z^2}{h^2} u_z(x,y) \tag{50a,b,c}$$

The stresses are expressed as stress resultants, or line-forces, in the plate. Integrating through the thickness of the plate, we find the following expressions:

$$M_{xx} = \int_{-h}^{h} \sigma_{xx} z dz, \quad M_{yy} = \int_{-h}^{h} \sigma_{yy} z dz, \quad M_{xy} = \int_{-h}^{h} \tau_{xy} z dz \tag{51a,b,c}$$

$$V_x = \int_{-h}^{h} \tau_{xz} dz, \quad V_y = \int_{-h}^{h} \tau_{yz} dz \tag{52a,b}$$

The equilibrium equations may also be formulated in terms of the stress resultants.

$$M_{xx,x} + M_{xy,y} = V_x, \quad M_{yy,y} + M_{xy,x} = V_y, \quad V_{x,x} + V_{y,y} = -q \tag{53a,b,c}$$

For $\eta = \nu_z \sqrt{E/E_z}$, the inverted form of the constitutive equations for a transversally isotropic material may be expressed as follows. It is assumed that $\sigma_{zz} = 0$.

$$\sigma_{xx} = \frac{2G}{1-\nu}\left[\varepsilon_{xx} + \nu \varepsilon_{yy}\right], \qquad \sigma_{yy} = \frac{2G}{1-\nu}\left[\varepsilon_{yy} + \nu \varepsilon_{xx}\right] \tag{54a,b}$$

$$\varepsilon_{zz} = -\frac{\eta^2}{\nu_z} \frac{\varepsilon_{xx} + \varepsilon_{yy}}{1-\nu} \tag{54c}$$

$$\tau_{xy} = G\gamma_{xy}, \quad \tau_{xz} = G_z\gamma_{xz}, \quad \tau_{yz} = G_z\gamma_{yz} \tag{54d,e,f}$$

By integration through the thickness of the plate, the constitutive equations (54a-f) may be used to express the stress resultants in terms of plate displacements.

$$M_{xx} = -Dh\left[w_{,xx} + \nu w_{,yy}\right], \quad M_{yy} = -Dh\left[w_{,yy} + \nu w_{,xx}\right] \tag{55a,b}$$

$$M_{xy} = -Dh(1-\nu)w_{,xy}, \qquad V_x = V_y = 0 \tag{55c,d}$$

To satisfy the assumed displacement field, which neglects shear deformations, the shear forces must vanish. To proceed with the development of the classical model, we proceed despite this inconsistency. The plate bending constant, D, takes the classic form:

$$D = \frac{4h^2}{3(1-\nu)}G = \frac{2h^2}{3(1-\nu^2)}E \tag{56}$$

For the case of no transverse load, the equilibrium equations (53) reduce to the following.

$$M_{xx,xx} + 2M_{xy,xy} + M_{yy,yy} = 0 \tag{57}$$

Substitution of the constitutive laws (55) leads directly to the bi-harmonic plate model expressed in terms of w, the lateral deflection of the neutral axis of the plate.

$$\nabla^4 w = 0 \tag{58}$$

This system requires two boundary conditions, the normal moment $M_{\varsigma\varsigma}$ and the effective shear force V_ς. The effective shear force or Kirchoff boundary condition arises from the combination of the applied shear force and twisting moment boundary conditions, and provides a means of including the shear force boundary conditions. Denoting boundary data as barred quantities, the boundary conditions follow.

$$M_{\varsigma\varsigma} = \overline{M}_{\varsigma\varsigma}, \quad V_\varsigma = \overline{V}_\varsigma + \overline{M}_{\xi\varsigma,\xi} \tag{59a,b}$$

The direction ξ is along the boundary and ς is along the outward normal.

D.3.1 Bending of a cracked plate under plane stress conditions

Having captured the behaviour of the bending plate, it is possible to develop a solution to the problem of a cracked plate. Applying Fourier transforms in the manner used for the plane stress extension, the plate deflection may be expressed as follows.

$$w = \frac{1}{2\pi}\int_{-\infty}^{\infty}\left(A_1 e^{-|\alpha|x} + A_2 x e^{-|\alpha|x}\right)e^{-i\alpha y}d\alpha. \tag{60}$$

Symmetry dictates that shear stresses vanish along the line of the crack. From (59b), we may now find the symmetry condition.

$$V_x(0,y)+M_{xy,y}(0,y)=0. \tag{61}$$

By substitution from equilibrium equation (53a) and constitutive equations (55a,c) we find the following restriction on the plate deflection w and integration constant A_1.

$$w_{,xxx}+(2-\nu)w_{,xyy}=0, \qquad \alpha A_1=-\frac{1+\nu}{1-\nu}A_2 \tag{62a,b}$$

The crack face rotation, $\beta=\frac{u_x}{h}=-w_{,x}(0,y)$, may now be expressed in a simple form.

$$\beta(y)=\frac{-1}{2\pi}\int_{-\infty}^{\infty}\frac{2}{1-\nu}A_2e^{-i\alpha y}d\alpha \tag{63}$$

The final integration constant arises from the boundary condition $M_{xx}(0,y)=-\overline{M}(y)$. From constitutive equation (55a), we find the following.

$$\overline{M}(y)=\frac{-1}{2\pi}\int_{-\infty}^{\infty}Dh(3+\nu)\alpha A_2e^{-i\alpha y}d\alpha \tag{64}$$

We may now express the moment along the line of the crack in terms of the crack face rotation. Inverting Fourier transform (63), we find an expression for A_2.

$$-\frac{2}{1-\nu}A_2=\int_{-\infty}^{\infty}\beta(t)\ e^{i\alpha t}d\alpha \tag{65}$$

By substitution, we find the following integral equation.

$$\overline{M}(y)=\frac{Dh}{4\pi}(3+\nu)(1-\nu)\int_L\beta(t)\int_{-\infty}^{\infty}\alpha\ e^{i\alpha(t-y)}d\alpha\ dt \tag{66}$$

Observing integral identity (3a), this may be rewritten as a hyper-singular integral.

$$\overline{M}(y)=\frac{-Dh}{2\pi}(3+\nu)(1-\nu)\int_L\frac{\beta(t)}{(t-y)^2}dt \tag{68}$$

With the bending stress given by $\sigma_x(z)=\frac{3M}{2h^2}\frac{z}{h}$, the stress in the outer fibre is given by $\sigma_b=\frac{3M}{2h^2}$ and (68) may be expressed as follows.

$$\overline{\sigma_b}(z)=\frac{-Eh}{2\pi}\left(\frac{3+\nu}{1+\nu}\right)\int_L\frac{\beta(t)}{(t-y)^2}dt \tag{69}$$

This form varies from equation (25) for plane stress extension by a multiplicative constant. Using the non-dimensional parameters r and s, this my be written as:

$$\overline{\sigma_b}(s)=\frac{-E}{2\pi}\left(\frac{3+\nu}{1+\nu}\right)\frac{h}{a}\int_{-1}^{1}\frac{\beta(r)}{(r-s)^2}dr \tag{70}$$

Substituting $\beta(r)=\sum_i\sqrt{1-r^2}U_i(r)h_i$ and making $\overline{\sigma_b}(s)$ constant, only one term is required to find the solution.

$$\overline{\sigma_b}=\frac{-E}{2\pi}\left(\frac{3+\nu}{1+\nu}\right)\frac{h}{a}h_0\int_{-1}^{1}\frac{\sqrt{1-r^2}U_0(r)}{(r-s)^2}dr=\frac{E}{2}\left(\frac{3+\nu}{1+\nu}\right)\frac{h}{a}h_0 \tag{71}$$

$$h_0=\frac{2\overline{\sigma_b}}{E}\left(\frac{1+\nu}{3+\nu}\right)\frac{a}{h} \tag{72}$$

The crack face rotation and bending moment may now found as follows.

$$\beta(y)=2\frac{\overline{\sigma_b}}{Eh}\left(\frac{1+\nu}{3+\nu}\right)\sqrt{a^2-y^2}\,,\quad |y|<a \tag{73a}$$

$$\sigma_b(y)=\overline{\sigma_b}\frac{y-\sqrt{y^2-a^2}}{\sqrt{y^2-a^2}},\quad |y|>a \tag{73b}$$

From (32a,b), the stress intensity may be determined from either the bending stress or the crack face deflection. The stress- and deflection-based definitions give different results, as noted by Erdogan and Joseph [3,4].

$$k_1=\overline{\sigma_b}\sqrt{\pi a} \tag{74a}$$

$$k_1=\left(\frac{1+\nu}{3+\nu}\right)\overline{\sigma_b}\sqrt{\pi a} \tag{74b}$$

The strain energy release rate follows, where r is the distance from the crack tip.

$$g_1=\lim_{\delta\to 0}\ \frac{2}{\delta}\int_0^{\delta}\frac{\sigma_x(r)u_x(r)}{2}dr=\frac{k_1^2}{E}\left(\frac{1+\nu}{3+\nu}\right) \tag{75}$$

The strain energy release rate for plane stress bending is found to differ from the relationship for plane stress plate extension by a multiplicative constant.

D.4 Plane strain bending

Similar to the plate extension, one may also develop a plane strain formulation for plate bending. For a plate of thickness 2h, neglecting shear deformations, the displacement field may be approximated as shown.

$$u_x = -zw_{,x}(x,y), \quad u_y = -zw_{,y}(x,y), \quad u_z = w(x,y) \tag{76a,b,c}$$

Again, the stresses are expressed in terms of stress resultants (51,52), with an extra term arising to account for pressurization of the plate.

$$P_{zz} = \int_{-h}^{h} \sigma_{zz} z dz \tag{53c}$$

The equilibrium equations for plane stress bending (53) do not change. The constitutive equations for a transversally isotropic material in plane strain are expressed as follows.

$$\sigma_{xx} = \frac{2G(1-\eta^2)}{1-\nu-2\eta^2}\left[\varepsilon_{xx} + \frac{\nu+\eta^2}{1-\eta^2}\varepsilon_{yy}\right] \tag{77a}$$

$$\sigma_{yy} = \frac{2G(1-\eta^2)}{1-\nu-2\eta^2}\left[\varepsilon_{yy} + \frac{\nu+\eta^2}{1-\eta^2}\varepsilon_{xx}\right] \tag{77b}$$

$$\sigma_{zz} = \frac{2G\nu_z(1+\nu)}{1-\nu-2\eta^2}\left[\varepsilon_{xx} + \varepsilon_{yy}\right] \tag{77c}$$

$$\tau_{xy} = G\gamma_{xy}, \quad \tau_{xz} = G_z\gamma_{xz}, \quad \tau_{yz} = G_z\gamma_{yz} \tag{77d,e,f}$$

The stress resultants may now be expressed in terms of w by integration.

$$M_{xx} = -Dh\left[w_{,xx} + \frac{\nu+\eta^2}{1-\eta^2}w_{,yy}\right], \quad M_{yy} = -Dh\left[w_{,yy} + \frac{\nu+\eta^2}{1-\eta^2}w_{,xx}\right] \tag{78a,b}$$

$$P_{zz} = -Dh\left[\frac{\nu_z(1+\nu)}{1-\eta^2}\left(w_{,xx} + w_{,yy}\right)\right], \quad M_{xy} = -Dh\left(\frac{1-\nu-2\eta^2}{1-\eta^2}\right)w_{,xy} \tag{78c,d}$$

$$V_x = V_y = 0 \tag{78e}$$

Again, strictly speaking, the model is only valid for vanishing shear forces in the body of the plate. The bending constant takes a different form for plane strain.

$$D = \frac{4h^2}{3}\left(\frac{1-\eta^2}{1-\nu-2\eta^2}\right)G \tag{79}$$

By the same method applied to plane stress bending, the biharmonic equation will arise expressed in terms of the deflection of the plate.

D.4.1 A cracked plate under plane strain bending conditions

The solution follows by the same process as for plane stress bending. Symmetry is enforced using the effective shear boundary condition (61) and the deflection must obey the following relationship.

$$\nabla^2 w_{,x} + \left(\frac{1-\nu-2\eta^2}{1-\eta^2}\right) w_{,xyy} = 0 \tag{80}$$

This leads to the following restriction on integration constant A_1.

$$\alpha A_1 = -\left(\frac{1+\nu}{1-\nu-2\eta^2}\right) A_2 \tag{81}$$

The rotation of the crack face and the bending moment may be expressed as follows.

$$\beta(y) = \frac{-1}{2\pi} \int_{-\infty}^{\infty} 2\left(\frac{1-\eta^2}{1-\nu-2\eta^2}\right) A_2 e^{-i\alpha y} d\alpha \tag{82a}$$

$$\overline{M}(y) = \frac{-1}{2\pi} \int_{-\infty}^{\infty} Dh\left(2 + \frac{1+\nu}{1-\eta^2}\right) \alpha A_2 e^{-i\alpha y} d\alpha \tag{82b}$$

Inverting (82a) and substituting into (82b), we find:.

$$\overline{M}(y) = \frac{Dh}{4\pi}\left(\frac{1-\nu-2\eta^2}{1-\eta^2}\right)\left(2 + \frac{1+\nu}{1-\eta^2}\right) \int_L \beta(t) \int_{-\infty}^{\infty} \alpha\, e^{i\alpha(t-y)} d\alpha\, dt \tag{83}$$

By integral identity (3a), this may be written as a hyper-singular integral.

$$\overline{M}(y) = \frac{-Dh}{2\pi}\left(\frac{1-\nu-2\eta^2}{1-\eta^2}\right)\left(2 + \frac{1+\nu}{1-\eta^2}\right) \int_L \frac{\beta(t)}{(t-y)^2} dt \tag{84}$$

This may be expressed in terms of the bending stress.

$$\overline{\sigma_b}(y) = \frac{-Eh}{2\pi}\left(\frac{1}{1-\eta^2}\right)\left(1 + 2\frac{1-\eta^2}{1+\nu}\right) \int_L \frac{\beta(t)}{(t-y)^2} dt \tag{85}$$

By polynomial expansion, the crack face rotation and bending stress may now found in the same manner as for plane stress bending.

$$\beta(y) = 2\overline{\sigma_b}\left(\frac{1+\nu}{3+\nu-2\eta^2}\right)\left(\frac{1-\eta^2}{Eh}\right)\sqrt{a^2-y^2}, \quad |y| < a \tag{86a}$$

$$\sigma_b(y) = \overline{\sigma_b}\frac{y - \sqrt{y^2 - a^2}}{\sqrt{y^2 - a^2}}, \quad |y| > a \tag{86b}$$

The stress intensity may now be found from (47a,b). Note that the stress- and deflection-based definitions give different results, as found above for plane stress bending.

$$k_1 = \overline{\sigma_b}\sqrt{\pi a} \tag{87a}$$

$$k_1 = \left(\frac{1+\nu}{3+\nu-2\eta^2}\right)\overline{\sigma_b}\sqrt{\pi a} \tag{87b}$$

The strain energy release rate for plane strain bending differs from the relationship for plane strain plate extension by a multiplicative constant.

$$g_1 = k_1^2\left(\frac{1+\nu}{3+\nu-2\eta^2}\right)\left(\frac{1-\eta^2}{E}\right) \tag{88}$$

The inconsistencies observed in the definitions of the stress intensity factors and the strain energy release rate can be addressed by including shear deformations in the plate models, which is the subject of the next section.

D.5 Shear-deformable plane stress bending

Here we develop a 6th order model for bending of a shear-deformable plate. The development follows from the assumption of vanishing transverse stresses. For a plate of thickness 2h, the displacement field may be approximated as shown.

$$u_x = \frac{z}{h}u_x(x,y), \quad u_y = \frac{z}{h}u_y(x,y), \quad u_z = w(x,y) + \frac{z^2}{h^2}u_z(x,y) \tag{89a,b,c}$$

The stress resultants $M_{xx}, M_{yy}, M_{xy}, V_x, V_y$, equilibrium equations, and constitutive equations are identical to those developed for plane stress bending in equations (51) through (54). By integration through the thickness, the constitutive equations may be used to express the stress resultants in terms of the displacements of the plate.

$$M_{xx} = D\left[u_{x,x} + \nu u_{y,y}\right], \qquad M_{yy} = D\left[u_{y,y} + \nu u_{x,x}\right] \tag{90a,b}$$

$$M_{xy} = \frac{2h^2G}{3}\left[u_{x,y} + u_{y,x}\right], \quad V_x = 2G_z\left[u_x + hw_{,x}\right] \tag{90c,d}$$

$$V_y = 2G_z\left[u_y + hw_{,y}\right] \tag{90e}$$

The plate bending constant, D, takes the form for plane stress.

$$D = \frac{4h^2}{3(1-\nu)} G = \frac{2h^2}{3(1-\nu^2)} E \tag{91}$$

Substitution of the constitutive equations (90) into the equilibrium equations (53) yields a system of differential equations expressed in terms of the displacements. It proves convenient to define two functions ϕ, ψ as in (11a,b) Transverse equilibrium then requires ϕ to obey the following condition.

$$\phi = -h\nabla^2 w \tag{92}$$

Adding the derivatives of equations (53a) and (53b), equilibrium in the plane of the plate, and using equation (53c) to cancel the shear stress resultants leads to the following.

$$\nabla^2 \phi = 0 \tag{93}$$

By subtracting the derivatives of equations (53a) and (53b), one finds:

$$\nabla^2 \psi - k_\psi^2 \psi = 0, \text{ where } k_\psi^2 = \frac{3G_z}{h^2 G}. \tag{94}$$

From (92) and (93), we find the biharmonic plate model, $\nabla^4 w = 0$. The shear deflections result in the additional relationship (94) for ψ, resulting in a 6th order system. The three boundary conditions are the normal moment, twisting moment, and shear force. Denoting boundary data as barred quantities, and defining co-ordinates with directions ξ along the boundary and ς along the outward normal, the boundary conditions are:

$$M_{\varsigma\varsigma} = \overline{M}_{\varsigma\varsigma}, \quad M_{\xi\varsigma} = \overline{M}_{\xi\varsigma}, \quad V_\varsigma = \overline{V}_\varsigma. \tag{95a,b,c}$$

The functions ϕ, ψ describe the normal and shear deformations, and lead to a simple derivation of the governing equations, but are not convenient for determining moments or shear forces acting in a plate. Instead, one may define a pair of stress functions. From equilibrium, we note that functions Φ, χ must exist such that.

(96a,b,c) $$M_{xx} = \Phi_{,yy} + \int \chi_{,y} dx, \qquad M_{yy} = \Phi_{,xx} - \int \chi_{,x} dy, \qquad M_{xy} = -\Phi_{,xy}$$

(96a,b) $$V_x = \chi_{,y}, \qquad V_y = -\chi_{,x}$$

From the definition of ψ, and constitutive equations (90d,e) we find the following.

$$\nabla^2 \chi = 2G_z \psi \tag{97}$$

A differential equation for χ may now be found from (94).

$$\nabla^4 \chi - k_\psi^2 \nabla^2 \chi = 0 \tag{98}$$

D.5.1 A shear deformable cracked plate under plane stress conditions

By Fourier transforms, we may find a solution. Keeping roots that vanish as $x, y \to \infty$.

$$w = \frac{1}{2\pi} \int_{-\infty}^{\infty} \left(A_1 e^{-|\alpha| x} + A_2 x e^{-|\alpha| x} \right) e^{-i\alpha y} d\alpha . \tag{99a}$$

$$\psi = \frac{1}{2\pi} \int_{-\infty}^{\infty} \left(B_1 e^{-R_\psi x} \right) e^{-i\alpha y} d\alpha , \text{ where } R_\psi{}^2 = \alpha^2 + k_\psi^2 . \tag{99b}$$

Symmetry dictates that shear stresses vanish along the line of the crack.

$$M_{xy}(0, y) = 0 , \qquad V_x(0, y) = 0 . \tag{100a,b}$$

Shear equations (90d,e) imply the following restrictions along the line of the crack.

$$u_{x,y} + u_{y,x} = 0 , \qquad u_x + h w_{,x} = 0 . \tag{101a,b}$$

The following useful relationships also arise from (101).

$$u_{x,y} = \frac{1}{2}\psi , \quad u_{y,x} = -\frac{1}{2}\psi \tag{102a,b}$$

The first symmetry condition arises from (100a) by substitution from (101a).

$$\psi + 2h w_{,xy} = 0 \tag{103}$$

From equilibrium equation (54a), we find that $M_{xx,x}(0, y) = 0$. Substituting into constitutive equation (90a), we find the second symmetry condition

$$\phi_{,x} + \frac{1}{2}(1-\nu)\psi_{,y} = 0 \tag{104}$$

Symmetry then leads to the following restrictions on the integration constants.

$$B_1 + 2hi\left[A_1 \alpha^2 - A_2 \alpha\right] = 0 , \quad 2A_2 \alpha + \frac{i(1-\nu)}{2h} B_1 = 0 \tag{105a,b}$$

After some manipulation, we find that A_1 and B_1 may be expressed as follows.

$$\alpha A_1 = -\left(\frac{1+\nu}{1-\nu}\right) A_2 , \qquad \frac{i}{2h} B_1 = \frac{-2\alpha}{1-\nu} A_2 \tag{106a,b}$$

The rotation of the crack face, $\beta = -w_{,x}(0, y)$, may be expressed in a simple form.

$$\beta(y) = \frac{-1}{2\pi} \int_{-\infty}^{\infty} \frac{2}{1-\nu} A_2 e^{-i\alpha y} d\alpha \tag{107}$$

The final integration constant arises from the boundary condition $M_{xx}(0, y) = -\overline{M}(y)$, however one must first find an expression for either $u_{x,x}(0, y)$ or $u_{y,y}(0, y)$. This requires consideration of the stress function χ. From equation (98) we find:

$$\chi = \frac{1}{2\pi} \int_{-\infty}^{\infty} \left(C_1 e^{-|\alpha| x} + C_2 e^{-R_\psi x} \right) e^{-i\alpha y} d\alpha \tag{108}$$

From (100b), we find that $C_1 + C_2 = 0$ and χ may be expressed as follows.

$$\chi = \frac{1}{2\pi} \int_{-\infty}^{\infty} C_1 \left(e^{-|\alpha| x} - e^{-R_\psi x} \right) e^{-i\alpha y} d\alpha \tag{109}$$

From equation (97), we find that.

$$C_1 = -2(1-\nu) D B_1 = -2Dhi\alpha A_2 \tag{110}$$

From constitutive equations (90d,e) we find expressions for $u_{x,x}(0, y)$ and $u_{y,y}(0, y)$.

$$u_{x,x} = \frac{\chi_{,xy}}{2G_z} - h w_{,xx}, \qquad u_{y,y} = \frac{-\chi_{,xy}}{2G_z} - h w_{,yy} \tag{111a,b}$$

By constitutive equation (90a), we define the boundary condition $\overline{M}(y) = M(0, y)$.

$$\overline{M}(y) = -D \left[\frac{1-\nu}{2G_z} \chi_{,xy} - h w_{,xx} - \nu h w_{,yy} \right] \tag{112}$$

Substituting for χ, w.

$$\overline{M}(y) = \frac{-Dh}{2\pi} \int_{-\infty}^{\infty} \left((3+\nu)\alpha + \frac{4}{k_\psi^2} (\alpha - R_\psi) \alpha^2 \right) A_2 e^{-i\alpha y} d\alpha \tag{113}$$

We may now form a hyper singular equation for the crack face rotations. Inverting (107), we find an expression for integration constant A_2.

$$-\frac{2}{1-\nu} A_2 = \int_{-\infty}^{\infty} \beta(t)\ e^{i\alpha t} dt \tag{114}$$

Substitution into (113) leads to an equation relating the rotation to the bending moment.

$$\overline{M}(y)=\frac{Dh(1-\nu)}{4\pi}\int_L \beta(t)\int_{-\infty}^{\infty}\left(\alpha+\frac{4}{k_\psi^2}(\alpha-R_\psi)\alpha^2\right)e^{i\alpha(t-y)}d\alpha\,dt \tag{115}$$

Noting the integral identities (3a-c), this may be rewritten as a hyper-singular integral, resulting in the form found from the Riessner bending model [3,4]. Differences are due to the consideration of a transversely isotropic plate and changes to k_ψ resulting from use of a displacement- rather than stress-based formulation. Denoting $z=k_\psi(t-y)$.

$$\overline{M}(y)=\frac{Dhk_\psi^2(1-\nu)}{4\pi}\int_L \beta(t)\left(\frac{-2(3+\nu)}{z^2}+\frac{48}{z^4}-4\left(K_2(z)-K_0(z)\right)-\frac{24}{z^2}K_2(z)\right)dt \tag{116}$$

Separating the strongly singular parts from the Modified Bessel functions, one may define a function $L_\psi(z)$ from the regular and weakly singular parts such that.

$$L_\psi(z)=-\frac{48}{z^4}+\frac{4}{z^2}+4\left(K_2(z)-K_0(z)\right)+\frac{24}{z^2}K_2(z) \tag{117}$$

The moment along the line $x=0$ may now be expressed as follows.

$$\overline{M}(y)=\frac{-Dhk_\psi^2(1-\nu)}{4\pi}\int_L \beta(t)\left(\frac{2(1+\nu)}{z^2}+L_\psi(z)\right)dt \tag{118}$$

Expressed in terms of the bending stress, this may be written in the simpler form.

$$\overline{\sigma_b}(y)=\frac{-Ghk_\psi^2}{2\pi}\int_L \beta(t)\left(\frac{2(1+\nu)}{z^2}+L_\psi(z)\right)dt \tag{119}$$

For a short crack, $L_\psi(z)$ vanishes, and we find the expression for plane stress extension.

$$\overline{\sigma_b}(y)=\frac{-Eh}{2\pi}\int_L \frac{\beta(t)}{(t-y)^2}dt \tag{120}$$

D.6 Shear-deformable plane strain bending

Here we develop a plane strain formulation for a shear deformable plate, assuming a form for the displacements by which the transverse strains vanish.

$$u_x=\frac{z}{h}u_x(x,y),\quad u_y=\frac{z}{h}u_y(x,y),\quad u_z=w(x,y) \tag{121a,b,c}$$

The stress resultant and equilibrium equations are identical to equations (51) through (53), and the assumed displacement field satisfies compatibility. The constitutive equations (77) may be used to express the stress resultants in terms of the displacements.

$$M_{xx} = D\left[u_{x,x} + \frac{\nu+\eta^2}{1-\eta^2}u_{y,y}\right], \qquad M_{yy} = D\left[u_{y,y} + \frac{\nu+\eta^2}{1-\eta^2}u_{x,x}\right] \tag{122a,b}$$

$$P_{zz} = D\left(\frac{\nu_z(1+\nu)}{1-\eta^2}\right)\left[u_{x,x} + u_{y,y}\right], \qquad M_{xy} = \frac{D}{2}\left(\frac{1-\nu-2\eta^2}{1-\eta^2}\right)\left[u_{x,y} + u_{y,x}\right] \tag{122c,d}$$

$$V_x = 2G_z\left[u_x + hw_{,x}\right], \qquad V_y = 2G_z\left[u_y + hw_{,y}\right] \tag{122e,f}$$

The plate bending constant, D, takes the form for plane strain bending.

$$D = \frac{4h^2}{3}\left(\frac{1-\eta^2}{1-\nu-2\eta^2}\right)G \tag{123}$$

The remainder of the derivation is identical to that for shear deformable plane stress bending. The result is the same set of equations, which describe a 6th order system.

$$\nabla^4 w = 0. \tag{124a}$$

$$\nabla^2\psi - k_\psi^2\psi = 0, \qquad k_\psi^2 = \frac{3G_z}{h^2 G}. \tag{124b}$$

The stress function χ takes the same form.

$$\nabla^4\chi - k_\psi^2\nabla^2\chi = 0 \tag{125}$$

D.6.1 A shear deformable cracked plate under plane strain conditions

Differences between the plane stress and plane strain shear deformable plate models arise only from the definition of the constitutive equations (122) and the plate constant (123). Solutions to (124a,b) and (125) are:

$$w = \frac{1}{2\pi}\int_{-\infty}^{\infty}\left(A_1 e^{-|\alpha|x} + A_2 x e^{-|\alpha|x}\right)e^{-i\alpha y}d\alpha. \tag{126a}$$

$$\psi = \frac{1}{2\pi}\int_{-\infty}^{\infty}\left(B_1 e^{-R_\psi x}\right)e^{-i\alpha y}d\alpha, \text{ where } R_\psi{}^2 = \alpha^2 + k_\psi^2. \tag{126b}$$

$$\chi = \frac{1}{2\pi}\int_{-\infty}^{\infty}\left(C_1 e^{-|\alpha|x} + C_2 e^{-R_\psi x}\right)e^{-i\alpha y}d\alpha \tag{126c}$$

Symmetry requires $M_{xy}(0, y) = 0$ and $V_x(0, y) = 0$, leading to the following conditions.

$$\psi + 2hw_{,xy} = 0, \qquad \phi_{,x} + \frac{1}{2}\left(\frac{1-\nu-2\eta^2}{1-\eta^2}\right)\psi_{,y} = 0, \quad \chi_{,x} = 0 \tag{127a,b,c}$$

Observing these symmetry conditions, equations (126a,b,c) will become:

$$w=\frac{1}{2\pi}\int_{-\infty}^{\infty}\left(x-\frac{1+\nu}{1-\nu-2\eta^2}\frac{1}{\alpha}\right)A_2e^{-|\alpha|x}e^{-i\alpha y}d\alpha\,. \tag{128a}$$

$$\psi=\frac{1}{2\pi}\int_{-\infty}^{\infty}4ih\frac{1-\eta^2}{1-\nu-2\eta^2}\alpha A_2e^{-R_\psi x}e^{-i\alpha y}d\alpha \tag{128b}$$

$$\chi=\frac{1}{2\pi}\int_{-\infty}^{\infty}-2ihD\alpha A_2\left(e^{-|\alpha|x}-e^{-R_\psi x}\right)e^{-i\alpha y}d\alpha \tag{128c}$$

The rotation of the crack face, $\beta=-w_{,x}(0,y)$, may now be expressed in a simple form.

$$\beta(y)=\frac{1}{2\pi}\int_{-\infty}^{\infty}2\frac{1-\eta^2}{1-\nu-2\eta^2}A_2e^{-i\alpha y}d\alpha \tag{129}$$

The last boundary condition $M_{xx}(0,y)=-\overline{M}(y)$ may be arises from equation (122a).

$$\overline{M}(y)=-D\left[\frac{1-\nu-2\eta^2}{2G_z(1-\eta^2)}\chi_{,xy}-hw_{,xx}-\frac{\nu+\eta^2}{1-\eta^2}hw_{,yy}\right] \tag{130}$$

Substituting for χ, w.

$$\overline{M}(y)=\frac{-Dh}{2\pi}\int_{-\infty}^{\infty}\left(\left(2+\frac{1+\nu}{1-\eta^2}\right)\alpha+\frac{4}{k_\psi^2}(\alpha-R_\psi)\alpha^2\right)A_2e^{-i\alpha y}d\alpha \tag{131}$$

Inverting (129) and substituting for A_2 results in an integral equation relating the crack face rotation to the bending moment.

$$\overline{M}(y)=\frac{Dh}{4\pi}\left(\frac{1-\nu-2\eta^2}{1-\eta^2}\right)\int_L\beta(t)\int_{-\infty}^{\infty}\left(\left(2+\frac{1+\nu}{1-\eta^2}\right)\alpha+\frac{4}{k_\psi^2}(\alpha-R_\psi)\alpha^2\right)e^{i\alpha(t-y)}d\alpha\,dt \tag{132}$$

By (3a-c), a hyper-singular integral arises. Here, $z=k_\psi(t-y)$ and $L_\psi(z)$ is unchanged.

$$\overline{M}(y)=\frac{-Dhk_\psi^2}{4\pi}\left(\frac{1-\nu-2\eta^2}{1-\eta^2}\right)\int_L\beta(t)\left(\left(\frac{1+\nu}{1-\eta^2}\right)\frac{2}{z^2}+L_\psi(z)\right)dt \tag{133}$$

This may be expressed in terms of the stress in the outer fibre.

$$\overline{\sigma_b}(y)=\frac{-Ghk_\psi^2}{2\pi}\int_L\beta(t)\left(\left(\frac{1+\nu}{1-\eta^2}\right)\frac{2}{z^2}+L_\psi(z)\right)dt \tag{134}$$

For a short crack, the regular part vanishes and this reduces to the form for plane strain extension.

$$\overline{\sigma_b}(y) = \frac{-1}{2\pi}\left(\frac{Eh}{1-\eta^2}\right)\int_L \frac{\beta(t)}{(t-y)^2}dt \tag{135}$$

D.7 References

[1] Reissner E. The effect of transverse shear deformation on the bending of elastic plates. Journal of Applied Mechanics 12, 1945, A69-77

[2] Mindlin RD. Influence of rotary inertia and shear on flexural motions of isotropic, elastic plates. Journal of Applied Mechanics 18, 1951, 31-38

[3] Joseph PF and Erdogan F. Surface crack problems in plates. International Journal of Fracture 41, 1989, 105-131

[4] Joseph PF and Erdogan F. Plates and shells containing a surface crack under general loading conditions. NASA CR178232, NASA Langley Research Centre, 1987.

[5] Muskhelishvilli NI. Some Basic Problems in the Mathematical Theory of Elasticity. P. Noordhoff, 1953

[6] Westergaard HM. Bearing Pressures and Cracks. Journal of Applied Mechanics 6, 1939, 49-53

[7] Wang CH and Rose LRF. A crack bridging model for bonded plates subjected to tension and bending. International Journal of Solids and Structures 36, 1999, 1985-2014

[8] Irwin GR. Analysis of Stresses and Strains Near the End of a Crack Traversing a Plate. Journal of Applied Mechanics 24, 1957, 361-364

Appendix E: Material properties

E.1 Boron/Epoxy 5521/4 Laminate

Following are the material properties for Textron Specialty Materials Boron 5521/4

Thickness	0.132 mm (0.0052 in)
Resin content (wt.)	33%
Cure cycle	2.2-3.3°C (4-6°F) per minute to 120°C (250°F) 60 minutes at 120°C (250°F)
Cure pressure	345-586 kPa (50-85 psi)
Test temperature	Room temperature
Longitudinal Tensile Modulus	210 GPa (30 msi)
Transverse Tensile Modulus	25 GPa
Longitudinal Compressive Modulus	210 GPa (30 msi)
Longitudinal Poisson's Ratio	0.21
Transverse Poisson's Ratio	0.019
Ultimate Tensile Stress	1520 MPa (220 msi)
Ultimate Compressive Stress	2930 MPa (425 msi)
Ultimate Interlaminar Shear Stress	97 MPa (14.1 msi)
Coef. Of Thermal Expansion	4.5 PPM/°C (2.5 PPM/°F)
Density	2 g/cm^3 (0.072 lbm/in^3)

Table E-1: Material properties for 5521/4 boron/epoxy

E.2 Aluminum 2024-T3 (A-Basis)

Mechanical properties for 2024-T3 aluminum in the rolling direction [98] are;

Thickness	3.175 mm (0.125 in)
Test temperature	Room temperature
Tensile Modulus	72.4 GPa (10.5 msi)
Compressive Modulus	73.8 GPa (10.7 msi)
Shear Modulus	27.6 GPa
Poisson's Ratio	0.33
Tensile Yield Stress	331 MPa (48 ksi)
Compressive Yield Stress	276 MPa (40 ksi)
Shear Yield Stress	276 MPa (40 ksi)
Ultimate Tensile Stress	448 MPa (65 ksi)

Table E-2: Material properties for aluminum 2024-T3 (A-basis)

E.3 Adhesive FM 73M

The properties for Cytec's FM 73M follow. Note the properties were measured without pre- or post-bond environmental exposure [99].

Thickness	0.25 mm (0.010 in)
Nominal weight	300 g/m^2 (0.06 psf)
Primer	BR 127
Cure cycle	30 minutes to 120°C
	60 minutes at 120°C
Cure pressure	280 MPa (40 psi)
Test temperature	24°C
Shear Modulus	842 MPa (122 ksi)
Elastic Shear Stress	17.3 MPa (2510 psi)
Elastic Shear Strain	0.021
Ultimate Shear Stress	40.9 MPa (5.93 ksi)
Ultimate Shear Strain	0.873

Table E-3: Material properties for adhesive FM-73